Quantum Wires in Shallow Heterostructures

by Christopher Barton

Thesis submitted to the University of Glasgow's

Department of Physics and Astronomy

for the degree of

Doctor of Philosophy. March 1995

Acknowledgements

Abstract

In order to maximise the temperature at which the quantisation of the conductance is resolved in quasi-one dimensional GaAs-Al$_x$Ga$_{1-x}$As structures, the induced sub-bands must be widely spaced in energy. For surface gated structures, this requires that feature sizes are below 100nm and that the two dimensional electron gas (2DEG) is formed near the surface (~30nm). Achieving sub 100nm feature sizes makes strong demands on electron beam lithography processes but suitable techniques, described in Chapter 2 have made it possible to routinely fabricate such structures. Developing a heterostructure which can exploit these feature sizes is a much more difficult task, but this too has been successful. Capacitance and magneto-transport measurements which have helped in this development process are described in detail in Chapter 4. In addition, problems in understanding various parameters such as carrier concentration and threshold voltages are analysed closely. It becomes clear when analysing the data that the characteristics of GaAs-Al$_{0.3}$Ga$_{0.7}$As heterostructures are explicable in terms of simple electrostatic models. It is found that applying the same model to heterostructures which include spacer layers of GaAs-AlAs in place of the conventional Al$_{0.3}$Ga$_{0.7}$As is complicated by evidence of free charge in the donor region at low temperatures. The transport experiments also show strong evidence of such charge accumulation.

A comprehensive investigation of the smearing of the conductance quantisation with increasing temperature and source-drain is presented in Chapter

5. The sub-band spacing and the temperatures at which the quantisation smears are compared for various devices fabricated on the optimised heterostructure i.e. where the 2DEG is formed 28nm below the surface. Comparisons are also made with similar measurements carried out on two other heterostructures where the 2DEG is formed at depths of 40nm and 107nm. The data is used to determine the experimental sub-band spacing in the devices and they are found to be consistent with smaller sub-band spacings in heterostructures where the 2DEG is formed at a greater depth. The experimental sub-band spacings also compare fairly well to theoretical calculations using the actual device geometry. An equivalence between the thermal and electric smearing measurements is also discussed but no evidence is found that anything other than smearing due to broadening of the differential Fermi function is responsible for the washing out of the sub-band structure.

Finally in Chapter 6 experiments are presented which map out the distance over which the conductance quantisation is robust to scattering in the optimised heterostructure. In this particular structure the donors are only separated from the 2DEG by 11nm and as such, scattering is expected to be strong. It is therefore surprising that quantisation persists in wires up to 400nm long. Conventional modelling of the donors as a fully ionised random distribution of charge cannot explain why this is the case. Similar discrepancies are also found when the mobility in the 2DEG is compared with the theoretical prediction. The possibility that this is evidence for correlations in the position of ionised donors is discussed.

Contents

Histograms

List of Figures

xviii

Tables

Chapter 1

Introduction and Theoretical Overview

1.1 Introduction

In this chapter various aspects of the formation of a silicon doped heterostructure from layers of GaAs and $Al_xGa_{1-x}As$ will be discussed. In particular, the electrostatics of the heterostructure are reviewed, along with the charge state of the silicon impurities in the structure. The formation of a two dimensional electron gas (2DEG) at the GaAs-$Al_xGa_{1-x}As$ interface is also described. The low temperature transport properties of this region are explained with particular consideration being given to the effect of additional electrostatic confinement into quasi-one dimensional channels. Finally, electronic conduction is described in both two and one dimensions, with a magnetic field perpendicular to transport plane.

1.2 GaAs-$Al_xGa_{1-x}As$ Heterostructures

A crystal grown from two or more different types of semiconductor is known as a heterostructure. The successful formation of a heterostructure requires

manipulation of the growth process on an atomic scale. It was therefore not until the advent of sophisticated processes like molecular beam epitaxy (MBE) [1], that structures were grown successfully [2, 3]. The interfaces between the different semiconductors which make up a heterostructure are called heterojunctions. Either side of a heterojunction the semiconductors will have different band gaps and hence there will be discontinuities in the conduction and valence bands. These discontinuities can cause the formation of accumulation and depletion regions. The application of simple electrostatic arguments, first proposed by Anderson [4], can be used to give a clear physical picture into how an ideal heterojunction forms and the relative extent of the inversion layers.

Consider two isolated n-type semiconductors with different energy gaps ($E_{g1, 2}$), work functions ($\phi_{1, 2}$), electron affinities ($\chi_{1, 2}$), dielectric constants ($\varepsilon_{1, 2}$) and chemical potentials ($\mu_{1, 2}$), where subscripts 1 and 2 refer to the smaller and larger band gap materials respectively, see Figure 1.1. The vacuum level is used as a reference and space charge neutrality is assumed to exist in both the semiconductors giving horizontal conduction and valance bands. The difference in energy between the conduction bands (E_{c1} and E_{c2}) is denoted by ΔE_c and from inspecting Figure 1.1, it is clear that this sharp discontinuity can be expressed in terms of the electron affinities, χ_1 and χ_2, see Equation 1.1.

$$\Delta E_c = e(\chi_1 - \chi_2) \tag{1.1}$$

Figure 1.2 depicts the situation on forming the heterojunction. In this diagram the electrostatic potential difference between any two points is represented by a vertical displacement, and the electric field is represented by the gradient of the band edges. Charge flows due to the difference in the chemical potentials either side of the interface. An equilibrium is eventually set up and further flow of charge is prevented as diffusion is balanced by the electric field created between the ionised donors and the free electrons at the

Figure 1.1: Schematic energy band diagram for two isolated n-type semiconductors with different band gaps.
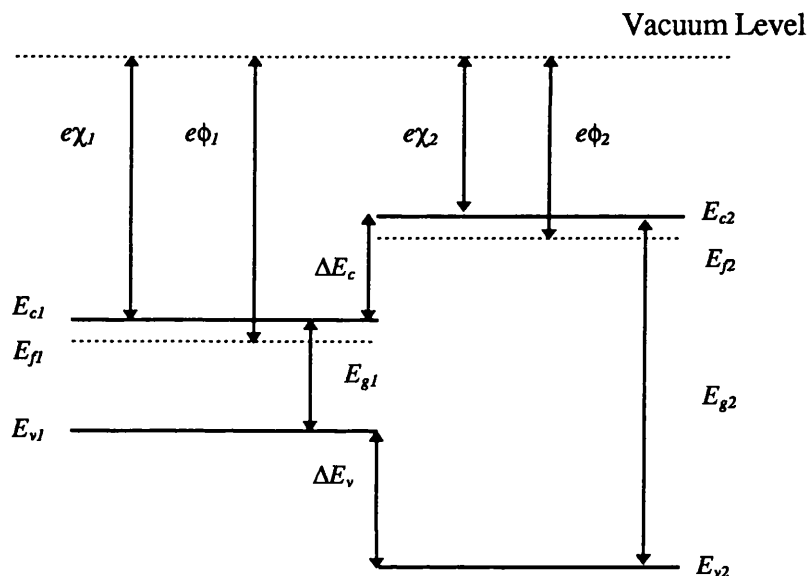
Figure 1.2: Schematic energy band diagram illustrating the formation of an n-n heterojunction at equilibrium.
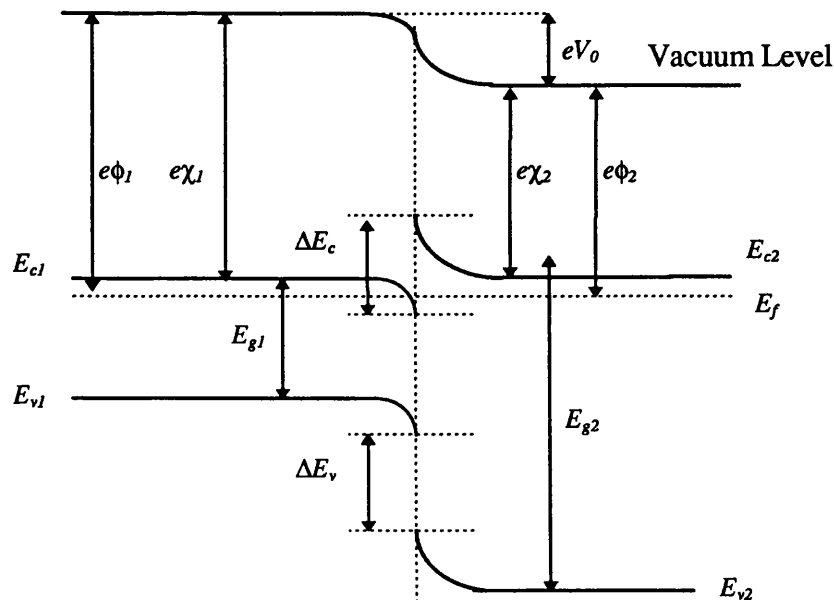
heterojunction. The chemical potential will now be equal either side of the interface and the junction has a total built-in potential V_0.

1.2.1 Modulation Doped GaAs-Al$_x$Ga$_{1-x}$As Heterostructure

The modulation doped GaAs-Al$_x$Ga$_{1-x}$As heterostructures, engineered by molecular beam epitaxy, have long been the subject of experimental investigation [5-7]. The importance of these structures lies in confining the doping to the Al$_x$Ga$_{1-x}$As material. The band bending at the heterojunction, and the requirement to maintain a constant chemical potential throughout the structure, leads to ionisation of the impurities in the Al$_x$Ga$_{1-x}$As and transfer of electrons across the interface. On crossing the heterojunction, the carriers are confined in a potential well that has formed in the GaAs as a result of the discontinuity ΔE_c in the conduction band, see Figure 1.3 [9, 10].

Figure 1.3: Schematic energy diagram illustrating the band bending in a GaAs-Al$_{0.3}$Ga$_{0.7}$As heterostructure and the formation of quantised energy levels in the triangular well.
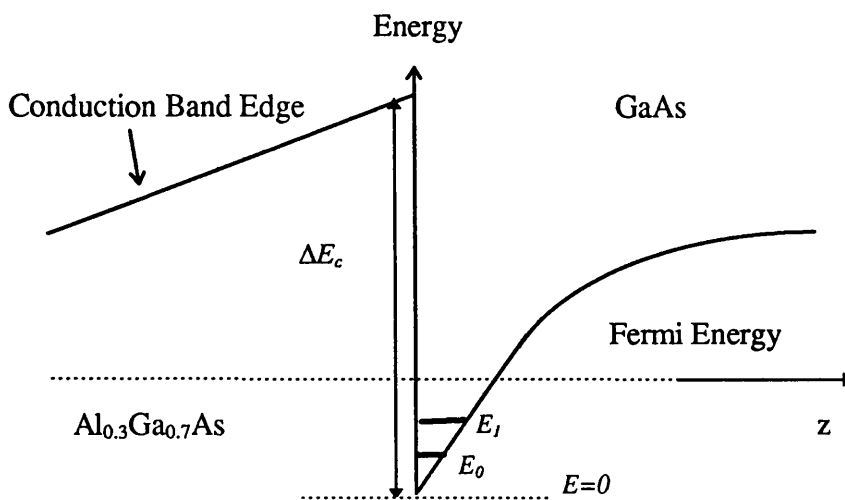
The confinement of the carriers can be very strong, leading to a potential well commensurate in size with the Fermi wavelength. Assuming an isotropic semiconductor that has energy bands in three dimensions which can be approximated by parabolic wells, we arrive at the dispersion relationship given in Equation 1.2 for the allowed carrier energies $E_n(k)$ in the well. E_n are the energy eigenstates associated with the quantisation of energy perpendicular to the heterojunction, m^* is the effective mass of an electron in GaAs and k_x and k_y are the wave vectors associated with electron transport in the x and y planes.

$$E_n(k) = E_n + \frac{\hbar^2 k_x^2}{2m^*} + \frac{\hbar^2 k_y^2}{2m^*} \qquad (1.2)$$

Hence, E_n forms the bottom of a band of allowed energy states associated with motion parallel to the interface. Each group of energy states is known as a sub-band. The formation of sub-band structure has surprising implications for the density of states in the potential well. Consider the number of states in two dimensional k-space $n(k)\delta k$ that lie in the interval $k \rightarrow k + \delta k$

$$n(k)\delta k = D(k)2\pi k\delta k \qquad (1.3)$$

where $D(k) = 1/(2\pi)^2$ is the density of states per spin in two dimensions. If $D(E)$ is the density of states in the corresponding energy interval $E \rightarrow E + \delta E$, then the total number of states in this energy interval will be given by

$$D(E)\delta E = n(k)\delta k = \frac{1}{(2\pi)^2} 2\pi k\delta k$$

$$\Rightarrow \quad D(E) = g_s g_v \left[\frac{2\pi}{k} \frac{dE_n(k)}{dk} \right]^{-1}$$

where g_s accounts for the spin degeneracy of the electron and $g_v=1$ accounts for the valley degeneracy of the conduction band edge in GaAs. Using Equation 1.2 to substitute for E gives

$$D(E) = \frac{g_s g_v m^*}{\pi \hbar^2} \qquad \text{for } E > E_o \qquad\qquad (1.4a)$$

and

$$D(E) = 0 \qquad \text{for } E < E_o \qquad\qquad (1.4b)$$

From Equations 1.4a and b it is clear that the density of states is a constant in any sub-band, and zero below the first sub-band edge. As the energy increases, more of the sub-bands become populated and the density of states increases in units of $m^*/\pi\hbar^2$, see Figure 1.4 [11].

Figure 1.4: Graph illustrating the quasi-two dimensional electronic density of states which result from confinement at the interface of a suitably engineered GaAs-Al$_{0.3}$Ga$_{0.7}$As heterostructure.
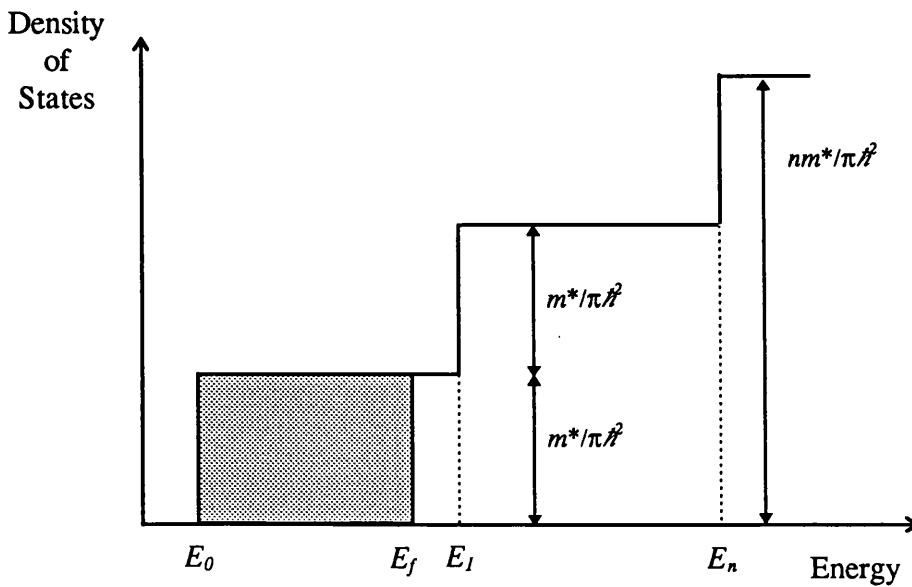
So if the doping level in the $Al_xGa_{1-x}As$ is chosen carefully, it is possible to reduce the Fermi energy to a level such that only the first sub-band can become occupied. This sub-band is then referred to as a two dimensional electron gas (2DEG). The main importance of a 2DEG is the greatly reduced ionised impurity scattering due to the spatial separation of the conduction electrons in the undoped GaAs from the donors in the $Al_xGa_{1-x}As$. Additional reduction in ionised impurity scattering can be achieved by including a region of undoped $Al_xGa_{1-x}As$ between the donor centres and the confined electrons. Finally, the formation of an accumulation layer at the interface also helps to screen out the effects of background impurities in the GaAs substrate and together all of these effects result in large increases in mobility.

1.2.2 *DX* Centres

GaAs has a zincblende lattice structure consisting of two interpenetrating face centred cubic lattices with one lattice having Ga atoms and the other having As atoms. The basis is a Ga and As diamond tetrahedral structure with alternate Ga and As atoms, see Figure 1.5 [12]. The bonding is covalent, with the electrons in the outer shells being shared between the Ga and As atoms. In order to provide conduction electrons for the 2DEG, it is necessary to dope GaAs with group IV silicon atoms. The silicon atom is a hydrogenic substitutional donor in GaAs, taking the place of one group III Ga atom. It is known that substitutional doping of GaAs causes a small amount of lattice distortion and results in an energy level lying approximately 260meV above the Γ conduction band minima [13]. This excited state, for historical reasons, is known as a *DX* state and is thought to be stabilised by the capture of two electrons. Because the state has such a high occupation energy, it is difficult to detect and the semiconductor must either be heavily doped, or the conduction band shifted by application of hydrostatic pressure before it can be stabilised. In $Al_xGa_{1-x}As$, silicon is again a substitutional

atom on a Ga site, but in this case the lattice is strongly distorted by the substitution of the Al alloy. These atoms replace Ga atoms and give rise to four possible *DX* states depending on whether there are zero, one, two or three Al nearest neighbours [14].

Figure 1.5: Three dimensional representation of the GaAs crystal lattice.
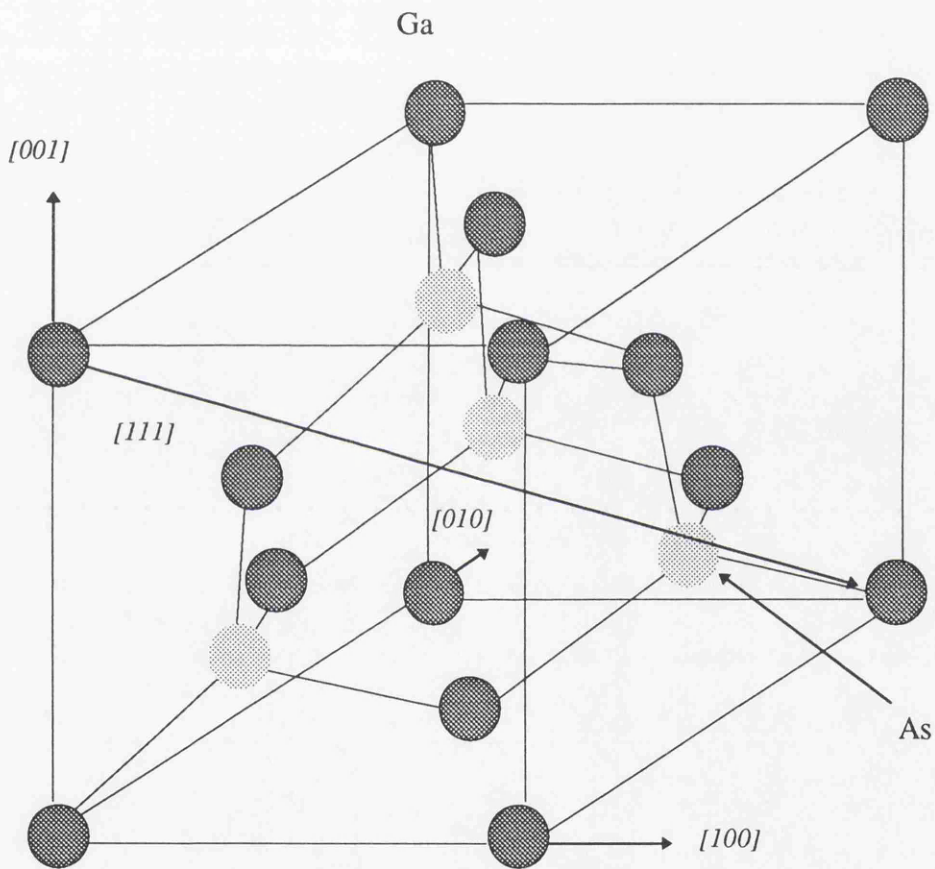
The microscopic model of *DX* states is based on the calculations of Chadi and Chang [15, 16] and describes the breaking of a bond between the Si donor and one of its' As neighbours. The silicon atom moves along the <111> axis to an interstitial site where it lies very close to three group III Ga atoms. This configuration is then stabilised by the trapping of two electrons. For GaAs, the

nearest neighbours to the distorted Si donor are all Ga, hence the single DX state. For $Al_xGa_{1-x}As$, the substitutional Al atom gives rise to configurations with zero, one, two or three possible non-equivalent substitutions of the alloy for a Ga atom. It is these substitutions that lead to the experimental observation of the four DX states shown in Figure 1.6 ($DX0$, $DX1$, $DX2$, $DX3$).

In thermal equilibrium, the stabilising of DX states by electron capture depends on the relative position of the energy level to the conduction band minimum and this is strongly dependent on the relative aluminium mole fraction, see Figure 1.6. For an aluminium mole fraction of 0.3 or higher, the DX levels are ground states for electrons in the Γ conduction band minimum, which means that emission and capture processes should occur frequently. This manifests itself experimentally in time, bias and temperature dependencies of the depletion characteristics of surface gated devices that include $Al_xGa_{1-x}As$ layers [17]. The temperature dependencies of the emission and capture processes are particularly interesting because they provide further information on the energy structure of the DX state. As the temperature drops, an energy barrier, associated with emission and capture of electrons by DX centres, becomes apparent. The rates drop until below some temperature (~100K) the signatures of DX activity (in particular, shifts in the threshold voltages) are no longer apparent. The threshold voltages are generally much lower, implying that there are far fewer free electrons in the structure and the high temperature threshold voltage is only recovered after intense illumination [18].

The energy transitions implied by these observations can be expressed concisely on a configuration co-ordinate diagram, see Figure 1.7. The parabola labelled $2U_\Gamma$, which has its minimum at Q_0, represents the energy for the conduction band containing two electrons, whereas the higher parabola is the energy for one electron in the conduction band. The parabola which has its minima near Q_T, represents the donor in the distorted metastable $2U_{DX}^-$, DX configuration. The formation of the DX^- state, which is occupied by

Figure 1.6: Graph illustrating the alloy composition dependence of the conduction band minima and the important donor related levels observed in $Al_xGa_{1-x}As$ [14]. The energy scale in referenced to the top of the valance band in GaAs.
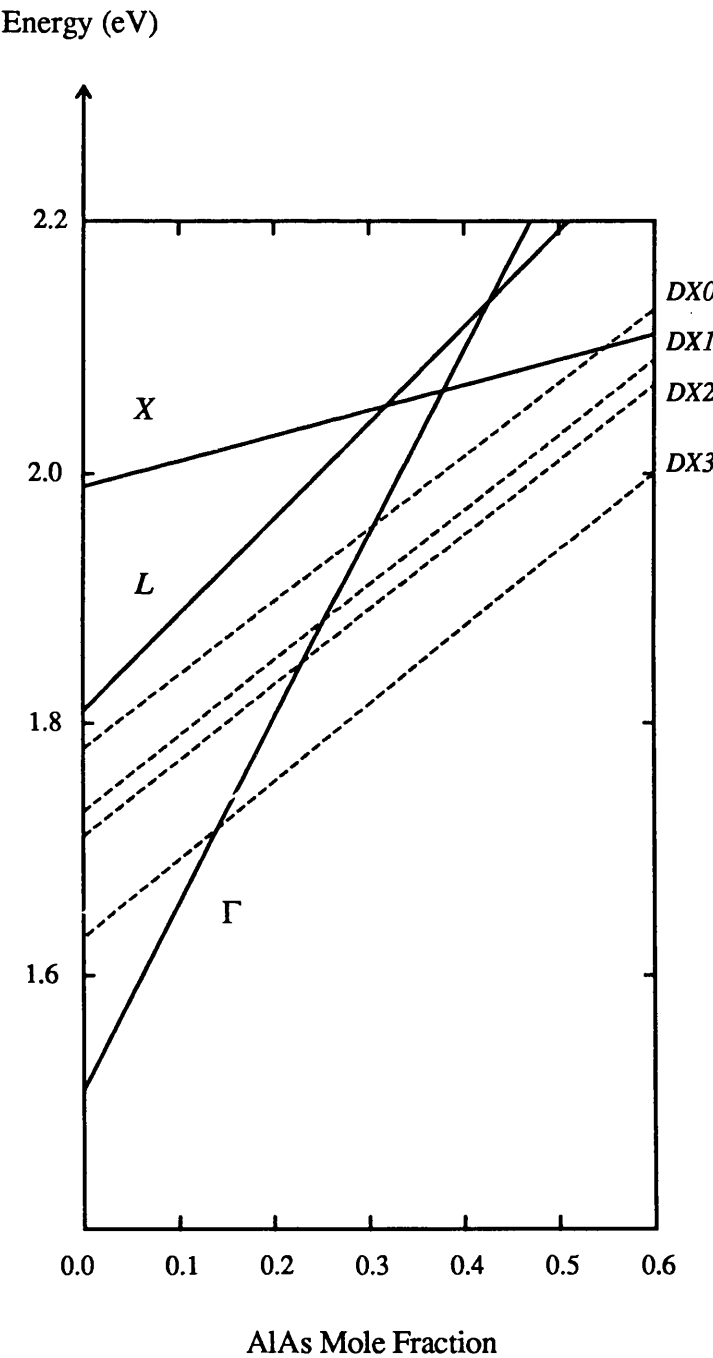
Figure 1.7: Configuration coordinate diagram illustrating the negative U model for the DX centre in $Al_xGa_{1-x}As$ [14].

Electronic Plus Elastic Energy
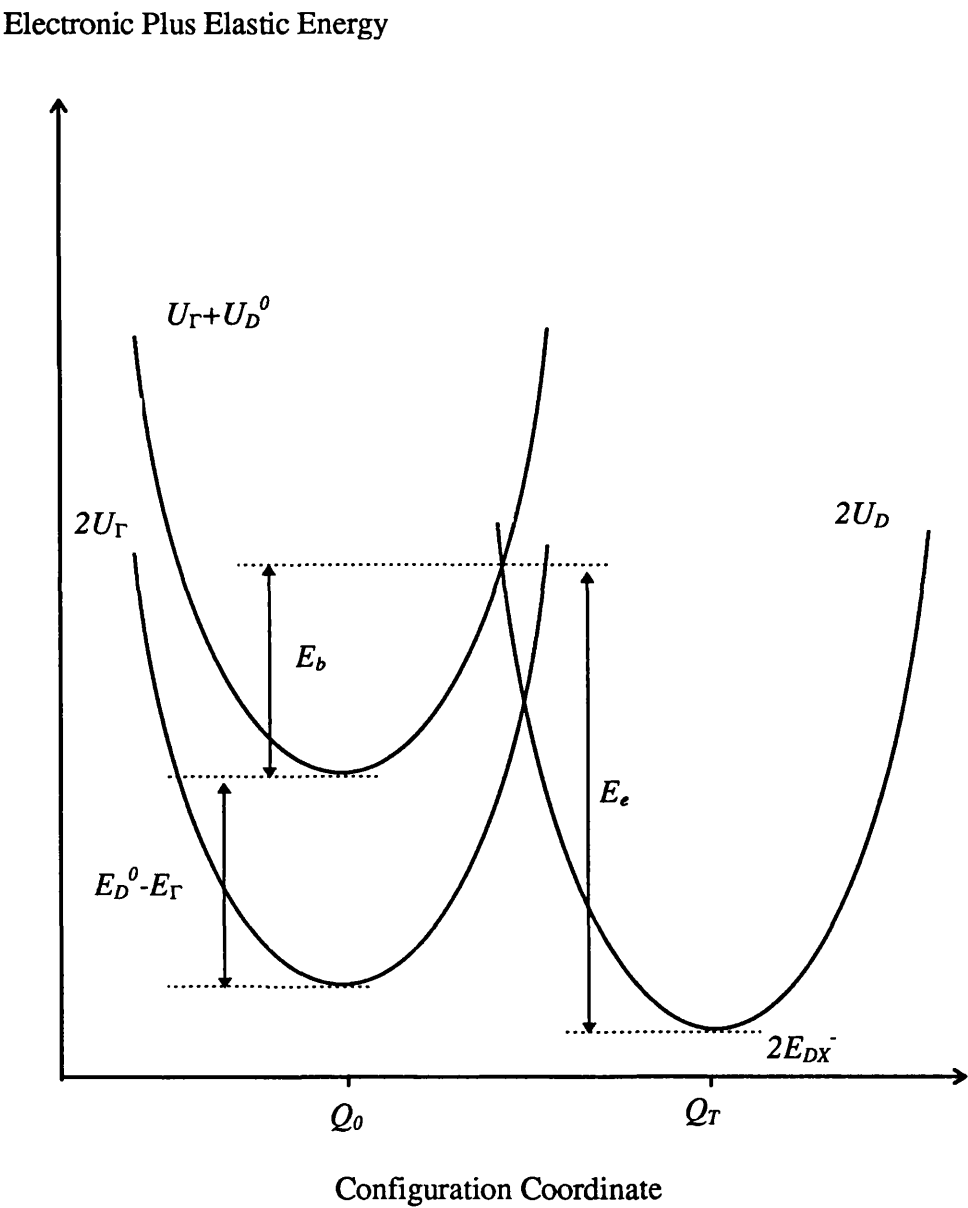
two electrons, is assumed to occur via the excited one electron state $U_\Gamma + U_D^0$. This process requires not only an energy equal to the difference between the two energy levels, but also a substantial quantity of energy to enable the lattice to distort and shift the configuration of the donor from Q_0 to Q_T.

Figure 1.8: Schematic of the energy barriers associated with capture ΔE_b and emission ΔE_e from the DX state. The energy barrier related to donor activation ΔE_T is also illustrated.
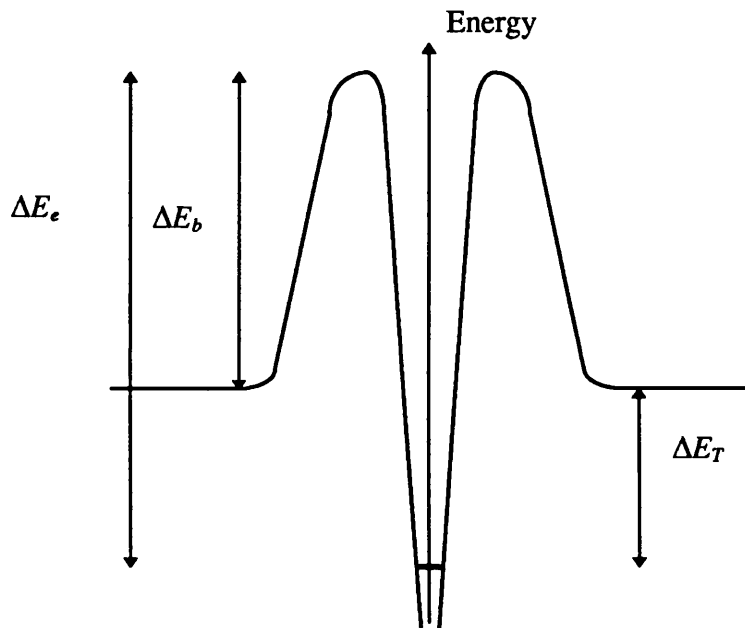
Once in the neutral state, capture of an electron and lattice distortion takes the donor into the metastable DX^- state. At low temperatures, the reduction in phonon activity means that DX states become frozen because the energy necessary to distort the lattice is no longer available. Electrons are trapped in these states and can no longer be depleted by the application of a voltage bias. However, it is still possible to cause ionisation of the DX centres at low temperatures if the structure is illuminated with radiation which supplies an energy greater than ΔE_e. The energy barriers associated with capture (ΔE_b) and emission (ΔE_e) of electrons

from the *DX* state are illustrated in Figure 1.8. The donor activation barrier ΔE_T is also included.

1.2.3 Two Dimensional Electron Gas (2DEG)

A 2DEG formed at the interface of a GaAs-Al$_x$Ga$_{1-x}$As heterostructure is usually characterised by the mobility and carrier concentration of the confined electrons. The carrier concentration ideally depends only on the spacer width, the pinning energy of the chemical potential by deep donor states and the conduction band offset, see Figure 1.9. In order to accurately understand these dependencies, it is necessary to find the energy levels in the 2DEG. This is done by solving Poisson's equation to find the confining potential, while simultaneously taking into account the effects on this potential of populating the potential well. If the effect of the electron population on the energy levels in the well is ignored, then too high a value for the position of the energy levels is deduced. This is because the maximum field generated by the electrons is used, whereas in reality, it is more likely to be substantially lower. Hence for accurate results a self-consistent solution of Poisson's equation and Schrödinger's equation is required, taking into account all energy related effects for the electronic charge distribution in the 2DEG. Having said this, much can be learned simply by approximating the confinement as a triangular potential well and solving Poisson's equation in order to find the magnitude of the confining potential [19]. The problem then reduces to simply finding the eigenstates of this potential well [20] and integrating the charge throughout the structure.

Assuming that the Fermi energy is pinned on the deep donor *DX* states at an average energy E_{dd} below the conduction band and that tunnelling out of the 2DEG can be neglected at low temperatures, then the carrier concentration n_{2D} in a 2DEG of effective thickness a is given by Equation 1.5 [18].

$$n_{2D} = \frac{(\Delta E_c - E_{dd})\varepsilon_0}{\left(\frac{s}{\varepsilon_a} + \frac{a}{\varepsilon_g}\right)e^2} \tag{1.5}$$

Figure 1.9: Conduction band edge in a slab doped GaAs-Al$_x$Ga$_{1-x}$As heterostructure with a surface potential V_0 and a Fermi energy E_F. The two dimensional electron gas is formed at a distance $c+u+s$ from the surface of the structure and in this illustration there is one bound sub-band E_0. The conduction band off-set between the GaAs and Al$_x$Ga$_{1-x}$As conduction bands is ΔE_c and the deep donor pinning energy is E_{dd}. Notice that the models assume that the doped region is neutral i.e. equal numbers of positive and negative charges due to DX occupation.
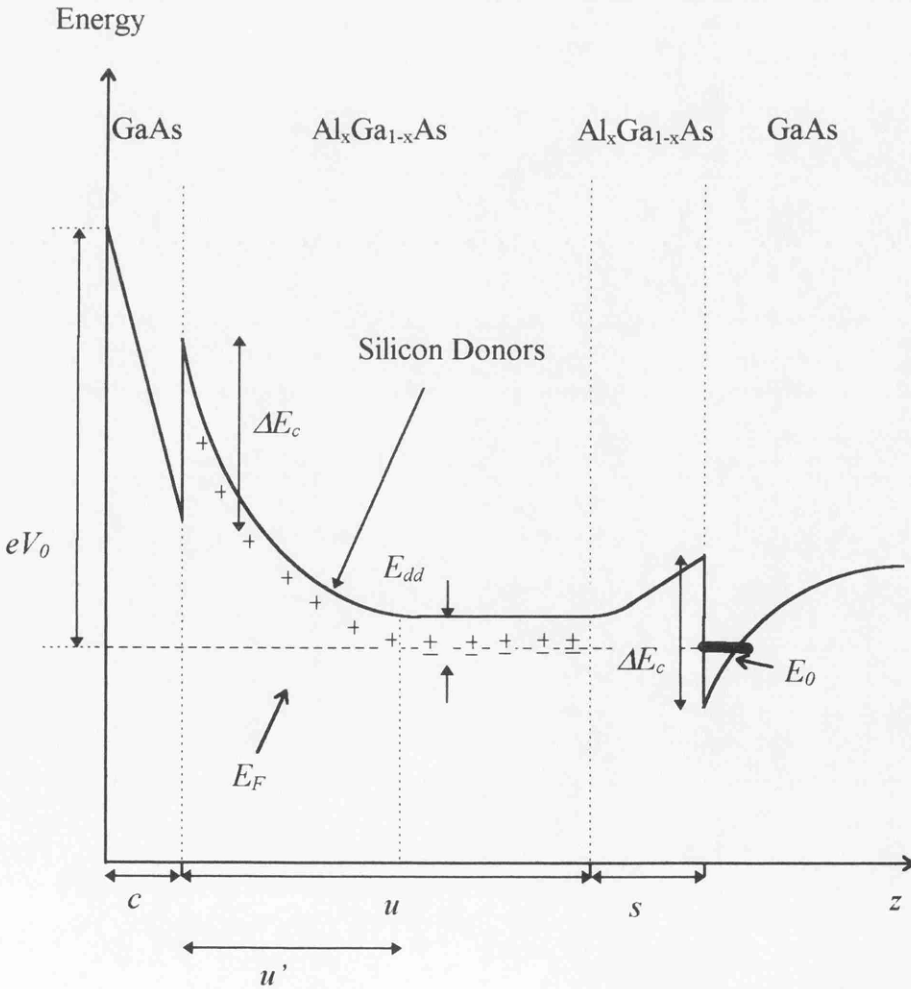
In addition, it can readily be shown that the conduction band edge E_c can be expressed as a function of the electric field in $Al_xGa_{1-x}As$ F_a at the 2DEG interface (defined as $z=0$), donor concentration N_d, cap thickness c, and a geometric parameter u' which defines the spatial extent of the depletion region, see Equation 1.6.

$$E_c(0) = -eF_a\left(\frac{a\varepsilon_a}{\varepsilon_g} + s\right) + \frac{N_d e^2}{\varepsilon_0}\left(\frac{u'^2}{2\varepsilon_a} + \frac{u'c}{\varepsilon_g}\right) \tag{1.6}$$

1.2.4 Schottky Gated GaAs-Al$_x$Ga$_{1-x}$As Heterostructure [18]

Once a heterostructure has been designed and grown to have a specific carrier concentration, it is still possible to vary this concentration by applying an external electric field. This is done by evaporating a Schottky contact onto the surface of the heterostructure, and then connecting the contact to an external voltage source. In order to understand how depletion of the donors takes place, it is necessary to understand the role played by DX centres in the dopant region. There are two cases that need to be considered, depending on whether the DX centres in the donor region can be depleted. At high temperatures the DX centres are active and respond to the application of gate bias. Hence when all the donors have been depleted the depletion region u' covers the entire region u and the electric field in $Al_xGa_{1-x}As$ F_a at the 2DEG interface is zero. At this point charge is completely removed from the channel i.e the threshold condition $V_g=V_T$. Hence assuming that the surface states are in equilibrium with the gate electrode [21], then the conduction band edge at the surface of the heterostructure is given by Equation 1.7, where V_0 is the potential of the free GaAs surface.

$$E_c(0) = e(V_0 - V_g) = e(V_0 - V_T) \tag{1.7}$$

Hence substituting into Equation 1.6 for $E_c(0)$ with $u'=u$ and F_a set to zero gives

$$e(V_0 - V_T) = \frac{N_d e^2}{\varepsilon_0}\left(\frac{u^2}{2\varepsilon_a} + \frac{uc}{\varepsilon_g}\right)$$

(1.8)

Thus Equation 1.8 enables the onset of depletion V_T to be calculated. This is in contrast to the low temperature regime where the *DX* centres are not active and hence cannot be depleted (frozen). In this case, there is an extra contribution δV_T^f to the surface potential due to their electric field F'_a, see Equation 1.9.

$$\delta V_T^f = eF'_a\left(u + \frac{c\varepsilon_a}{\varepsilon_g}\right)$$

(1.9)

Hence the conduction band edge at the surface of the heterostructure for frozen *DX* centres is given by

$$E_c(0) = e(V_0 - V_T^f) = e(V_0 - V_T - \delta V_T^f)$$

giving

$$E_c^f(0) = \frac{N_d e^2}{\varepsilon_0}\left(\frac{u'^2}{2\varepsilon_a} + \frac{u'c}{\varepsilon_g}\right) + eF'_a\left(u + \frac{c\varepsilon_a}{\varepsilon_g}\right)$$

(1.10)

Solving Poisson's equation to find F'_a, Equation 1.10 can be simplified to give an expression for the bias at which the channel starts to deplete in terms of the geometry of the heterostructure and the zero bias carrier concentration in the 2DEG, see Equation 1.11.

$$V_T^f = -\frac{e}{\varepsilon_0} n_{2D} \left(\frac{c}{\varepsilon_g} + \frac{u}{\varepsilon_a} + \frac{s}{\varepsilon_a} + \frac{a}{\varepsilon_g} \right) \tag{1.11}$$

The threshold voltage in this frozen approximation depends strongly on the doping level and the thickness of the doping regions. This effectively puts a limit on the minimum threshold voltage that can be designed into a heterostructure for a given doping density.

1.2.5 Electron Transport in a Two Dimensional Electron Gas

Classically, with the application of an electric field $\underline{F}$ in the plane of a 2DEG, electrons are accelerated until they experience some scattering event after some time τ. At low temperatures, the dominant mechanism which sets the scale of τ is elastic scattering from ionised impurities and this leads to transport being governed by a mean drift velocity

$$\underline{v}_{drift} = \frac{e\tau}{m^*} \underline{F} = \mu_e \underline{F} \tag{1.12}$$

where the mobility of the electrons in the 2DEG has been introduced to characterise the magnitude of the elastic scattering. Substitution of the current density $\underline{j} = e n_{2D} \underline{v}_{drift} = \sigma \underline{F}$ into Equation 1.12 gives

$$\sigma = \frac{e n_{2D} \underline{v}_{drift}}{\underline{v}_{drift} / \mu_e} = e \mu_e n_{2D} \tag{1.13}$$

where σ is known as the Drude conductivity. Experimentally it is the conductance G that is measured and this is related to the conductivity of a sample of width W and length L through Equation 1.14.

$$G = \frac{W}{L}\sigma = \frac{W}{L}e\mu_e n_{2D} = \frac{e^2}{h}\frac{W}{L}\frac{k_F l}{2} \qquad (1.14)$$

where a length scale l has been introduced to represent the mean distance between elastic collisions i.e. the mean free path of the electrons. Equation 1.14 describes the elastic scattering of electrons at the Fermi surface with wave vectors k_F and can now be used to define three different transport regimes: diffusive, quasi-ballistic and ballistic, depending on the relative size of the mean free path compared to the sample dimensions, see Figure 1.10.

In the diffusive case, where $L, W >> l$, the sample contains a large number of scattering centres and Equation 1.14 measures the mobility and mean free path in the 2DEG associated with elastic scattering from these centres. Inelastic scattering is generally weak at these temperatures and electrons lose their phase coherence over a length $l_\phi > l$ which is frequently larger than the dimensions of the sample. This in itself is interesting as it leads to novel interference effects from phase differences acquired by electron waves travelling between the same points by different trajectories [23, 24]. In the ballistic limit, where $L, W << l$, Equation 1.14 does not hold as there are no scattering centres in the sample. In this regime the conductivity, as defined in Equation 1.13, has no meaning and the conductance is determined solely by sample geometry [25] and specular scattering from the sample boundaries [26]. The intermediate case of quasi-ballistic transport, $W < l < L$, is where the conductance is determined by a combination of specular boundary effects and impurity related elastic scattering events.

Figure 1.10: Illustration of electron trajectories in the diffusive ($l << L$, W), quasi-ballistic ($W < l < L$) and ballistic ($l >> L$, W) regimes with specular boundary scattering [22].
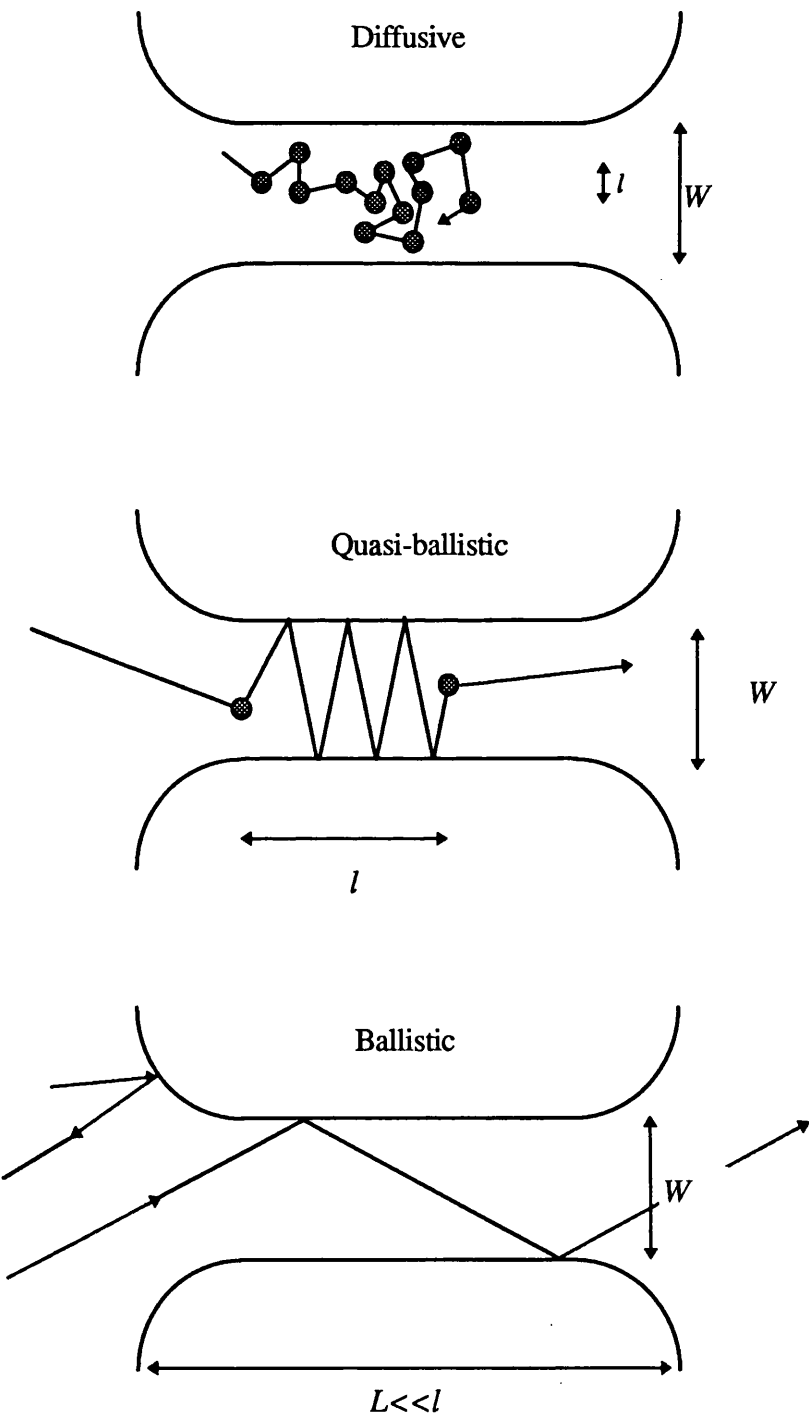
1.3 Transport in Reduced Dimensions

In this section, quasi-one dimensional electron transport will be discussed in terms of transmission probability matrices. The generalisation of this formalism to multi-channels is also discussed. Finally, the dependence of the quasi-one dimensional conductance on small increases in temperature and source drain bias is analysed.

1.3.1 Adiabatic Quasi-One Dimensional Transport [27]

Adiabatic Quasi-one dimensional transport is transport in the ballistic regime determined by the Hamiltonian

$$H = \frac{p_x^2}{2m*} + \frac{p_y^2}{2m*} + eV(x) \tag{1.15}$$

where the transition from the wide 2DEG region to the constriction defined by the potential V(x) is assumed to be smooth. If the confinement is commensurate with the Fermi wavelength of the electrons in the 2DEG, then assuming a parabolic confinement potential, the Schrödinger equation for the electrons leads to the dispersion relationship

$$E_n(k) = \left(n - \frac{1}{2}\right)\hbar\omega_0 + \frac{\hbar^2 k_y^2}{2m*} \qquad n = 1,2,etc \tag{1.16}$$

Hence $\left(n - \frac{1}{2}\right)\hbar\omega_0$ forms the bottom of a band of allowed energy states associated with free motion in the y direction and separated in energy by $\hbar\omega_0$. Electrons will

Figure 1.11: Illustration of the subband energy versus longitudinal wave vector k_y. The net current results from the electronic states in the interval μ_1-μ_2 where μ_1 and μ_2 are the chemical potentials either side of the constriction [28].
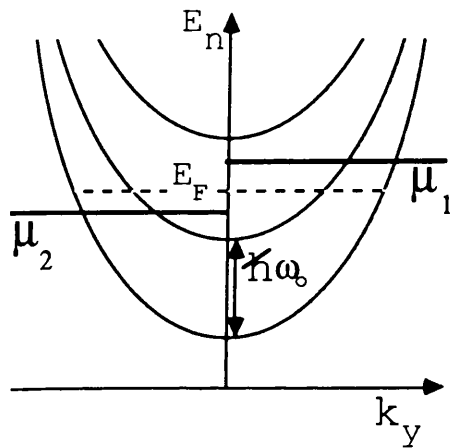
Figure 1.12: Schematic representation of the density of states in quasi-one dimensions showing four occupied energy levels.
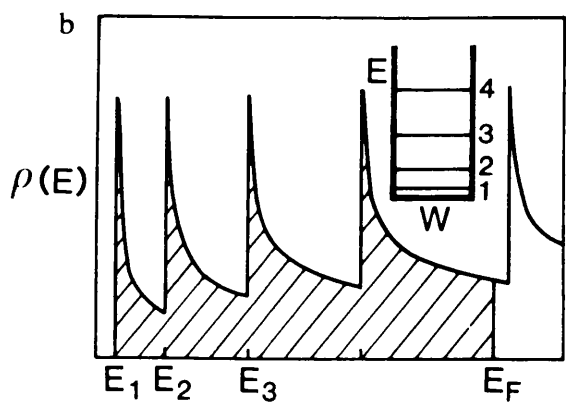
occupy n of these parabolic bands or sub-bands, depending on the Fermi energy in the constriction, see Figure 1.11.

In order to calculate the current carried in the nth occupied sub-band it is necessary to know the density of states $D(k)$, which in one dimensional k-space is given by $1/2\pi$. The total number of states in the k-space interval $k \to k + \delta k$ will then be $D(k)\delta k$ and the equivalent number of states in the energy interval $E \to E + \delta E$ will then be given by

$$D(E)\delta E = D(k)\delta k$$

Hence

$$D(E) = \left(2\pi \frac{dE}{dk} \right)^{-1} \tag{1.17}$$

Plotting this function in Figure 1.12 shows the quasi one dimensional nature of the density of states associated with the sub-band structure described above. Now consider the transport picture illustrated in Figure 1.13.

Figure 1.13: Illustration of various transport parameters which govern conduction through a quasi-one dimensional constriction.
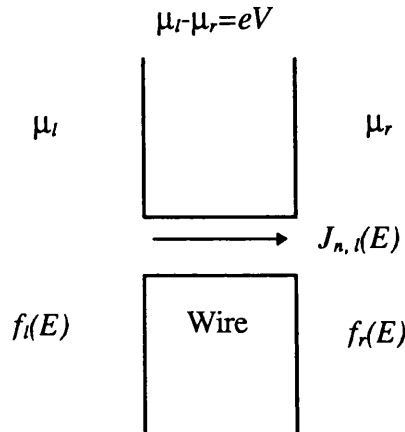
A current $J_n(E)$ flows in the nth sub-band with a group velocity $v_n(E)$ due to the difference in the Fermi distribution functions either side of the constriction i.e.

$$j_n(E) = \frac{2e}{h} \int\limits_{-\infty}^{+\infty} D(E) v_n(E) T_n(E) (f(E,\mu_l) - f(E,\mu_r)) dE \qquad (1.18)$$

Where $T_n(E)$ is a transmission probability relating the incident flux of electrons in sub-band n and the integral includes the contribution to the current from all conduction electrons either side of the constriction.

$$v_n = \left(\frac{1}{\hbar} \frac{dE_n}{dk} \right)_E \qquad (1.19)$$

Substituting the group velocity (Equation 1.19) and the density of states (Equation 1.17) into Equation 1.18 gives

$$j_n = \frac{2e}{h} \int\limits_{-\infty}^{+\infty} (f(E,\mu_l) - f(E,\mu_r)) T_n(E) dE \qquad (1.20)$$

i.e. the current $J_n(E)$ is independent of sub-band index n due to the unique property of the density of states in one dimension. This reflects the fact that although states with higher values of n will have higher group velocities associated with them, they do not carry larger currents because of the smaller density of states. Finally the total transmitted current involves a sum over all values of n and is expressed as

$$I = \sum_{n=1}^{N} \frac{2e}{h} \int\limits_{-\infty}^{+\infty} [(f(E,\mu_l) - f(E,\mu_r)) T_n(E)] dE \qquad (1.21)$$

At low bias ($eV=\mu_l-\mu_r<<k_BT$), where μ is the equilibrium chemical potential, the difference in the Fermi function can be expanded as a Taylor series over the range $\mu_l=\mu+eV$ to $\mu_r=\mu-eV$. Hence

$$I = \sum_{n=1}^{N} \frac{2e}{h} \int_{-\infty}^{+\infty} eV \frac{df(E,\mu)}{d\mu} T_n(E)dE \qquad (1.22)$$

and so

$$I = \sum_{n=1}^{N} \frac{2e}{h} \int_{-\infty}^{+\infty} eV \left(-\frac{\partial f(E,\mu)}{\partial E}\right) T_n(E)dE \qquad (1.23)$$

The final form for the current I comes from the dependence of the Fermi function $f(E,\mu)$ on $E-\mu$. Now at low temperatures, the Fermi function will be much sharper than any features in $T_n(E)$ and so the differential Fermi function can then be replaced by the delta function $\delta(E-\mu)$ giving

$$I = \frac{2e^2}{h} V \sum_{n=1}^{N} T_n(\mu) \qquad (1.24)$$

Rearranging to give the conductance G, shows that the conductance of the constriction is equi-partitioned in units of $2e^2/h$ between the N available sub-bands.

$$G = \frac{2e^2}{h} \sum_{n=1}^{N} T_n(\mu) \qquad (1.25)$$

1.3.2 Multi-Mode Transport [29]

In the previous section, it was assumed that transport was adiabatic, i.e. that the scattering between the N different sub-bands could be ignored. However when a real constriction is formed, the conduction band bottom rises to a height E_c above the conduction band bottom in the bulk 2DEG [30]. This saddle like potential barrier causes the kinetic energy of the electrons to reduce, increasing their Fermi wavelength and making them more susceptible to inter-sub-band scattering. This is not so important because the total transmission probability will remain the same. A more important problem is that if the potential profile varies sharply enough, then the electrons can undergo backscattering processes which will lead to conduction through the wire not being simply determined by the Fermi distribution of electrons to the immediate right and left. Clearly it is important to be able to describe the scattering between all the various propagating modes, in order to be able to accurately understand the conductance in real devices. The starting point of the more realistic analysis is the observation that any particular wavefunction describing propagation in mode m, immediately to the left (l) of the constriction, can be expressed as the sum of the initial incident wave vector k_m^l and all other possible backscattered waves vectors k_n^l, from the n other propagating modes, see Equation 1.26 where r_{nm} is the reflection coefficient describing the various scattering mechanisms that mix the different modes together. Similarly the wavefunction for all the electrons on the right which were injected into a mode m, can be expressed by using a transmission coefficient t_{nm} describing how mode m becomes mixed into a mode n. Summing over all n will then account for all scattering processes in the constriction, see Equation 1.27.

$$\psi_{left} = exp(ik_m^l z) + \sum_{n=1}^{\infty} r_{nm} \, exp(-ik_n^l z) \tag{1.26}$$

$$\Psi_{right} = \sum_{n=1}^{\infty} t_{nm} \, exp(ik_n^r z) \tag{1.27}$$

Hence the transmission probability amplitude $T_n(\mu)$ used in Equation 1.25, can be modified to include all inter-sub-band mixing to give

$$G = \frac{2e^2}{h} \sum_m \sum_n |t_{nm}|^2 \tag{1.28}$$

In the analysis above, Equation 1.28 was derived assuming only two connections to the constriction. However it is more usual to use four leads, where two are used to pass current (current probes) and two are used to measure voltage (voltage probes). The generalisation of Equation 1.28 to four leads is given by Equation 1.29 where T_{nm} represents the transmission probability from lead n to lead m, see Appendix A for a full derivation [31].

$$G_{12,34} = \frac{2e^2}{h} \frac{(T_{31}T_{42} - T_{32}T_{41})}{(T_{21}T_{31} + T_{21}T_{32} + T_{31}T_{23})} \tag{1.29}$$

1.3.4 Thermal and Electric Smearing of Conductance Quantisation

Consider the physical picture described by Equation 1.21 in Section 1.3.1. This can be written in terms of the conductance G and the difference in the Fermi functions $f(E-eV/2)$ and $f(E+eV/2)$, either side of the wire, where e is the electronic charge, V is the potential difference and E denotes energy.

$$G = \frac{2e^2}{h} \sum_n \int \frac{dE}{eV} \left[f\left(E - \frac{eV}{2}\right) - f\left(E + \frac{eV}{2}\right) \right] T_n(E) \tag{1.30}$$

Defining

$$g_n = \frac{G}{2e^2/h} \qquad v = \frac{eV}{k_B T} \quad \text{and} \quad \xi = \frac{E}{k_B T}$$

(1.31)

and assuming that $T_n(E)$ is a Heaviside function of E_n then for one mode

$$g_n = \int_{\xi_n}^{\infty} \frac{d\xi}{v} \left[\frac{1}{e^{\xi - \frac{v}{2}} + 1} - \frac{1}{e^{\xi + \frac{v}{2}} + 1} \right]$$

(1.32)

evaluating the integral gives

$$g_n = \left\{ 1 - \frac{1}{v} \ln \left[\frac{1 + e^{\xi_n + \frac{v}{2}}}{1 + e^{\xi_n - \frac{v}{2}}} \right] \right\}$$

(1.33)

In the limit $v \ll 1$ this reduces to

$$g_n \approx \left\{ 1 - \frac{1}{v} \ln \left[\frac{1 + \left(1 + \frac{v}{2}\right) e^{\xi_n}}{1 + \left(1 - \frac{v}{2}\right) e^{\xi_n}} \right] \right\}$$

(1.34)

which simplifies to

$$g_n \approx 1 - \frac{e^{\xi_n}}{1 + e^{\xi_n}} = f(\xi_n)$$

(1.35)

Now the quantisation can be analysed in terms of the maxima in the differential conductance with respect to the gate voltage V_g. Hence differentiating Equation 1.35 to express the problem in these terms gives

$$\frac{dg_n}{dE_n} = \frac{1}{k_B T}\frac{dg_n}{d\xi} = \frac{1}{k_B T}\left[\frac{e^{\xi_n - \frac{v}{2}}}{1 + e^{\xi_n - \frac{v}{2}}} - \frac{e^{\xi_n + \frac{v}{2}}}{1 + e^{\xi_n + \frac{v}{2}}}\right]$$ (1.36)

This function has a maximum value when the nth sub-band coincides with the Fermi energy i.e. $\xi_n = 0$ when measured with respect to the Fermi level. Hence

$$\frac{dg_n}{dE_n} = \frac{1}{eV}tanh\left(\frac{eV}{4k_B T}\right)$$ (1.37)

Equation 1.37 can now be used to compare the effect of an increase in the temperature with an increase in the source-drain bias on the quantisation of the conductance. Clearly Equation 1.38 shows that increasing the voltage dropped across the wire to a value V has an equivalent effect to increasing the temperature to a value $eV/4k_B$.

As $\quad V \rightarrow 0 \qquad \dfrac{dg_n}{dE_n} \rightarrow \dfrac{1}{4k_B T}$

$$\Rightarrow \quad T \equiv \frac{eV}{4k_B}$$ (1.38)

As $\quad \dfrac{V}{k_B T} \gg 1 \qquad \dfrac{dg_n}{dE_n} \rightarrow \dfrac{1}{eV}$

In order to compare the experimental smearing temperatures and voltages with the model, it is necessary to look at the region $\Delta E \leq k_B T \ll E_F$ ($\Delta E \leq eV/4 \ll E_F$), where $\Delta E = E_{n+1} - E_n$ is the sub-band spacing in the wire. In this regime the 'high

temperature' conductance g_0 can be expressed approximately as a sum of the number of sub-bands propagating below the Fermi energy, see Equation 1.39

$$g_0 \approx \frac{E_F}{\Delta E} \approx n - \frac{1}{2} \qquad (1.39)$$

where a parabolic well has been assumed for the shape of the confinement potential. If the well is filled up to the nth energy level and E_n is measured with respect to the Fermi energy then clearly

$$E_n = \left(n - \frac{1}{2} \right) \Delta E - E_F \qquad (1.40)$$

Differentiating Equation 1.39 with respect to the gate voltage gives

$$\frac{dE_n}{dV_g} = \left(n - \frac{1}{2} \right) \frac{d\Delta E}{dV_g} - \frac{dE_F}{dV_g} \qquad (1.41)$$

Differentiating Equation 1.41 gives

$$\frac{dg_0}{dV_g} = \frac{1}{\Delta E} \frac{dE_F}{dV_g} - \frac{E_F}{\Delta E^2} \frac{d\Delta E}{dV_g} \qquad (1.42)$$

The smearing temperature (voltage) of the nth sub-band can be defined as the ratio of the low temperature (voltage bias) differential conductance maximum to the high temperature (voltage bias) differential conductance. Mathematically this can be expressed in the form

$$\frac{dg_n/dV_g}{dg_0/dV_g} = \frac{dg_n/dE_n \times dE_n/dV_g}{dg_0/dV_g} \qquad (1.43)$$

Hence substitution of Equations 1.36, 1.41 and 1.42 gives

$$\frac{dg_n/dV_g}{dg_0/dV_g} = \frac{-\left[\frac{1}{eV}\tanh\left(\frac{eV}{4k_BT}\right)\right]\left[\left(n-\frac{1}{2}\right)\frac{d\Delta E}{dV_g}-\frac{dE_F}{dV_g}\right]}{\frac{1}{\Delta E}\frac{dE_F}{dV_g}-\frac{E_F}{\Delta E^2}\frac{d\Delta E}{dV_g}} \qquad (1.44)$$

Now this relationship can be greatly simplified, through the use of Equation 1.39 to eliminate E_F, see Equation 1.45. This final result will be used extensively in Chapter 6, Section 5.5 to analyse the variation in the sub-band spacing in several narrow constrictions as they deplete. It will also be used to analyse the differences obtained by measuring the sub-band spacing through thermal and electric smearing of the differential conductance [32].

$$\frac{dg_n/dV_g}{dg_0/dV_g} = \frac{\Delta E}{eV}\tanh\left(\frac{eV}{4k_BT}\right) \qquad (1.45)$$

1.4 Electron Transport in a Magnetic Field

In this section a discussion is presented of the dynamics of electron motion in a 2DEG, with a magnetic field applied perpendicular to the transport plane. The effect of the magnetic field on electrons confined in quasi-one dimensional channels is also considered. Finally, a brief explanation of the quantum Hall effect is given in terms of the edge state model.

1.4.1 Two Dimensional Electron Gas in a Magnetic Field

Choosing the magnetic field to be perpendicular to the 2DEG in the z-direction and to be described by the vector potential $\underline{A}$ such that $\underline{B}=curl\underline{A}$, then using the Landau gauge $\underline{A}=(0,Bx,0)$, the Schrödinger equation for an electron is given by [33]

$$\left\{ \frac{1}{2m*}\left[-\hbar^2 \frac{\partial^2}{\partial x^2} + \left(-i\hbar \frac{\partial}{\partial y} + eBx \right)^2 - \hbar^2 \frac{\partial^2}{\partial z^2} \right] + V(z) \right\} \varphi(r) = E\varphi(r)$$

where $V(z)$ is the potential confining the electrons in the 2DEG. Hence

$$\left[-\frac{\hbar^2}{2m*}\nabla^2 - \frac{ie\hbar Bx}{m*}\frac{\partial}{\partial y} + \frac{(eBx)^2}{2m*} + V(z) \right]\psi(r) = E\psi(r) \qquad (1.47)$$

This equation has two new terms associated with the magnetic field. The first couples the first derivative of y with x in an imaginary term which breaks time reversal invariance. The second term is a magnetic, parabolic confinement potential. The method of separation of variables is used to solve Equation 1.47 in terms of functions $\phi(x,y)$ and $\phi(z)$. The final wavefunction is then given as the product $\phi(x,y)\phi(z)$ and the total energy will be given by $E(x,y,z)=E(x,y)+E(z)$. The vector potential has no dependence in the y direction, indicating that a reasonable solution would be the product of a plane wave $\phi(y)$ and some function $u(x)$, see Equation 1.48.

$$\phi(x,y) = u(x)e^{iky} \qquad (1.48)$$

On substituting Equation 1.48 into the separated Schrödinger equation, the y dependence disappears leaving

$$\left[-\frac{\hbar^2}{2m^*}\frac{\partial^2}{\partial x^2} + \frac{1}{2}m\omega_c^2\left(x + \frac{\hbar k}{eB}\right)^2 \right]u(x) = \varepsilon_n u(x)$$

(1.49)

where ω_c is the cyclotron frequency $|eB/m^*|$ as in the classical case and ε_n are the energy eigenvalues associated with the eigenfunctions $u(x)$. Equation 1.49 is just a linear harmonic oscillator but with the vertex of the parabolic potential displaced by $x_k = -(\hbar k)/(eB)$. Equation 1.49 can now be solved for the energies and wavefunctions of the bound states of the potential, see Equations 1.50 and 1.51, where a magnetic length $l_B^2 = \hbar/|eB|$ has been introduced and H_{n-1} are hermite polynomials.

$$\varepsilon_{n,k} = \left(n - \frac{1}{2}\right)\hbar\omega_c \qquad n = 1,2,3, etc$$

(1.50)

$$\phi_{n,k}(x,y) = H_{n-1}\left(\frac{x - x_k}{l_B}\right)\exp\left[-\frac{(x - x_k)^2}{2l_B^2}\right]e^{iky}$$

(1.51)

It is immediately apparent from Equation 1.50, that the density of states in any two dimensional sub-band has become a series of δ-functions referred to as Landau levels, each of which is labelled by the quantum numbers n and degenerate in wave number k.

Consider a rectangular system in the Landau gauge which has dimensions (L_x, L_y) [34]. There is the usual periodic boundary condition in y, such that

$$k_y = \left(\frac{2\pi}{L_y}\right)j \qquad j = 1,2,3, etc$$

(1.52)

The boundary condition in the x-direction comes about from the wavefunction being centred on x_k. Hence $0 < x_k < L_x$ or substituting for x_k

$$0 < -\frac{\hbar k}{eB} < L_x \tag{1.53}$$

Using these relationships, the number of allowed states per Landau level per unit area will be given by

$$n_B = \frac{eB}{h} \tag{1.54}$$

Including both spins and rewriting Equation 1.54 in terms of the cyclotron energy gives

$$2n_B = \frac{m^*}{\pi \hbar^2} \hbar \omega_c \tag{1.55}$$

Comparing with Equation 1.4 shows immediately that each Landau level (including both spins) contains the states that originally filled the constant two dimensional density of states over an energy range $\hbar \omega_c$.

The number of occupied Landau levels or filling factor υ at a given field is defined as the ratio of the total number of electrons to the number of allowed states per Landau level per unit area, see Equation 1.56 where each spin is counted separately.

$$\upsilon = \frac{n_{2D}}{n_B} = \frac{h}{eB} n_{2D} \tag{1.56}$$

Now as the magnetic field increases, the energy spacing ($\hbar\omega_c$) of the Landau levels increases and the density of states per Landau level (n_B) increases. This means that fewer electrons will occupy the highest level, see Equation 1.57

$$B_n = \frac{h n_{2D}}{ev(n)} \tag{1.57}$$

At some field B_n, where $v(n)$ is the filling factor at the point n the topmost Landau level empties, n reduces by one and the next Landau level begins to empty. If initially $B_{n+1}<B<B_n$ then $n<\upsilon<n+1$ i.e. there are n completely filled Landau levels with a partially filled $n+1$ level in which the Fermi energy resides. At the point where the $n+1$ level empties, the longitudinal resistivity falls to zero as the Fermi energy resides between Landau levels, see Figure 1.14.

Figure 1.14: Illustration of the density of states at various magnetic fields with their associated filling factors. The movement of the Fermi energy with respect to the occupied Landau levels is also shown. In this picture, the Landau level delta functions have been thermally broaden [34].
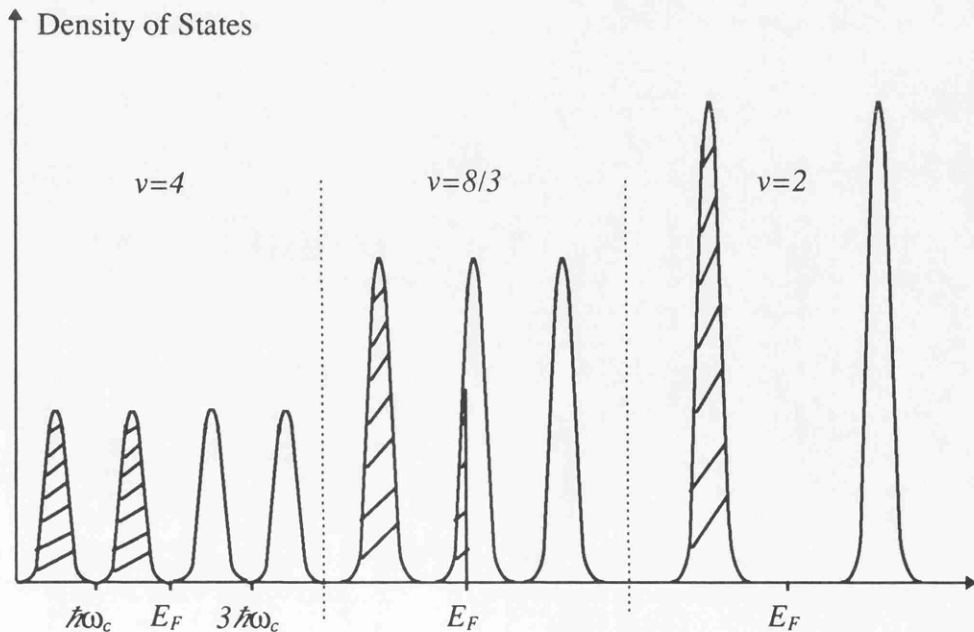
The oscillations in the longitudinal resistivity (the so called Shubnikov-de Haas effect) can also be understood in terms of the two dimensional resistivity tensor [11]

$$
\rho = \begin{pmatrix} \rho_0 & B/n_{2D}e \\ -B/n_{2D}e & \rho_0 \end{pmatrix}
\tag{1.58}
$$

Here ρ_O is the Drude result for the zero field resistivity given by

$$
\rho_0 = \frac{m*}{n_{2D}e^2\tau}
\tag{1.59}
$$

and the scattering time τ is related to the density of states $D(E_F)$ through the simple Born approximation

$$
\tau^{-1} = \left(\frac{\pi}{\hbar}\right)D(E_F)c_i u^2
\tag{1.60}
$$

where c_i is the areal density of impurities whose potential is modelled with a two dimensional delta function of strength u. Hence combining Equations 1.58, 1.59 and 1.60, the longitudinal resistivity can be shown to be directly proportional to the density of states at the Fermi energy. It is clear that the oscillations in the density of states as the magnetic field changes will be reflected in the longitudinal resistivity.

This effect is experimentally very important because it allows the density of electrons in the 2DEG to be calculated by applying Equation 1.57 at two consecutive minima, n and $n+1$, and then subtracting to eliminate n, i.e.

$$
\Delta\left(\frac{1}{B}\right) = \frac{e}{hn_{2D}} \times (v(n+1) - v(n)) = \frac{e}{hn_{2D}} \times 2
\tag{1.61}
$$

1.4.2 Electron Transport in Narrow Channels in a Magnetic Field

Consider the application of a magnetic field to a 2DEG confined in a channel by some potential $V(x)$. The Schrödinger equation for electrons with wavefunction $\psi(r)$ will be similar to Equation 1.48 but with an extra term to account for the electrostatic confinement, see Equation 1.62 [34].

$$\left[-\frac{\hbar^2}{2m^*}\nabla^2 - \frac{ie\hbar Bx}{m^*}\frac{\partial}{\partial y} + \frac{(eBx)^2}{2m^*} + V(x) + V(z) \right]\psi(r) = E\psi(r) \qquad (1.62)$$

Separating Equation 1.62 to extract the x-y dependence gives

$$\left[-\frac{\hbar^2}{2m^*}\left(\frac{\partial^2}{\partial x^2} + \frac{\partial^2}{\partial y^2}\right) - \frac{ie\hbar Bx}{m^*}\frac{\partial}{\partial y} + \frac{(eBx)^2}{2m^*} + V(x) \right]\psi(x,y) = E_{xy}\psi(x,y)$$

This can now be solved with the function

$$\phi(x,y) = u(x)e^{iky} \qquad (1.63)$$

giving

$$\left[-\frac{\hbar^2}{2m^*}\frac{d^2}{dx^2} + \frac{1}{2}m^*\omega_c^2\left(x + \frac{\hbar k}{eB}\right)^2 + V(x) \right]u(x) = \varepsilon_n u(x) \qquad (1.64)$$

where the cyclotron frequency $\omega_c = eB/m^*$ has been introduced. If the electrostatic confinement potential is parabolic, such that $V(x)=\infty$ at $x=\pm a/2$ and elsewhere the

potential is given by $V(x) = (m^* \omega_0^2 x^2)/2$, then Equation 1.64 will have energy eigenvalues

$$\varepsilon_n = \left(n - \frac{1}{2}\right)\hbar\omega_B + \frac{\hbar^2 k^2}{2m_B} \tag{1.65}$$

where

$$\omega_B = \left(\omega_0^2 + \omega_c^2\right)^{\frac{1}{2}} \quad \text{and} \quad m_B = m\left(\frac{\omega_B}{\omega_c}\right)^2 \tag{1.66}$$

The first term in Equation 1.65 is a potential energy term associated with confinement in discrete energy levels, whereas the second term accounts for the kinetic energy of the carriers with wave vectors k.

It is interesting to consider the dependence of the eigenstates in a hard walled potential where $V(x)=0$ for $-a/2<x<+a/2$ and $V(x)=\infty$ elsewhere, see Figure 1.15.

The application of a magnetic field superimposes a parabolic confinement potential onto $V(x)$ and if $k=0$, the potential will be centred on $x=0$. At low magnetic fields the main confinement is still provided by $V(x)$. However increasing the field, increases the magnetic potential until it becomes the dominant confinement mechanism. The energy of the electrons is now confined in Landau levels $\left(n - \frac{1}{2}\right)\hbar\omega_c$ which lie below the Fermi energy and hence carry no current. However, if the wave vector is increased, the vertex of the magnetic parabola shifts and can actually lie outside the wire. At sufficiently high values of k, the electrons are confined at the edge of the channel in a narrow potential well set up between the magnetic potential and $V(x)$. The magnetic potential has broken the degeneracy of electrons with differing k vectors. At sufficiently high values of k,

the eigenstates lie above the Fermi energy and hence any propagation will occur at the sample edge [35]. An important additional aspect to edge state transport is the spatial separation to opposite sides of the channel for edge states with different signs of k. This has important implications because it means that backscattering processes, which rapidly degrade quantisation, are much less likely.

Figure 1.15: Potential energy and lowest eigenstate in a magnetic field for an electron with wavevector k in a hard walled wire of width $0.1\mu m$ in GaAs [34].
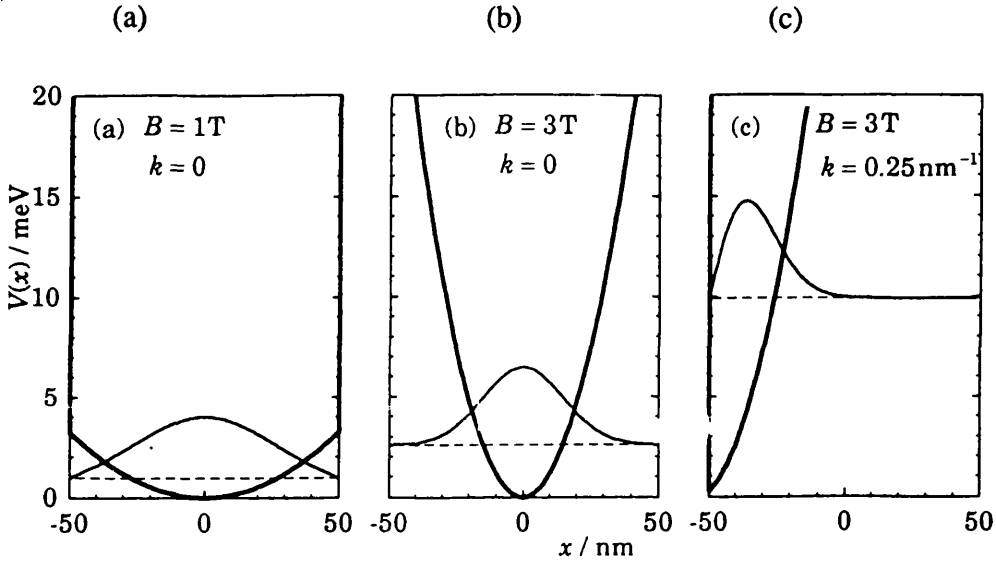
1.4.3 Quantum Hall Effect

Consider the Hallbar geometry in Figure 1.16. The magnetic field is such that Landau levels form in the channel but lie below the Fermi energy. At the sample boundaries these levels rise in energy, as outlined in the previous section, and where they intersect the Fermi energy, edge states form. Applying a negative bias V_1 to contact *1* injects electrons into the edge states. If contacts *3* and *4* are voltage probes, they draw no current and hence in the absence of scattering must inject the same number of electrons into the edge states as they receive. Thus

$V_1=V_3=V_4$. After leaving contact *4* the injected electrons flow into contact *2* where they suffer scattering and dissipate their energy. By symmetry, edge states also exist on the opposite side of the sample and a similar argument gives $V_2=V_5=V_6$ which can be set to zero by defining $V_2=0$.

Figure 1.16: Schematic representation of the Hall bar geometry showing edge state transport in a magnetic field.
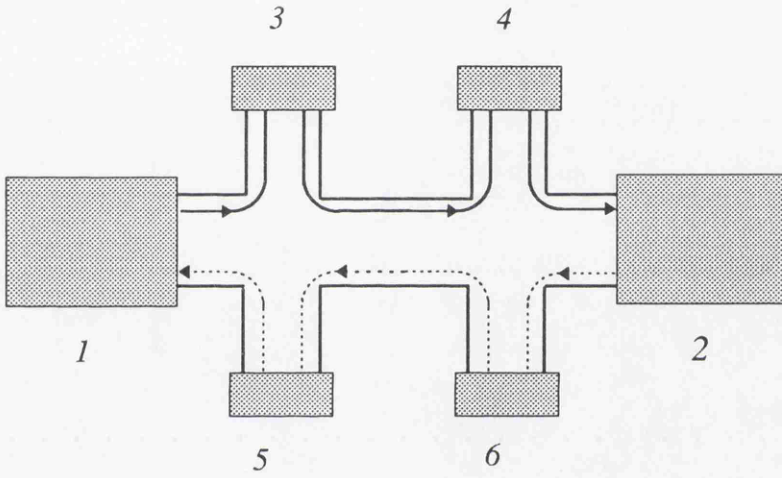
Here contacts *1* and *2* are being modelled as electron reservoirs in equilibrium with the 2DEG. As each edge state carries a current $-(e^2/h)V_1$, the total current flowing in the 2DEG is given by

$$I = -N\frac{e^2}{h}V_1 \qquad (1.67)$$

where N is the number of edge states (counting both spins separately) that exist at the Fermi energy [36]. The Hall resistance is thus

$$\frac{V_5-V_3}{I} = \frac{-V_1}{I} = \frac{1}{N}\frac{e^2}{h} \qquad (1.68)$$

i.e. it is quantised in units of e^2/h.

The main assumption which underpins the argument given above is the absence of scattering. This assumption is justified because forward scattering between edge states with the same wave vector does not alter the overall transmission probability and so the current is unchanged. Backscattering into edge states with wave vectors of opposite sign will alter the transmission probability, but due to the spatial separation of forward and backward flowing edge states to opposite sides of the sample, the effect is small. The implicit assumption is that conduction only takes place at the sample edges, requiring that the Fermi energy lies between Landau levels in the bulk, see Figure 1.17a.

Figure 1.17: (a) The magnetically induced density of states $n(E)$ in a 2DEG showing the regions of localised and extended states. (b) Edge states localised in a slowly varying potential [34].
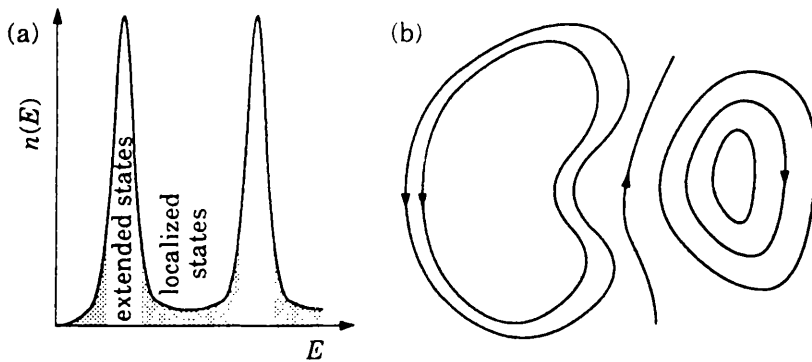
However this is quite a stringent condition and would limit quantisation to very small ranges of magnetic field as the Landau levels are not delta functions. In practise this does not happen and is due to the formation of localised states in the tails of the Landau levels, see Figure 1.17b. These localised states play only a limited part in conduction and encircle regions of potential fluctuations. Therefore as long as the Fermi energy lies within a region of localised states in the bulk, quantisation will persist.

1.4.4 Selective Transmission of Edge States

Consider a sample essentially the same as that analysed in the previous section but this time with some potential barrier between voltage probes *3* and *4*, see Figure 1.18. In this system we have a current *I* injected into *N* edge states which leave probe *3* with *M* of them entering probe *4*. Hence *(N-M)* modes are reflected by the barrier into probe *5* and a voltage is developed between probes *3* and *5*.

Figure 1.18: Schematic representation of the Hall bar geometry showing edge state transport through a partially transmitting barrier in a magnetic field.
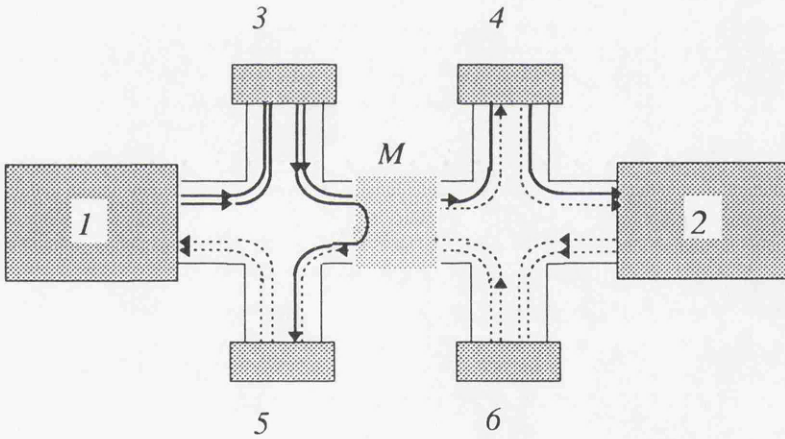
Using the Landauer-Büttiker formalism set out in Appendix A the current flowing between probes *m* and *n* can be related to the voltage set up between probes *m* and *n* by a series of transmission coefficients T_{mn} summed over all the probes. In matrix notation this can be expressed as Equation 1.69 [38, 39]. Now, remembering that only current probes V_1 and V_2 draw a current, this relation can be simplified in terms of the number of propagating edge states, to give

Equation 6.69: The transmission matrix derived using the Landauer-Büttiker formalism relating the current flowing between all the probes in Figure 1.18 [34].

$$\begin{pmatrix} T_{12}+T_{13}+T_{14}+T_{15}+T_{16} & -T_{12} & -T_{13} & -T_{14} & -T_{15} & -T_{16} \\ -T_{21} & T_{21}+T_{23}+T_{24}+T_{25}+T_{26} & -T_{23} & -T_{24} & -T_{25} & -T_{26} \\ -T_{31} & -T_{32} & T_{31}+T_{32}+T_{34}+T_{35}+T_{36} & -T_{34} & -T_{35} & -T_{36} \\ -T_{41} & -T_{42} & -T_{43} & T_{41}+T_{42}+T_{43}+T_{45}+T_{46} & -T_{45} & -T_{46} \\ -T_{51} & -T_{52} & -T_{53} & -T_{54} & T_{51}+T_{52}+T_{53}+T_{54}+T_{56} & -T_{56} \\ -T_{61} & -T_{62} & -T_{63} & -T_{64} & -T_{65} & T_{61}+T_{62}+T_{63}+T_{64}+T_{65} \end{pmatrix} \times \begin{pmatrix} V_1 \\ V_2 \\ V_3 \\ V_4 \\ V_5 \\ V_6 \end{pmatrix} = \frac{h}{e^2} \times \begin{pmatrix} I_1 \\ I_2 \\ I_3 \\ I_4 \\ I_5 \\ I_6 \end{pmatrix}$$

$$\begin{pmatrix} N & 0 & 0 & 0 & N & 0 \\ 0 & N & 0 & N & 0 & 0 \\ N & 0 & N & 0 & 0 & 0 \\ 0 & 0 & M & N & 0 & N-M \\ 0 & 0 & N-M & 0 & N & M \\ 0 & N & 0 & 0 & 0 & N \end{pmatrix} \times \begin{pmatrix} V_1 \\ V_2 \\ V_3 \\ V_4 \\ V_5 \\ V_6 \end{pmatrix} = \frac{h}{e^2} \begin{pmatrix} -I \\ I \\ 0 \\ 0 \\ 0 \\ 0 \end{pmatrix} \qquad (1.70)$$

Equation 1.70 is a complete description of the system set out in Figure 1.18 and can be used to find the resistance between any two probes for a current I flowing between probes 1 and 2. For instance

$$\frac{h}{e^2}I = \frac{h}{e^2}I_2 = NV_2 - NV_4 \qquad (1.71)$$

and

$$0 = \frac{h}{e^2}I_4 = NV_4 - MV_3 - (N-M)V_6 \qquad (1.72)$$

remembering that $V_1=V_3$ and $V_2=V_6$, Equations 1.71 and 1.72 can be used to eliminate V_2 giving the resistance between probes 4 and 3 as

$$R = \frac{V_4 - V_3}{I} = \frac{h}{e^2}\left(\frac{1}{M} - \frac{1}{N}\right) \qquad (1.73)$$

Hence the resistance in a swept magnetic field is not a continuous function but rather takes on particular values depending on the number of edge states that propagate in the 2DEG and the transmission coefficient of the potential barrier.

References

[1] A.Y.Cho and J.R.Arther, Prog. Solid State Chemistry Vol. 10, edited by G. Somerjai and J. McCaldin, (Pergamon, New York), 157 (1975).

[2] L. Esaki, L. L. Chang, Phys. Rev. Lett. 33, 495 (1974).

[3] R. Dingle, Wiegmann, C. H. Henry, Phys. Rev. Lett. 33, 827 (1974).

[4] R. L. Anderson, Solid-State Electronics Vol. 5, 341 (1962)

[5] L. Esaki, L. L. Chang, Thin Solid Films 36, 285 (1976).

[6] R. Dingle, Festkörperprobleme Vol. XV, (Advances in Solid State Physics), edited by H. J. Queisser, (Pergamon Vieweg, Braunschweig), 21 (1975).

[7] R. Dingle, A.C. Gossard, W. Wiegmann, Phys. Rev. Lett. 34, 1327 (1975).

[8] H. L. Strömer, R. Dingle, A. C. Gossard, W. Wiegmann, M. D. Sturge, J. Vac. Sci. Technol. 16, 1517 (1979)

[9] R. Dingle, H. L. Strömer A. C. Gossard, W. Wiegmann, Appl. Phys. Lett. 33, 665 (1978).

[10] H. L. Strömer, R. Dingle, A. C. Gossard, W. Wiegmann, M. D. Sturge, Solid State Commun. 29, 705 (1979).

[11] See for example C. W. J. Beenakker and H. van Houten, Solid State Physics 44, edited by H. Ehrenreich and D. Turnbull, (Academic Press), 17 (1991).

[12] C. M. Wolfe, N. H. Holonyak, G. E. Stillman, Physical Properties of Semiconductors, Prentice-Hall International Editions (1989).

[13] T. N. Theis, P. M. Mooney, S. L. Wright, Phys. Rev. Lett. 60, 360 (1988).

[14] P. M. Mooney, Semicond. Sci. Technol. 6, B1 (1991).

[15] D. J. Chadi, K. J. Chang, Phys. Rev. Lett. 61, 873 (1988).

[16] D. J. Chadi, K. J. Chang, Phys. Rev. B 39, 10063 (1989).

[17] See for example S. Tiwari, Compound Semiconductor Device Physics, (Academic Press Limited), 528 (1992).

[18] A. R. Long, J. H. Davies, M. Kinsler, S. Vallis, M. C. Holland, Semicond. Sci. Technol. 8, 1581 (1993).

[19] See for example C. Weisbuch, B. Vinter, Quantum Semiconductor Structures Fundamentals and Applications, (Academic Press Limited), 19 (1991).

[20] F. Stern, Appl. Phys. Lett. 43, 974 (1983).

[21] J. H. Davies, I. A. Larkin, E. V. Sukhorukov (Accepted J. Appl. Phys 1995).

[22] H. van Houten et al., Physics and Technology of Submicron Structures, edited by H. Heintich, G. Bauer, F. Kuchar, (Springer, Berlin), (1988).

[23] S. Chakravarty, A. Schmid, Physics Reports 140, 193 (1986).

[24] P. A. Lee, D. A. Stone, H. Fukuyama, Phys. Rev. B35, 1039 (1987).

[25] H. van Houten, C. W. J. Beenakker, Semiconductors and Semimetals 35, edited by M. Reed, (Academic Press, New York), 19 (1990).

[26] H. van Houten, B. J. van Wees, J. E. Mooji, C. W. J. Beenakker, J. G. Williamson, C. T. Foxon, Europhys. Lett. 5, 721 (1988).

[27] L. I. Glazman, G. B. Lesovick, D. E. Khmel'nitskii, R. I. Shekhter, JETP Lett. 48, 238 (1988).

[28] L. P. Kouwenhoven, Transport of Electron-Waves and Single-Charges in Semiconductor Nanostructures, Thesis, 11 (1992).

[29] M. J. Laughton, J. R. Barker, J. A. Nixon, J. H. Davies, Phys. Rev. B 44, 1150 (1991).

[30] M. Büttiker, Phys. Rev. B41, 7906 (1990).

[31] M. Büttiker, Phys. Rev. B 57, 1761 (1986).

[32] C. Barton, J. H. Davies, E. Skuras, M. C. Holland, A. R. Long, (unpublished).

[33] L. D. Landau, E. M. Lifshitz, Quantum Mechanics: Vol. 3, (Pergamon Press), (1977).

[34] J. H. Davies, Lectures (unpublished).

[35] B. I. Halperin, Phys. Rev. B 25, 2185 (1982).

[36] M. Büttiker, Phys. Rev. B 38, 9375 (1988).

[37] See for example C. W. J. Beenakker and H. van Houten, Solid State Physics 44, edited by H. Ehrenreich and D. Turnbull, (Academic Press), 170 (1991).

[38] B. J. van Wees, L. P. Kouwenhoven, E. M. M. Willems, C. J. M. Harmans, J. E. Mooij, H. van Houten, C. W. J. Beenakker, J. G. Williamson, C. T. Foxon, Phys. Rev. B 43, 12431 (1991).

[39] M. Büttiker, IBM J. Res. Develop. 32, 317 (1988).

Chapter 2

Sample Fabrication

2.1 Introduction

In order to study the electrical properties of a heterostructure it is necessary to define some standard circuit through which electrons can be injected into the two dimensional electron gas and various parameters such as resistance and depletion can be measured. The circuit chosen was a Hall bar geometry which was analysed in terms of the Landauer-Büttiker formalism in the previous chapter. The pattern was designed using the MICAD software package and consisted of four layers. The initial layer is to enable Ohmic contacts to be made to the 2DEG, with a second layer to isolate a channel through which electrons can be injected, see Figure 2.1. The third layer is a gate to enable the depletion characteristics of the heterostructure to be investigated i.e. a quantum device or large area gate. Finally a wiring layer is designed to give a robust connection to both gates and devices. The types of metal-semiconductor contacts used in the project are well understood and widely used in commercial devices [1]. Connection to external instruments was made through wire bonds to the Ohmic contacts. Both optical and elecctron beam lithography techniques were employed in fabricating complete devices.

Figure 2.1: Schematic showing a general overview of the complete fabricated structure.
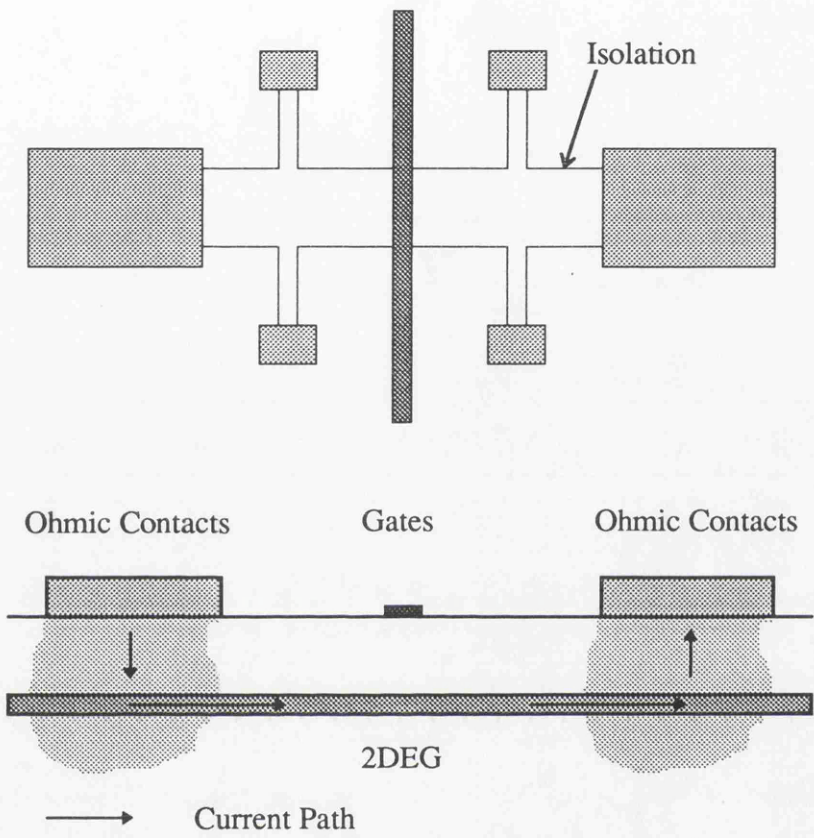
2.1.1 Optical Lithography

Optical lithography is used to define features with a resolution $\Delta x \approx \lambda / sin\theta$ where λ is the wavelength of the light source and $sin\theta$ is the numerical aperture of the optical system. For the ultra violet light sources used at Glasgow, this enables features of approximately 0.3 microns to be fabricated. Hence for all the layers described above, it is only the quantum devices that require exploitation of the more complicated electron beam lithography techniques to produce feature sizes

of around 50nm. Despite this, electron beam lithography is still used as a convenient method of writing the mask plates for the optical lithographic processing. Once these mask plates are fabricated they are then used in a photographic process in which an image of the mask is projected through the transparent areas of the plates and onto the heterostructure. The use of optical masks greatly increases the efficiency of the entire fabrication process by exploiting the parallel nature of resist exposure by light, compared to the sequential exposure by an electron beam gun. Hence a large number of devices can be processed in parallel using optical lithography saving expensive writing time on the electron beam facility for only the features beyond the optical resolution limit. A typical mask for optical lithography will be an array of 20 by 20 identical device structures, with four different mask plates (Ohmics, isolation, wiring and large area gates) being required for the project.

2.1.2 Basic Lithographic Process

Certain polymers or resists can have their molecular composition altered by chain scission when exposed to particular types of radiation. This property can be exploited in an analogous way to photography to produce differing areas of the resist, with differing molecular weights. The action of a developer is to selectively dissolve away regions of lower molecular weight, see Figure 2.2.

There are two basic types of resist, positive resist which has its molecular weight decreased by exposure to radiation and negative resist which increases in molecular weight after irradiation. The devices measured in this project were all fabricated with positive resist. Subsequent application of a chemical etch or evaporation of metal onto the surface of the sample, followed by an immersion in a solvent to dissolve the remaining resist, leads to a permanent trace where the resist was developed away, see Figure 2.3. The two processes of metallic lift off and chemical etch are described in detail below.

Figure 2.2: Schematic illustrating: (a) The resist bi-layer structure under exposure and (b) The undercut profile which results after development.

Radiation

Resist bi-layer

Substrate

(a) Exposure

(b) Development
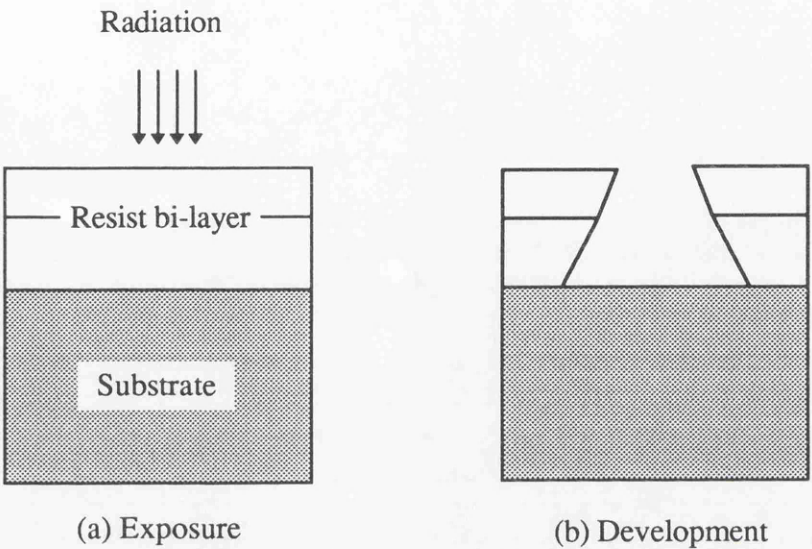
Figure 2.3: Schematic illustrating: (a) Metal evaporation onto the developed pattern and (b) Subsequent lift-off.

(a) Metallization
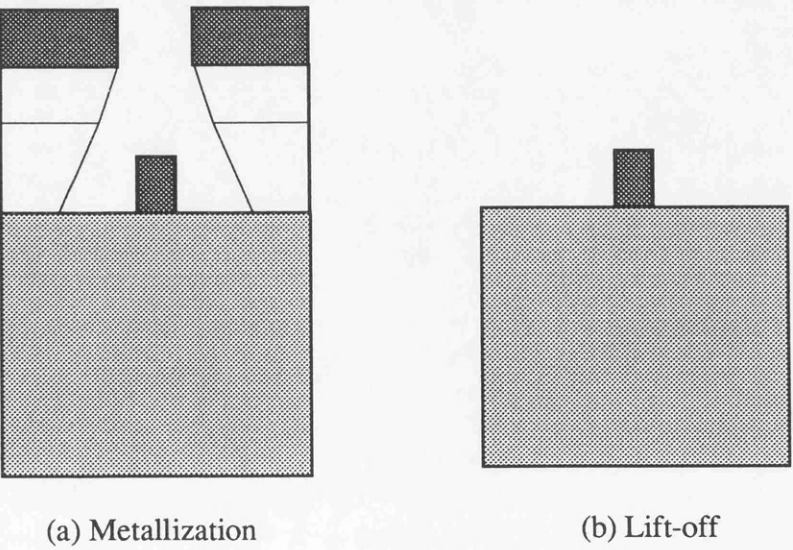
(b) Lift-off

2.1.3 Metallic Lift off after Optical Lithography

This is a standard method for putting a fine metal pattern onto a substrate and has a number of stages which are all carried out in a clean room environment.

Step 1. Sample Preparation

The wafer supplied by MBE is scribed into 10mm by 10mm chips using a diamond tipped scribe. These chips are blown with nitrogen gas and then immersed in four different chemicals for five minutes in an ultrasonic bath. The chemicals are given below in order of use.

1. Trichloroethylene
2. Methanol
3. Acetone
4. Iso Propyl Alcohol (IPA)

The chips are then blown dry with nitrogen gas ready for the application of the resist.

Step 2. Resist Application

Each chip is placed on the vacuum chuck of a spinner and Microposit S1400-31 resist is applied using a filtered syringe. The sample is then spun at 4000rpm for 30 seconds to achieve a uniform layer of resist approximately 1.8μm thick. The thickness of the resist defines the amount of metal it is possible to lift off. The sample is then baked for 15 minutes at 90°C and then removed from the oven and soaked for 10 minutes in chlorobenzene. There is then a final bake at 90° C for a further 15 minutes. The purpose of the chlorobenzene is to make the surface of the resist more resistant to the action of the developer thus giving an under cut profile to ensure easier lift off, see Figure 2.2.

Step 3. Exposure of the Resist

To transfer the desired pattern from a mask plate onto the chip a System 3 Hybrid Technology Group's High Performance Mask Alignment and Exposure System was used. This piece of apparatus enables precision alignment of any pattern to be made to within a few microns of any other pattern. With alignment completed, the sample is brought into contact with the mask plate and an ultra violet light source is then shone through the mask.

Step 4. Development of the Pattern

The exposed samples are placed for 70 seconds in solutions of one part Microposit S1400-31 developer to one part distilled water and gently agitated. When the pattern has developed out, the chips are rinsed in distilled water and blown dry with nitrogen gas.

Step 5. Metalisation and Lift off

The samples are loaded into a metal evaporator. When the evaporation is complete, the samples are unloaded and placed in a beaker of acetone for 30 minutes at 44°C. The acetone acts as a solvent, dissolving the resist and so removing the metal which was in contact with the resist. The chip now has an inverted metallic copy of the pattern which was written onto the mask plate.

2.1.4 Chemical Etch

The procedure for producing a chemical etch pattern on the surface of the scribed chips follows Steps 1 to 4 described in the previous section, however there is now no need for the chlorobenzene soak described in Step 2. When the chip has been patterned using an appropriate mask plate (usually aligned to a previous metalisation layer) it is placed in a beaker containing the etch solution. The chip is then removed from the etch after the required etch time has elapsed and then

initially rinsed in distilled water and then acetone. The sample now has an inverted, etched copy of the pattern which was written onto the mask plate.

2.1.5 Electron Beam Lithography

Both metalisation and chemical etch can be carried out through the use of electron beam lithographic techniques instead of the optical method described above. The main importance of this type of process, apart from the writing of mask plates, is the very small features sizes which can be achieved due to the much smaller wavelength associated with the imaging electrons compared to ultra violet light. The general processing is very similar to optical lithography, except that the type of resist differs, as do the spin speeds and baking times. In addition, an under-cut profile is created in the developed resist by using a resist bi-layer structure. Each of the two elements of this bi-layer has a different molecular weight to mimic the chlorobenzene soak described in step 2 of the optical lithographic process.

2.2 Sample Fabrication

The following section gives a complete description of the actual sample design and fabrication process used to create the necessary circuitry in order to carry out the various experiments on the different heterostructures investigated in the course of this project. The process consists of four mask plates for optical lithography and one set of pattern data for electron beam lithography each of which is aligned to the previously fabricated level. The complete set of pattern data used to create a single quantum device with the necessary circuitry is given in Figure 2.4.

Figure 2.4: Illustration of pattern data for (a) Ohmics, (b) Isolation, (c) Wiring and (d) Quantum devices. In addition, the allignment of these four layers into the completed sample structure is also shown in (e).
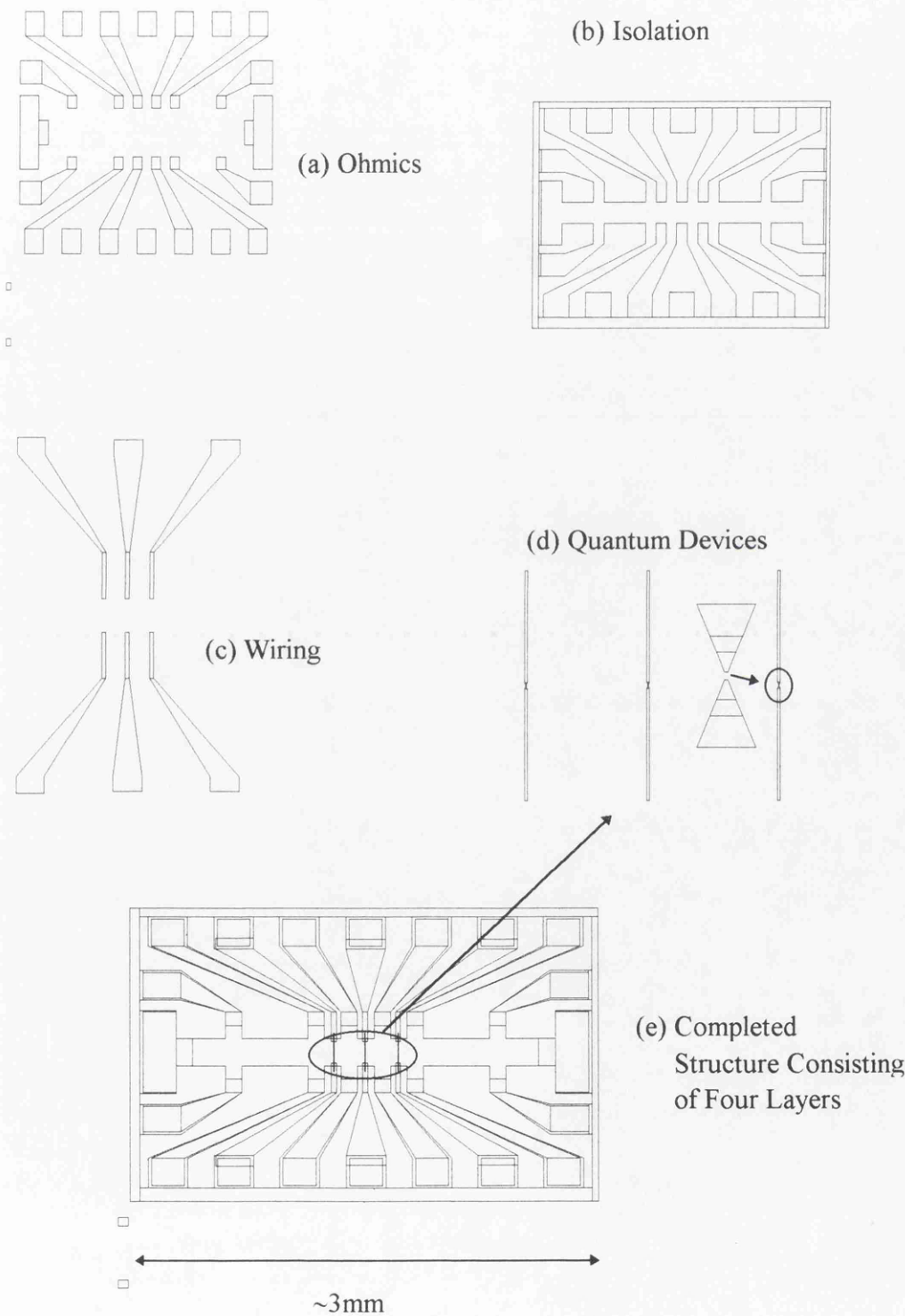
2.2.1 Ohmic Contacts

Non-rectifying or Ohmic contacts to a GaAs-$Al_xGa_{1-x}As$ heterostructure are made by artificially doping the metal-semiconductor interface. Diffusion of the dopants into the semiconductor, reduces the width of the depletion region, allowing electrons to tunnel through. The evaporation takes place in a Plassys Automated Deposition System operated at 10kV and containing five possible choices of materials: gold, titanium, nickel, nichrome, and germanium. These substances can be deposited in any order with a pre-defined thickness accurate to ±1nm. A typical Ni-Ge-Au recipe is evaporated in the following quantities:

1. Ni 8nm
2. Ge 120nm
3. Au 130nm
4. Ni 80nm
5. Au 250nm

In this recipe the 120nm of Ge and the 130nm of Au are included in order to diffuse into the semiconductor to form the contact. Ni is used as a wetting agent to improve surface adhesion and the 250nm of Au is included in order to prevent oxidation and to provide a good connection to external circuit wiring. After evaporation, the contacts are annealed at 370°C for 70 seconds in a chamber flushed with argon gas in order to diffuse the Ge into contact with the 2DEG.

2.2.2 Isolation

The isotropic etch solution H_2O:HCl:NH_4 mixed in the ratio 1000:2:0.7 is used to isolate a piece of 2DEG. This particular etch has an etch rate of 100nm

per minute and so for the heterostructures used in the course of this project, it was usual to etch for approximately 40 seconds.

2.2.3 Quantum Device Fabrication

This part of the process was carried out using electron beam lithography with PMMA (poly-methyl methacrylate) resists. Two types of PMMA were used one supplied by BDH Chemicals Ltd. (180000 average molecular weight) and one supplied by DuPont Co. called Elvacite or Elv (360000 average molecular weight). Initially a 4% solution of BDH in chlorobenzene is applied to the sample and spun at 5000rpm for 60 seconds. The sample is then baked at 180°C for 1 hour. A second layer of 4% Elv in xylene is then applied and again spun at 5000rpm for 60 seconds. After a further bake at 180°C for one more hour, the sample is ready for exposure.

The choice of PMMA resists ensure maximum resolution with reliable lift off. For instance, a 70nm thick BDH layer, allows lift off of about the same amount of evaporated metal. After exposure, the sample is developed in a solution of 3 parts MIBK (methyl isobutyl ketone) to 1 part IPA (iso propyl alcohol) for 35 seconds. The solubility of PMMA in a 1:1 solution of MIBK:IPA is inversely proportional to its' molecular weight. Hence the larger molecular weight Elv layer gives a slower development, leading to the undercut profile sketched in Figure 2.2. The sample is then placed in a Plassys Automated Deposition System and 11nm of Ti and 15nm of Au is evaporated onto the surface. After unloading the evaporator, the sample is placed in a beaker of warm acetone and lift off of the metal on the unexposed areas of the resist will occur under strong agitation. A scanning electron micrograph of a typical quantum wire is shown aligned to Ohmic, isolation and wiring layers in Figure 2.5. The equivalent pattern data is given in Figure 2.6.

Figure 2.5: A scanning electron micrograph showing a high resolution image of a 400nm long quantum wire in addition to how it is aligned to the Ohmic, isolation and wiring layers. The lower image has been taken at an angle of 90° with respect to the upper image.
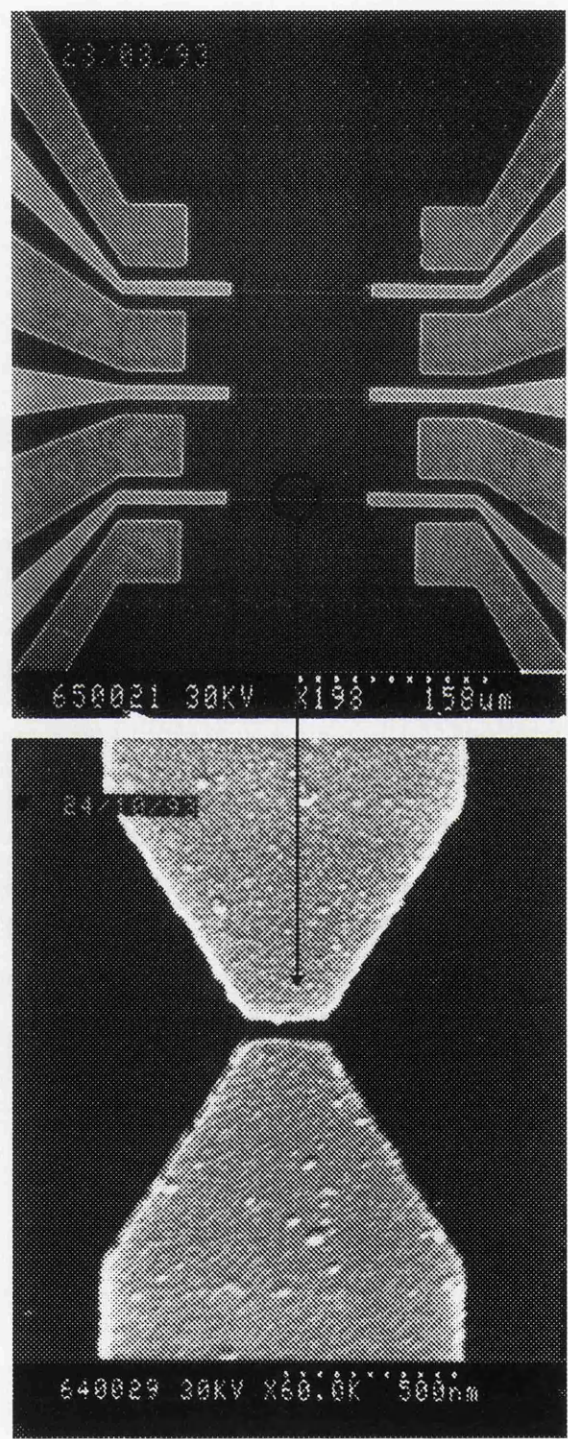
Figure 2.6: Pattern data illustrating quantum point contacts to be fabricated by electron beam lithography and aligned to previous Ohmic and isolation levels.
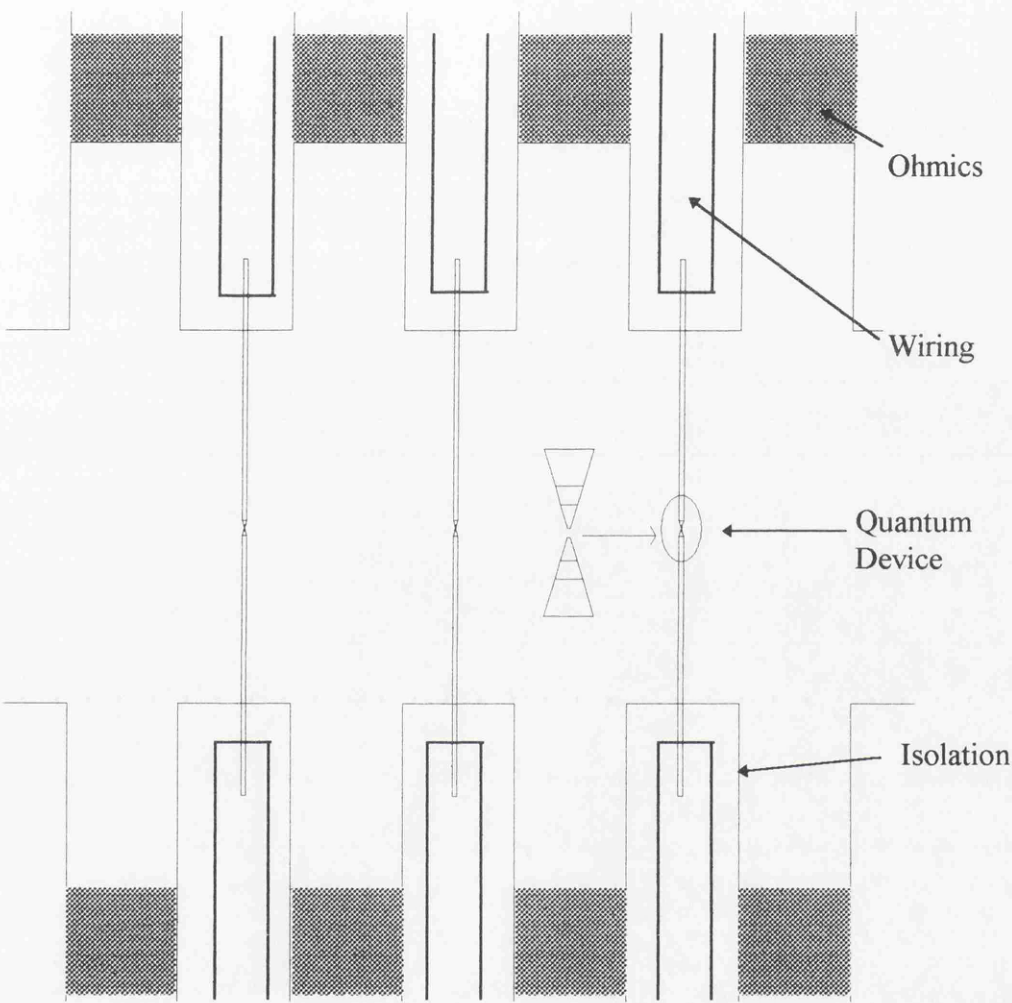
2.2.4 Large Area Gates

Fabrication of large area gates was done by optical lithography using the metal lift-off technique. The Schottky contact was formed from 11nm of Ti and 15nm of Au evaporated onto the sample. Figure 2.7 shows the resulting pattern data aligned to the previous Ohmic and isolation layers.

Figure 2.7: Pattern data illustrating the necessary level required to fabricate optically a large gate along with the Ohmic and isolation levels needed to complete the circuit.
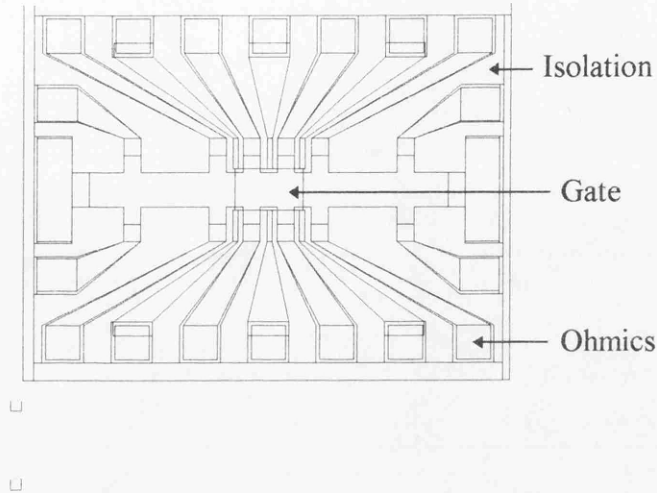
2.2.5 Wiring

The final level in the process is a wiring level used to ensure robust connection of the quantum devices to thick gold pads. Through the thick gold pads, connection is then made to the external circuitry. The recipe typically used was 30nm of Ti followed by 160nm of Au, evaporated onto an optically defined pattern.

2.3 Electron Beam Facility

The electron beam lithography was carried out using a Philips Beamwriter EBPG-5 system. The system uses a vector scan with a Gaussian beam to write circuit pattern data onto a substrate, with one pattern representing one layer. The pattern data was generated in the computer aided design software packages: MICAD and Wavemaker.

2.3.1 Main Elements of an Electron Lithography System

The main elements of the machine are the beam forming, spot forming, deflection, substrate positioning and detection system, see Figure 2.8. A detailed technical drawing of the actual column is presented in Figure 2.9 [3].

Figure 2.8: Schematic illustrating the main elements of an electron beam system suitable for lithography [2].
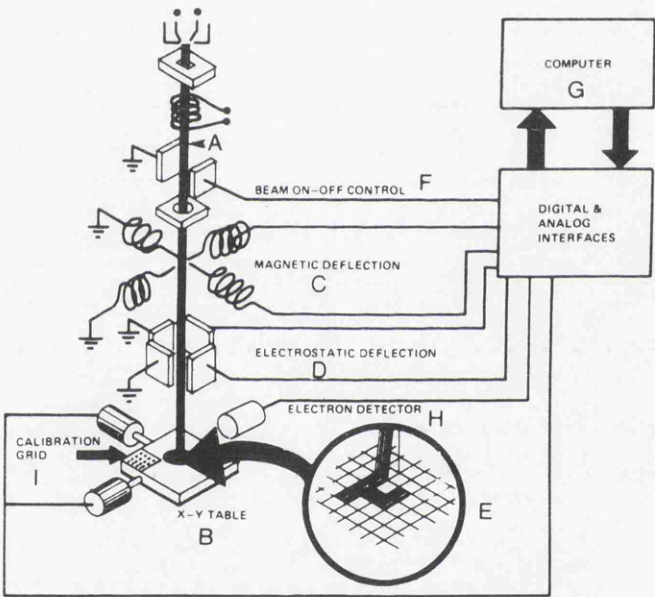
Beam Forming

The electron beam is formed in the electron gun which consists of a tungsten filament heated to 2300-2700°C by a low voltage and a Wehnelt cylinder. The filament, together with the Wehnelt cylinder, act as an electrostatic lens to form the beam. The emission current is controlled by regulating the

Figure 2.9: A detailed technical drawing of the column of a Philips Beamwriter EBPG-5 electron lithography system.
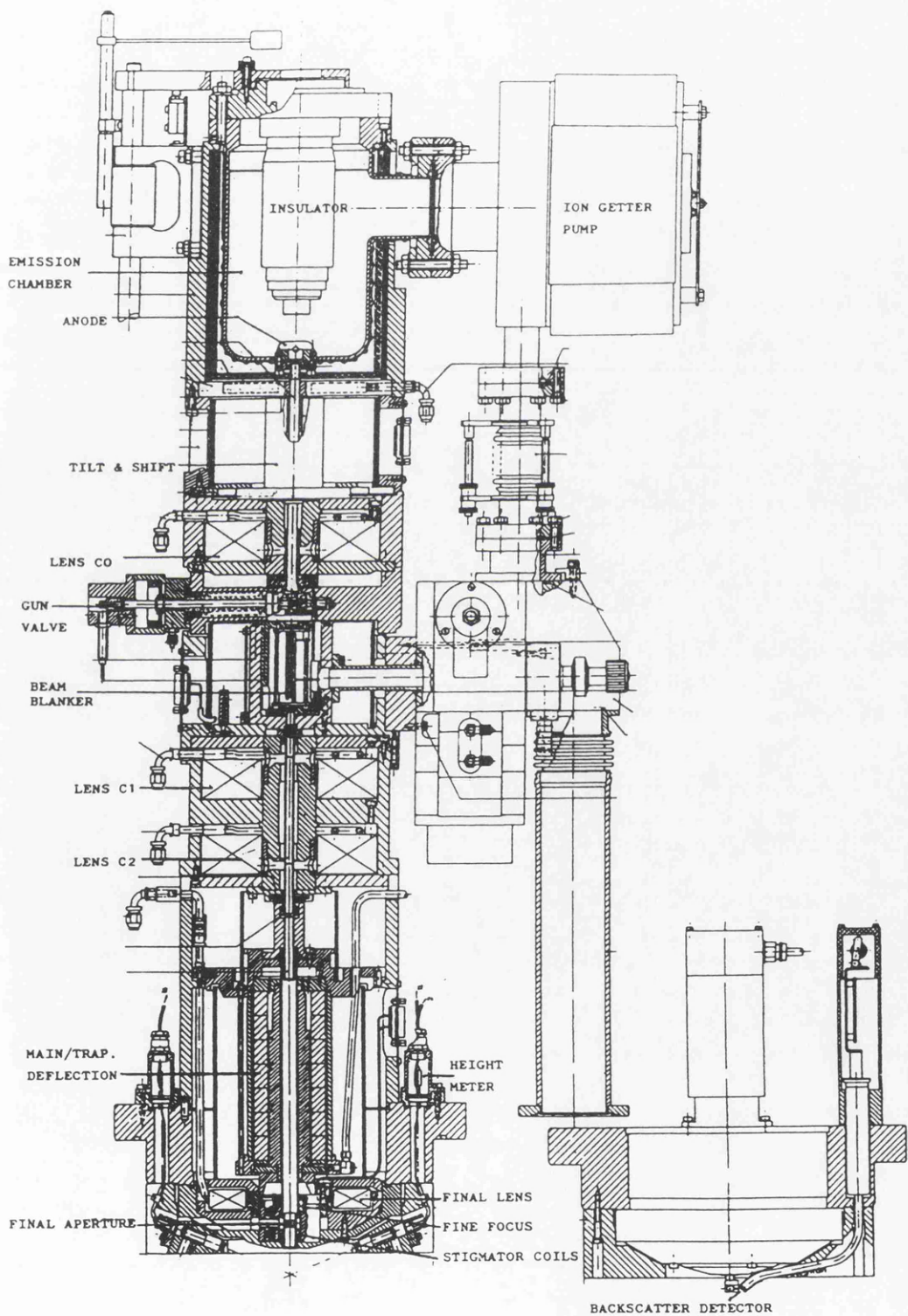
Wehnelt bias voltage and the filament current. After emerging from the electron gun, the beam passes through two sets of coils which direct the beam along their 'optical' axis. Finally a high tension voltage supply accelerates the electrons under a bias of 50 or 100kV supplied to the cathode of the electron gun. The electric field in the emission chamber is optimised with the positioning of anode rings, one for each high tension setting.

Spot Formation

Four electromagnetic lenses focus the beam to a spot in the plane of the substrate. Beam divergence is limited by various apertures with fine focus coils, double quadrupole stigmator coils are also included. Blanking plates allow the beam to be electrostatically diverted away from the optical axis. Lenses C1 and C2 control the beam diameter on the surface of the substrate and the final lens provides coarse focus of the spot on the substrate.

Beam Deflection

Deflection coils are positioned between the condenser lenses (C1, C2) and the final lens and consist of two separate magnetic coil systems. A main deflector for large area coverage and a trapezium deflector to position the beam to within an area $8.125\mu m^2$ are included.

Substrate Positioning

An X-Y table carries the sample which is clamped in one place and optically aligned to the table to an accuracy of $\pm 1°$. A solid state laser interferometer is then used to determines the X-Y position of the sample, relative to the table. In this way a co-ordinate system is set up in order that patterns can be

accurately aligned to previous lithographic levels. There is an additional semiconductor laser detection system to determine the height of the sample at various points. Too great a variation in height across the sample will lead to the beam being out of focus at some of the positions it is addressing.

Detection and Display

Detection circuits provide information about the electron beam (beam current, focus, position etc.) which is used for calibration purposes and displayed on video screens.

2.3.2 Concepts in Electron Beam Writing

Spot Sizes

Figure 2.10: Formation of a single line from the overlap of a Gaussian electron beam [2].
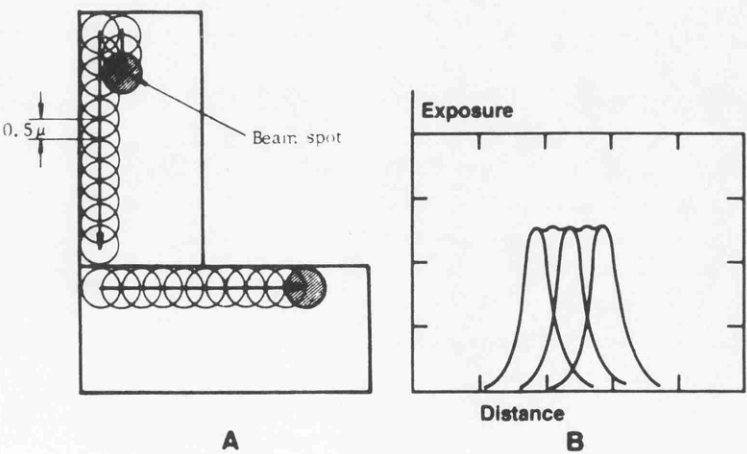
The spot size is the diameter of the focused electron beam and can be varied from 12nm to 400nm. The spot size required depends on the resolution but

typically it is chosen to be about twice the resolution to give a continuous line, see Figure 2.10 [2].

Resolution and Beam Step Size

The electron beam writer has a 15 bit digital pattern generator giving 32000 by 32000 pixels in the x-y plane. The accuracy with which the beam can be placed is known as the resolution. The beam resolution is determined by the desired pixel spacing, which can vary continuously from 5nm to 312.5nm and the beam spot size, which can vary from 12nm to 400nm. Once the beam has addressed a particular pixel it is moved to the next pixel site through a distance called the beam step size or through some other multiple of the resolution, see Figure 2.11.

Figure 2.11: Illustration of the vector addressing system employed by a Phillips EGPB-5 electron lithography facility.

Arrows give the scanning direction of the beam
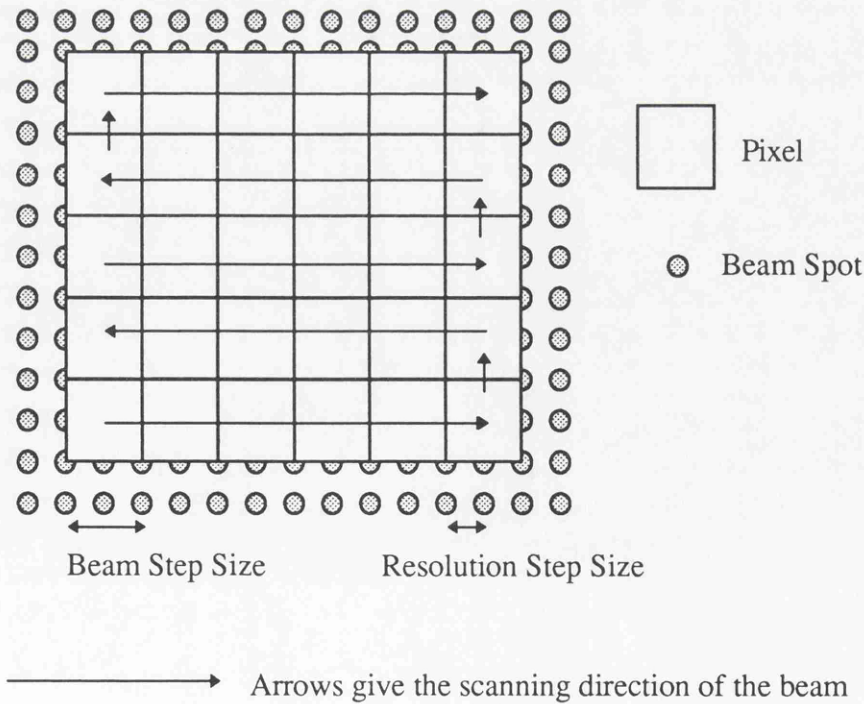
The beam can be positioned with an accuracy denoted by the points. However when scanning a rectangle, it can move a greater distance between exposure points (twice in this case). Clearly the resolution determines the accuracy to which the pattern is placed and the beam step size determines the accuracy to which it is drawn.

Writing Frequency

The writing frequency is a function of pixel size, beam current and the exposure dose. The frequency can vary from 0.5KHz to 10MHz and care must be taken in choosing the appropriate dose and resolution to maximise this frequency.

Dose

The dose is the charge per pixel, measured in units of micro-Coulombs/cm^2. This value must be high enough to change the solubility of the resist by a sufficient amount to enable the pattern to develop out. However too high a value can lead to proximity effects described below.

Proximity Effect

Electrons incident on the sample do not simply pass through the resist exposing it and then disappear. They can be backscattered from the substrate and pass through the resist again, but this time spread over a much larger area, 2-5µm^2 at 50KeV. This exposure mechanism gives rise to the proximity effect which manifests itself in two ways.

a) Intra-Proximity Effect: With a single shape, the total integrated dose in the resist at the centre of the shape is twice that of the edge and four times that of a

corner. Consequently, for given development conditions, the middle develops out more quickly that the edges and corners.

b) Inter-Proximity Effect: This case affects features that are separated by less than the range of the back scattered electrons. The exposure of one shape affects that of the other and leads to merging of separate patterns.

Figure 2.12: Schematic illustrating the relative importance of backscattered electrons depending on penetration depth.
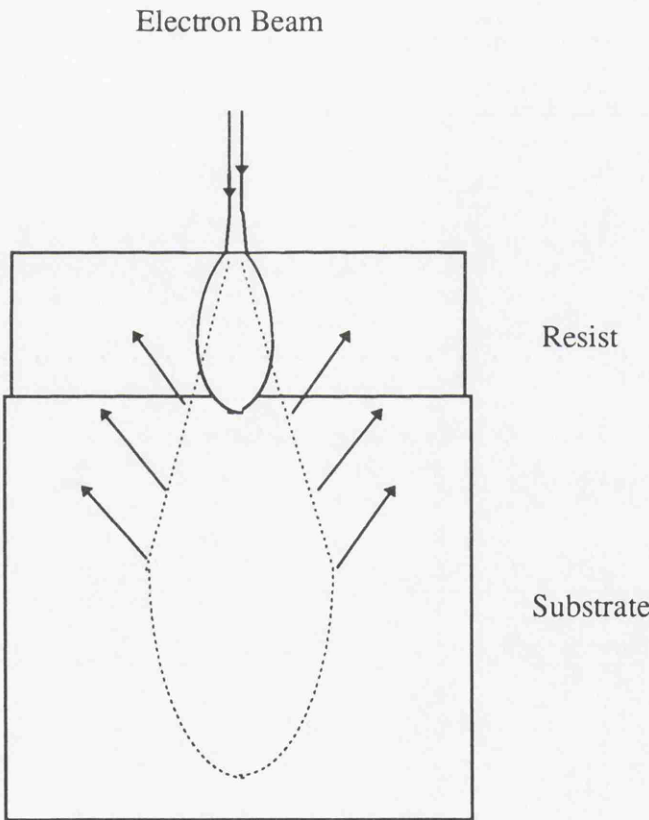
Both inter and intra-proximity effect are overcome by reducing the probability of electrons in the substrate suffering backscattering events by using

thin substrates. In addition the relative importance of backscattered electrons can be reduced by using more energetic electrons. Figure 2.12 compares the backscattering of electrons when the penetration range equals the resist thickness and when the range is deep into the substrate [4]. Clearly at larger penetration depths (higher electron energies) there are less backscattered electrons incident in the region of the primary exposure.

Exposure Tests

In writing small structures it is necessary to maximise exposure dose to achieve the correct resist solubility for development and yet avoid proximity effects. To achieve this, test patterns known as exposure tests are written. This involves writing the pattern at a particular exposure dose and then changing the dose by some small fraction and repeating the process. This is carried out a number of times until there are a sufficient number of patterns to optimise the exposure dose.

Registration

After the optimal exposure dose has been determined using exposure tests, the pattern is ready to be written onto the actual heterostructure. If the pattern is to be written in a particular location, then a registration procedure is used. This involves the electron beam machine finding three previously defined rectangles which are perpendicular to each other and separated by some known distance. These rectangles or markers are used to define a stable co-ordinate system that allows the machine to adjust for rotation of the sample. In this way the pattern is written relative to the markers on the substrate and is independent of the position of the sample on the substrate table.

2.3.3 Electron Beam Resist Processing

The resist used to define quantum device structures is PMMA or poly-methyl methacrylate which is an organic polymer formed by long chains molecules, see Figure 2.13 where the letters are the manufacturers names. In general the higher the molecular weight of the PMMA the less sensitive it is to development because more chain scissions are required to break each molecule into sections small enough to be dissolved by the developer.

Figure 2.13: The Chemical composition of PMMA (poly-methyl methacrylate).

$$CH_3$$
$$|$$
$$---CH_2---C---$$
$$|$$
$$COOCH_3$$
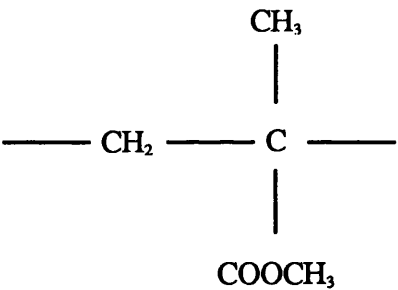
PMMA comes in various molecular weights and for electron beam lithography the weights generally used are:

BDH Mwt=180000 (BDH Chemicals Ltd.)

Elv Mwt=350000 (DuPont Co.)

The resists are dissolved in either chlorobenzene (BDH) or xylene (Elv), before application to the sample. Chlorobenzene is a good solvent and is used to form thick layers from 500nm upwards (depending of the spin speed). Xylene however, is a much poorer solvent and is used in a bi-layer process in order to prevent the first layer dissolving away. Table 2.1 [6] summarises various important data on

Table 2.1: Important parameters for fabrication of various structures by electron beam lithography [6].

Recipe	Development (23±1°C)	Metal Thickness	Use	Pattern Type	Exposure Dose ($\mu C/cm^2$)
2.5%BDH 2.5% Elv	3:1 30s	<30nm	Very High Resolution	Gratings: <100nm Pitch 20nm Features	300-400: Large Areas >1μm 600: ≈0.1μm Up To 2000 For Isolated Shapes
4% BDH 2.5% Elv	3:1 30s	<60nm	Very High Resolution	Gratings: 100nm Pitch 20nm Features	300-400: Large Areas >1μm 600: ≈0.1μm Up To 2000 For Isolated Shapes
4% BDH 4% Elv	3:1 30s	<60nm	Very High Resolution	Gratings: 120nm Pitch 20nm Features	300-400: Large Areas >1μm 600: ≈0.1μm Up To 2000 For Isolated Shapes
8% BDH 4% Elv	2.5:1 30s	<160nm	High Resolution	30-40nm Features	300-400: Large Areas >1μm 600: ≈0.1μm Up To 2000 For Isolated Shapes
12% BDH 4% Elv	2:1 45s	<350nm	Medium Resolution	>150nm Features	300-400: Large Areas >1μm 500: <0.5μm
15% BDH 4% Elv	1:1 60s	<1000nm	Low Resolution	>300nm Features	250-300: Large Areas >1μm 400: <0.5μm
18% BDH 4% Elv	1:1 90s	<1500nm	Low Resolution	>500nm Features	250: Large Areas >1μm 300: ≈1μm

resist thickness depending on the different percentage concentration of polymer and which solvent is used. Other data included in Table 2.1 is the amount of metal that a particular resist structure is capable of lifting off and the feature sizes expected for 50keV electrons. Development times and concentration, in addition to the necessary exposure doses, are all included and are discussed in detail in the next section.

Each resist layer is baked at 180°C for 1 hour and after exposure of the resist, development is carried out in MIBK (methyl isobutyl ketone) diluted in IPA (iso propyl alcohol) at 23°C. Various concentrations yield different development speeds, contrasts and resolution. In general different concentrations of developers are required depending on the type of resist used.

2.3.4 Understanding Electron Beam Resist

In order to fabricate small structures it is necessary to reduce the contribution of backscattered electrons from the substrate and inelastic scattering events in the PMMA. In practice this means minimising the exposure dose applied to the resist when writing any particular feature. We first define the sensitivity of PMMA resist as the minimum exposure that is required for the effected area of the resist to be dissolved during development. This concept is then used to interpret a typical plot of the thickness of resist remaining after development, as a function of exposure dose for different concentrations of developer, see Figure 2.14 [7]. The more concentrated the MIBK developer, the higher the molecular weight of PMMA that can be dissolved. Hence the concentration of the developer defines the contrast between the exposed and unexposed regions. Higher concentrations of MIBK reduces the sensitivity of the resist but at the expense of a reduction in the resist contrast, due to the development of unexposed areas of the resist. On the other hand, a weak solution of MIBK gives high contrast, but in this case, with

increased sensitivity and a tail in the profile due to difficulties in dissolving all the resist. In general high contrast resist/developer systems are required to give good resolution due to small differences in exposure resulting in large differences in developed thickness.

Figure 2.14: Plot of the resist sensitivity to exposure under different development conditions.

Thickness of Resist
Remaining after Development
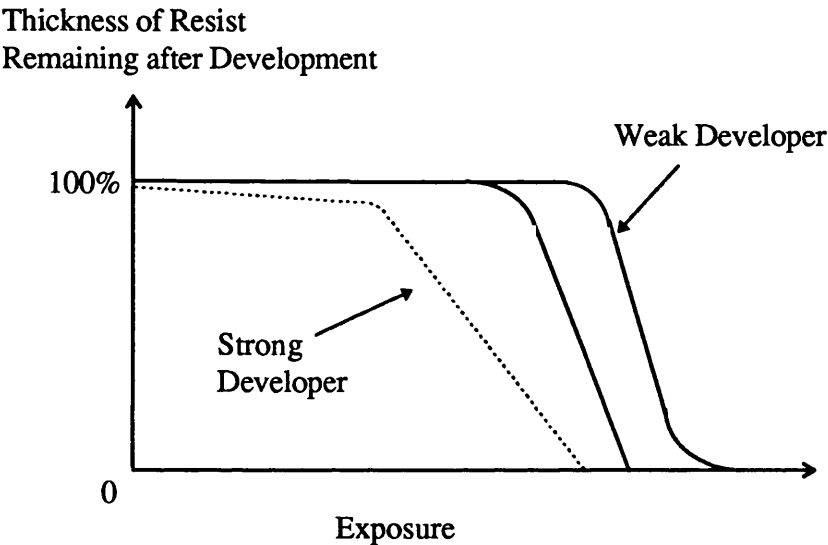
In addition to developer concentration, the resist sensitivity also increases as the temperature of the MIBK solution is raised. The optimal temperature is approximately 23°C, with a factor of 3 increase in sensitivity as the temperature is increased to 38°C. Finally, the accelerating voltage of the electrons during the exposure process also greatly effects sensitivity. This is due to secondary electrons generated by inelastic scattering of primary beam electrons off electrons in the outer shells of the resist atoms. The mean free path for events such as these is proportional to the accelerating voltage; hence the energy deposited in the resist, and thus the sensitivity, will be inversely proportional to the incident beam energy.

References

[1] E. H. Rhoderick and R. H. Williams, Metal Semiconductor Contacts: 2nd edition, (Clarendon Press, Oxford), (1988).

[2] W. M, Moreau, Semiconductor Lithography: Principles, Practises and Materials, (Plenum), (1988).

[3] Philips Beamwriter EBPG-5 System Manual.

[4] A. Barraud, C. Rosillo, A. Raudel-Texrier, J. Vac. Sci. Technol. 16, 2003 (1979).

[5] Nanoelectronic Research Centre, The University of Glasgow. (Unpublished).

[6] M. J. Bowden, Electron Irradiation of Polymers and its Application to resists for Electron-Beam Lithography, CRC Critical Reviews in Solid State Science, 223 (1979).

M. Kinsler, PhD. Thesis, Glasgow, 1992.

R. Cuscó-Cornet, PhD. Thesis, Glasgow, 1994.

Chapter 3

Experimental Techniques and Apparatus

3.1 Introduction

In this chapter the experimental apparatus and the general measurement techniques used in the course of this study are described. The use and control of various cryogenic systems is discussed, along with the types of measurements that were carried out using these systems. In addition, the steps taken to improve the signal to noise ratio and avoid unwanted radiation coupling into the measuring system are also described.

3.2 Cryogenic Equipment

The initial experiments were carried out using a closed circuit cryocooler in order to investigate the doping concentrations and depletion characteristics from room temperature to 15K. Magneto-conductance experiments were then carried out using a superconducting magnet surrounding either a He^3/He^4 dilution refrigerator or a variable temperature pumped helium insert. This enabled carrier concentration and mobility to be determined as a function of channel depletion

over the temperature range 100mK to 30K. Quantised conductance experiments were then carried out on the optimised heterostructure mainly in the regime 1.2K-30K.

3.2.1 Closed Circuit System

A CTI Cryogenics 21SC CRYODYNE cryocooler was used to access temperatures from 15K to room temperature. Helium gas is compressed at room temperature and flows through an inlet valve into one end of a cylinder. The gas is then displaced through the action of a piston through a regenerator to the other end of the cylinder. An exhaust valve opens, allowing the gas to expand providing the cooling mechanism. Finally the piston moves to expel the remaining gas through the exhaust valve and allow more to enter through the inlet valve.

A silicon diode is used as a temperature sensor exploiting the increasing voltage drop across the diode (from 0.4V to 2V) as the temperature falls from 300K to 15K. The temperature control unit operates by comparing the voltage dropped across the silicon diode with a reference signal corresponding to the desired temperature. The cooling process is stabilised by a variable current heat load supplied to the cold end of the cylinder. The temperature at which stabilisation of the cooling process is required can be set through the Set Point-Volts control. This digital control selects the sensor voltage at which cooling is to stop and heat is to be supplied to the cold head. To minimise fluctuations in temperature about the set point, Gain and Reset controls must be properly adjusted.

3.2.2 Oxford Instruments' Cryogenic Equipment

An Oxford Instruments He^4 Cryostat and Cryomag is the basis of the low temperature measurement system used during this project. The magnet sits in a bath of liquid He^4 at 4.2K and is capable of supplying fields up to 13T. Higher fields of up to 15T can be attained by pumping on the main bath, reducing the temperature of the He^4 to 2.2K. Wire containing niobium titanium filaments in a matrix of copper is wound into solenoids and the magnet is made up of a number of these solenoids, together with compensating coils. In addition, there is also an inner coil of niobium-tin allowing fields in excess of 11T to be produced. The magnet is powered by an Oxford Instruments PS120-10 (120A, 10V) power supply which can be controlled with a computer via an RS232 interface. Linear ramp rates of 0.3T/min and 0.1T/min were chosen for the measurements of resistance as a function of magnetic field. The samples sit in the centre of the magnet, perpendicular to the field, in either a dilution refrigeration or pumped helium insert.

Pumped Helium Insert

The pumped helium or variable temperature insert is an Oxford Instruments VTI. This relatively simple piece of equipment enables temperatures over the range 1.2K to 100K to be accurately accessed. Liquid helium from the main bath in the cryostat is supplied to the VTI via a pick up line as shown in Figure 3.1. The sample sits in an evacuated space to which liquid helium can be supplied through a needle valve. Opening the needle valve allows helium to flow through the sample space and into a helium return line which is connected to a rotary pump. Closing the return line and filling up the sample space with liquid

Figure 3.1: Schematic illustration of an Oxford Instruments Variable Temperature Insert.

Sample Space
Relief Valve

Ten Pin Seal/Electrical Access

Sample Space
Pumping Port

Inner Vacuum Chamber
Pumping Port/Vacuum Relief

Needle Valve Top

Needle Valve

Capillary
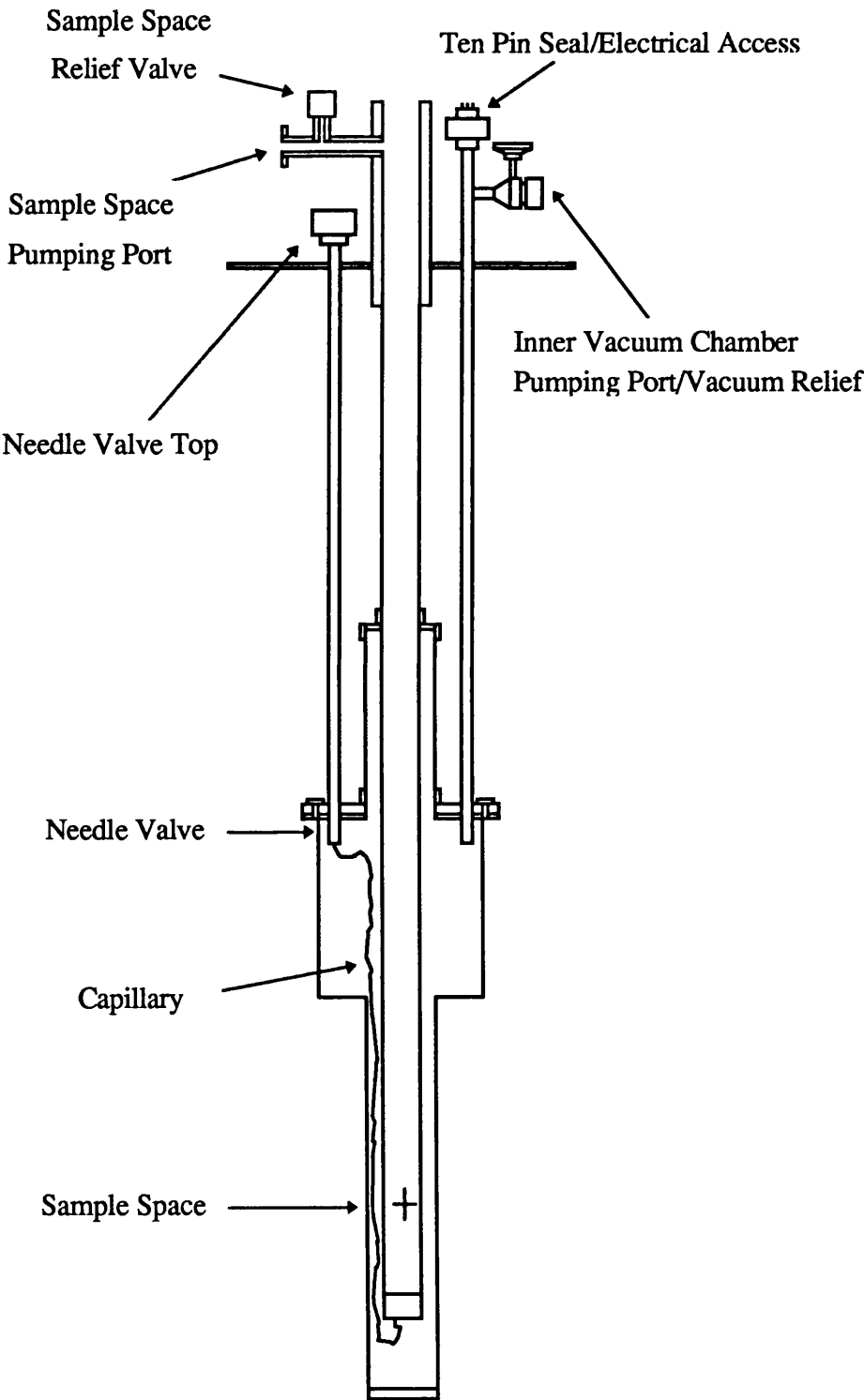
Sample Space

helium brings the sample space to 4.2K. Opening the return line reduces the vapour pressure in the sample space through the action of the pump and after some time the temperature reduces to 1.2K. To achieve temperatures above 4.2K, a flow of helium is set up through the needle valve and into the return line and a heat load is supplied to a heater at the helium inlet point. In this way warm vapour is allowed to flow over the sample raising the temperature. A carbon glass thermometer is also mounted at the inlet point so that the temperature of the incoming gas can be measured and thus stabilised by altering the heat load. The sample temperature is measured to $\pm 0.1°C$ with a Rh-Fe thermometer in thermal contact with the sample.

Dilution Refrigeration Insert

An Oxford Instruments Kelvinox He^3/He^4 dilution refrigerator was used to produce temperatures below 1.2K. A controlled mixture of He^3 in He^4 provides the cooling mechanism by exploiting the fact that below 0.7K a homogeneous mixture of these two isotopes of helium will separate into a He^3 rich phase (concentrated) floating on a more dense He^4 rich phase (dilute). The He^3 concentration in the dilute phase tends to a constant 6% as the temperature approaches absolute zero. Hence if the He^3 is pumped from the dilute phase, it is immediately replaced by He^3 from the concentrated phase in order to maintain the equilibrium at the phase boundary. It is this removal of the He^3 that cools the sample by removing heat of dilution.

3.3 Sample Mounting

Samples are mounted on 18 contact ceramic chip carriers which fit into a socket to which measurement leads are connected, see Figure 3.2. Contact

Figure 3.2: Schematic illustration of the sample holder which is screwed onto the appropriate measurement rod.

Sample

18 pin ceramic capsule

Copper cylinder

Insert
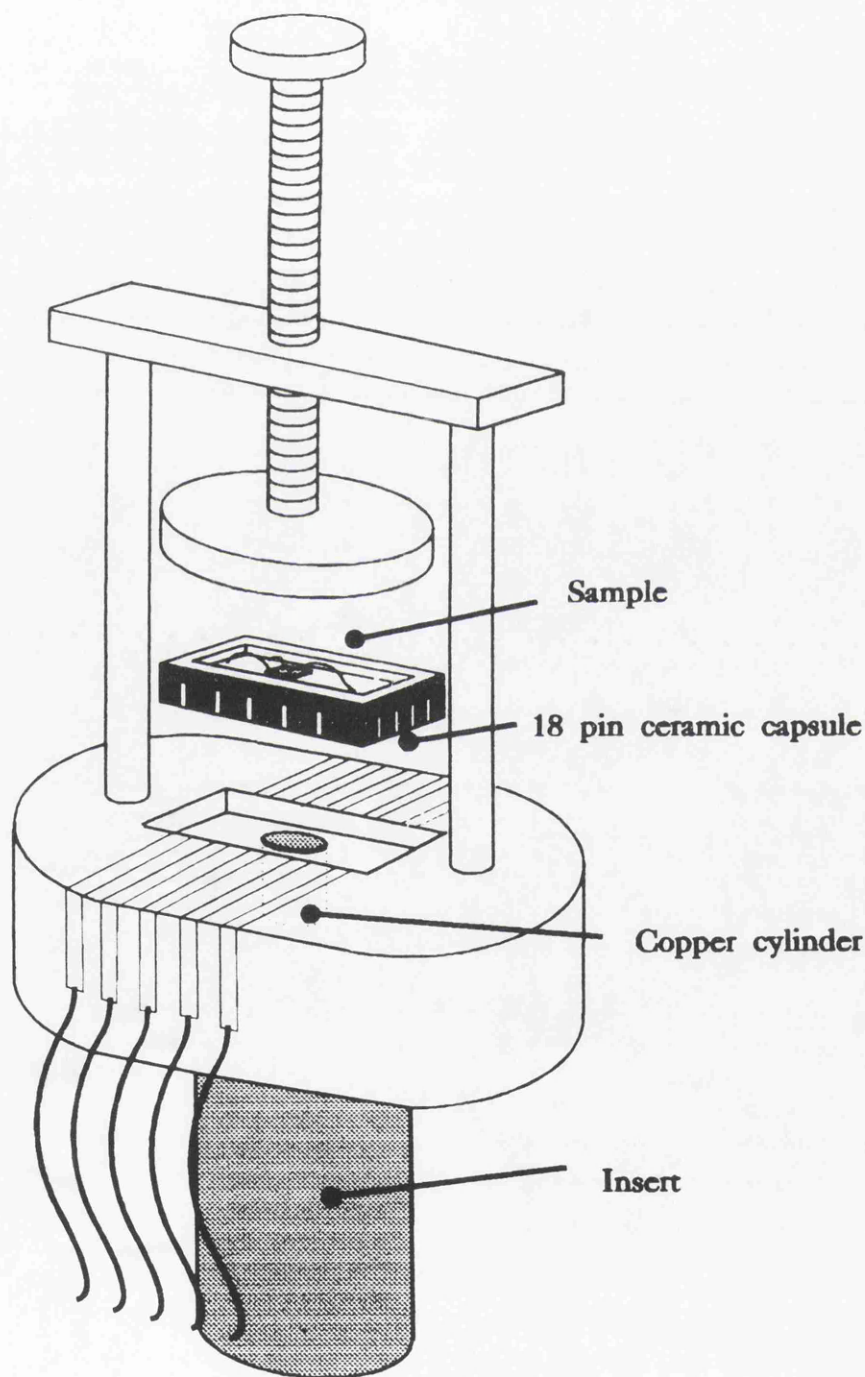
between the optically defined circuitry of the samples and the gold contacts on the ceramic chip holders is made with 40μm gold wire using an ultra sonic deep access wedge bonder. Thermal earthing is provided by a spring loaded copper cylinder which is in contact with the chip carrier when it is screwed into place.

3.4 A.C Capacitance Measurements

A Hewlett Packard 4274A Multi-Frequency LCR Meter was used to measure the capacitance of a large gate to the 2DEG beneath as a function of gate bias between room temperature and 15K. The internal bias supplied by the meter would be applied to the gate on the sample and the capacitance between the gate and the 2DEG would then be measured at a frequency of 100kHz, see Figure 3.3. The LCR meter is computer controlled via an IEEE488 bus, using standard Turbo-Pascal routines developed in the group to run on an IBM compatible personal computer.

Figure 3.3: Schematic of the circuit to measure the capacitance of a large gate to the 2DEG beneath as a function of gate bias.
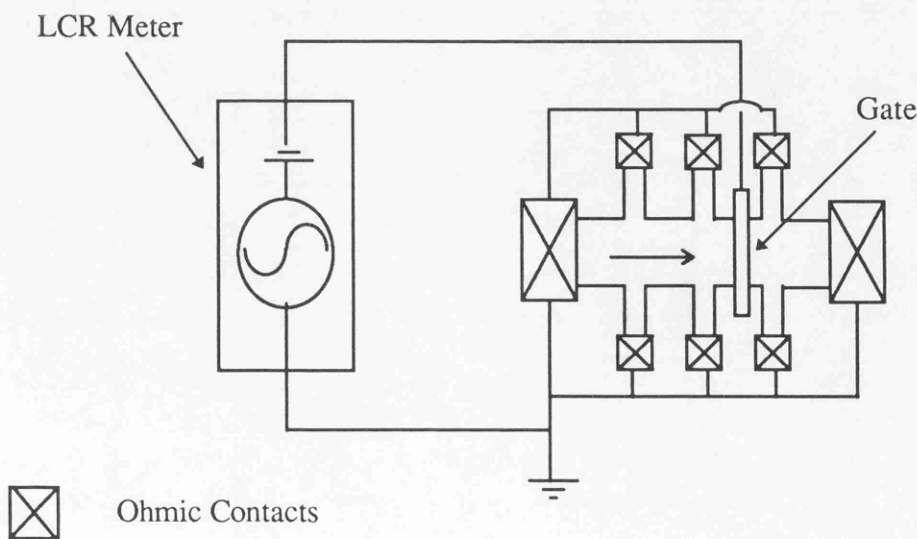
3.5 Low Frequency Conductance Measurements

A 18Hz signal (of typical amplitude 100mV) from the internal oscillator of a lock-in amplifier is fed into a resistor network, which is usually set to reduce the signal by a factor of 1000. The signal is then dropped across a 10kΩ resistor in series with the sample. The voltage across the series resistor is measured by one of two Princeton 5210 dual phase lock-in amplifiers. Lock-in amplifiers are used because they improve the signal to noise ratio in the experiments by measuring the response of the sample to the signal level in a very narrow bandwidth centred on the frequency of the internal oscillator in the unit [1]. Essentially the lock-in amplifier measures the input signal at a pre-set reference frequency. The input signal is then amplified and applied to the phase sensitive detector operated at the same reference frequency. The phase sensitive detector gives a non linear response to frequencies different from the reference frequency. This results in frequency varying a.c. components which can be attenuated by an internal low pass filter. The standard low frequency conductance measurement configuration is given in Figure 3.4.

Conductance measurements as a function of gate bias are carried out using the configuration outlined above with the gate voltage being supplied by a Hewlett Packard 3245A Universal Voltage Source. In the same way as the capacitance measurements described in Section 3.4, all the equipment is controlled with an IBM compatible personal computer via IEEE488 interfaces using standard Turbo-Pascal routines developed in the group. The voltage supplied to the gate is changed and then after a delay, the resistances in the circuit are measured. Magneto-conductance experiments are carried out using an IEEE bus via an IEEE to RS232 converter through suitable Turbo-Pascal routines. In this case the magnetic field is a continuous function and so the circuit resistance is recorded with the mean magnetic field. This average is obtained from the measured field values before and after the measurement of the circuit resistances.

Figure 3.4: Schematic illustrating the standard low frequency conductance measurement configuration.

Voltage Dropped Across 10kΩ Series Resistor R

V_{ref}

PSD

Gate Supply

R

PSD

Voltage Dropped Across Device

⊠   Ohmic Contacts
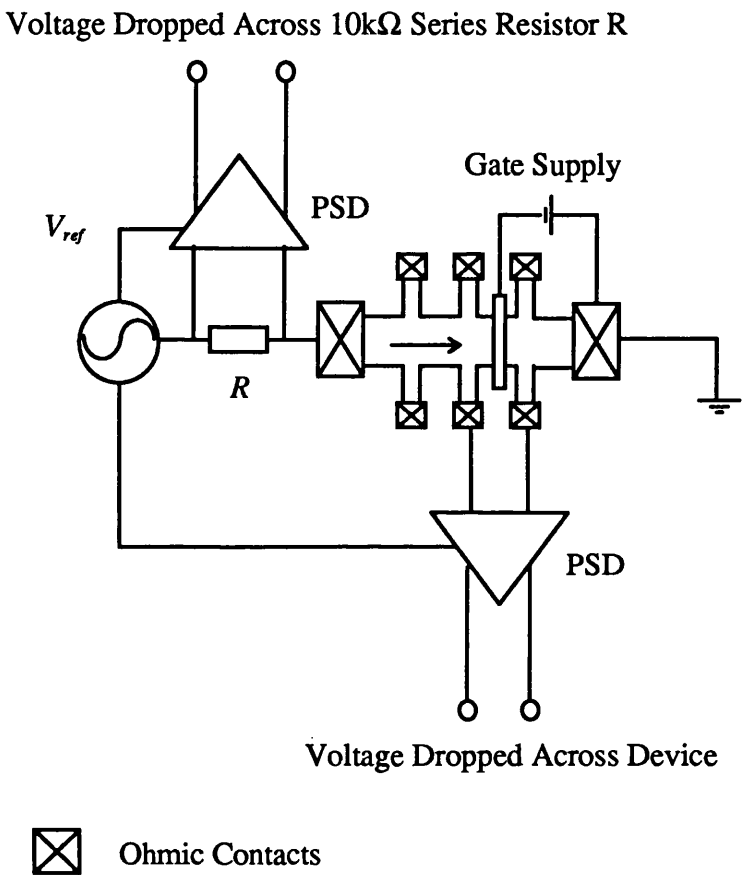
3.6 Shielding, Filtering and Earthing

The experimental apparatus is enclosed in a screened room, see Figure 3.5. Coaxial cables carry the measurement signals into and out of the screened area, passing through low pass filters. The filtering together with the metal screening minimises the amount of unwanted radiation that couples through the measurement leads onto the sample. This is important because electric noise can produce significant electron heating in a 2DEG.

Figure 3.5: Schematic illustrating the measurement system used for experiments below 15K.

Voltage Measurement Leads

EG&G 5210

EG&G 5210

18 Pin BNC-Fischer Adapter

Screened Room

Oscillator

100kΩ

100Ω

Sample

HP 3245A

1MΩ

Cryostat

▓ Low Pass Filters
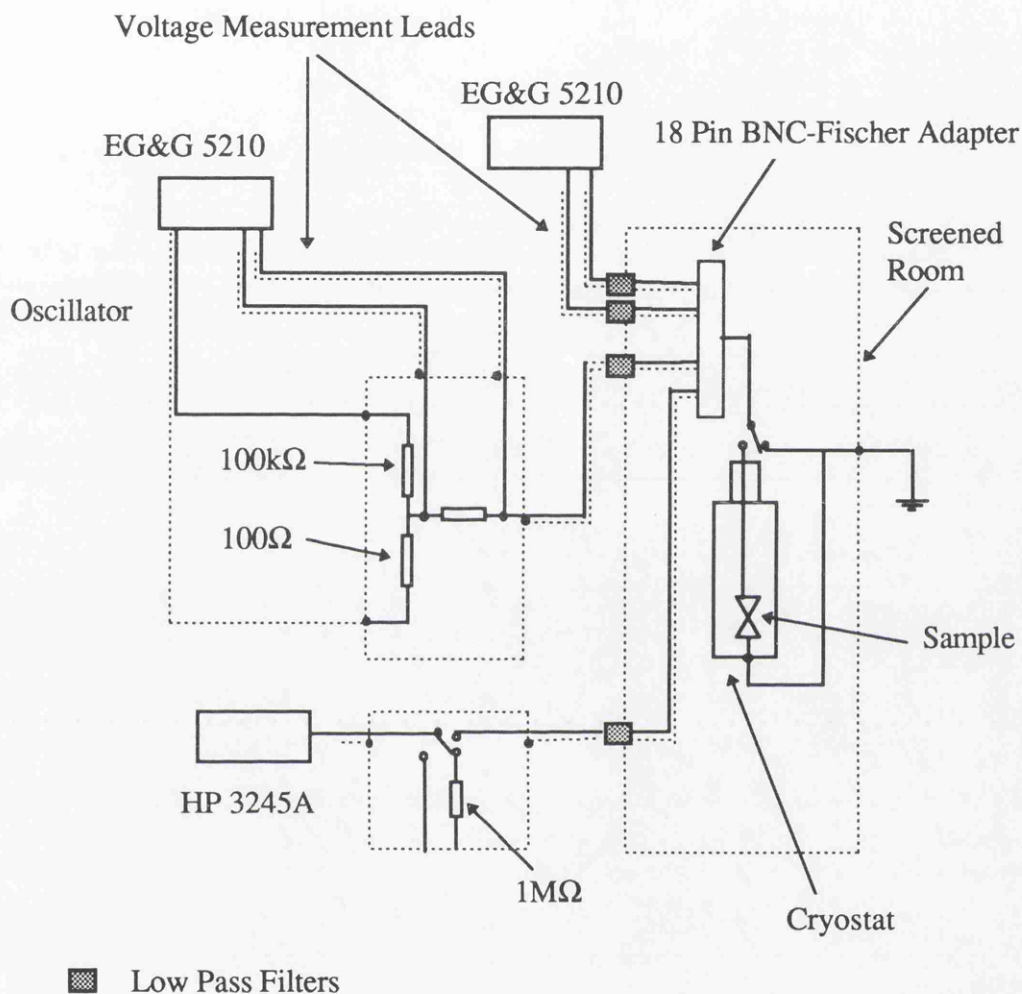
Once inside the screened area, a potential divider is used to reduce the excitation signal from the driving lock-in amplifier, typically by a factor of 1000 or 100. This allows measurement of the sample characteristics in the linear response regime i.e. electrons in the 2DEG have energies well below k_BT. Mechanical vibrations are reduced by damping the pumping lines connected to the cryostat with lead foam and standing the cryostat and pumps on damping mats. Finally, care is taken to electrically isolate the cryostat from the outside world and then earth the

equipment at a single point. This helps to prevent the formation of "earth loops", small stray currents flowing between different parts of the equipment which are at slightly different potentials.

References

Frontiers in Physics: Experimental Techniques in Condensed Matter Physics at Low Temperatures, edited by R. C. Richardson, E. N. Smith (Addison Wesley Publishing Company, Inc), (1988).

M. Kinsler, PhD. Thesis, Glasgow, 1992.

R. Cuscó-Cornet, PhD. Thesis, Glasgow, 1994.

Chapter 4

Shallow GaAs-Al$_x$Ga$_{1-x}$As Heterostructures

4.1 Introduction

In order to operate quantum devices at higher temperatures, it is necessary to form the two dimensional electron gas as close to the surface and the gate electrodes as possible. This ensures strong confinement of the electrons and hence an optimum sub-band separation in the device [1, 2]. This chapter outlines the experiments carried out in order to design such a heterostructure using GaAs and Al$_x$Ga$_{1-x}$As. In forming the interface close to the surface care must be taken to ensure that the mobility is high enough to enable wires to be measured in the ballistic regime [3, 4]. In order for this to be successful, it is necessary to ensure that the doping level is optimised for a particular heterostructure and this requires an understanding of the various electrostatic parameters involved. To this end the model of Long et al. (see Chapter 1, Sections 1.2.3 and 1.2.4) is employed [5]. Briefly, if too few donors are incorporated into the structure, then a solution to Equation 4.1 is not possible.

$$n_{2D}\left(\frac{c}{\varepsilon_g} + \frac{s}{\varepsilon_a} + \frac{u}{\varepsilon_a} + \frac{a}{\varepsilon_g}\right) = N_\delta\left(\frac{c}{\varepsilon_g} + \frac{u}{\varepsilon_a}\right) - \frac{\varepsilon_0}{e^2}E_c(0) \qquad (4.1)$$

On the other hand, the use of more donors than required to satisfy this relation, implies a longer growth interrupt during the preparation and also more silicon diffusion towards the transport plane, both these effects give enhanced coulomb scattering. In addition, a higher doping level may lead to many electrons residing in the doping region or the population of a second sub-band. Neither of these effects is desirable because electrons in the doping region (which do not become trapped at low temperatures by deep donors) and those in the second sub-band will screen the electrons in the 2DEG from the effects of a surface gate. It is therefore necessary to investigate these effects in order to optimise the doping level and so produce material which can be used to produce working quantum devices.

4.2 Description of the Heterostructures

The emphasis of this part of the project was to develop and understand shallow GaAs-Al$_x$Ga$_{1-x}$As heterostructures grown by MBE. Two types of structures were investigated: GaAs-Al$_{0.3}$Ga$_{0.7}$As [6] and GaAs-AlAs [7], see Figure 4.1. These structures were δ-doped with various concentrations of silicon donors with a monolayer of GaAs grown either side of the dopant plane [8]. These monolayers are included in order to inhibit the incorporation of carbon and oxygen impurities during the growth interrupt of the order of 100 seconds which was necessary for the deposition of the silicon. More conventional GaAs-Al$_{0.3}$Ga$_{0.7}$As slab doped heterostructures grown in the same deposition cycle were also investigated for comparison purposes.

The experiments on these materials were aimed at understanding the role of the doping level and hence a number of different structures with different doping concentrations were studied. The complete set of samples, with their main growth parameters, are given in Table 4.1. The two main methods of investigation employed were high frequency capacitance measurements and low temperature

Table 4.1: Various useful data associated with the different heterostructures discussed in this chapter.

Sample Identification	Sample Type	Doping Type	Doping Level (m^{-2})	Spacer Width (nm)	Depth of 2DEG (nm)	Experiment Temperature (K)	Dark Carrier Conc. (m^{-2})	Illuminated Carrier Conc. (m^{-2})	Dark Mobility (m^{2}V^{-1}s^{-1})	Illuminated Mobility (m^{2}V^{-1}s^{-1})
A502	AlAs	Delta	1×10^{17}	10+1.1	28	4.2	3.4×10^{15}		68.0	
A601	AlAs	Delta	4×10^{16}	10+1.1	28	0.07	3.5×10^{15}	3.8×10^{15}	86.4	116.0
A601	AlAs	Delta	4×10^{16}	10+1.1	28	4.2	3.5×10^{15}	3.7×10^{15}	80.0	110
A685	AlAs	Delta	4×10^{16}	10+1.1	28	1.2	3.5×10^{15}		38	
A627	AlAs	Delta	2×10^{16}	10+1.1	28	4.2	1.1×10^{15}	3.8×10^{15}	1	3.4
A686	Al$_{0.3}$Ga$_{0.7}$As	Delta	4×10^{16}	10+1.1	28	1.2	$5.8\text{-}6.7\times10^{15}$	6.9×10^{15} (cf.5.8×10^{15})	18-30	21 (cf.18)
A707	Al$_{0.3}$Ga$_{0.7}$As	Delta	2×10^{16}	10+1.1	28	1.2	5.6×10^{15}	7.7×10^{15}	21.4	34.8
A665	Al$_{0.3}$Ga$_{0.7}$As	Delta	2×10^{16}	10+1.1	28	1.2	2.6×10^{15}	2.7×10^{15}	1.1	1.5
A688	Al$_{0.3}$Ga$_{0.7}$As	Slab	5×10^{16}	20	40	1.2	4.0×10^{15}		71.0	
A629	Al$_{0.3}$Ga$_{0.7}$As	Slab	8×10^{16}	40	92	1.2	3.4×10^{15}	4.2×10^{15}	243.0	410.0

magneto-transport measurements, see Chapter 3, Section 3.4 and 3.5 for the technical details of the experimental procedure.

Figure 4.1: Illustration of the layer structure for the shallow GaAs-Al$_{0.3}$Ga$_{0.7}$As and GaAs-AlAs heterostructures investigated in this project. The important physical dimension are also included.

GaAs-AlAs   GaAs-AlGaAs

| GaAs 19ML |
| AlAs 10nm |
| AlGaAs 4ML |
| GaAs 1ML |
| Silicon δ Doping |
| GaAs 1ML |
| AlGaAs 4ML |
| AlAs 10nm |
| GaAs 1.6μm |

c=5.4nm

u=11nm

s=11nm

2DEG

| GaAs 19ML |
| AlGaAs 10nm |
| AlGaAs 4ML |
| GaAs 1ML |
| Silicon δ Doping |
| GaAs 1ML |
| AlGaAs 4ML |
| AlGaAs 10nm |
| GaAs 1.6μm |
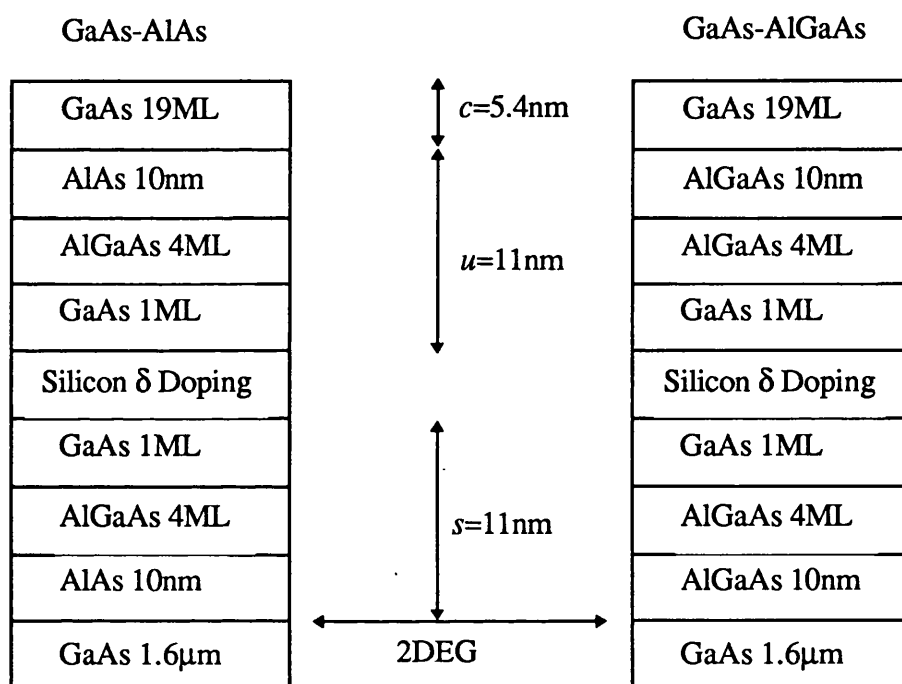
ML: Monolayer (1ML=0.28nm)

4.3 Capacitance Measurements

This section details measurements of the capacitance of a large gate to the 2DEG beneath as a function of gate bias between room temperature and 15K. The measurements were carried out on the five different GaAs-Al$_{0.3}$Ga$_{0.7}$As and GaAs-AlAs heterostructures detailed in Table 4.2, see page 95.

4.3.1 Description of the Capacitance Experiments

The experimental data for the shallow (A686) and the deeper (A688) GaAs-Al$_{0.3}$Ga$_{0.7}$As heterostructures are given in Figures 4.2 and 4.3 respectively. In both sets of data there is a positive shift in the cut-off as a function of decreasing temperature in the region 180K→20K. This dominating effect is associated with *DX* centre traps which were discussed in Chapter 1, Section 1.2.2 [9, 10]. At higher temperatures, these traps must be depleted before the charge in the 2DEG is effected by the gate potential. As the temperature is lowered, less electrons have sufficient thermal energy to move out of *DX* traps and these less energetic electrons are no longer effected by the action of the gate bias, they are said to be 'frozen'. Consequently there is less free charge in the system for the gate bias to remove and so the channel depletes at more positive voltages. The qualitative results are consistent with similar measurements carried out on conventional deeper heterostructures [5].

Figure 4.2: Capacitance as function of gate voltage at various temperatures for the A686 GaAs-Al$_{0.3}$Ga$_{0.7}$As heterostructure.
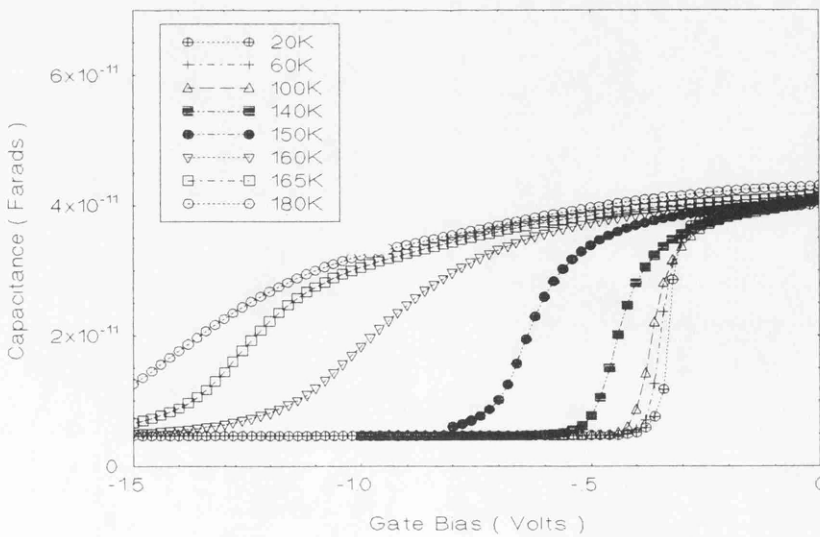
Figure 4.3: Capacitance as function of gate voltage at various temperatures for the A688 GaAs-Al$_{0.3}$Ga$_{0.7}$As heterostructure.
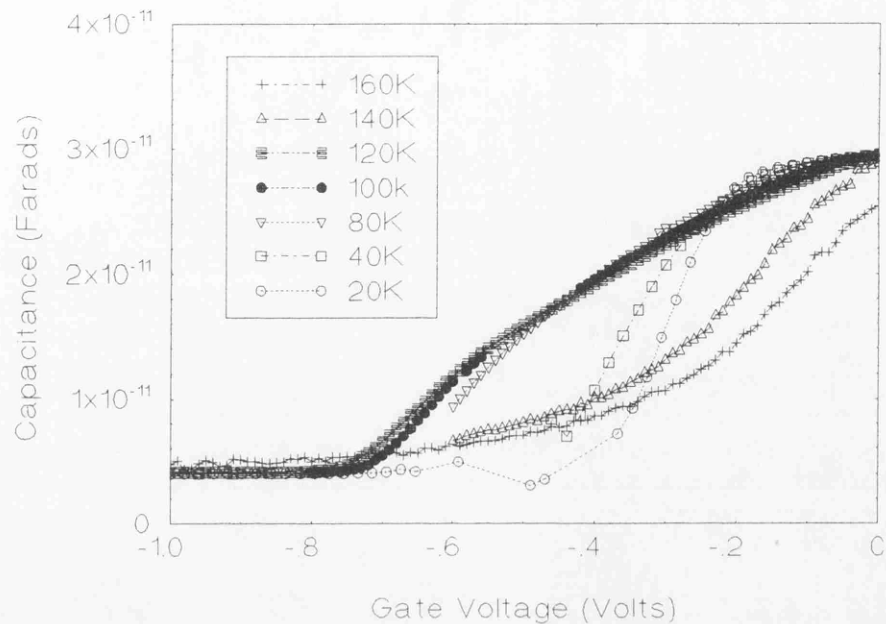
Figure 4.4: Capacitance as a function of gate voltage at various temperatures for the A601 GaAs-AlAs heterostructure.
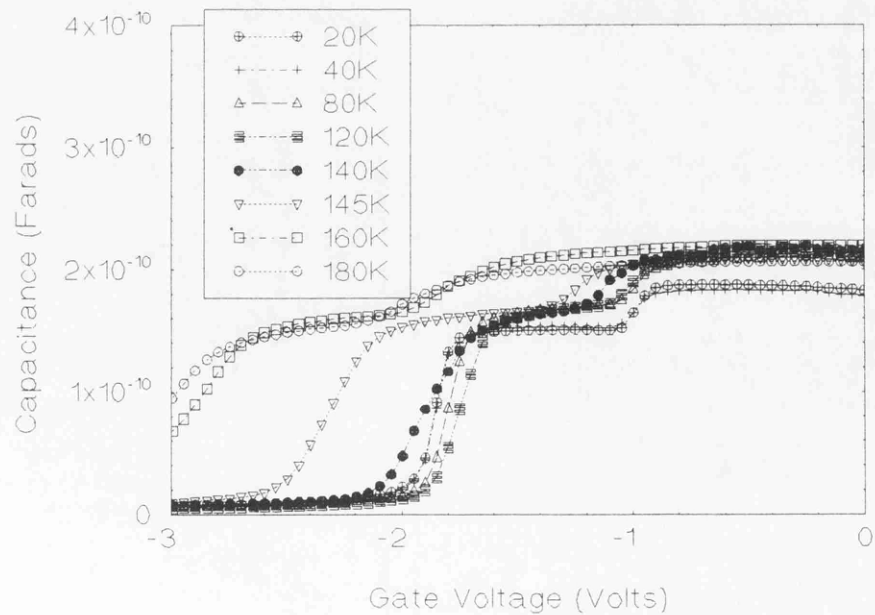
Figure 4.5: Capacitance as a function of gate voltage at various temperatures for the A627 GaAs-AlAs heterostructure.
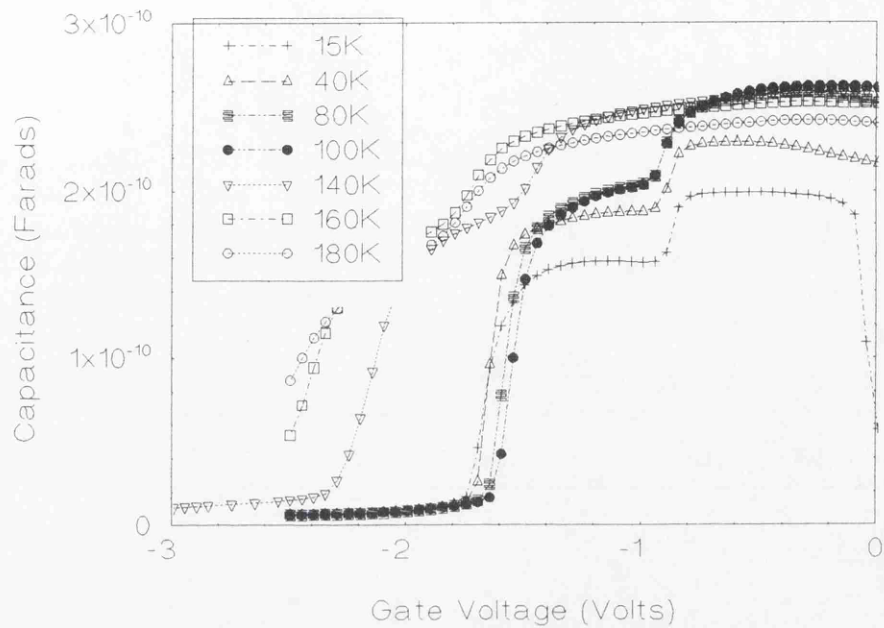
Figure 4.6: Capacitance as a function of gate voltage at various temperatures for the A502 GaAs-AlAs heterostructure.
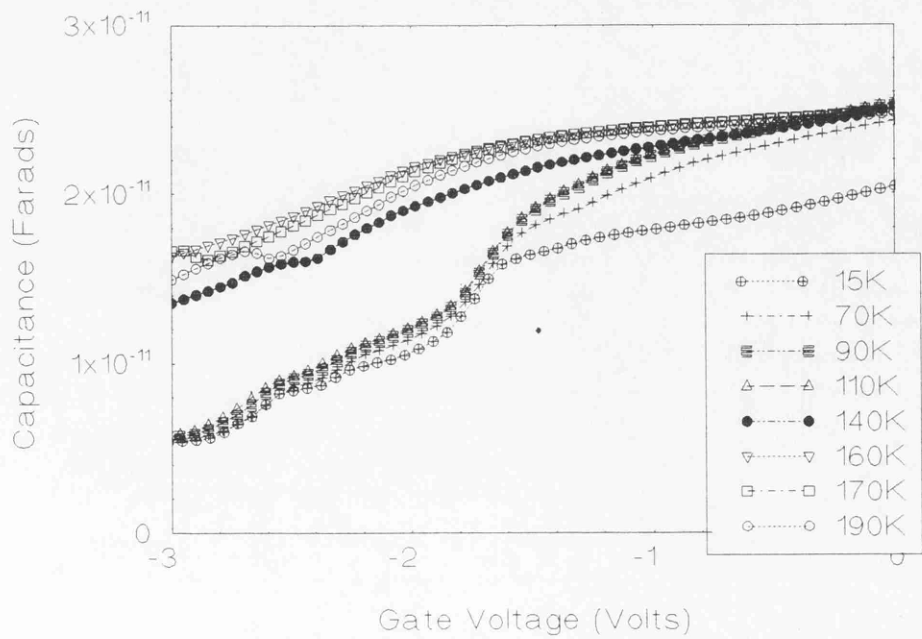
The same type of experiments were also carried out on the three GaAs-AlAs heterostructures: A502, A601 and A627, see Figures 4.4-6. Comparison with the GaAs-Al$_{0.3}$Ga$_{0.7}$As structures gives a generally similar positive shift in the cut-off voltage as a function of temperature, however the cut-off voltages are much more negative. These large negative cut-off voltages are indicative of a large amount of free charge, much of which is still free at low temperatures. Either the concentration of *DX* centres in GaAs-AlAs is lower than in GaAs-Al$_{0.3}$Ga$_{0.7}$As, or else a substantial quantity of electrons must be located in other types of traps which can be depleted at low temperatures.

The experiments on the GaAs-AlAs structures also show a relationship between the threshold voltages and doping densities. There is a clear trend towards a smaller shift in the cut-off as the doping density is reduced from $4 \times 10^{16} \text{m}^{-2}$ silicon donors in A601, to $2 \times 10^{16} \text{m}^{-2}$ in A627. This is to be expected because at lower doping densities there will be a lower density of *DX* centres and hence the shift in the threshold (due to the condensation of electrons into these traps) will be smaller. In the highly doped A502 sample, there is again a large *DX* centre shift and this heterostructure is difficult to deplete, even at low temperatures, indicating that this structure in grossly over doped.

Finally there is a clear double bump in all GaAs-AlAs capacitance data which is not apparent in the GaAs-Al$_{0.3}$Ga$_{0.7}$As structures. This may be due to different concentrations of charge in the alternate layers of Al$_{0.3}$Ga$_{0.7}$As and AlAs layers either side of the doping region in GaAs-AlAs. More direct evidence to justify this conclusion will be presented when the low temperature magneto-transport experiments are discussed in Section 4.4.

4.3.2 Charge Depletion in GaAs-Al$_{0.3}$Ga$_{0.7}$As and GaAs-AlAs

In the experiments described in the previous section, the capacitance measurements probe all the mobile charge under the gate. It is possible to quantify

how much charge has been depleted by the action of the gate and compare this value with the known charge in the 2DEG. In Chapter 1, Section 1.2.4 a model is outlined which enables the magnitude of the depleted charge to be determined from the known capacitance C and threshold voltage V_T of a GaAs-Al$_{0.3}$Ga$_{0.7}$As heterostructure, see Equation 4.2 [5]. Essentially this involves integrating under the low temperature (20K) capacitance curve, assuming that the entire area A of the gate is active and uniform, with most of the free charge is concentrated in the 2DEG.

$$n_{2D}e \approx -V_T\left(\frac{C}{A}\right) \tag{4.2}$$

The actual charge in the 2DEG comes from magneto-transport data carried out on ungated samples at 1.2K, see Section 4.4. By comparing the charge measured by these two types of measurement it is possible to estimate the probable location of regions of free charge in the various structures. The difference in the temperatures at which the two types of measurements are carried out should not be significant because experiments showed that the carrier concentration in the 2DEG only changes by a few percent over this regime. The data is summarised in Table 4.2. The experimental errors are derived from variations in the carrier concentration measured in different magneto-transport experiments. The errors in calculating the carrier concentration are determined from the uncertainty in estimating the position of the threshold voltage, the fluctuations of ±5% in the zero gate bias capacitance and the uncertainty in the area of the gate (±2μm). The A627 sample is only included for completeness because at this doping level, a solution to Equation 4.1 is not possible and indeed the sample is found to have quite different characteristics depending on its position on the wafer and the cooling rate.

For the GaAs-Al$_{0.3}$Ga$_{0.7}$As samples, the difference between the charge density in the structure and the charge density in the 2DEG is less than 50% i.e.

most of the low temperature free charge in these structures is located in the actual 2DEG. The fairly large difference between the carrier concentrations determined by the two methods is significant and will be addressed in the following section. For the GaAs-AlAs samples, the difference between the charged density measured in the structure and the charge density in the 2DEG is an order of magnitude. In addition it would seem that there is more charge in the two GaAs-AlAs structures than the doping charge, clearly the model is inadequate here.

Table 4.2: The estimated charge depleted in capacitance measurements on various GaAs-Al$_x$Ga$_{1-x}$As heterostructures is compared with the low temperature carrier concentration measured in the 2DEG.

Sample Number	Sample Structure	Doping Level (m^{-2})	Carrier Conc. (Magneto-transport) (m^{-2})	Carrier Conc. (Capacitance) (m^{-2})
A502	GaAs-AlAs	1×10^{17}	(3.4±0.1)×10^{15}	Does not deplete
A601	GaAs-AlAs	4×10^{16}	(3.5±0.1)×10^{15}	(6.7±0.6)×10^{16}
A627	GaAs-AlAs	2×10^{16}	(1.1±0.1)×10^{15}	(6.2±0.6)×10^{16}
A686	GaAs-Al$_{0.3}$Ga$_{0.7}$As	4×10^{16}	(6.3±0.5)×10^{15}	(3.7±0.6)×10^{15}
A688	GaAs-Al$_{0.3}$Ga$_{0.7}$As	5×10^{16}	(4.0±0.1)×10^{15}	(2.8±0.7)×10^{15}

Most of the electrons supplied by the donors go to the surface states in both GaAs-Al$_{0.3}$Ga$_{0.7}$As and GaAs-AlAs structures. The other major concentrations of electrons are expected to be confined in either the 2DEG or *DX* centres. At low temperatures electrons trapped in *DX* centres cannot be depleted and so the charge depleted by the gate should be all located in the 2DEG. The data in Table 4.2 and the complicated behaviour of the threshold in Figures 4.2 and 4.3 indicates that for GaAs-Al$_{0.3}$Ga$_{0.7}$As structures this is an adequate description.

For the GaAs-AlAs structures the model simply breaks down. There is clearly a large amount of free charge in these types of heterostructures which is not confined at low temperatures to the 2DEG or *DX* centres. This could be a

result of a lower concentration of *DX* centres in the GaAs-AlAs structure, which leads to free charge remaining in the donor region at low temperatures. This is possible because the *DX* is an resonant state, approximately 30meV above the *X* conduction band minimum in AlAs and so a large concentration of these defects are not expected to be occupied [11]. However the threshold voltages in Figures 4.4-6 show large shifts associated with the occupation of *DX* centres, similar to those found in the GaAs-Al$_{0.3}$Ga$_{0.7}$As samples. This may be due to the fact that the GaAs-AlAs heterostructures have been grown with four monolayers of Al$_{0.3}$Ga$_{0.7}$As either side of the silicon doping, see Figure 4.1. Therefore the shifts in the threshold voltages may be associated with the occupation of *DX* centres in this region and not the AlAs. An explanation of the large quantities of free charge in GaAs-AlAs is much more difficult.

4.3.3 Capacitance and Threshold Voltages

It is also possible to use the model developed by Long et al. to analyse the capacitance per unit area of a gate of area *A* to the 2DEG beneath, as a function of the dimensions of the structure (see Figure 4.1) and the 'thickness' *a* ($\approx$10nm) of the 2DEG. This relation is reproduced in Equation 4.3, where ε_o is the electric permitivity of free space and ε_g(13.1) and ε_a(12.2) are the respective, relative electric permitivities of GaAs and Al$_{0.3}$Ga$_{0.7}$As. For AlAs, ε_a becomes 10.1.

$$\frac{C}{A} = \varepsilon_0 \left(\frac{a}{\varepsilon_g} + \frac{s}{\varepsilon_a} + \frac{u}{\varepsilon_a} + \frac{c}{\varepsilon_g} \right)^{-1} \tag{4.3}$$

Table 4.3 compares the results of applying Equation 4.3 to the heterostructures described above, with the experimental capacitance per unit area.

Table 4.3: The expected capacitance per unit area is compared with the value obtained from measurements of the depletion characteristics of various GaAs-Al$_x$Ga$_{1-x}$As heterostructures.

Sample Number	Sample Structure	Experimental Capacitance/unit area (Fm^{-2})	Calculated Capacitance/unit area (Fm^{-2})
A601	GaAs-AlAs	$(5.6\pm0.4)\times10^{-3}$	$(2.6\pm0.6)\times10^{-3}$
A627	GaAs-AlAs	$(6.3\pm0.5)\times10^{-3}$	$(2.6\pm0.6)\times10^{-3}$
A686	GaAs-Al$_{0.3}$Ga$_{0.7}$As	$(2.0\pm0.2)\times10^{-3}$	$(2.9\pm0.8)\times10^{-3}$
A688	GaAs-Al$_{0.3}$Ga$_{0.7}$As	$(1.5\pm0.1)\times10^{-3}$	$(2.2\pm0.5)\times10^{-3}$

The errors in the experimental capacitance per unit area come from fluctuations of $\pm5\%$ in the capacitance when no bias is applied to the gate electrode and also from the error in the area of the gate ($\pm2\mu$m). For the calculation, the errors come from the dimensions of the layers: which are approximately $\pm$ 1 or 2 monolayers (at the very most) i.e. ±0.56nm and the estimate of the 'thickness' of the 2DEG a ($\propto 1/n_{2D}$). It is difficult to treat the error in a, quantitatively, as this requires knowledge of the error in the strength of the confinement potential. In the triangular well approximation [12], $a\propto 1/n_{2D}$ and so the error in a approximates as the uncertainty in n_{2D}. For the shallow GaAs-Al$_{0.3}$Ga$_{0.7}$As structure (A686), n_{2D} varies by 8% between samples from different parts of the wafer, for GaAs-AlAs and the deeper GaAs-Al$_{0.3}$Ga$_{0.7}$As structure (A688) the variation is just 3%. The reasons for these variations is discussed in Section 4.4. It is immediately clear from the data in Table 4.3 that for the A686 and A688 GaAs-Al$_{0.3}$Ga$_{0.7}$As samples, there is just about agreement with the simple electrostatic model. However for the GaAs-AlAs sample (A601) the model is simply not an adequate description of the measurement.

Finally substituting Equation 4.3 into Equation 4.2 an expression for the estimated threshold voltage V_T can be derived in terms of the dimensions of the structure and the carrier concentration in the 2DEG, see Equation 4.4.

$$V_T = -\frac{e}{\varepsilon_0} n_{2D} \left(\frac{c}{\varepsilon_g} + \frac{s}{\varepsilon_a} + \frac{u}{\varepsilon_a} + \frac{a}{\varepsilon_g} \right) \qquad (4.4)$$

Applying this relation to the carrier concentration data in Table 4.2, the expected threshold voltages can be deduced, see Table 4.4. The errors in experimental threshold voltages simply come from the uncertainty in estimating its position from the experimental data. The errors in the calculated threshold voltages are derived in a similar way to those for the calculated capacitance per unit area i.e. variations in n_{2D} and the uncertainty in the dimensions of the layers.

Table 4.4: The estimated threshold voltage required to deplete the low temperature magneto-transport carrier concentration is compared to the threshold voltage obtain by measuring the capacitance of various GaAs-Al$_x$Ga$_{1-x}$As heterostructures as a function of depletion.

Sample	Experimental Carrier Concentration n_{2D} (m^{-2})	Experimental Threshold Voltage (Volts)	Calculated Threshold Voltage (Volts)
A601	$(3.5\pm0.1)\times10^{15}$	-1.90 ± 0.02	-0.21 ± 0.05
A627	$(1.1\pm0.1)\times10^{15}$	-1.60 ± 0.02	-0.07 ± 0.02
A686	$(6.3\pm0.5)\times10^{15}$	-0.30 ± 0.02	-0.34 ± 0.09
A688	$(4.0\pm0.1)\times10^{15}$	-0.30 ± 0.05	-0.29 ± 0.08

For the GaAs-Al$_{0.3}$Ga$_{0.7}$As heterostructures the calculation of the threshold voltages is seen to be in excellent agreement with the experimental measurements. When the same model was used to estimate the capacitance per unit area of the GaAs-Al$_{0.3}$Ga$_{0.7}$As heterostructures, the agreement with the experimental results was found to be not quite as good, but still just within the experimental error.

For the GaAs-AlAs heterostructure (A601), both the threshold voltages and the capacitance per unit area were measured and found to be very different from the calculated values. It is obvious that the implicit assumption of a neutral spacer layer is accurate for Al$_{0.3}$Ga$_{0.7}$As but not for AlAs. These results and their

possible implications for the charge distribution in the layers will be discussed further in Section 4.4.5 in the light of gated magneto-transport experiments.

4.3.4 GaAs-AlAs and the Simple Electrostatic Model

The simple electrostatic model assumes that there is sufficient diffusion of the dopant to form deep donor or *DX* centres in the spacer layers. Electrons will then condense into these traps as the structure is cooled and it is this mechanism that will pin the Fermi level in the donor layer at an effective energy E_{dd} below the conduction band. This model works well for GaAs-Al$_{0.3}$Ga$_{0.7}$As when an effective energy E_{dd}=0.07eV is used. It was explained in Section 4.3.2 that the occupation of *DX* centres in AlAs is unlikely and that the *DX* trapping effects in these GaAs-AlAs structures may be associated with the formation of *DX* centres in the four monolayers of Al$_{0.3}$Ga$_{0.7}$As either side of the doping layer. In this case the pinning energy should be the same as that in the GaAs-Al$_{0.3}$Ga$_{0.7}$As structures. However this may not be a reasonable assumption because the diffusion of silicon may not be limited to the Al$_{0.3}$Ga$_{0.7}$As. Silicon in AlAs can form *DX* centres but they are resonant states for electron occupation and so require substantial concentrations of electrons to fill up the intervening energy states before becoming occupied. This is speculation but it would substantially alter the pinning energy.

4.3.5 Description of Bias Cooling Capacitance Experiments

The A686 GaAs-Al$_{0.3}$Ga$_{0.7}$As sample was cooled with a bias of -2V on the gate electrode. Capacitance measurements were then taken at increasing temperatures between 15K and 180K, see Figure 4.7. At low temperatures, the channel in sample A686 depletes at a gate bias of -0.34V which compares to a value of -0.3V obtained by measuring the same sample, but cooled without an

applied bias beyond cut-off. If these two low temperature capacitance characteristics are integrated to estimate the charge contained beneath the gate, see Equation 4.2, then it is found that the mobile electronic charge contained in the structure has increased from 3.7×10^{15}m^{-2} to 4.2×10^{15}m^{-2}. This can be understood by remembering that beyond cut-off, the Al$_{0.3}$Ga$_{0.7}$As is fully depleted of carriers. Hence, very few electrons are available to become trapped in *DX* centres. When the bias is removed, the Fermi level lies above the conduction band of the Al$_{0.3}$Ga$_{0.7}$As and electrons can tunnel into hydrogenic and conduction band states in the Al$_{0.3}$Ga$_{0.7}$As. *DX* centres play no part in electron capture as the thermal activation energy required to distort the lattice, and trap an electron, is no longer available at these low temperatures. As the temperature rises, charge begins to condense into *DX* traps because less energy is needed to become bound in a *DX* centre, than to escape. As a result, the cut-off voltage begins to become more positive, as there are less electrons to deplete. Once above about 150K, electrons are energetic enough to escape from *DX* centres and hence the cut-off shifts to more negative voltages. The trends in the data at these high temperatures are now identical to those in the original measurement presented in Figure 4.2.

The GaAs-AlAs heterostructures were also bias cooled, in this case with a bias of -3V on the gate electrode i.e. beyond cut-off. Figures 4.8-10 show the results for this type of measurement on the same three GaAs-AlAs heterostructures which were described in the previous section. At low temperatures, the channel in sample A601 depletes at a gate bias of -3.2V, which compares to -1.9V given by measuring the same sample but cooled without an applied bias beyond cut-off. As the temperature rises, the shifts in the threshold voltages are qualitatively similar to those measured in the A686 GaAs-Al$_{0.3}$Ga$_{0.7}$As heterostructure. The main difference between the threshold voltages measured in the two types of heterostructures is that they are much larger in GaAs-AlAs. As with GaAs-Al$_{0.3}$Ga$_{0.7}$As, once above approximately 150K, the bias cooling

Figure 4.7: Capacitance as a function of gate voltage at various temperatures for the A686 GaAs-Al$_{0.3}$Ga$_{0.7}$As heterostructure after being cooled with a bias of -2V on the gate.
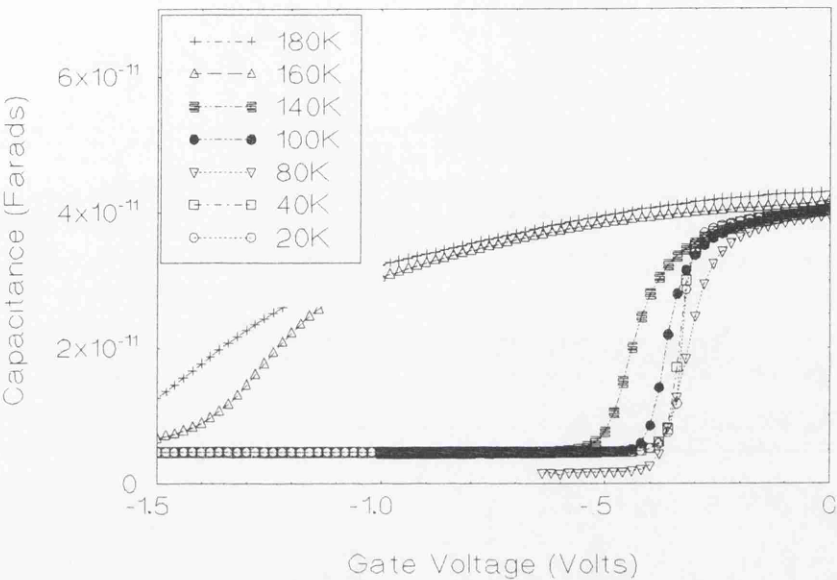
Figure 4.8: Capacitance as a function of gate voltage at various temperatures for the A601 GaAs-AlAs heterostructure after being cooled with a bias of -3V on the gate.
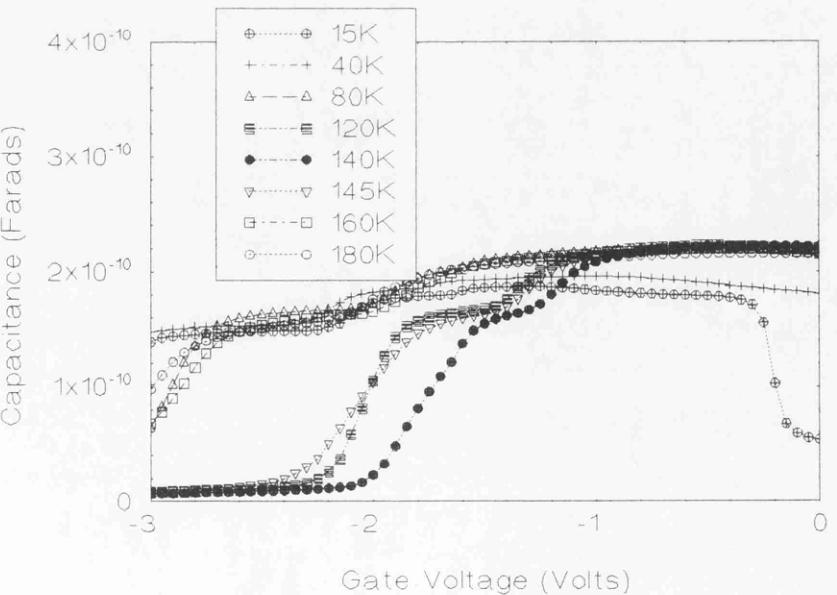
Figure 4.9: Capacitance as a function of gate voltage at various temperatures for the A627 GaAs-AlAs heterostructure after being cooled with a bias of -3V on the gate.
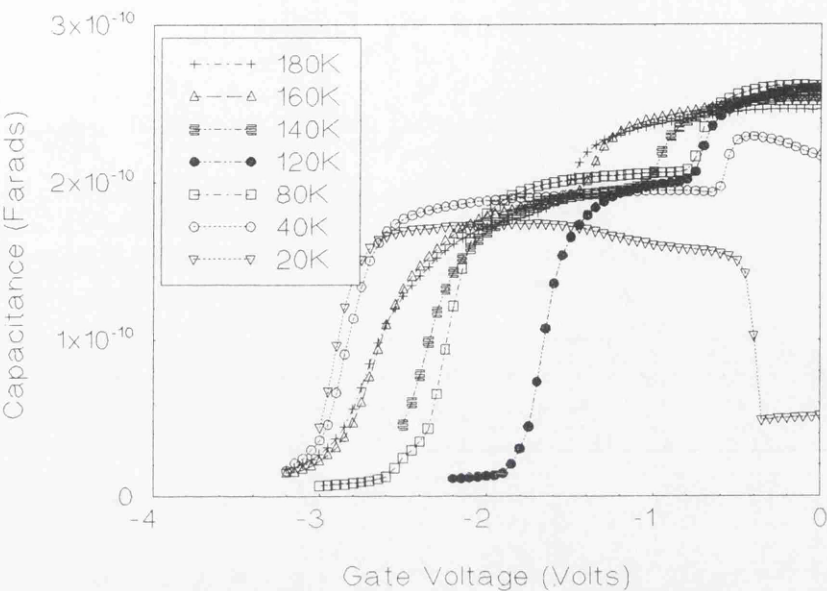
Figure 4.10: Capacitance as a function of gate voltage at various temperatures for the A502 GaAs-AlAs heterostructure after being cooled with a bias of -3V on the gate.
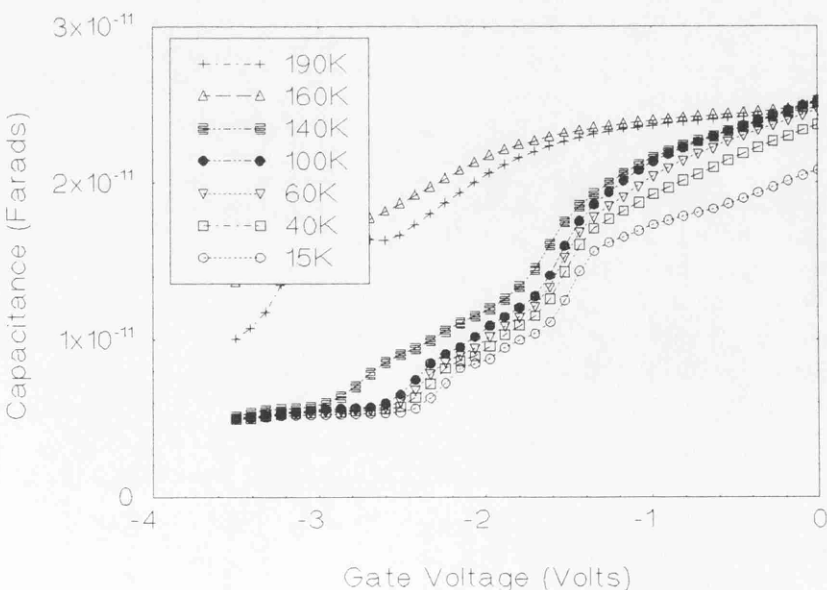
measurements become similar to the original measurements presented in Figure 4.4.

The measurements on A627 are similar to those taken on the more highly doped A601 sample. In this case the low temperature cut-off is -1.6V compared to the original -2.9V. This is again consistent with many more mobile electrons in the structure which have not been trapped by *DX* centres.

The results for sample A502 are less interesting because this sample is so highly doped that it is not possible to remove all the free electrons from the structure. Hence there will always be electrons present which can be trapped in *DX* centres, whether a bias is applied during the cooling process or not. The results in Figure 4.10 should therefore be generally similar to those taken on the structure without the bias cooling, and this is clearly the case.

A more detailed comparison of the low temperature data is given in Table 4.5 which contains cut-off data and the estimated charge that needs to be depleted in A686, A601 and A627. It is immediately clear from this data that the bias cooling of the A686 GaAs-Al$_{0.3}$Ga$_{0.7}$As structure has had only a small effect on the mobile charge contained beneath the gate at low temperatures.

Table 4.5: Data illustrating the change in the low temperature free charge when various heterostructures are cooled with large negative bias' applied to the gate electrode.

Sample Number	Low Temperature Cut-Off (Volts)	Low Temperature Cut-Off Bias Cooled (Volts)	Low Temperature Electronic Charge (m^{-2})	Low Temperature Electronic Charge Bias Cooled (m^{-2})
A686	-0.30±0.02	-0.34±0.02	(3.7±0.6)×10^{15}	(4.2±0.7)×10^{15}
A601	-1.90±0.02	-3.20±0.02	(6.7±0.6)×10^{16}	(1.2±0.1)×10^{17}
A627	-1.60±0.02	-2.90±0.02	(6.2±0.6)×10^{16}	(1.0±0.1)×10^{17}

In contrast, the low temperature charge changes by a factor of about 60 in GaAs-AlAs. This difference is difficult to interpret because GaAs-Al$_{0.3}$Ga$_{0.7}$As is in the

transition region for *DX* centres being ground or excited states in the Γ minimum of the conduction band. Hence a large concentration of these defects is expected. In contrast, the *DX* state is an excited state in AlAs and so a large concentration of these defects would not be expected. This problem was touched on in Section 4.3.2 and again may be evidence of *DX* trapping in the four monolayers of Al$_{0.3}$Ga$_{0.7}$As either side of the silicon doping in the GaAs-AlAs structure. This would explain why both GaAs-Al$_{0.3}$Ga$_{0.7}$As and GaAs-AlAs heterostructures show *DX* associated shifts in the threshold voltages on warming up the samples. Again the large difference in the low temperature threshold voltages between the two types of structure is much more difficult to explain.

Finally it is important to note that the bias cooled data is very complicated when closely analysed. The general features are clear, however many of the details are difficult to interpret. For instance, biasing the gate beyond threshold depletes the whole of the structure during the cooling down process. At low temperatures, removing the bias allows electrons to flow into the GaAs-Al$_x$Ga$_{1-x}$As where they cannot occupy *DX* centres because there is not sufficient thermal energy available at these temperatures. The situation is now similar to the high temperature case and so similar threshold voltages would be expected. For GaAs-AlAs this is not the case and the difference in the threshold voltages is 0.5V. However we know there are difficulties in describing this structure. More worrying is the GaAs-Al$_{0.3}$Ga$_{0.7}$As structure; no evidence has been found for low temperature free charge outside the 2DEG and so the differences between the high and low temperature depletion voltages (~0.7V) is difficult to understand.

4.4 Magneto-Transport Measurements

Experiments to determine the bulk mobility and carrier concentrations of the various heterostructures were carried out by measuring the four terminal

longitudinal resistance of the samples in a swept magnetic field at 1.2K and 70mK, see Figure 4.11. Various measurements of the transport characteristics of the 2DEG on application of a negative bias to a surface Schottky gate at fixed magnetic fields were also carried out.

Figure 4.11: Magneto-resistance oscillations at 70mK in the A601 GaAs-AlAs heterostructure.
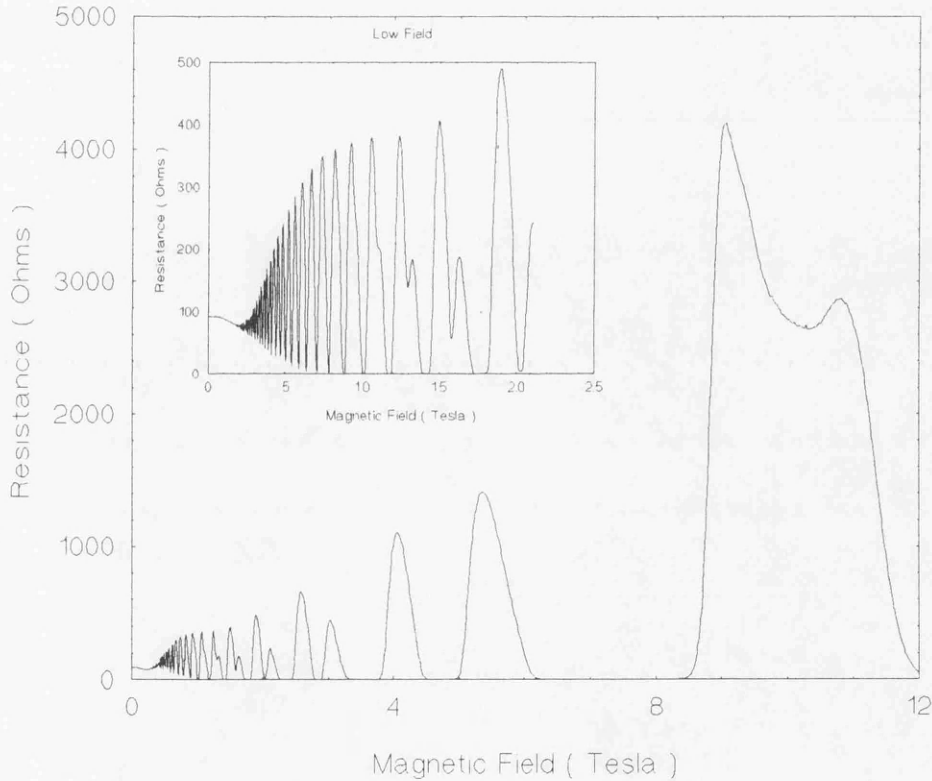
The mathematical description of such a measurement is set out in Chapter 1, Section 1.4.1 and leads to the derivation of equations for the mobility μ_e and carrier concentration n_{2D} of the 2DEG in terms of the electronic charge e, the zero magnetic field longitudinal resistance $R(0)$, Planck's constant h and periodicity of

the resistance minima as a function of the reciprocal magnetic field i.e. $\Delta(1/B_n)$, see Equations 4.5 and 4.6, where L_x/L_y is the aspect ratio of the channel.

$$n_{2D} = \frac{2e}{h}\left[\Delta\left(\frac{1}{B_n}\right)\right]^{-1} \qquad (4.5)$$

$$\mu_e = \frac{L_x}{L_y}\frac{1}{R(0)en_{2D}} \qquad (4.6)$$

These two equations can be used together with the experimental data to obtain the estimated mobility and carrier concentrations for all the heterostructures analysed in the previous section, see Table 4.1.

4.4.1 Description of the Experimental Results

Table 4.1 contains data for the carrier concentration in three GaAs-AlAs heterostructures, each of which has a different doping level. For the A627 sample, 2×10^{16}m^{-2} silicon donors give a carrier concentration of 1.1×10^{15} m^{-2}. Increasing the doping level to 4×10^{16}m^{-2} in the A601 sample, increases the carrier concentration to 3.5×10^{15}m^{-2}. At this point, further increases in the doping level leaves the carrier concentration virtually unchanged i.e. for the A502 sample, 1×10^{17}m^{-2} donors give a carrier concentration of 3.4×10^{15}m^{-2}. There is clearly a critical doping level above which the carrier concentration is determined by some pinning mechanism. In fact this can be viewed in terms of the excess silicon diffusing into the AlAs where they have a very high binding energy for electrons. These states will then be very effective at trapping electrons and thus provide an adequate pinning mechanism.

This is in contrast to GaAs-Al$_{0.3}$Ga$_{0.7}$As where the carrier concentration is found to vary over a much larger range, 5.8-6.7×10^{15}m^{-2} for a doping level of 4×10^{16}m^{-2}. This can be interpreted as a manifestation of the different pinning mechanism. In this structure, the pinning of the Fermi level takes place on *DX* centres, the formation of which are very sensitive to the local doping level (i.e. the position of the sample on the wafer) and the cooling rate.

It is also interesting to compare the mobility data obtained in the A601 and A502 heterostructures. The more lightly doped structure has a 27% higher mobility, 80m^{2}V^{-1}s^{-1} compared to 68m^{2}V^{-1}s^{-1}. This could be due to increased silicon diffusion in the heavily doped sample which would lead to more scattering centres close to the 2DEG and so a less uniform potential. The doping level in A601 was reduced by 50% in sample A627 and resulted a dramatically reduced mobility, 1m^{2}V^{-1}s^{-1} compared to 80m^{2}V^{-1}s^{-1} in A601. There seems to be substantially more scattering in the very lightly doped material, indicating a much rougher potential at the 2DEG plane. This may be due to reduced screening of the 2DEG by free electronic charge residing in the doping region.

GaAs-Al$_{0.3}$Ga$_{0.7}$As structures have a lower mobility at a doping level of 4×10^{16}m^{-2} silicon atoms than GaAs-AlAs structures i.e. 18-30m^{2}V^{-1}s^{-1} for various A686 samples compared with 80-86m^{2}V^{-1}s^{-1} for A601 and A685 samples (A685 is an identical structure to A601). The reason is that in GaAs-Al$_{0.3}$Ga$_{0.7}$As, the free electronic charge condenses into *DX* centres at low temperatures and so screening of the impurity charge is relatively poor. In GaAs-AlAs, there is evidence from electrostatic measurements that free electronic charge condenses into *DX* centres in the four monolayers of Al$_{0.3}$Ga$_{0.7}$As either side of the silicon doping. However, these measurements also showed that despite this there is still a large amount of free electronic charge in the GaAs-AlAs structures. This charge can redistribute itself at low temperatures and thus give additional screening of the impurity potential.

The effect of altering the spacer thickness was also studied. In sample A688, the width of the spacer is twice that of A686, hence, the effect of potential irregularities on scattering in the 2DEG is greatly reduced, leading to an enhanced mobility. However, this structure has a lower carrier concentration and hence a lower Fermi energy than the equivalent, shallower A686 sample. The spacing of the energy levels in any potential well formed in this structure will therefore be smaller, and consequently, quantum confinement effects will smear more rapidly with temperature. In sample A629, the spacer thickness is 25nm, which leads to a conventional high mobility structure.

4.4.2 Comparing Carrier Concentrations with Calculations

In this section Equation 4.7 (derived from the simple electrostatic model outlined in Chapter 1, Section 1.2.3) is used to estimate the expected carrier concentration for the GaAs-Al$_{0.3}$Ga$_{0.7}$As and GaAs-AlAs heterostructures detailed in Table 4.1.

$$n_{2D} = \frac{(\Delta E_c - E_{dd})\varepsilon_0}{\left(\frac{s}{\varepsilon_a} + \frac{a}{\varepsilon_g} \right)e^2} \tag{4.7}$$

For the shallow A686 heterostructure, Equation 4.7 gives a carrier concentration of 5.3×10^{15}m^{-2}, which is close to the lower end of the measured range i.e. 5.8×10^{15}m^{-2}. There is also very good agreement for the intermediate A688 GaAs-Al$_{0.3}$Ga$_{0.7}$As heterostructure, the calculated value is 3.8×10^{15}m^{-2}, compared to a measured carrier concentration of 4.0×10^{15}m^{-2}. However for the A601 GaAs-AlAs heterostructure, the agreement is not so close, 4.8×10^{15}m^{-2} compared to a measured carrier concentration of 3.5×10^{15}m^{-2}.

Another important aspect of Equation 4.7 is that the carrier concentration is predicted to be independent of the doping level in the structure. This is due to the assumption that the Fermi level is pinned by deep donor impurities round the doping layer and this is the main mechanism which fixes the carrier concentration in the 2DEG. This is obvious when Equation 4.1 is considered. For a shallow GaAs-Al$_{0.3}$Ga$_{0.7}$As heterostructure the doping density required to obtain a solution to this equation must be $\geq 4 \times 10^{16}$m^{-2}. This is born out by experiments which show that GaAs-Al$_{0.3}$Ga$_{0.7}$As heterostructures with a doping level of 2×10^{16}m^{-2} have either very low mobilities or do not conduct at all.. The analysis can also be applied to the shallow GaAs-AlAs heterostructures where it predicts a minimum doping level of 3.8×10^{16}m^{-2} silicon donors.

4.4.3 Illuminating GaAs-Al$_x$Ga$_{1-x}$As Heterostructures

Illumination of the various structures can effect both carrier concentration and mobility. The exact mechanism involved here is far from clear but generally it is assumed that depopulation of *DX* centres and interfacial traps occurs and this allows electrons to take part in both conduction and screening processes.

Concentrating on illumination of the structures doped with 4×10^{16}m^{-2} silicon donors, it was found that for GaAs-Al$_{0.3}$Ga$_{0.7}$As (A686), the mobility increased from 18m^{2}V^{-1}s^{-1} to 21m^{2}V^{-1}s^{-1} and the carrier concentration increased from 5.8×10^{15}m^{-2} to 6.9×10^{15}m^{-2}. For GaAs-AlAs (A601) the mobility increased from 86.4m^{2}V^{-1}s^{-1} to 116.0m^{2}V^{-1}s^{-1} and the carrier concentration increased from 3.5×10^{15}m^{-2} to 3.7×10^{15}m^{-2}. The model of Long et al. is used to obtain Equation 4.8 which relates the carrier concentration after illumination, in terms of the dark value and some electrostatic parameters of the structure [5].

$$n_{2D}^L = \frac{\Delta E_c}{\Delta E_c - E_{dd}} n_{2D} \qquad (4.8)$$

The idea is that the illumination depopulates the *DX* centres and so the pinning energy E_{dd} can be set to zero. For GaAs-Al$_{0.3}$Ga$_{0.7}$As the expected carrier concentration after illumination using Equation 4.8 would be 8.3×10^{15}m^{-2} and for GaAs-AlAs it would be 5×10^{15}m^{-2}. The model is not actually very useful for our data because both structures exhibit parallel conduction (due to parasitic channels of electrons in the spacer layers) i.e. the electrons do not all go to the 2DEG to increase the carrier concentration.

4.4.4 Carrier Concentration as a Function of Depletion

Measurements of the low temperature (1.2K) quantised conductance of quantum wires at fixed magnetic fields has been carried out on both the shallow GaAs-Al$_{0.3}$Ga$_{0.7}$As (A686) and GaAs-AlAs (A685) heterostructures. If the resistance of a wire in a fixed magnetic field is measured before threshold it is found to oscillate as a function of gate voltage. These oscillations are due to interference between the Landau levels in the bulk and the Landau levels in the partially depleted 2DEG underneath the gate electrodes [13, 14].

In Figure 4.12 a 100nm wire on GaAs-Al$_{0.3}$Ga$_{0.7}$As is measured at four different magnetic fields. The field values B=1.70T, 1.95T, 2.30T, 2.88T are chosen to correspond to integer filling factors v=14, 12, 10, 8 in the bulk i.e. at minima in the longitudinal bulk magneto-resistance.

These values for the filling factors are calculated by applying Equation 4.9, where n_{2D} is the bulk carrier concentration, e is the electronic charge and h is Planck's constant.

$$\nu = \frac{hn_{2D}}{eB} \hspace{4cm} (4.9)$$

Figure 4.12: Resistance oscillations in a surface gated quantum wire before threshold. Measurements are made at various fixed magnetic fields at 1.2K.
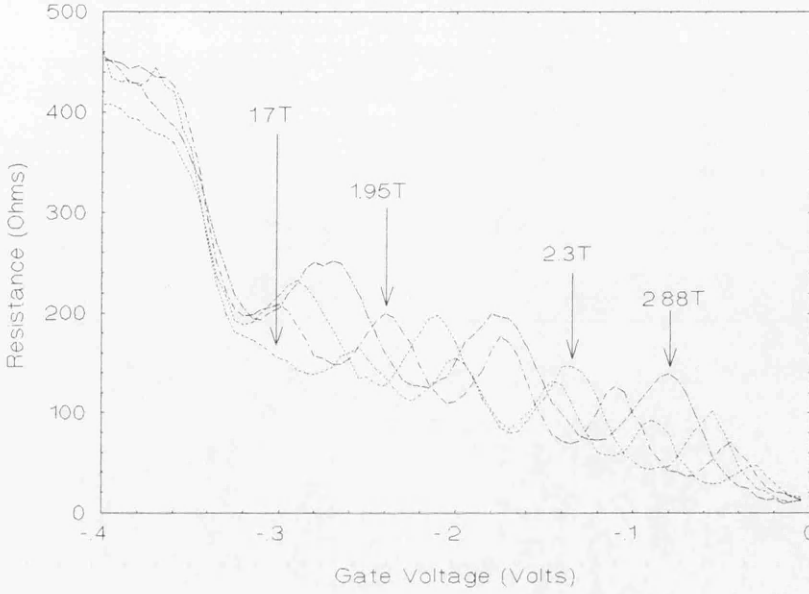
As a negative bias is applied to the 2DEG underneath the gate electrodes, the local carrier concentration $n_{2D}(g)$ is reduced. This leads to a consequent reduction in the number of filled Landau levels beneath the gate and hence a lower filling factor $\nu(g)$. Hence as the gate voltage is lowered and the filling factor is reduced, a stepwise increase in the resistance should occur as the number of propagating modes is reduced. For the trace in Figure 4.12, taken at 2.88T, there are three maxima before threshold. At this field value, the bulk filling factor is 8 but the application of a negative bias reduces this to 6 in the region of the gates and is responsible for the first maximum in the resistance. The second and third maxima correspond to filling factors of four and two respectively. Thermal broadening of the Landau levels and the fact that these measurements were carried

out on split not continuous gates, accounts for the fact that maxima are observed instead of plateaux.

Now the relations between the carrier concentrations and filling factors for the bulk and gated regions of the 2DEG are given by Equations 4.10 and 4.11 respectively.

$$\nu = \frac{h n_{2D}}{eB} \qquad\qquad (4.10)$$

$$\nu(g) = \frac{h n_{2D}(g)}{eB} \qquad\qquad (4.11)$$

Dividing and rearranging for $n_{2D}(g)$ gives

$$n_{2D}(g) = n_{2D} \frac{\nu(g)}{\nu} \qquad\qquad (4.12)$$

Equation 4.12 can now be used to analyse the change in the carrier concentration as a function of gate voltage. From the data presented in Figure 4.12, the different carrier concentrations at different gate voltages (corresponding to the various maxima involved) can be obtained, see Tables 4.6a-c. Similar experiments were carried out using a 100nm quantum wire fabricated in a GaAs-AlAs heterostructures, the results for this experiment are summarised in Tables 4.7a and b. The carrier concentration for both the GaAs-Al$_{0.3}$Ga$_{0.7}$As and GaAs-AlAs heterostructures are plotted as a function of gate voltage in Figure 4.13. The error in the data comes from an estimation of a 3% uncertainty in the carrier concentration. The uncertainty in the peak position is typically less than 1%.

Figure 4.13: Comparison between the variation of carrier concentration with gate voltage in GaAs-Al$_{0.3}$Ga$_{0.7}$As (A686) and GaAs-AlAs (A685) before threshold.
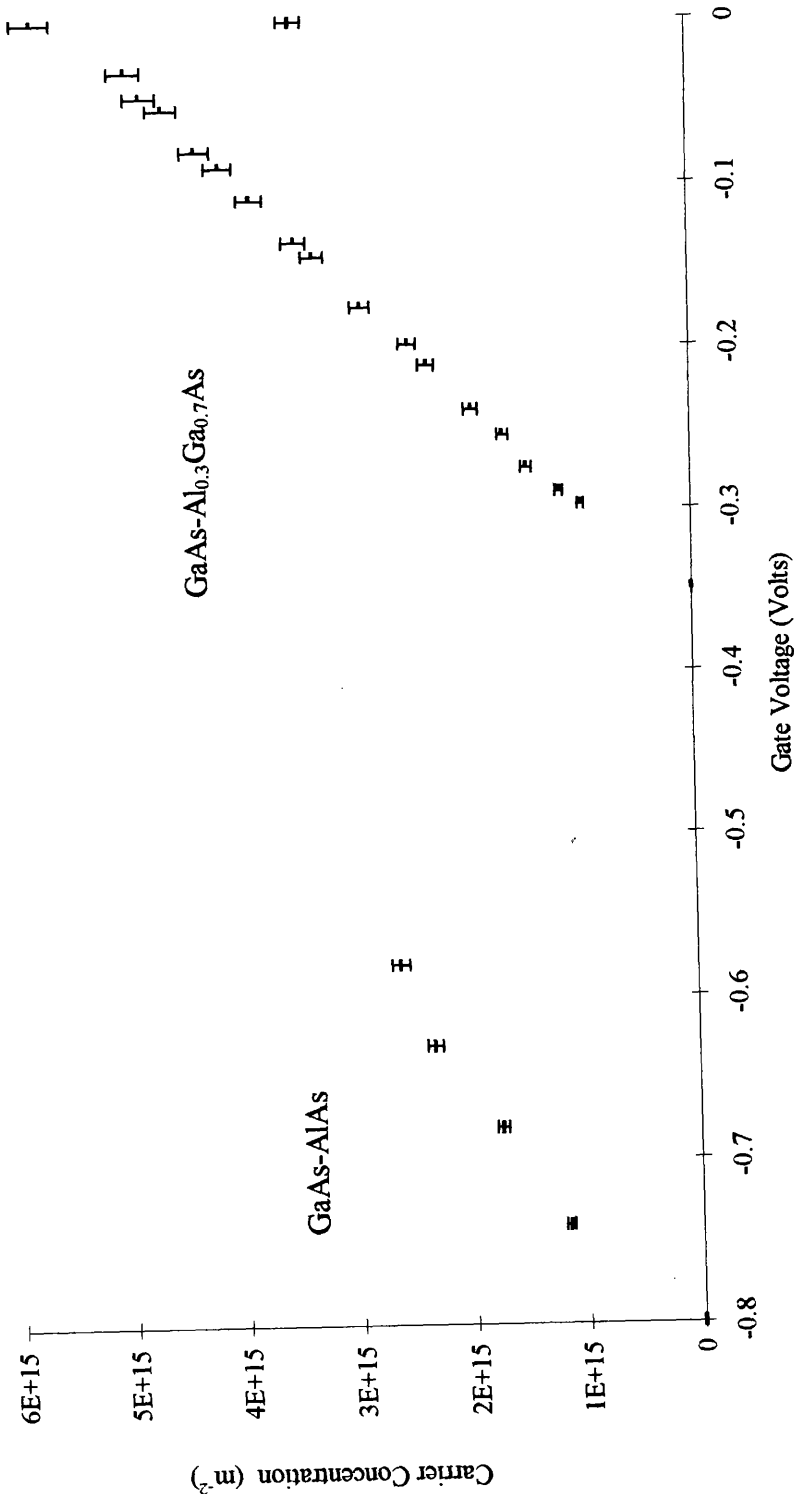
Tables 4.6: The filling factor, peak position and carrier concentration as a function of magnetic field and gate voltage for a 100nm quantum wire form in the A686 shallow GaAs-Al$_{0.3}$Ga$_{0.7}$As heterostructure.

(a)

Magnetic Field (Tesla)	Bulk Filling Factor v	Peak Position (Volts)				
		First Peak	Second Peak	Third Peak	Forth Peak	Fifth Peak
2.88	8	-0.079	-0.175	-0.274		
2.30	10	-0.053	-0.135	-0.211	-0.289	
1.95	12	-0.046	-0.109	-0.175	-0.238	-0.297
1.70	14	-0.030	-0.089	-0.144	-0.198	-0.254

(b)

Magnetic Field (Tesla)	Bulk Filling Factor v	Filling Factor v(g)				
		First Peak	Second Peak	Third Peak	Forth Peak	Fifth Peak
2.88	8	2	4	6		
2.30	10	2	4	6	8	
1.95	12	2	4	6	8	10
1.70	14	4	6	8	10	12

(c)

Magnetic Field (Tesla)	Bulk Filling Factor v	Carrier Concentration ($\times 10^{15}$m^{-2})				
		First Peak	Second Peak	Third Peak	Forth Peak	Fifth Peak
2.88	8	4.35	2.90	1.45		
2.30	10	4.64	3.48	2.32	1.16	
1.95	12	4.83	3.87	2.90	1.93	0.97
1.70	14	4.97	4.14	3.31	2.49	1.66

Tables 4.7: The filling factor, peak position and carrier concentration as a function of magnetic field and gate voltage for a 100nm quantum wire form in the A685 shallow GaAs-AlAs heterostructure.

(a)

Magnetic Field (Tesla)	Bulk Filling Factor v	Filling Factor v(g)	
		First Peak	Second Peak
7.00	2	1	
3.40	4	2	
2.30	6	4	2
1.76	8	4	6

(b)

Magnetic Field (Tesla)	Bulk Filling Factor v	First Peak		Second Peak	
		Peak Position (Volts)	Carrier Conc. (m^{-2})	Peak Position (Volts)	Carrier Conc. (m^{-2})
7.00	2	-0.68	1.75×10^{15}		
3.40	4	-0.68	1.75×10^{15}		
2.30	6	-0.63	2.33×10^{15}	-0.74	1.17×10^{15}
1.76	8	-0.68	1.75×10^{15}	-0.58	2.63×10^{15}

Once again the clear difference between the two structures is apparent from the data. In the GaAs-Al$_{0.3}$Ga$_{0.7}$As structure the carrier concentration in the 2DEG is immediately effected by the gate voltage in a linear way. This reflects the fact that at low temperatures all the carriers in the donor region are trapped in metastable states and cannot be removed by an applied bias. In contrast, the GaAs-AlAs structure requires approximately -0.55V or so to be applied before any significant change in carrier concentration occurs and only at this point does depletion begin to be linear in gate voltage. This data is consistent with the discussion of threshold voltages in the previous section and reflects the relatively

large amount of removable screening charge in the doping region in GaAs-AlAs structures.

It is also possible to analyse the rate at which depletion of the carrier concentration in the 2DEG occurs in the two types of heterostructures. This is done using Equation 4.13

$$gradient = \frac{dn_{2D}}{dV_g} = \frac{\varepsilon_0}{e}\left(\frac{a}{\varepsilon_g} + \frac{s}{\varepsilon_a} + \frac{u}{\varepsilon_a} + \frac{c}{\varepsilon_g}\right)^{-1}$$ (4.13)

where a simple gate channel capacitance model has been assumed, see Equation 1.11, Chapter 1, Section 1.2.4. Applying this equation to both GaAs-Al$_{0.3}$Ga$_{0.7}$As and GaAs-AlAs, gives gradients of $(1.87\pm0.50)\times10^{16}$m^{-2}V^{-1} and $(1.65\pm0.36)\times10^{16}$m^{-2}V^{-1} respectively. The experimental data in Figure 5.13 have depletion gradients of $(1.60\pm0.32)\times10^{16}$m^{-2}V^{-1} for GaAs-Al$_{0.3}Ga_{0.7}$As and $(1.53\pm0.16)\times10^{16}$m^{-2}V^{-1} GaAs-AlAs in close agreement with those calculated, see Table 4.8. Another interesting point about these gradients is that they are essentially a measure of the capacitance per unit area in units of the electronic charge e. As such, they can be compared directly with the capacitance per unit area obtained through the capacitance measurements in Section 4.3.3.

Table 4.8: Comparison between the rate of change of the carrier concentration with respect to the depletion voltage for shallow GaAs-Al$_{0.3}$Ga$_{0.7}$As heterostructures.

Heterostructure Type	Gradient (Quantum Wire) m^{-2}V^{-1}	Gradient (Calculation) m^{-2}V^{-1}	Capacitance Gradient (Continuous Gate) m^{-2}V^{-1}
GaAs-AlAs (A685 & A601)	$(1.53\pm0.16)\times10^{16}$ (A685)	$(1.65\pm0.36)\times10^{16}$	$(3.50\pm0.19)\times10^{16}$ (A601)
GaAs-Al$_{0.3}$Ga$_{0.7}$As (A686)	$(1.60\pm0.32)\times10^{16}$	$(1.87\pm0.50)\times10^{16}$	$(1.25\pm0.13)\times10^{16}$

The agreement with the calculation is within the experimental errors for the magneto-transport measurements. This reflects the fact that the complicating factor in the GaAs-AlAs structure is due to the extra free charge in the doping region. Once this charge has been depleted i.e. where the gate voltage nears threshold, the structure behaves very similarly to GaAs-Al$_{0.3}$Ga$_{0.7}$As and can be understood in terms of the simple electrostatic model.

4.5 Conclusions

A detailed experimental investigation has been carried out into the structure and transport properties of various shallow (the 2DEG being 28nm below the surface) GaAs-Al$_x$Ga$_{1-x}$As heterostructures. The properties of the GaAs-Al$_{0.3}$Ga$_{0.7}$As heterostructures are found to be explicable in terms of a conventional electrostatic theory, if pinning of the Fermi level occurs on the deep *DX* states in the Al$_{0.3}$Ga$_{0.7}$As. Measurements of the depletion characteristics of the GaAs-Al$_{0.3}$Ga$_{0.7}$As structure confirm this picture. Both low temperature capacitance and transport threshold voltages indicate that the free charge is located in the 2DEG. The carrier concentration in the 2DEG is shown to be immediately affected by the action of the gate bias, which indicates that any electrons in the donor layer are trapped in metastable *DX* states and cannot be removed by the application of an electric field.

In the GaAs-AlAs structures, the carrier concentration is lower (3.5×10^{15}m^{-2} compared with 5.8-6.7×10^{15}m^{-2}) which reflects the larger conduction band offset at the AlAs-GaAs interface. The depletion voltages for the GaAs-AlAs heterostructures are also very different from those in GaAs-Al$_{0.3}$Ga$_{0.7}$As. They are in fact much larger than would be expected from the measured carrier concentration in the 2DEG. The dependence of the carrier concentration on the gate voltage is also more complicated. When a voltage bias is

initially applied there is a broad region where the carrier concentration remains fairly constant. This continues until a point is reached where the gradient changes sharply. After this point the gradient is much steeper and compares very closely with the depletion gradient measured in the GaAs-Al$_{0.3}$Ga$_{0.7}$As structure. These results are interpreted as evidence for free charge in the donor layers which screens the 2DEG from the action of the gate bias. Only when this charge has been depleted, does the 2DEG then begin to deplete strongly.

Simultaneous investigation of the mobility and carrier concentration as a function of gate voltage, gives further evidence of low temperature free charge around the doping region in GaAs-AlAs [15]. This data compares a GaAs-Al$_{0.3}$Ga$_{0.7}$As heterostructure (B416, which has an identical structure to A686) with the GaAs-AlAs heterostructures (A601, A685). At zero bias and before the onset of depletion, the 2DEG formed in the GaAs-AlAs structure has a much higher mobility. However comparing mobility in the two structures at points where the carrier concentrations are equal, shows the mobility is actually lower in the GaAs-AlAs. Again this suggests that once the free charge in the donor region has been depleted, the impurity scattering in the 2DEG is similar to that in GaAs-Al$_{0.3}$Ga$_{0.7}$As.

References

[1] J. H. Davies, Semicond. Sci. Technol. 3, 995 (1988).

[2] J. H. Davies, I. A. Larkin, E. V. Sukhorukov, J. Appl. Phys., Accepted (1995).

[3] G. L. Snider, M. S. Miller, M. J. Rooks, E. L. Hu, Appl. Phys. Lett. 59, 2727 (1991).

[4] G. L. Snider, I-Hsing Tan, M. S. Miller, M. J. Rooks, E. L. Hu, Superlattices and Microstructures Vol. 11, No. 3, 297 (1992).

[5] A. R. Long, J. H. Davies, M. Kinsler, S. Vallis, M. C. Holland, Semicond. Sci. Technol. 8, 1581 (1993).

[6] H. L. Strömer, R. Dingle, A. C. Gossard, W. Wiegmann, M. D. Sturge, Solid State Commun. 29, 705 (1979).

[7] J. E. Frost, D. A. Ritchie, G. A. C. Jones, Journal of Crystal Growth 111, 305 (1991).

[8] M. C. Holland, E. Skuras, J. H. Davies, I. A. Larkin, A. R. Long, C. R. Stanley, Journal of Crystal Growth, Accepted (1995).

[9] P. M. Mooney, Semicond. Sci. Technol. 6, B1 (1991).

[10] P. M. Mooney, J. Appl. Phys. 67, R1 (1990).

[11] P. Jeanjean, J. Sicart, J. L. Roberts, R. Planel, F. Mollot, Semicond. Sci. Technol. 8, 1977 (1993).

[12] F. Stern, W. E. Howard, Phys. Rev. 3, 816 (1967).

[13] R. J. Haug, A. H. MácDonald, P. Streda, K. von Klitzing, Phys. Rev. Lett. 61, 2797, (1988).

[14] R. J. Haug, J. Kucera, P. Streda, K. von Klitzing, Phys. Rev. B 39, 10892 (1989).

[15] E. Skuras, M. C. Holland, C. J. Barton, J. H. Davies, A. R. Long, Semicond. Sci. Tech., Accepted (1995).

Chapter 5

Quantised Conductance in Split Gated Quantum Wires

5.1 Introduction

In this chapter the quantisation of the conductance in short, narrow constrictions, defined by surface gates fabricated on four different GaAs-Al$_x$Ga$_{1-x}$As heterostructures is described. Initially an overview is set out describing the main mechanisms which limit the observation of conductance quantisation in any particular heterostructure. This sets the context for a detailed description of the observed experimental conductance quantisation as a function of both temperature and source-drain bias in 2DEG's 28nm, 40nm and 107nm below the surface of the heterostructure. The conductance quantisation in a GaAs-AlAs heterostructure, with the interface 28nm below the surface, is discussed in relation to the equivalent GaAs-Al$_{0.3}$Ga$_{0.7}$As structure. The sensitivity of the quantisation to thermal and voltage smearing is discussed in the context of the sub-band spacing in the various wires. The various results are also compared with the sub-band spacing obtained by modelling the measured wires semi-classically.

5.2 Overview

The evaporation of Schottky split gates onto the surface of a GaAs-$Al_xGa_{1-x}As$ heterostructure is a useful way of controlling the electrons in a 2DEG and investigating the properties of narrow channels [1, 2]. However in order for this method to be successful in quantising the conductance of the channel, the width of the constriction must be of the order of the Fermi wavelength of the electrons and the length must be very much smaller than the mean free path in the 2DEG. With this in mind, the original experiments used GaAs-$Al_{0.3}Ga_{0.7}As$ heterostructures with thick spacer layers to produce 2DEG's with elastic mean free paths of several microns. The experiments showed well quantised conductance in units of $2e^2/h$ for point contact constrictions and for wires with lengths of approximately 500nm [3, 4].

The important points about these measurements are firstly that the mean free paths in the 2DEG's were much larger than the dimensions of the constrictions. This is a necessary requirement for observing quantisation because the mean free path in the region of the constriction is much lower than it is in the bulk. The difference is a result of the formation of a saddle potential which lowers the local carrier concentration, thus reducing the screening of the impurity potential, leading to enhanced backscattering in the constriction [5]. The second point is that well resolved quantisation was reported in the temperature regime 0.1K to 0.6K. At temperatures much greater than these, the plateaux acquired a finite slope which increases with temperature until the quantisation is no longer resolved [6]. This is theoretically explicable in terms of Equation 5.1

$$G(E_n,T) = \frac{2e^2}{h} \sum_n \int_0^\infty \frac{T_n(E)}{eV} f(E,T)dE \qquad (5.1)$$

where for a temperature T, the quantised conductance $G(E_n, T)$ is a function of the Fermi-Dirac distribution function $f(E, T)$ and the transmission probability $T_n(E)$ for incident electrons in sub-band n [6, 7]. Expanding the Fermi function as a Taylor series gives:

$$G(E_n, T) = \frac{2e^2}{h} \sum_n \int_0^\infty T_n(E) \frac{\partial f(E, T)}{\partial E} dE \qquad (5.2)$$

At low temperatures the width of the differential Fermi function ($\approx 4k_BT$) is much sharper than any features in $T_n(E)$ and so it can be replaced by the delta function $\delta(E, E_F)$, hence Equation 5.2 reduces to:

$$G(E_F) = \frac{2e^2}{h} \sum_n T_n(E_F) \qquad (5.3)$$

A more rigorous derivation of this result was presented in Chapter 1, Section 1.3. Equation 5.3 is the low temperature description of a stepwise increase in the conductance in units of $2e^2/h$ for each of the n sub-bands. However at finite temperatures, the conductance quantisation is no longer resolved when the width, or thermal smearing of the differential Fermi function is comparable to the spacing of the sub-bands in the constriction i.e. $\Delta E \approx 4k_BT$. For the measurements of B. J. van Wees et al. the sub-band spacing was estimated to range from about 1.8meV for the 11th plateaux to 4meV for the last sub-band in the wire before pinch off [8]. These energy spacings correspond to a loss of the resolution of the sub-band structure at temperatures of about 5K and 11K respectively. However these are the temperatures at which complete smearing of the quantisation occurs and in fact the stepwise nature in lost between 1.6K and 4.2K.

More recently, Snider et al. and Frost et al. have demonstrated conductance quantisation at much higher temperatures [9-11]. The idea that these groups exploited was to increase the sub-band separation in the constriction and

so increase the temperature at which the separation becomes comparable with the width of the differential Fermi function. This was done by reducing the thickness of the spacer layer s, which increases the Fermi energy E_F and in doing so increases the sub-band spacing in the constriction, see Equations 5.4 and 5.5 from Davies et al. [12, 13].

$$E_F \propto \left(\frac{1}{s} + \frac{1}{a} \right)^{-1} \tag{5.4}$$

$$\Delta E = F(b/d) \times \left(\frac{e^2}{\varepsilon\varepsilon_0} \right)^{1/2} \left(\frac{E_F}{d} \right)^{1/2} \tag{5.5}$$

Of course, decreasing the spacer thickness, reduces the mobility in the 2DEG [14] ($85m^2v^{-1}s^{-1}$ in [3] compared to in $29m^2v^{-1}s^{-1}$ in [9, 10]) however this does not cause problems if the lengths of the constrictions are small <200nm (see Chapter 6). The approximate sub-band spacing obtained in Snider and Frost for the last conductance plateaux before pinch off was 10meV. This corresponds to complete smearing of the quantisation at a temperature of 29K which is in dramatic contrast to the conventional value of 11K obtained in the original experiments. It is also important to note that Equation 5.5 gives not only the dependence of the sub-band spacing on the Fermi energy, but also the dependence on the width $2b$ of the constriction and the separation d of the gate electrodes from the 2DEG. In this relation $F(b/d)$ is a dimensionless parameter which has a maximum value of 0.46 when b/d=0.79. Consideration of all these points is important when optimising the temperature performance of quantum wires. For instance, the dimensions of the heterostructures which Snider and Frost worked with were very different. They had spacer layers with widths 15nm and 10nm respectively and the depth of the interface against which the 2DEG is formed was 60nm in Frost's structure and 25nm in Snider's. There are two important points here. Firstly, consideration of

Figure 5.1: Flow chart describing the basic requirements which need to be optimised in order to fabricate high temperature ballistic quantum wires.

```
    ┌─────────────────┐              ┌─────────────────┐
    │ High Temperature│              │ Specified Device│
    │   Operation     │              │    Length L     │
    └─────────────────┘              └─────────────────┘
             │                                │
             ▼                                ▼
    ┌─────────────────┐              ┌─────────────────┐
    │  Large Subband  │◄············ │  Low Scattering │
    │ Separation ΔE   │              │ Mean Free Path >> L│
    └─────────────────┘              └─────────────────┘
             │                                │
             ▼                                │
    ┌─────────────────┐                       │
    │   Large Fermi   │                       │
    │   Energy E_F    │                       │
    └─────────────────┘                       │
             │                                │
        E_F∝(s+a_0)^-1                        │
             ▼                                ▼
    ┌─────────────────┐              ┌─────────────────┐
    │   Thin Spacer   │              │   Thick Spacer  │
    └─────────────────┘              └─────────────────┘
              \                          /
               ╲                        ╱
                ┌──────────────────────┐
                │     Compromise       │
                │     on Spacer        │
                │    Thickness s       │
                └──────────────────────┘
                          │
                   s Contributes to
                   2DEG Depth d
    ┌─────────────────┐
    │  Optimal Width  │◄──────────────
    │     w≈2d        │
    └─────────────────┘
```

$E_F \propto (s+a_0)^{-1}$

s Contributes to 2DEG Depth d

Optimal Width $w \approx 2d$
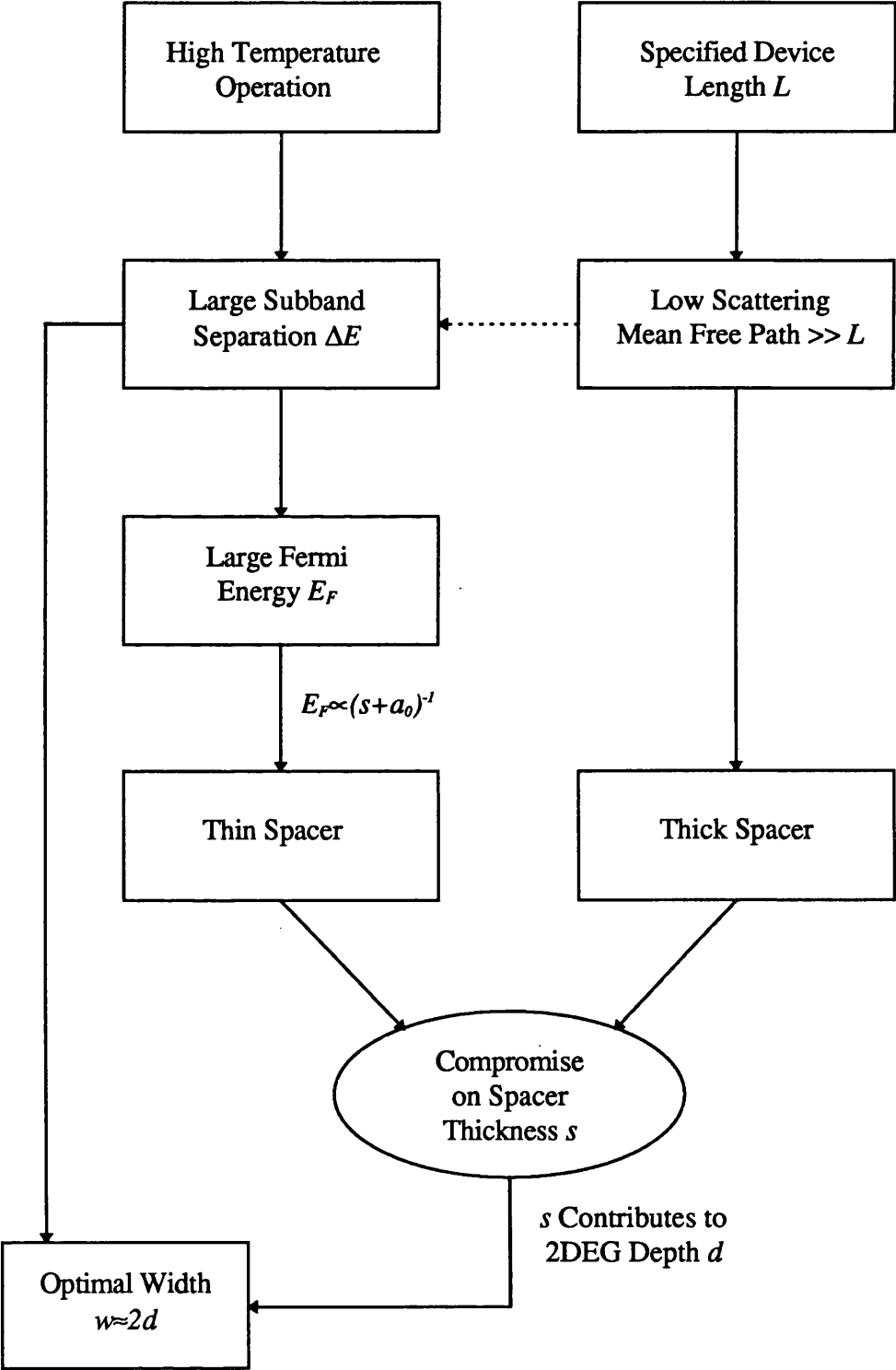
Equation 5.5 shows that the optimal sub-band spacing in these two structures will require different device dimensions, a 50nm width for Snider's device and a 100nm width for Frost's. Secondly, the similar measured sub-band spacing, despite the differences in these two structures (i.e. only the dimensions of the spacer layer are similar) is consistent with Davies' analytical model that the spacer width is the main determining factor. The important relations between the various design parameters are summarised in Figure 5.1.

5.3 Conductance Quantisation with Energetic Electrons

In addition to the thermal smearing of the differential Fermi function, an equivalent smearing effect can be produce by injecting electrons into the constriction with energies eV_{ds} much larger than the Fermi energy, where V_{ds} is the source drain bias.

$$G(E_n,T) = \frac{2e^2}{h} \sum_n \int_0^\infty \frac{T_n(E)}{eV} \left[f\left(-E_n + \frac{eV}{2}, T\right) - f\left(-E_n - \frac{eV}{2}, T\right) \right] dE$$

This physical picture is described in Chapter 1, Section 1.3.4 where it was used to derive an expression comparing the ratio of the differential conductance maxima when the differential Fermi function is narrow, to the differential conductance maxima when the function is broad, see Equation 5.6.

$$\frac{dg_n/dV_g}{dg_0/dV_g} = \frac{\Delta E(V_g)}{eV} \tanh\left(\frac{eV}{4k_BT}\right) \tag{5.6}$$

In order to understand the relation between the temperature and voltage effects, it is instructive to analyse Equation 5.6 in the following limits:

$$\text{As}\quad 4k_B T \gg eV \quad \frac{dg_n/dV_g}{dg_0/dV_g} \rightarrow \frac{1}{4k_B T}$$

$$\Rightarrow \quad T \equiv \frac{eV}{4k_B} \qquad (5.7)$$

$$\text{As}\quad eV \gg 4k_B T \quad \frac{dg_n/dV_g}{dg_0/dV_g} \rightarrow \frac{1}{eV}$$

Equation 5.7 can clearly be used to compare the thermal smearing of the conductance quantisation with the smearing induced by increasing the source drain bias. For Snider's data, the 30K trace and the trace for a source drain bias of 12meV at 4.2K are approximately similar which is consistent with Equation 5.7. Essentially the argument is that the width of the differential Fermi function varies as $4k_B T$ with temperature and as eV_{ds} with applied source drain bias. The mechanism for smearing with increasing source drain bias is due to injection of electrons into the constriction with a large range of energies. Of course this assumes that any joule heating in the series regions of 2DEG does not contribute significantly.

5.4 Quantisation of the Conductance in Short Wires

As explained in Chapter 2, optical lithography was used to define Hallbar patterns using Au-Ge-Ni Ohmic contacts and a NH_4-H_2O_2-H_2O wet etch isolation. Surface gated quantum wires were then fabricated onto these patterns using electron beam lithography.

In this section, a qualitative description of the conductance quantisation is given for the four GaAs-Al$_x$Ga$_{1-x}$As heterostructures summarised in Table 5.1. Both the temperature and source-drain bias dependencies are described. The magnitudes of the expected random errors associated with the measurements are discussed.

Table 5.1: The important characteristics of the four GaAs-Al$_x$Ga$_{1-x}$As heterostructures in which conductance quantisation was investigated.

Sample Type	Spacer Width	Si Doping Level	Fermi Energy (meV)	Carrier Conc. (m^{-2})	Mobility (m^{2}V^{-1}s^{-1})
Shallow (A685) GaAs-AlAs	10nm AlAs 1.1nm Al$_{0.3}$Ga$_{0.7}$As	4×10^{16}m^{-2} ∂-doped	12.1-12.5	3.4-3.5×10^{15}	46-65
Shallow (A686) GaAs-Al$_{0.3}$Ga$_{0.7}$As	11nm	4×10^{16}m^{-2} ∂-doped	21.4-23.9	6.0-6.7×10^{15}	20-30
Intermediate (A688) GaAs-Al$_{0.3}$Ga$_{0.7}$As	20nm	5×10^{16}m^{-3} over 10nm	14.3	4.0×10^{15}	69-71
Deep (A449) GaAs-Al$_{0.3}$Ga$_{0.7}$As	40nm	8×10^{16}m^{-3} over 50nm	9.7	2.7×10^{15}	240

5.4.1 Deep GaAs-Al$_{0.3}$Ga$_{0.7}$As Heterostructure

Figure 5.2 shows the quantised conductance in units of $2e^2/h$ measured as a function of gate voltage at 1.2K and 4.2K for a quantum wire 200nm wide and 200nm long, fabricated on the deep GaAs-Al$_{0.3}$Ga$_{0.7}$As heterostructure by Dr. E. Skuras. The conductance quantisation is clearly visible at 1.2K, even though it is smeared. At 4.2K the gate voltage versus conductance trace (offset by $2e^2/h$ for clarity) is very smeared as broadening of the Fermi function becomes similar to the sub-band spacing in the wire.

Figure 5.2: Data for the conductance as a function of gate voltage for a quantum wire on a deep GaAs-$Al_{0.3}Ga_{0.7}As$ (A449) heterostructure. The curves are measured at 1.2K and 4.2K and offset from one another by $2e^2/h$ for clarity.

Figure 5.3: Data for the conductance as a function of gate voltage for a quantum wire on a deep GaAs-$Al_{0.3}Ga_{0.7}As$ (A449) heterostructure. The curves are measured at three different a.c. signal levels (see Appendix B) and offset from one another by $2e^2/h$ for clarity.
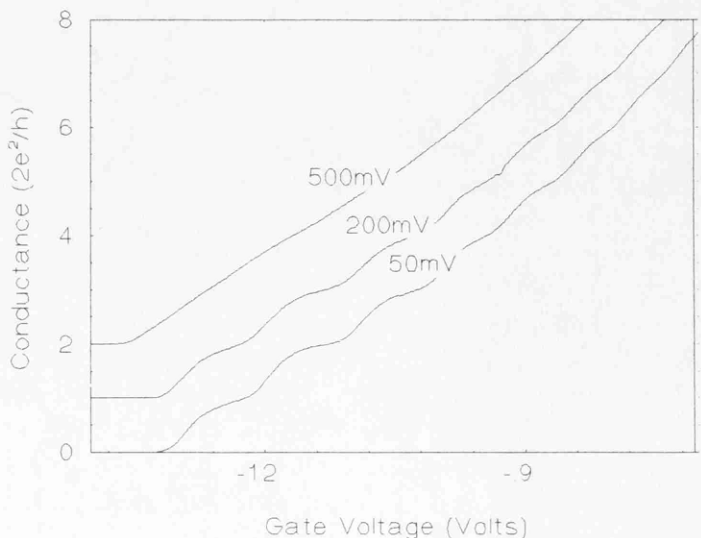
The experiment was repeated at 1.2K but this time using different excitation voltages, see Figure 5.3. Using Equation 5.7 to interpret the data, the rate of smearing is found to be similar to that obtained in the thermal smearing experiments. The actual source-drain bias' are low frequency a.c. signals, developed across a resistor network in which the sample is one component. Following the prescription set out in Appendix B, the voltage dropped across the constriction can be determined for each plateaux. These voltages can then be interpreted as equivalent electron temperatures T_e if approximated to d.c. signals. For the lowest ($N=1$) sub-band, excitation voltages of 50, 200 and 500mV correspond to roughly 0.7, 1.7 and 3.8mV across the constriction. This gives approximate electron temperatures of 2K, 5K and 11K. For the same gate voltage sweep, the higher sub-bands will be at lower effective electron temperatures, simple because less excitation voltage is dropped across the quantum wire due to its lower resistance.

When comparing the smearing of the conductance quantisation with both increasing temperature and source-drain bias, it is important to understand the accuracy of the two types of measurements. Assuming good thermal contact, the calibration of the rhodium iron thermometer gives the temperature of the sample to within ±0.1K. Interpreting the accuracy of the source drain bias experiments is more difficult. First of all there is the assumption that all the bias is developed across the constriction which may well be a source of systematic error. In Appendix B, an estimate is made of the various random errors associated with the determination of an effective electronic smearing temperature. Using this analysis, the last sub-band in the constriction at 10K should be approximately similar to the same sub-band at 500mV i.e. an electron temperature of (11±1)K Hence there is good agreement between the data in Figures 5.2 and 5.3 within the accuracy of the experiments. More detailed analysis of the agreement between electronic and thermal smearing is carried out in Section 5.5.

Figure 5.4: Data for the conductance as a function of gate voltage for a quantum wire on an intermediate (A688) GaAs-$Al_{0.3}Ga_{0.7}As$ heterostructure. The curves are measured at 1.2K, 4.2K and 10K and offset from one another by $2e^2/h$ for clarity.
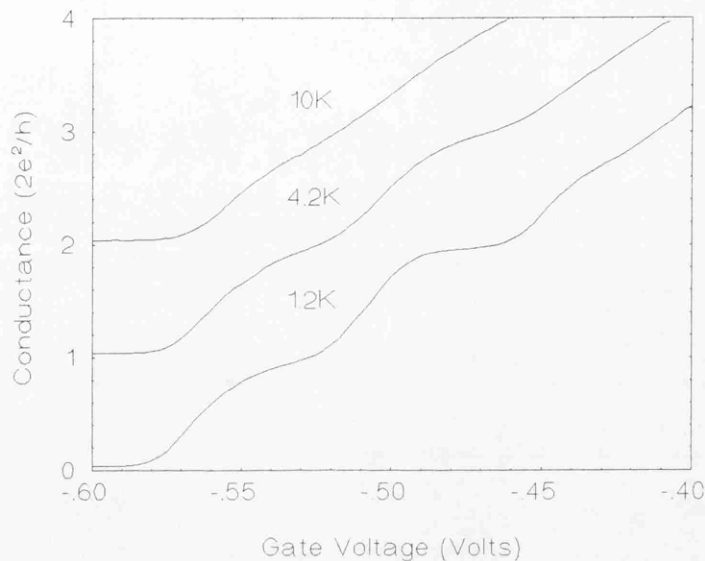
Figure 5.5: Data for the conductance as a function of gate voltage for a quantum wire on an intermediate GaAs-$Al_{0.3}Ga_{0.7}As$ (A688) heterostructure. The curves are measured at three different a.c. signal levels (see Appendix B) and offset from one another by $2e^2/h$ for clarity.
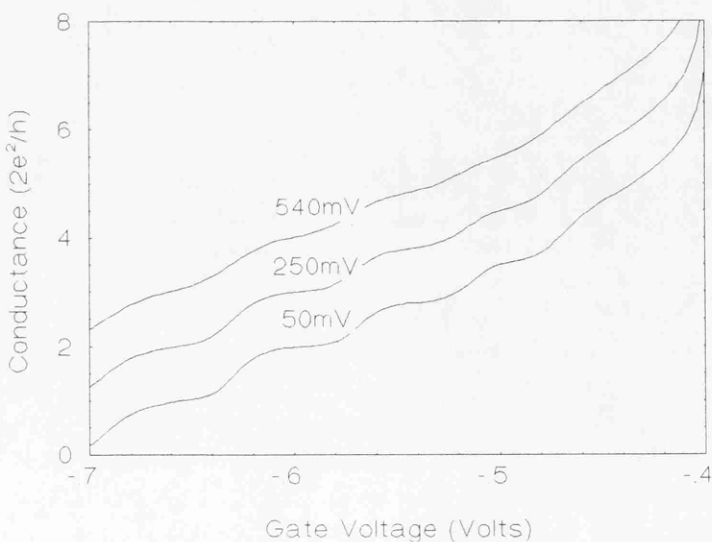
5.4.2 Intermediate GaAs-Al$_{0.3}$Ga$_{0.7}$As Heterostructure

A similar experiment was carried out using a quantum wire (lithographically 80nm wide and 50nm long) on the intermediate GaAs-Al$_{0.3}$Ga$_{0.7}$As heterostructure. In this case the spacer width has been reduced from 40nm to 20nm and inspecting Figure 5.4, the conductance quantisation at 1.2K is much clearer. This is despite a factor of three reduction in mobility compared with the sample discussed above. At 4.2K, the quantisation is still visible and even at 10K there is a point of inflexion corresponding to the lowest (N=1) sub-band. Investigating the quantum wire over a range of source-drain bias' shows the quantisation smearing in the same equivalent temperature regime ($\pm$1K) as was found in the thermal smearing measurements, see Figure 5.5.

5.4.3 Shallow GaAs-Al$_{0.3}$Ga$_{0.7}$As Heterostructure

Figure 5.6 shows the quantised conductance for a 100nm wide, 100nm long quantum wire formed in the shallow GaAs-Al$_{0.3}$Ga$_{0.7}$As heterostructure. Fully resolved conductance quantisation is seen at 1.2K and 4.2K. It is still visible at 10K, although somewhat smeared by temperature broadening of the Fermi function. A qualitative comparison can immediately be made between this data and the curves obtained on the slightly deeper 2DEG. Clearly the conductance quantisation in this 11nm spacer material is less sensitive to the effect of increasing the temperature. These trends are qualitatively consistent with the reduction in spacer thickness giving an increase in the sub-band separation in the wires and hence effectively reducing the relative importance of broadening of the sub-bands.

Another important effect is the additional structure visible in the transition region between plateaux. These effects are not seen in the conductance quantisation measured on the deeper structures described above until the length of

Figure 5.6: Data for the conductance as a function of gate voltage for a quantum wire on a shallow (A686) GaAs-$Al_{0.3}Ga_{0.7}As$ heterostructure. The curves are measured at 1.2K, 4.2K and 10K and offset from one another by $2e^2/h$ for clarity.
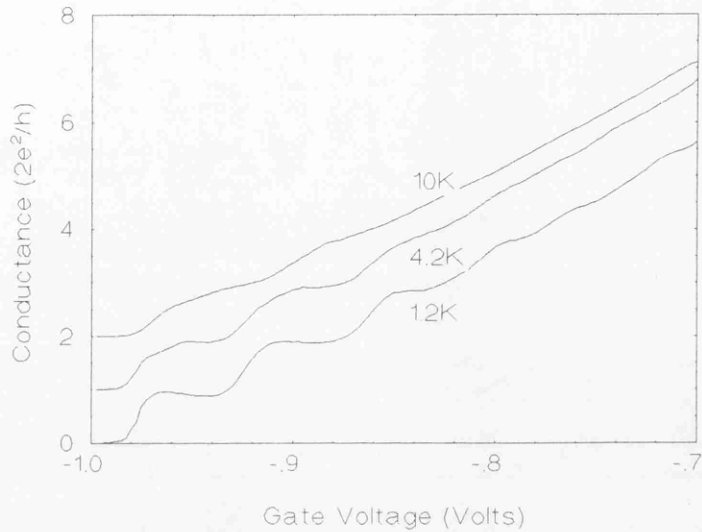
Figure 5.7: Data for the conductance as a function of gate voltage for a quantum wire on a shallow GaAs-$Al_{0.3}Ga_{0.7}As$ (A686) heterostructure. The curves are measured at three different a.c. signal levels (see Appendix B) and offset from one another by $2e^2/h$ for clarity.
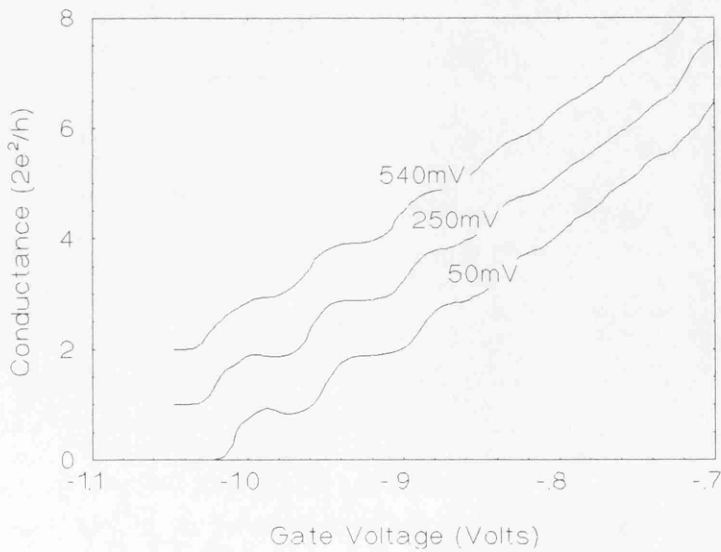
Figure 5.8: Data for the conductance as a function of gate voltage for a quantum wire on a shallow (A685) GaAs-AlAs heterostructure. The curves are measured at 1.2K, 4.2K and 10K and offset from one another by $2e^2/h$ for clarity.
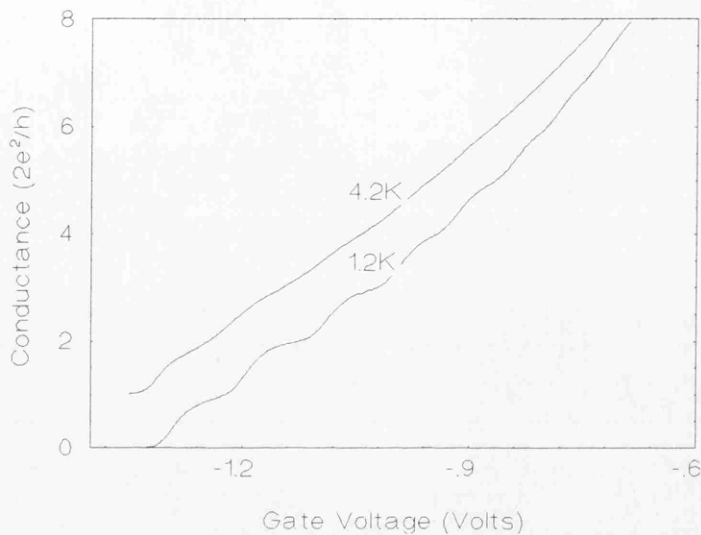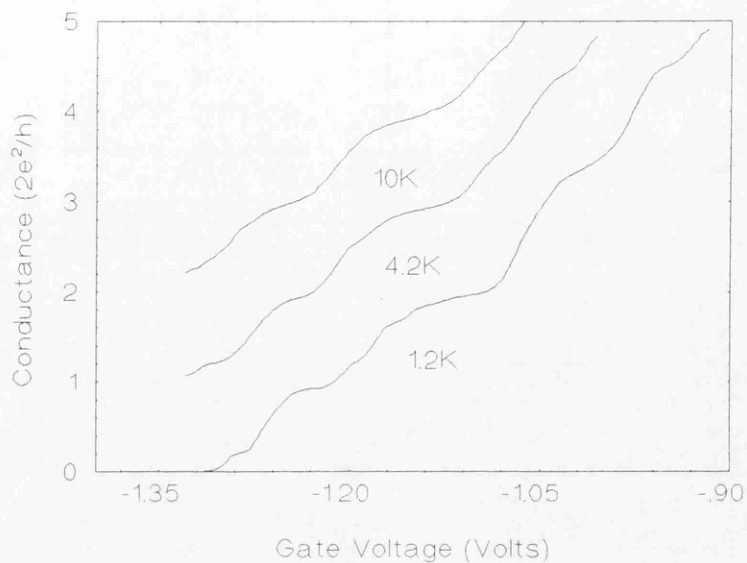

Figure 5.9: Data for the conductance as a function of gate voltage for a quantum wire on a shallow GaAs-AlAs (A685) heterostructure. The curves are measured at three different a.c. signal levels (see Appendix B) and offset from one another by $2e^2/h$ for clarity.
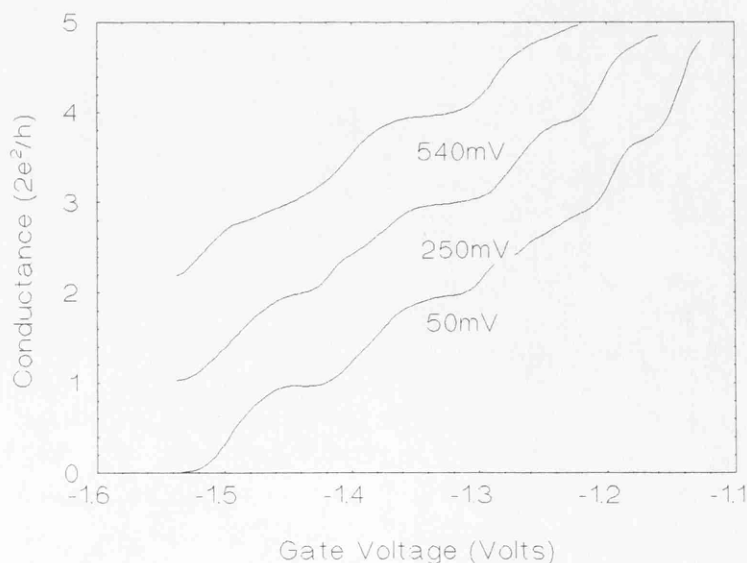
the constrictions are made very much longer [15]. This suggests that the structure may be a result of resonant transmission due to scattering from random impurity fluctuations [16]. In heterostructures with thick spacers, the length scale of these fluctuations is relatively long and hence short constrictions in these structures do not show the effect. However in material with narrow spacers, the length scale of the fluctuation will be shorter and so it would be reasonable to expect to observe the effect in shorter wires, see Chapter 6 for a more detailed discussion and analysis of the fluctuation length scales in 11nm spacer material. The measurements of the smearing temperatures of the conductance quantisation for large source-drain bias are within ±1K of the smearing temperatures obtained in the thermal experiments, see Figure 5.7. Also notice that the resonant structure is also visible in these experiments.

5.4.4 Shallow GaAs-AlAs Heterostructure

The substitution of AlAs for $Al_{0.3}Ga_{0.7}As$ substantially increases the mobility in the 2DEG but does not improve the robustness of the quantisation very dramatically, see Figure 5.8. At 10K the steps are slightly clearer but much more erratic. The source-drain bias smearing experiment gives similar results for the robustness of the quantisation, however the details on the curves differ, see Figure 5.9.

5.5 Quantifying the Smearing of the Conductance Quantisation.

The previous section clearly showed the conductance quantisation smearing at different rates in different heterostructures. The smearing with

Figure 5.10: Data for the conductance as a function of gate voltage for a quantum wire in a shallow (A686) GaAs-$Al_{0.3}Ga_{0.7}As$ heterostructure. The curves are measured at 1.2K, 4.2K and 10K and offset by $2e^2/h$ for clarity.
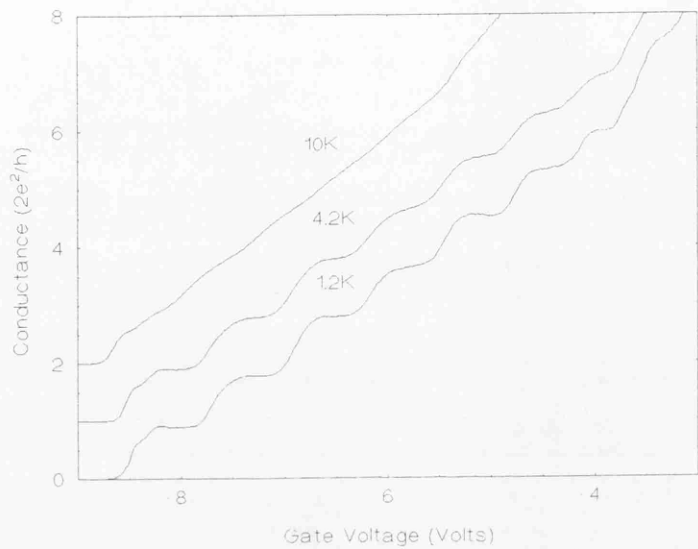

Figure 5.11: The differential conductance in units of $2e^2/h$ per volt for the three curves given in Figure 5.10. The curves are again offset for clarity.
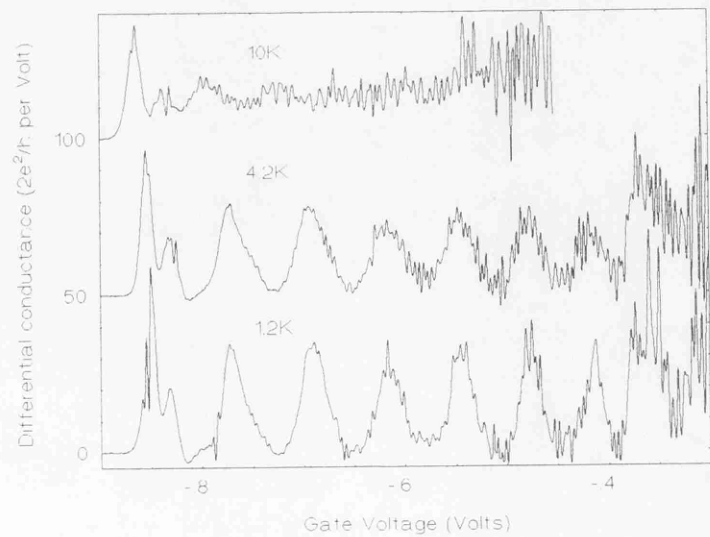
temperature and source-drain bias was found to be qualitatively consistent. In addition, different sub-bands were observed to also smear at different rates. In order to make a more detailed analysis of the smearing of the conductance quantisation it is necessary to define some characteristic point in the resolution of the step structure at which it can be said to be smeared. This procedure allows significant and random effects to be distinguished.

For example, the quantised conductance of a 100nm long, 80nm wide wire on the shallow GaAs-$Al_{0.3}Ga_{0.7}As$ heterostructure is measured over a large range of temperatures (1.2K to 30K), see Figure 5.10. Each data set is then differentiated numerically as shown in Figure 5.11. Only three temperatures are presented here for clarity. The value of the differential conductance at each peak (non-integer) and trough (integer) is then recorded for each temperature, see Table 5.2. These values are used to construct a graph of peak and trough differential conductance in units of $2e^2/h$ per volt as a function of inverse temperature. A set of curves is obtained which map out the temperature smearing of the sub-bands in the wire, see Figure 5.12. Clearly the peak conductance increases as the temperature decreases until it saturates a low temperature. The next step in the analysis is to define some characteristic smearing temperature at which the differential conductance falls to a certain multiple of the background or high temperature conductance. This multiple was chosen to be 3/2 (peak) or 2/3 (trough) that of the background or high temperature differential conductance. This method of analysis is fairly accurate and allows smearing temperatures to be defined with an accuracy of approximately ±1K enabling a more quantitative comparison to be made between different wires in different heterostructures.

The smearing of the quantised conductance with increasing voltage bias is analysed in a similar way, with the peaks and troughs in the differential conductance being plotted against an inverse effective temperature (see Equation 5.7). This procedure was repeated for all the quantum wires of different length, measured on the various heterostructures described in the previous section. The

Table 5.2: The magnitude of the differential conductance for the maxima and minima in Figure 5.12 at various temperatures.

Temperature (Kelvin)	Differential Conductance ($2e^2/h$ per volt)							
	1/2	1	3/2	2	5/2	3	7/2	4
1.2	60	-4	35	-1	35	-1	36	1
4.2	47	-2	29	1	28	0	24	0
5.4	37	0	27	2	25	2	23	3
6.5	31	2	26	1	24	3	18	4
8.0	26	5	21	5	21	6	15	5
10.0	24	5	19	6	18	8	17	8
14.0	24	9	16	10	15	10	13	12
20.0	19	10	15	11	12	12	12	12
30.0	16	11	12	12	12	12	12	12

Figure 5.12: The values of the differential conductance maxima (non-integers) and minima (integers) for the first three sub-bands in a shallow GaAs-Al$_{0.3}$Ga$_{0.7}$As heterostructure (A686) at the nine different temperatures given in Table 5.2.
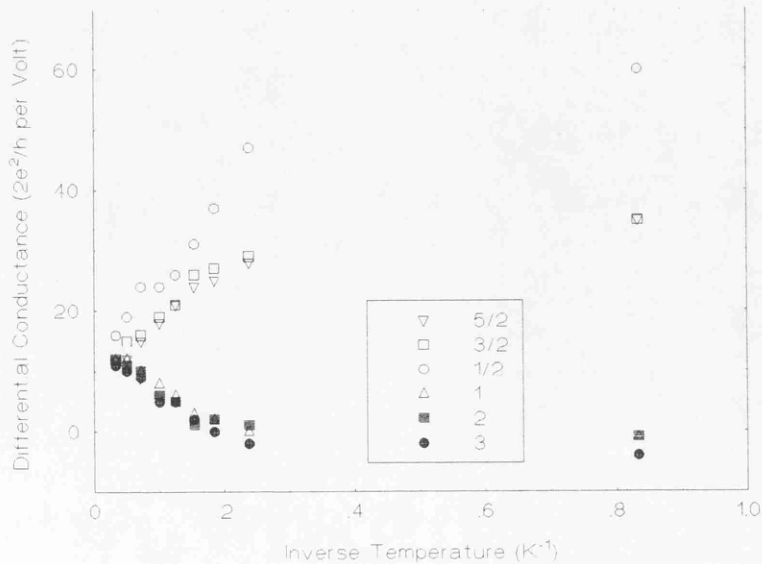
Table 5.3a: Data for various experiments carried out in various GaAs-Al$_x$Ga$_{1-x}$As heterostructures. The smearing of conductance quantisation with increasing source-drain bias V_{sd} and temperature is included where data is available. The numbers in parenthesis refer to the number of sub-bands present in the wire during the voltage smearing experiment.

	Sample Identification	Length (nm)	Width (nm)	Number of Sub-bands	Threshold Voltage	Cut Off Voltage	Smearing Temperature (Kelvin)		Smearing Voltage (eV/4k$_B$)*	
							Peaks	Troughs	Peaks	Troughs
Experiment 17	A686	400	50	3	-0.35	-0.48	25, 5, 4.5	20, 8, 6	15, 6, 5	16, 8, 4
Experiment 16	A688	200	50	2	-0.39	-0.58			6, 2	
	A688	100	50	2	-0.36	-0.44			10, 3	
Experiment 15	A686	200	100	4(5)	-0.50	-0.91	16, 9.5, 10.5	21, 5, 2	15, 9, 7	20, 7, 3
Experiment 14	A686	100	80	5	-0.60	-1.01	14, 8, 7, 6	15, 12, 9.5	17, 10, 7.5	15, 12, 8, 5
							3.5	6, 4	2.5	2
Experiment 13	A688	50	50	3(4)	-0.39	-0.70	10, 7, 2	11, 9, 2	9, 6.5, 3.5	10, 8, 5.5
									1.5	2.5
Experiment 12	A686	200	80	4	-0.46	-0.98				
	A686	150	80	2	-0.50	-0.84				
	A686	100	80	2	-0.50	-0.78				
Experiment 8	A686	200	80	6	-0.32	-0.86	19, 12, 9.5	14, 12, 10.5		
							7, 6, 6	10, 6.5		

Table 5.3b: Data for various experiments carried out in various GaAs-Al$_x$Ga$_{1-x}$As heterostructures. The smearing of conductance quantisation with increasing source-drain bias V_{sd} and temperature is included where data is available. The numbers in parenthesis refer to the number of sub-bands present in the wire during the voltage smearing experiment.

	Sample Identification	Length (nm)	Width (nm)	Number of Sub-bands	Threshold Voltage	Cut Off Voltage	Smearing Temperature (Kelvin)		Smearing Voltage ($eV/4k_B$)*	
							Peaks	Troughs	Peaks	Troughs
Experiment 37	A685	100	200	3	-0.70	-1.60				
		150	150	6	-0.70	-1.31				
		200	100	Resonances	-0.65	-0.85				
Experiment 28	A686	400	100	Resonances	-0.40	-0.55				
		500	100	Resonances	-0.40	-0.55				
Experiment 27	A685	100	150	5	-0.96	-1.50	14, 11, 9	13, 12, 11	11, 8, 6	9, 9, 5, 3
Experiment 26	A449	200	200	7	-0.35	-1.30			6, 4, 2.5 2, 1.5	5, 4, 3, 1.5
Experiment 25	A686	400	100	2	-0.40	-0.53	10, 10	12.5, 11.5	13, 10	11, 11
		500	100	Resonances	-0.40	-0.57				

experimental data is summarised in Table 5.3 and the smearing results for both temperature and voltage bias are discussed in the next two sections.

5.5.1 Comparing Thermal and Electronic Smearing Mechanisms

The smearing temperatures for three wires on a shallow GaAs-Al$_{0.3}$Ga$_{0.7}$As heterostructure and one wire on an intermediate GaAs-Al$_{0.3}$Ga$_{0.7}$As heterostructure are presented in Histogram 5.1a. A number of trends are immediately apparent from the data. As the sub-band index increases by one, the smearing temperature reduces. This is sensible because when a constriction forms, the bottom of the potential well is at some height E_c above the conduction band bottom in the bulk 2DEG [17]. This saddle like potential causes a reduction in the local carrier concentration, which reduces further as the constriction narrows. Hence at higher gate voltages or lower sub-band index, this reduction in the carrier concentration means there is less screening of impurity potential giving less curvature in the confining potential and hence a lower sub-band spacing [18]. This lower sub-band spacing results in the broadening of the differential Fermi function becoming a significant fraction of the energy interval at a lower temperature or source drain bias.

Another interesting aspect of the data is that for the shorter wires (A686, 100nm and A688, 50nm) the peaks in the differential conductance tend to smear at slightly lower temperatures than the troughs. This trend is also apparent in the smearing of the differential conductance with increasing source-drain bias (with the exception of the first sub-band (0.5, 1) in Expt 14), see Histogram 5.1b. This difference in the smearing is generally only one or two degrees and as such is comparable with the random errors in the two types of experiments. The effect is only mentioned as it is a theoretical prediction of models to be discussed in Section 5.5.2. Also clearly apparent in the data is the increase in smearing

Histogram 5.1a: Temperature smearing of the differential conductance as a function of subband index for various wires in shallow (A686) and intermediate (A688) GaAs-$Al_{0.3}Ga_{0.7}As$ heterostructures.
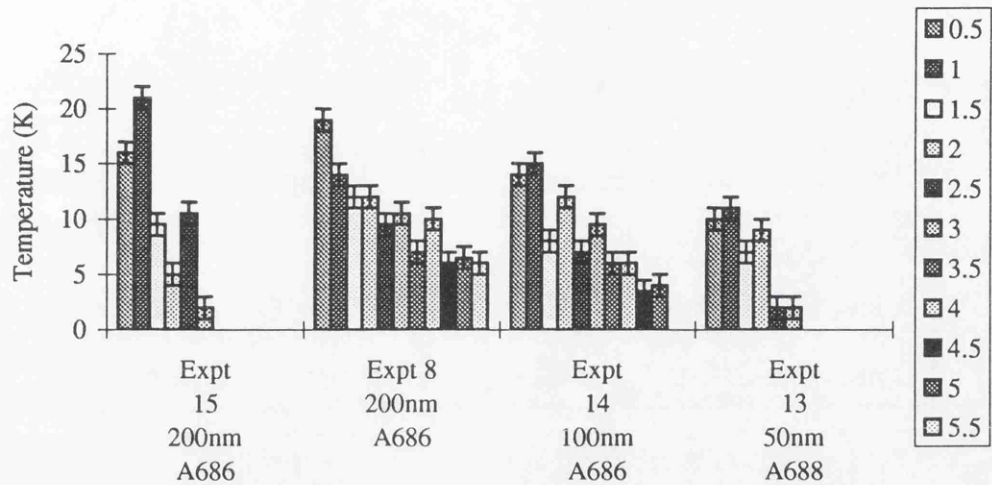
Histogram 5.1b: Smearing of the differential conductance as a function of subband index for increasing source-drain bias. Data for various wires in shallow, intermediate and deep GaAs-$Al_{0.3}Ga_{0.7}As$ heterostructures are presented.
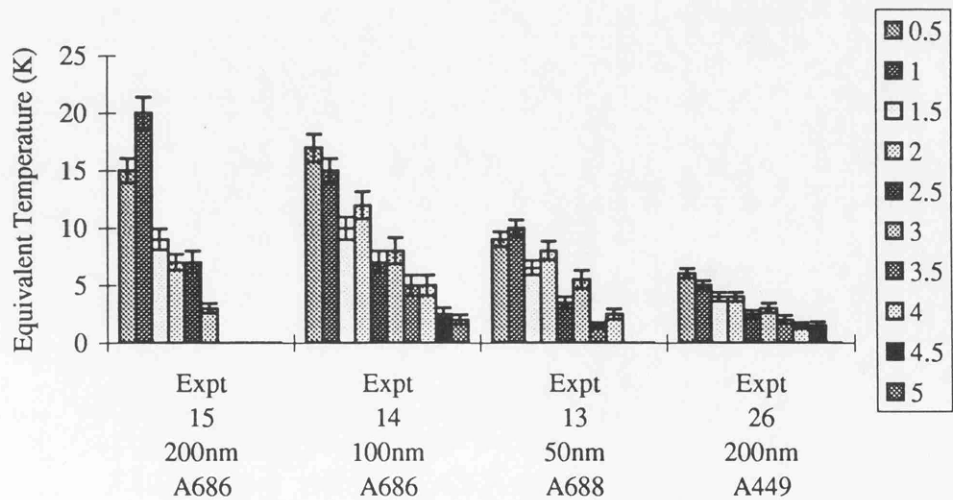
temperature that occurs as the 2DEG is formed closer to the surface. The first sub-band (0.5, 1) in the Shallow A686 structure smears in the temperature region 15K to 20K, depending on the wire length. The first sub-band in the Intermediate and Deep heterostructures smear at 10K and 6K respectively. Agreement between both thermal and voltage smearing experiments is very good.

Finally it is important to notice the more erratic nature of the smearing results taken on the 200nm A686 wires. There is still generally good agreement between thermal and electronic smearing rates, however large differences between the smearing of peaks and troughs is apparent. Notice also that some sub-bands with higher index smear at higher temperatures than those with a lower index. This is due to resonant structure superimposed on the differential conductance traces making it difficult to accurately analyse the data. This resonant structure was mentioned in Section 5.4.3 and interpreted as being due to the confinement length scale being similar to the length scale of potential fluctuations at the 2DEG plane, see Chapter 6. This explanation seems likely when measurements of the conductance of longer wires (400 and 500nm) is considered. These measurements initially showed no quantisation at all. However it was possible to observe quantised conductance in these longer wires (with much superimposed resonant structure) if the confining potential was electrostatically shifted to another region of the 2DEG [19]. This presumably is the result of sampling a region of 2DEG which has less potential fluctuations. It seems that for the shallow structure, beyond about 200nm, the quantisation is extremely sensitive to the detailed potential landscape in which the wire is formed. These ideas are dealt with in more detail in Chapter 6 but the smearing results are presented here in Histograms 5.2a and 5.2b for completeness. The thermal and electronic smearing temperatures agree within the random errors of the measurements for many of the sub-bands, but there can be significant differences indicating that care must be taken when interpreting the data.

The thermal and voltage smearing of the differential conductance of a 100nm wire in a shallow GaAs-AlAs heterostructure and a shallow GaAs-

Histogram 5.2a: Temperature smearing of the differential conductance as a function of subband index for 400 and 500nm wires in a shallow (A686) GaAs-$Al_{0.3}Ga_{0.7}As$ heterostructure.
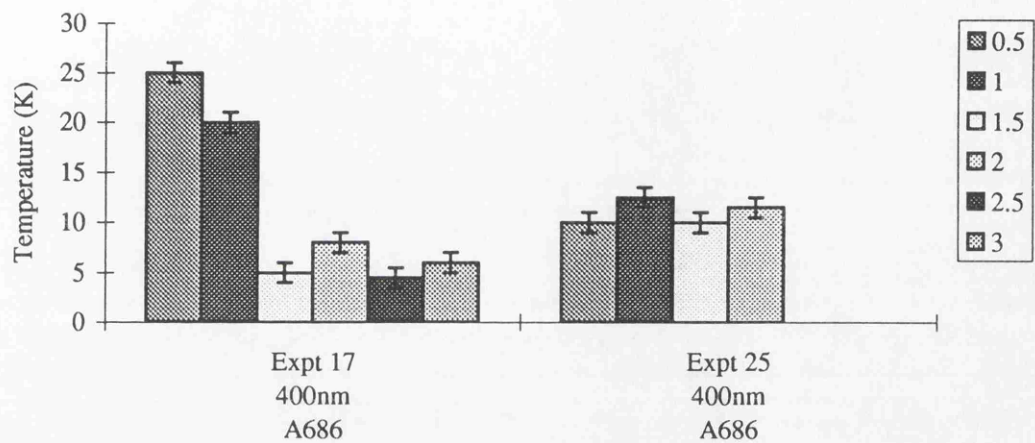
Histogram 5.2b: Smearing of the differential conductance as a function of subband index for increasing source-drain bias. Data for 400 and 500nm wires in a shallow (A686) GaAs-$Al_{0.3}Ga_{0.7}As$ heterostructure is presented.
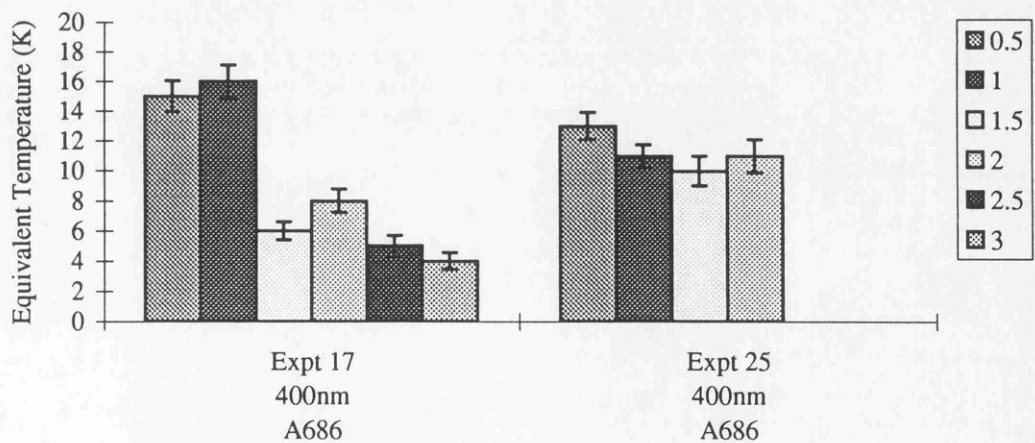
Histogram 5.3a: Temperature smearing of the differential conductance as a function of subband index for 100nm long wires in shallow GaAs-Al$_{0.3}$Ga$_{0.7}$As (A686) and GaAs-AlAs (A685) heterostructures.
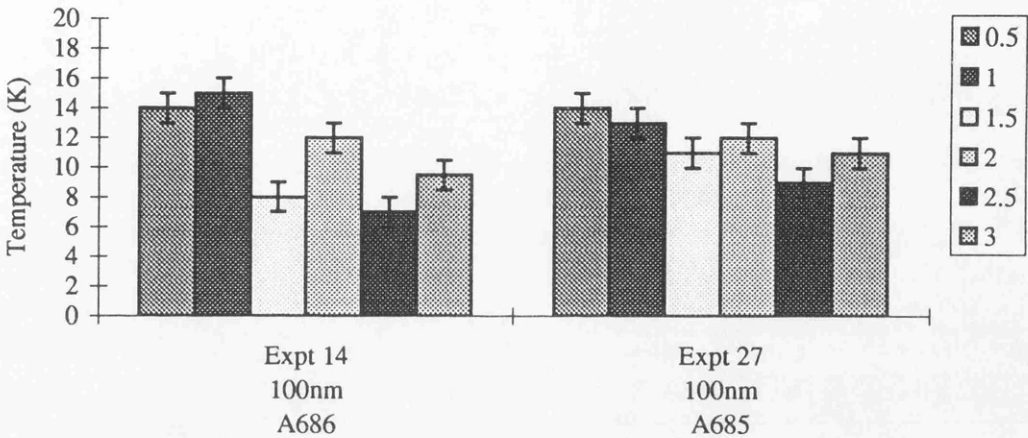
Histogram 5.3b: Smearing of the differential conductance as a function of subband index for increasing source-drain bias. Data for 100nm long wires in shallow GaAs-Al$_{0.3}$Ga$_{0.7}$As (A686) and GaAs-AlAs (A685) heterostructures is presented.
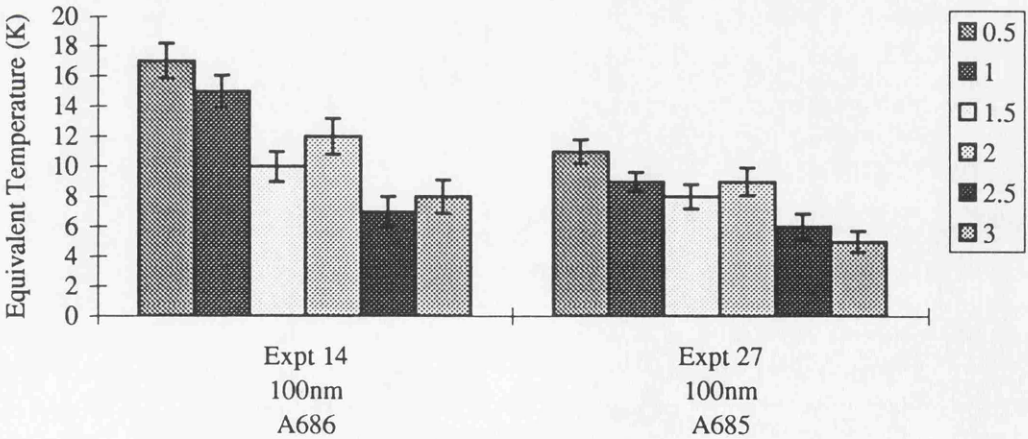
$Al_{0.3}Ga_{0.7}As$ are compared in Histograms 5.3a an 5.3b. The smearing temperatures show no significant differences, although the temperature smearing of the GaAs-AlAs is slightly more robust. In addition, the GaAs-AlAs source-drain smearing differs from the thermal smearing. This is consistent with inspection of Figures 5.8 and 5.9 but it is difficult to know whether this is significant. It most likely indicates the difficulty in defining the point at which the quantisation smears when resonant structure is superimposed on the conductance trace.

5.5.2   Analysing   the   Smearing   of   the   Conductance Quantisation

In the previous section, data was presented showing the smearing of the conductance quantisation with increases in temperature and source-drain bias in various wires, fabricated in different materials. A method of defining the thermal and electronic smearing of the different sub-bands in these various wires was also outlined. It was found that using the prescription described in Appendix B, the smearing of the conductance quantisation with increasing source drain bias was broadly consistent with the temperature smearing within the experimental errors. It was also remarked that the lower sub-band indices generally had higher associated smearing temperatures. This was qualitatively explained as a manifestation of reduced screening in the constriction because of the formation of a saddle potential which reduces the local carrier concentration. A number of important points can be made with these observations in mind.

Consider the physical picture described in Chapter 1, Section 1.3.4. An expression for the ratio of the low temperature differential conductance to the high temperature differential conductance was derived for maxima of the type presented in Figure 5.11, see Equation 5.8. In Section 5.3, this equation was

evaluated in the limit of a small excitation voltage V and high temperature T to give the variation in the normalised differential conductance as $\Delta E(V_g)/4k_BT$.

$$\frac{dg_n/dV_g}{dg_0/dV_g} = \frac{\Delta E(V_g)}{eV}\tanh\left(\frac{eV}{4k_BT}\right) \qquad (5.8)$$

Hence, in order to find the sub-band spacing $\Delta E(V_g)$ for the particular gate voltage V_g at which the maxima occurs, it is simply necessary to normalise the differential conductance in terms of the high temperature differential conductance and equate this to $\Delta E(V_g)/4k_BT_s(max)$ where $T_s(max)$ is the smearing temperature of the particular maxima to be evaluated i.e.

$$\frac{dg_n/dV_g}{dg_0/dV_g} \approx \frac{\Delta E(V_g)}{4k_BT_s(max)} \qquad (5.9)$$

For instance, consider the wire in Experiment 8. The smearing temperature T_s of this particular wire is estimated to be 12K for the $n=2$ sub-band maximum (which occurs at a gate voltage of -0.773V). Substituting these values into Equation 5.9 (remembering that by definition, a smeared temperature is the temperature at which the normalise differential conductance is 1.5) and then solving for the sub-band spacing $\Delta E(2)$ gives

$$\Delta E(2) \approx \frac{3}{2}4k_BT_s(max) = 6.2meV \qquad (5.10)$$

Repeating this calculation for all six sub-bands and plotting the results against gate voltage illustrates the dynamic nature of the sub-band spacing in the wire as it

increases from approximately 3meV at threshold to 10meV at cut-off, see Figure 5.13.

Figure 5.13: The sub-band spacing as a function of gate voltage in a 200nm quantum wire formed in a shallow GaAs-$Al_{0.3}Ga_{0.7}As$ heterostructure (Experiment 8). The data points are derived from the smearing of the differential conductance maxima and minima with increasing temperature.
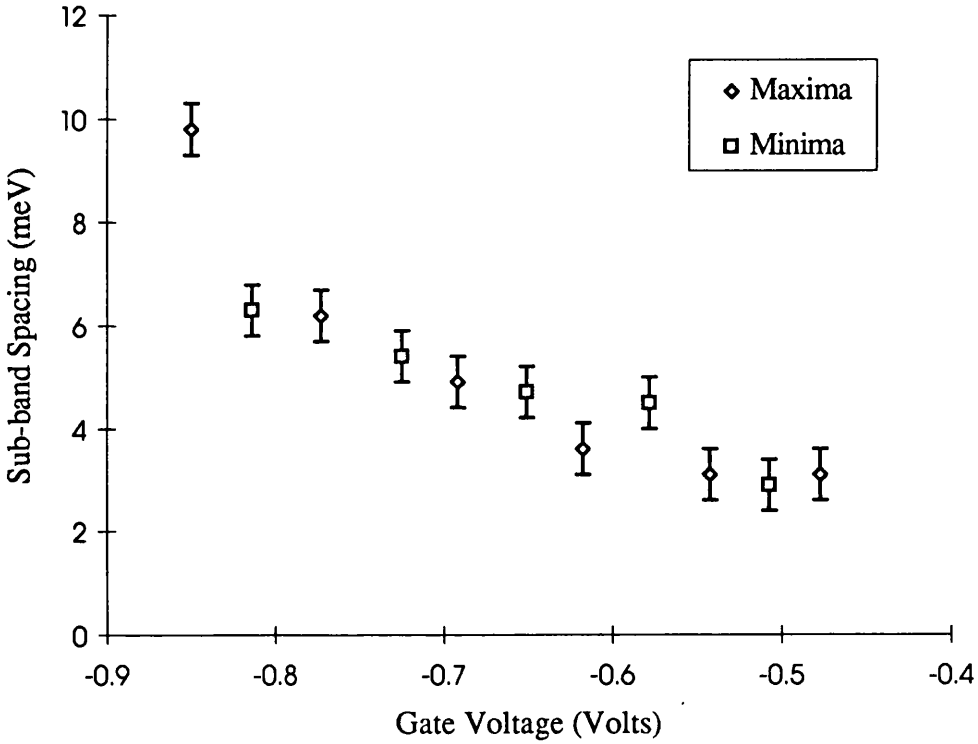
In Chapter 1, Section 1.3.4 a relation was also derived for the sub-band spacing in wires, in terms of the temperature smearing of the minima in the differential conductance, see Equation 5.11.

$$\cosh^2\left(\frac{\Delta E(V_g)}{4k_B T_s(\min)}\right) = 3\frac{\Delta E(V_g)}{4k_B T_s(\min)} \rightarrow \Delta E \approx 5.2 k_B T_s(\min) \qquad (5.11)$$

It is interesting to note that Equations 5.10 and 5.11 predict different smearing temperatures for the maxima and minima in the differential conductance. Although this difference is similar to the random error in the measurements ($\approx 13\%$), it is still generally observable in the data on short wires, see Section 5.5.1. For Experiment 8, Equation 5.11 is used to estimate the sub-band spacing for the minima in the differential conductance and these results are also plotted onto Figure 5.13.

It was described above that the best estimate of the experimental error in any particular device comes from irregularities in the experimental curves. Fluctuations and superimposed resonant structure can make it difficult to compare the high temperature (source-drain bias) differential conductance with the correct maximum or minimum. The magnitude of these random errors are estimated to contribute at least a degree or so of uncertainty to the smearing temperatures for the best devices (Experiment 8 and 14) and this corresponds to an error in the sub-band spacing of approximately ± 0.5meV. With this in mind, the data shows a strong trend for a smoothly varying sub-band spacing as the channel narrows. The variation in the sub-band spacing obtained using Equations 5.10 and 5.11 with all the data obtained on the various wires is detailed in Table 5.4. The analysis of this data is left until Section 5.6.2 where comparisons with theoretical calculations are made.

It is also interesting to compare the temperature and increasing source-drain bias smearing of the maxima in the differential conductance. It was discussed in Section 5.5.1 that these two smearing mechanisms gave generally similar results for short wires when the source-drain bias was interpreted as an equivalent temperature. In the case $eV_{ds} >> 4k_BT$, Equation 5.8 becomes

$$\frac{dg_n/dV_g}{dg_0/dV_g} = \frac{\Delta E(V_g)}{eV_{ds}} \equiv \frac{\Delta E(V_g)}{4k_BT_{se}(\text{max})} \tag{5.12}$$

Table 5.4: Sub-band spacing in various wires at particular gate voltages determined from the smearing of the differential conductance quantisation with increasing temperature and source-drain bias.

Exp't	Wire Length	Sample Type	Sub-band Spacing in meV (V_g) (Peaks, Temperature Smearing)	Sub-band Spacing in meV (V_g) (Peaks, Source-drain bias Smearing)	Sub-band Spacing in meV (V_g) (Troughs, Temperature Smearing)
Exp't 8	200nm	A686 Shallow	9.8(-0.850), 6.2(-0.773),4.9(-0.692)		6.3(-0.814), 5.4(-0.725)
		$Al_{0.3}Ga_{0.7}As$	3.6(-0.617),3.1(-0.542), 3.1(-0.477)		4.7(-0.651),4.5(-0.578),2.9(-0.507)
Exp't 13	50nm	A688 Intermediate	5.2(-0.57), 3.6(-0.509), 1.0(-0.45)	4.7(-0.695), 3.4(-0.630)	4.9(-0.535), 4.0(-0.476)
		$Al_{0.3}Ga_{0.7}As$		1.8(-0.569), 0.9(-0.513)	0.9(-0.424)
Exp't 14	100nm	A686 Shallow	7.2(-0.975), 4.1(-0.923),3.6(-0.851)	8.8(-1.000), 5.2(-0.919), 3.6(-0865)	6.7(-0.953), 5.4(-0.900)
		$Al_{0.3}Ga_{0.7}As$	3.1(-0.805), 1.8(-0.768)	2.6(-0.817), 1.3(-0.786)	4.3(-0.839),2.7(-0.786),1.8(-0.752)
Exp't 15	200nm	A686 Shallow	8.3(-0.910), 4.9(-0.832)	7.8(-0.906), 4.7(-0.813),	9.4(-0.870), 2.2(-0.800)
		$Al_{0.3}Ga_{0.7}As$	5.4(-0.767)	3.6(-0.746)	0.9(-0.737)
Exp't 16	100nm	A688 Intermediate		5.2(-0.433), 1.6(-0.388)	
		$Al_{0.3}Ga_{0.7}As$			
Exp't 16	200nm	A688 Intermediate		3.1(-0.569), 1.1(-0.500)	
		$Al_{0.3}Ga_{0.7}As$			
Exp't 17	400nm	A686 Shallow	12.9(-0.476), 2.6(-0.431)	7.8(-0.468), 3.1(-0.425)	9.0(-0.454), 3.6(-0.410)
		$Al_{0.3}Ga_{0.7}As$	2.3(-0.395)	2.6(-0.388)	2.7(-0.395)
Exp't 25	400nm	A686 Shallow	5.2(-0.545), 5.2(-0.482)	6.7(-0.542), 5.2(-0.475)	5.6(-0.511), 5.2(-0.465)
		$Al_{0.3}Ga_{0.7}As$			
Exp't 26	200nm	A449 Deep		3.1(-1.292), 2.1(-1.196)	
		$Al_{0.3}Ga_{0.7}As$		1.3(-1.088), 1.1(-0.993), 0.9(-0.916)	
Exp't 27	100nm	A685 Shallow	7.2(-1.398), 5.7(-1.290)	5.7(-1.497), 4.1(-1.383), 3.1(-1.24)	5.8(-1.335), 5.4(-1.236)
		AlAs	4.7(-1.174)		4.9(-1.128)

where $T_{se}(max)$ is the equivalent electronic smearing temperature. Clearly Equations 5.9 and 5.12 give $T_s(max)=T_{se}(max)$ consistent with the experiments. To see how good the agreement is, $T_s(max)$ is plotted against $T_{se}(max)$ for two different wires, one in a shallow (A686) and one in an intermediate GaAs-$Al_{0.3}Ga_{0.7}As$ heterostructure, see Figure 5.14.

Figure 5.14: A plot of the smearing temperature against the equivalent electronic smearing temperature for the quantised conductance in an intermediate (Experiment 13 A688) and a shallow (Experiment 14 A686) GaAs-$Al_{0.3}Ga_{0.7}As$ heterostructure.
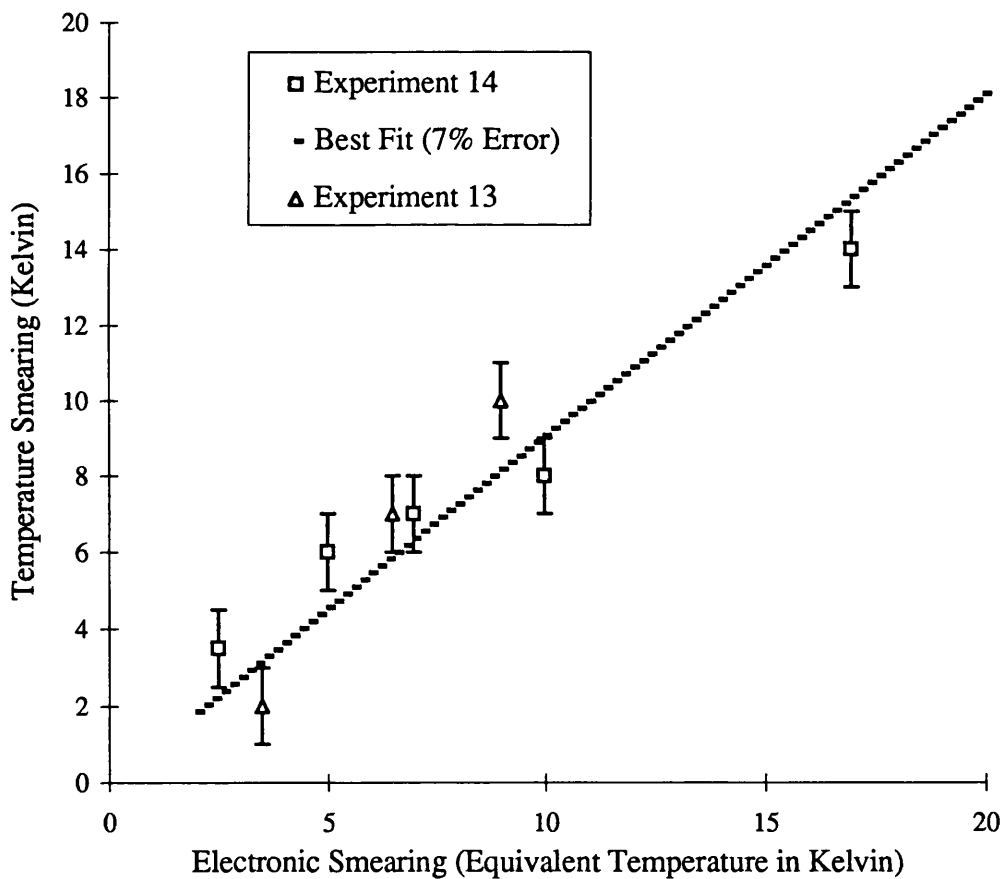
The data in Figure 5.14 is fairly scattered but the gradient trends to a value of 0.90 with a standard deviation in the data of 0.24. There is therefore no statistical

evidence in the interpretation of this data for a difference between $T_s(max)$ and $T_{se}(max)$ but the data may not be good enough to draw any definitive conclusions. This contrasts with measurements carried out recently by Taboryski et al. who argued that smearing of quantised conductance with increasing source-drain bias is in fact far stronger than could be explained by smearing of the differential Fermi function. The authors then go on to postulate that Joule heating in the series regions of 2DEG must make an important contribution [20].

5.6 Sub-band Spacing in Wires and Theoretical Models

The following section describes a brief outline of a theoretical model developed by John Davies who is a lecturer at the University of Glasgow's Department of Electrical and Electronic Engineering. The model will be used to calculate the variation of the sub-band separation with gate voltage and also the ratio of the cut-off voltages to the threshold voltages in the various measured wires. These calculations will then be compared with the experimental results.

5.6.1 Overview of the Model

The sub-band spacing ΔE in surface gated quantum wires depends strongly on the local Fermi energy. This local Fermi energy is lower than that for the bulk two dimensional electron gas due to the reduced carrier concentration n_{2D} in the quantum wires. With increasing gate voltage, the wire narrows and the carrier concentration continues to reduce, changing the screening of the impurity potential due to the donors. This in turn affects both the sub-band spacing and scattering in the wires. As the wire nears pinch-off, $n_{2D}(V_g) \rightarrow 0$ and screening of

the donors can be neglected. It is the region before pinch-off, where the screening is highly non-linear that is the most difficult to treat quantitatively and is the region we need to understand.

The model used is fully 3-dimensional and designed to simulate the characteristics of devices formed with arbitrary shaped polygonal surface gates on heterostructures of any depth. For each gate voltage, the wires are described by a bare parabolic potential due to the bias on the gate electrodes, assuming either a pinned or frozen surface potential [21]. In the pinned model, the Fermi energy throughout the structure is pinned by surface states in the GaAs to a fixed energy below the conduction band bottom. However the difficulty with this model is that with the application of a gate bias, it is unclear whether the free surface is pinned to the Fermi energy in the gate electrode or to that in the 2DEG. For a wire to form obviously the pinning cannot take place in the gate [18] and therefore pinning must be to the Fermi energy in the 2DEG. The problem is that charge must move between the 2DEG and the surface to maintain the equilibrium and this seems unlikely at 1K [13]. The case of the frozen surface potential attempts to get round this problem by treating the surface as a simple dielectric boundary, with a simple fixed charge density in response to a change in the applied gate voltage. The donors are also treated as having a fixed charge density and this implies that they are fully ionised and that any electrons in the region of the donors reside in deep traps and hence cannot respond to the gate bias at low temperatures.

Once the bare potential has been calculated under the assumptions outlined above, it is screened using the semi-classical Thomas-Fermi approximation for the electrons in the 2DEG. The quadratic term in the parabolic potential is then used to obtain the lateral sub-band energies, this in turn defines how many sub-bands are present and hence gives the sub-band spacing (assuming equal spacing of the energy levels). Corrections due to tunnelling through forbidden regions are also included. The procedure is repeated for N gate voltages from threshold to cut off, where N is the required degree of accuracy needed to resolve the sub-band

depopulation in the wire. Simulations were carried out for all the experiments detailed in Table 5.4 and the sub-band separation for each simulated peak and trough are summarised in Table 5.5.

Table 5.5: Calculated sub-band separations for wires with various lengths fabricated in various heterostructures.

	Wire Length	Sample Type	Calculated Sub-band Separation (meV)	
			Peaks	Troughs
Experiment 8	200nm	A686 Shallow GaAs-Al$_{0.3}$Ga$_{0.7}$As	9.8, 6.9, 5.4 4.3, 3.7	8.0, 6.1, 4.8 4.0, 3.4
Experiment 13	50nm	A688 Intermediate GaAs-Al$_{0.3}$Ga$_{0.7}$As	6.6, 4.7, 3.6	5.3, 4.0, 3.4
Experiment 14	100nm	A686 Shallow GaAs-Al$_{0.3}$Ga$_{0.7}$As	9.6, 6.6, 5.2 4.1, 3.7	7.7, 5.9, 4.7 4.0, 3.4
Experiment 15	200nm	A686 Shallow GaAs-Al$_{0.3}$Ga$_{0.7}$As	9.1, 6.3, 5.0	7.4, 5.5, 4.4
Experiment 17	400nm	A686 Shallow GaAs-Al$_{0.3}$Ga$_{0.7}$As	10, 6.8, 5.5	7.8, 5.9, 5.1
Experiment 25	400nm	A686 Shallow GaAs-Al$_{0.3}$Ga$_{0.7}$As	8.8, 6.1	7.0, 5.4
Experiment 26	200nm	A449 Deep GaAs-Al$_{0.3}$Ga$_{0.7}$As	3.9, 2.6, 2.1 1.7, 1.5	3.0, 2.3, 1.9 1.6, 1.4
Experiment 27	100nm	A685 Shallow GaAs-AlAs	5.6, 3.8, 2.9	4.4, 3.3, 2.7

5.6.2 Comparing Experimental Data and Calculations

The experimental sub-band spacings are obtained from the smearing of the differential conductance maxima and minima with increasing temperature and source-drain bias. This data is plotted with the calculated sub-band spacing as a function of sub-band index in Figures 5.15 to 5.17. The experimental trends are

Figure 5.15a: The calculated and measured sub-band spacing as a function of sub-band index for a 200nm quantum wire in a shallow (A686) GaAs-Al$_{0.3}$Ga$_{0.7}$As heterostructure (Experiment 8).
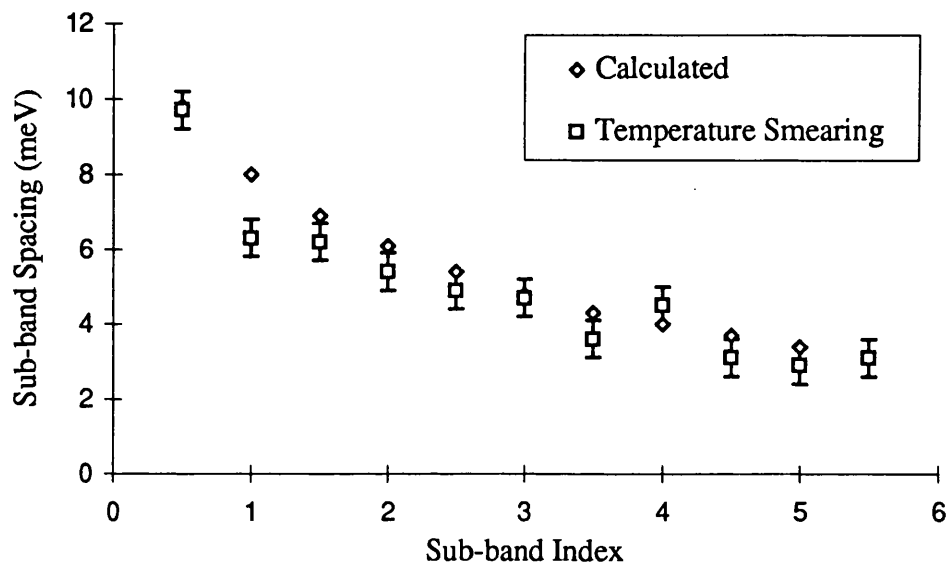
Figure 5.15b: The calculated and measured sub-band spacing as a function of sub-band index for a 100nm quantum wire in a shallow (A686) GaAs-Al$_{0.3}$Ga$_{0.7}$As heterostructure (Experiment 14).
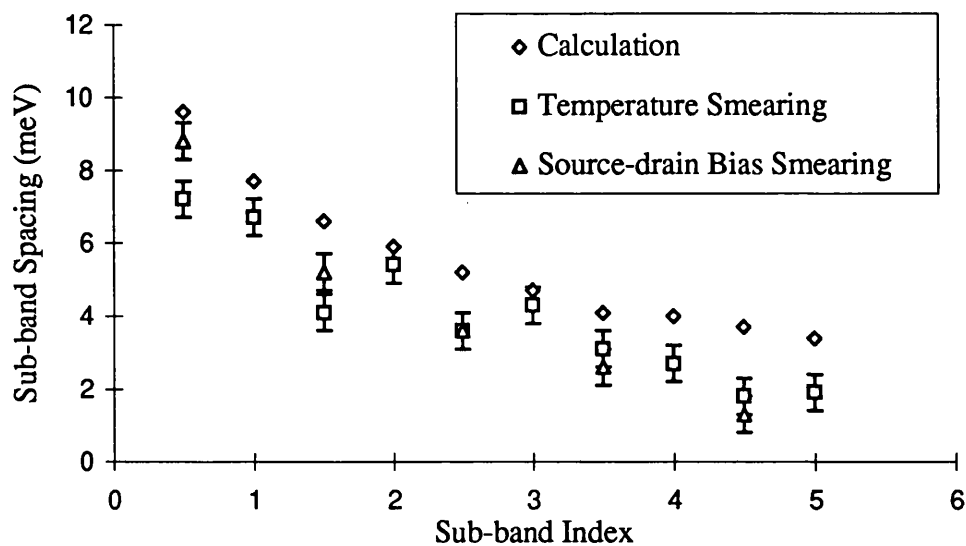
Figure 5.16a: The calculated and measured sub-band spacing as a function of sub-band index for a 200nm quantum wire in a shallow (A686) GaAs-Al$_{0.3}$Ga$_{0.7}$As heterostructure (Experiment 15).
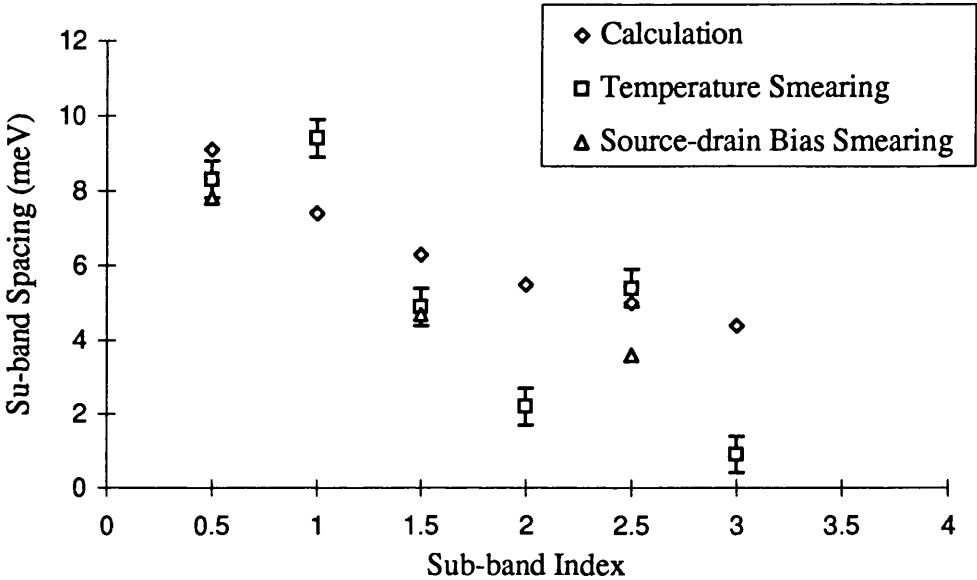
Figure 5.16b: The calculated and measured sub-band spacing as a function of sub-band index for a 400nm quantum wire in a shallow (A686) GaAs-Al$_{0.3}$Ga$_{0.7}$As heterostructure (Experiment 17).
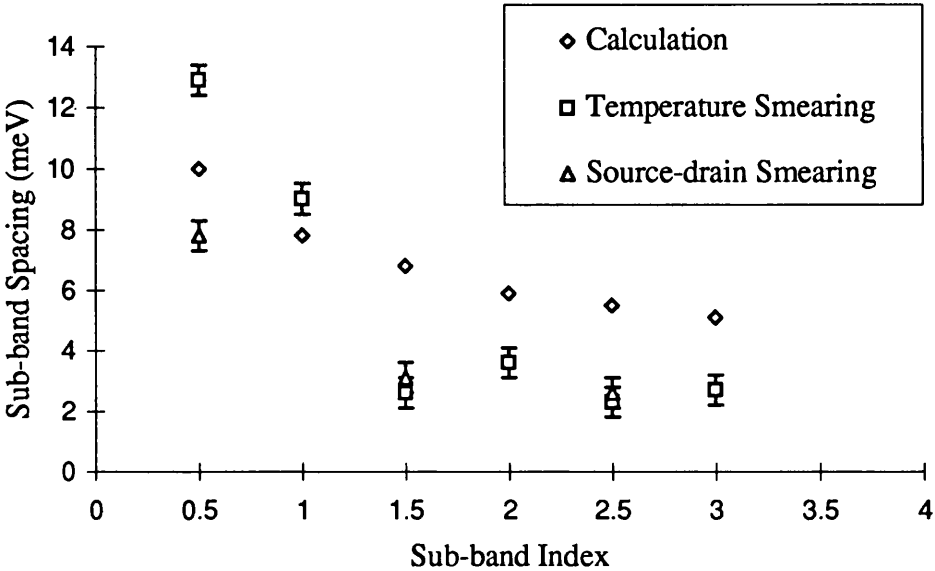
Figure 5.17a: The calculated and measured sub-band spacing as a function of sub-band index for a 200nm quantum wire in a deep (A449) GaAs-$Al_{0.3}Ga_{0.7}As$ heterostructure (Experiment 26).
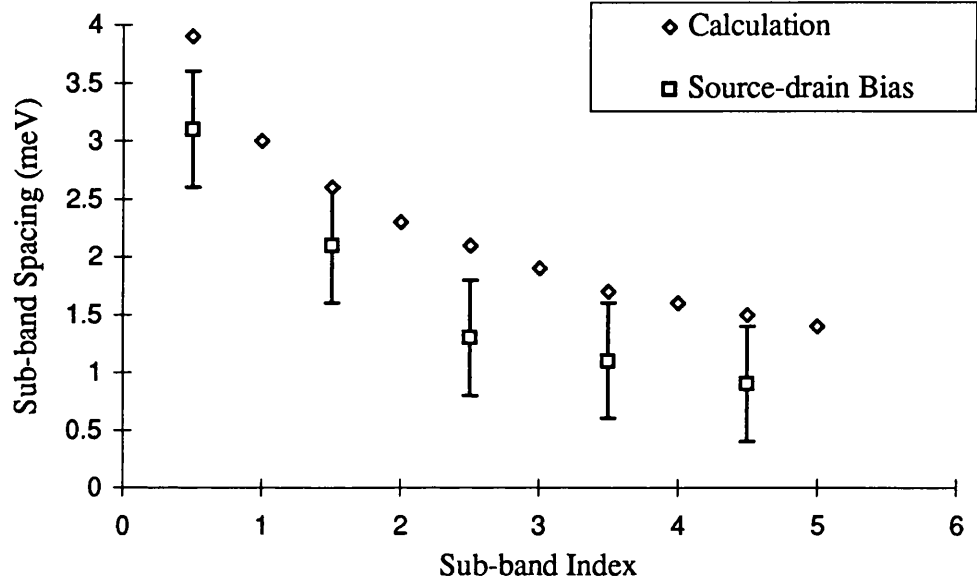
Figure 5.17b: The calculated and measured sub-band spacing as a function of sub-band index for a 50nm quantum wire in an intermediate (A688) GaAs-$Al_{0.3}Ga_{0.7}As$ heterostructure (Experiment 13).
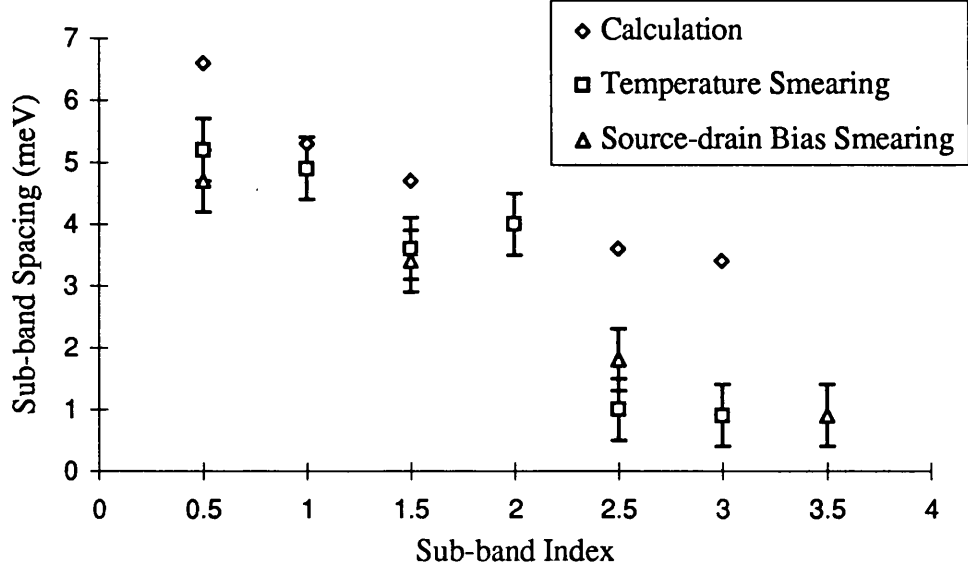
generally in good agreement with the calculations. The decrease in the sub-band spacing as the spacer thickness is reduced (from 40nm in Figure 5.18a to 11nm in Figure 5.16a) is clear. In addition, the reduction in the screening which leads to an enhanced sub-band spacing as the wire depletes is also well modelled. Inspecting the data more quantitatively shows up a systematic difference between the calculations and the experiments which cannot be accounted for by the random errors in the measurements. This trend towards lower experimental sub-band spacings compared to the calculations is difficult to interpret accurately. It may well be the result of difficulties in determining the exact geometry of the devices due to the edges of the gate electrodes not being in complete contact with the surface of the heterostructure. This problem with the lift-off procedure employed in fabricating the gates would result in large uncertainties in the electrostatic width of the wires. A greater separation between the electrodes and the 2DEG would of course lead to a lower sub-band separation at all gate voltages, consistent with the systematic error in the experiments. Finally, attention is drawn to the experiments presented in Figures 5.18a and b. This data is very scattered and when compared to data from other experiments shows that the quality of the sample can be a substantial factor in determining conduction through the device. Care must be taken in isolating relatively 'clean' device characteristics before drawing conclusions.

5.6.3 Analytical Models of Threshold and Cut-off Voltages

The ratio of the cut-off voltages to the threshold voltages is estimated from Davies' model of an infinitely long wire under the assumptions described in Section 5.6.1. Broadly speaking, it determines the voltages required to deplete electrons using a simple parallel plate capacitor model. The additional voltage

Table 5.6: Data comparing experimental threshold V_T and cut-off voltages V_c with calculated values for various wires of length L.

	Sample Identification	2DEG Depth d^* (nm)	Carrier Concentration (m^{-2})	Length L (nm)	Width* (nm)	Experimental $V_c/V_T \pm 0.01$ (Volts)	Calculated V_c/V_T as $L\to\infty$ Pinned	Calculated V_c/V_T as $L\to\infty$ Frozen
Experiment 37	A685	35	$(3.5\pm0.1)\times10^{15}$	100	200	2.29	4.67	3.03
				150	150	1.87	3.60	2.36
				200	100	1.31	2.57	1.74
Experiment 27	A685	35	$(3.5\pm0.1)\times10^{15}$	100	150	1.56	3.60	2.36
Experiment 26	A449	99	$(3.4\pm0.1)\times10^{15}$	200	200	3.71	2.01	1.42
Experiment 16	A688	47	$(4.0\pm0.1)\times10^{15}$	200	50	1.49	1.45	1.13
				100	50	1.22	1.45	1.13
Experiment 15	A686	35	$(6.0\pm0.1)\times10^{15}$	200	100	1.82	2.57	1.74
Experiment 14	A686	35	$(5.7\pm0.1)\times10^{15}$	100	80	1.68	2.57	1.74
Experiment 13	A688	47	$(4.0\pm0.1)\times10^{15}$	50	50	1.79	1.45	1.13
Experiment 12	A686	35	$(6.2\pm0.1)\times10^{15}$	200	80	2.13	2.57	1.74
				150	80	1.68	2.57	1.74
				100	80	1.56	2.57	1.74
Experiment 8	A686	35	$(6.4\pm0.1)\times10^{15}$	200	80	2.69	2.19	1.52

* Separation of the gate electrodes measured directly from a scanning electron micro-graph of the device.

* Includes 7nm for the electron gas thickness.

necessary to take into account the binding energy of the electrons in the 2DEG is included in a term representing the 'thickness' of the 2DEG, see Equation 5.13 and 5.14, where $2b$ is the width of the wire and d is the depth of the 2DEG [13].

$$\frac{V_c}{V_T} = \left(1 - \frac{2}{\pi}\arctan\left(\frac{b}{d}\right)\right)^{-1} \quad \text{Pinned boundary conditions} \qquad (5.13)$$

$$\frac{V_c}{V_T} = \left[1 + \left(\frac{b}{d}\right)^2\right]^{1/2} \quad \text{Frozen boundary conditions} \qquad (5.14)$$

Table 5.6 summarises the experimental ratio of the cut-off voltage to the threshold voltage for various wires and also includes the calculated results under the pinned and frozen assumptions for the surface potential discussed in Section 5.6.1. Generally the ratio of cut-off voltages to threshold voltages are not in very good agreement with those calculated under either of the assumptions. In particular the values obtained for the GaAs-AlAs heterostructure are in much worst agreement than those obtained on GaAs-Al$_{0.3}$Ga$_{0.7}$As heterostructures. The scatter on the data makes it very difficult to draw quantitative conclusions from these observations. The problem may well be due to the treatment of the donor region as having a fixed charge density which does not respond to the gate bias. Clearly if residual free charge was located outside the 2DEG, it would indeed lead to problems in using a simple parallel plate capacitor model when carrying out the calculations. Bearing in mind that free charge is know to reside outside the 2DEG in GaAs-AlAs heterostructures [22], this idea would also explain the greater discrepancy found with these samples when compared to GaAs-Al$_{0.3}$Ga$_{0.7}$As. It would be particularly useful to know which of the boundary conditions best described the data. However this is not possible because the differences between the calculations and measurements are far larger than any errors which can be quantified. The basic problem is again the large uncertainties in the electrostatic

dimensions of the samples. These errors were described in Section 5.6.2 where they were stated as likely reasons for the large differences between the measured and calculated sub-band spacing in some of the wires.

The model of Davies et al. also leads to the following analytical expressions for the sub-band spacing as the penultimate sub-band is squeezed out of the wire. Either a pinned or frozen surface potential can be assumed.

$$\Delta E = F(b/d) \times \left(\frac{e^2}{\varepsilon \varepsilon_0}\right)^{1/2} \left(\frac{E_F}{d}\right)^{1/2} \tag{5.15}$$

where

$$F(b/d) = \frac{2}{\pi}\left(\frac{b}{d}\right)^{1/2}\left(1+\frac{b^2}{d^2}\right)^{-1}\left(1-\frac{2}{\pi}\tan^{-1}\frac{b}{d}\right)^{-1/2} \qquad \text{pinned} \tag{5.16}$$

and

$$F(b/d) = \frac{2}{\pi^{1/2}}\frac{b}{d}\left(1+\frac{b^2}{d^2}\right)^{-3/4} \qquad \text{frozen} \tag{5.17}$$

For Experiment 8 these relations give sub-band spacings of 12.5meV and 9.9meV for the pinned and frozen cases respectively which compares to the experimental value of 9.8meV. In measurements carried out by Snider et al. an experimental sub-band spacing of 10meV was deduced which is close to the value found in Experiment 8. However, using the above relations with the geometry of his device, gives estimated sub-band spacings of 10.6meV and 9.0meV for the respective pinned and frozen surface potentials. The differences are so small that it is very important to understand how precise the measurements of sub-band spacings are before trying to differentiate between likely models. As was noted

above, sample geometry is critical and small uncertainties in these dimensions can easily cause large errors in the estimation of sub-band spacings.

5.6.4 Sub-band Spacings and Magnetic Confinement

Measurements of the low temperature quantised conductance of wires at fixed magnetic fields have been extensively studied in conventional GaAs-$Al_{0.3}Ga_{0.7}As$ heterostructures by van Wees et al. [8]. In this section the methods of van Wees are employed to study the magnetic depopulation of sub-bands in wires formed in both the shallow GaAs-$Al_{0.3}Ga_{0.7}As$ (A686) and GaAs-AlAs (A685) heterostructures, see Figure 5.18

Figure 5.18: The conductance as a function of gate voltage at various magnetic fields is presented. The device is a 100nm quantum wire (Experiment 27) in a shallow GaAs-AlAs heterostructure (A685). The curves are offset by e^2/h for clarity.
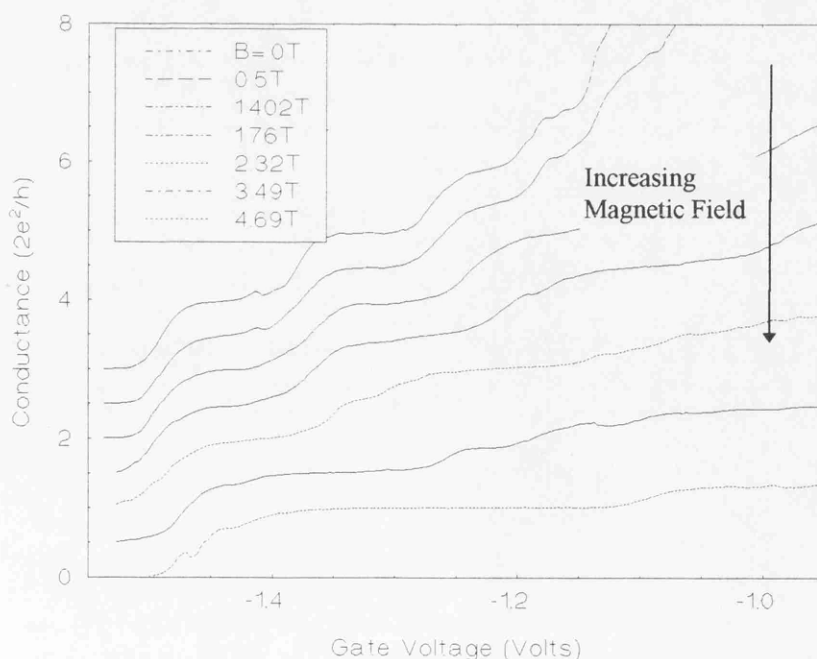
Zero field quantisation, due to confinement in electric sub-bands is seen to be smoothly replaced by confinement in magneto-electric sub-bands as the magnetic field increases in strength. Spin splitting of the electron energy occurs at high magnetic fields and the enhanced flatness of the plateaux, due to the suppression of backscattering in the wire, is also observed [23]. The different confinement regimes were discussed in Chapter 1, Section 1.4.2 where they were seen to lead to a magneto-electric confinement potential which could be modelled as a parabolic well with energy levels E_n in wire given by [24]

$$E_n = \left(n - \frac{1}{2}\right)\hbar\sqrt{\omega_0^2 + \omega_c^2}$$

(5.13)

The sub-band spacing is thus

$$\Delta E = E_{n+1} - E_n = \hbar\sqrt{\omega_0^2 + \omega_c^2}$$

(5.14)

where ω_0 characterises the strength of the electrostatic confinement and ω_c characterises the strength of the magnetic confinement. If there are N sub-bands in the constriction with a saddle potential E_c then Equation 5.14 can be written as

$$\Delta E = \hbar\sqrt{\omega_0^2 + \omega_c^2} = \frac{E_F - E_c}{N}$$

(5.15)

where E_F is the Fermi energy in the bulk 2DEG [25]. In the limit of high magnetic fields, when the cyclotron radius in the constriction is much smaller than the width of the well, the number of propagating modes is determined by

$$N \approx \frac{E_F - E_c}{\hbar\omega_c}$$

(5.16)

Equation 5.16 can thus be used with the high field data to estimate the rise in the saddle point potential as the wire narrows. This variation in E_F-E_c as a function of gate voltage can then be used with the two dimensional density of states to obtain the approximate reduction in the carrier concentration, see Equation 5.17 where $m*$ is the effective mass of the electrons in GaAs.

$$n_e(V_g) \approx (E_F - E_c)\frac{m*}{\pi\hbar^2} \qquad (5.17)$$

The results are plotted in Figures 5.19 and 5.20 for both of the wires discussed above. Data for the variation in the carrier concentration from measurements of the temperature smearing of the conductance quantisation is also included. This latter data is derived from treating the wire as a harmonic oscillator so that for N sub-bands, the sub-band spacing can be expressed in terms of the effective depth of the potential well, see Equation 5.18 (from Chapter 1, Section 1.4.2).

$$E_F - E_c = \left(N - \frac{1}{2}\right)\Delta E \qquad (5.18)$$

This relation can now be expressed in a similar way to Equation 5.17, if the density of states is again assumed to be two dimensional. This gives:

$$n_e(V_g) \approx (E_F - E_c)\frac{m*}{\pi\hbar^2} = \left(N - \frac{1}{2}\right)\Delta E \frac{m*}{\pi\hbar} \qquad (5.19)$$

The agreement between the estimated sub-band spacing as a function of gate voltage from the two method is fairly good. This seems strange, bearing in mind the assumption of a two dimensional density of states, which would seem to be a unlikely approximation to make in such narrow wires. Another unrelated but important point about the data is the marked difference in the voltage regime over

Figure 5.19: The subband spacing carrier concentration as a function of gate voltage in a quantum wire in a shallow GaAs-$Al_{0.3}Ga_{0.7}As$ heterostructure (A686).
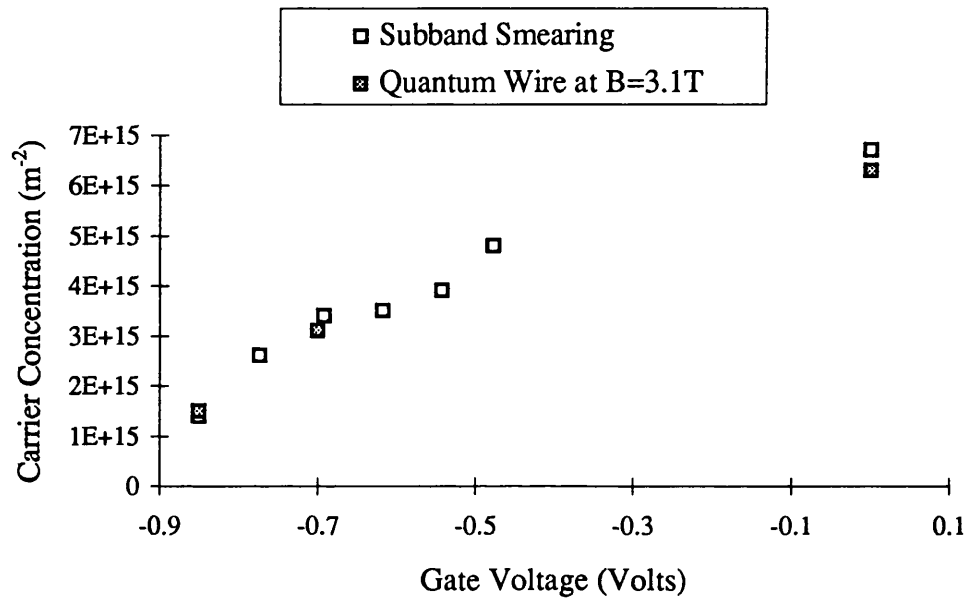
Figure 5.20: The carrier concentration as a function of gate voltage measured in a 100nm quantum wire in a shallow GaAs-AlAs heterostructure (A685).
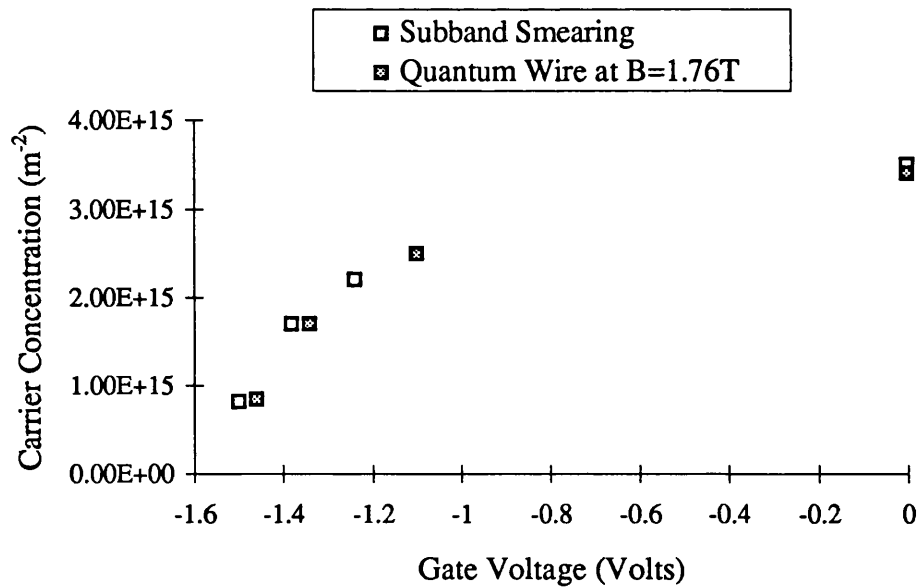
which these two wires deplete. This difference between GaAs-$Al_{0.3}Ga_{0.7}As$ and GaAs-AlAs is significant and was investigated extensively with measurements on continuous gates, see Chapter 4. We are seeing again the effect of free electrons in the donor region which need to be depleted before the carriers in the 2DEG are effected by the gate potential and a wire can be formed.

5.7 Conclusions

The basic physical arguments in realising high temperature quantised conductance in wires in GaAs-$Al_xGa_{1-x}As$ have been introduced. The robustness of the smearing of the quantisation to both increases in temperature and source-drain bias has been analysed in three GaAs-$Al_{0.3}Ga_{0.7}As$ heterostructures of different depths and one GaAs-AlAs heterostructure. The equivalence between thermal and source-drain bias smearing mechanisms is apparent in all the measurements and has been shown to be explicable in simple terms. No systematic difference has been found between the estimates of the sub-band separation obtained from the temperature and source-drain voltage dependence for any sample. No systematic difference is apparent between calculations and measurements of the reduction in the sub-band spacing in the wires as they deplete. The semi-classical screening assumptions implicit in the theoretical model seem to be adequate to interpret the experimental data.

The reduction in the carrier concentration as a function of gate voltage for shallow GaAs-$Al_{0.3}Ga_{0.7}As$ and GaAs-AlAs heterostructures has been estimated from smearing of the conductance quantisation and sub-band depopulation in a magnetic field. Both sets of data are found to be in good agreement. The ratio of the cut-off voltages to the threshold voltages and the sub-band spacing before cut-off have been analysed in terms of Davies' wire model for frozen and pinned surface potentials. Unfortunately, problems in determining exact sample

dimensions make it difficult to interpret the data with sufficient accuracy to distinguish between these two models.

References

[1] T. J. Thornton, M. Pepper, H Ahmed, D. Andrews, G. J. Davies, Phys. Rev. Lett. 56, 1198 (1986).

[2] H. Z. Zheng, H. P. Wei, D. C. Tsui, Phys. Rev. B 34, 5635 (1986).

[3] B. J. van Wees, H. van Houten, C. W. J. Beenakker, J. G. Williamson, L. P. Kouwenhoven, D. van der Marel, C. T. Foxon, Phys. Rev. Lett. 60, 848 (1988).

[4] D. A. Wharam, T. J. Thornton, R. Newbury, M. Pepper, H. Ahmed, J. E. F. Frost, D. G. Hasko, D. C. Peacock, D. A. Ritchie, G. A. C. Jones, J. Phys. C 21, L209 (1988).

[5] J. A. Nixon, J. H. Davies, Phys. Rev. B 41, 7929 (1990).

[6] P. F. Bagwell, T. P. Orlando, Phys. Rev. B 40, 1456 (1989).

[7] H. van Houten, B. J. van Wees, Semiconductors and Semimetals, M. A. Reed, Vol. ed. (Academic Press, New York, 1990).

[8] B. J. van Wees, L. P. Kouwenhoven, E. M. M. Willems, C. J. M. Harmans, J. E. Mooij, H. van Houten, C. W. J. Beenakker, J. G. Williamson, C. T. Foxon, Phys. Rev. B 43, 12431 (1991).

[9] G. L. Snider, M. S. Miller, M. J. Rooks, E. L. Hu, Appl. Phys. Lett. 59, 2727 (1991).

[10] G. L. Snider, I-Hsing Tan, M. S. Miller, M. J. Rooks, E. L. Hu, Superlattices and Microstructures Vol. 11, No. 3, 297 (1992).

[11] J. E. F. Frost, M. Y. Simmons, M. Pepper, A. C. Churchhill, D. A. Ritchie, G. A. C. Jones, J. Phys. C 5, L559 (1993).

[12] J. H. Davies, Semicond. Sci. Technol. 3, 995 (1988).

[13] J. H. Davies, I. A. Larkin, E. V. Sukhorukov (Accepted J. Appl. Phys 1995).

[14] J. J. Harries, C. T. Foxon, K. W. J. Barnham, D. E. Lacklison, J. Hewett, C. White, J. Appl. Phys. 61, 1219 (1987).

[15] G. Timp, R. Behringer, S. Sampere, J. E. Cunningham, R. E. Howard, Proceedings of the International Symposium on Nanostructure Physics and Fabrication, College Station, Texas, edited by M. A. Reed and W. P. Kirk (Academic, New York, 1989), pp 331-345.

[16] M. J. Laughton, J. R. Barker, J. A. Nixon, J. H. Davies, Phys. Rev. B 44, 1150 (1991).

[17] M. Büttiker, Phys. Rev. B 41, 7906 (1990).

[18] S. E. Laux, D. J. Frank, F. Stern, Surf. Sci. 196, 101 (1988).

[19] J. G. Williamson, C. E. Timmering, C. J. P. M. Harmens, J. J. Harris, C. T. Foxon, Phys. Rev. B 42, 7675 (1990).

[20] R. Taboryski, A. Kristensen, C. B. Sorensen, P. E. Lindelof, 22nd International Conference on the Physics of Semiconductors (Vancouver: World Scientific).

[21] L. Brey, N. Johnson, P. Halperin, Phys. Rev. B 40, 10647 (1989).

[22] E. Skuras, M. C. Holland, C. J. Barton, J. H. Davies, A. R. Long (Accepted Semicond. Sci. Technol. 1995).

[23] M. Büttiker, Phys. Rev. B 38, 9375 (1988).

[24] K. F. Berggren, G. Roos, H. van Houten, Phys. Rev. B 37, 10118 (1988).

[25] B. J. van Wees, L. P. Kouwenhoven, H. van Houten, C. W. J. Beenakker, J. E. Mooij, C. T. Foxon, J. J. Harris, Phys. Rev. B 38, 3625 (1988).

Chapter 6

Scattering in an Unconfined and Confined 2DEG

6.1 Introduction

In this chapter, the strength of the random impurity potential that is experienced by electrons in the 2DEG is investigated. This potential should strongly influence the expected mobility in a bulk 2DEG and also strongly influence the length scale over which quantised conductance should persists in a constricted 2DEG. The structure investigated is a shallow (A686) GaAs-$Al_{0.3}Ga_{0.7}As$ heterostructure in which the 2DEG is formed 11nm away from a δ-doped layer of $4\times10^{16}m^{-2}$ silicon donors. The length scale over which the quantisation degrades is investigated experimentally and comparisons are made with calculations using the actual device geometry. The agreement between the data and the calculations is interpreted in the context of the average size and spacing between fluctuations in the random impurity potential. The evidence for the magnitude of these fluctuations being lower than that expected from fully ionised, randomly positioned donors is discussed in terms of correlations in the position of occupied donors. The experimental mobility in bulk samples is also compared with calculations. Again the assumption in the calculations of fully ionised, randomly positioned donors is discussed.

6.2 Overview

The various contributions to scattering in a 2DEG, formed at the interface of a GaAs-Al$_x$Ga$_{1-x}$As heterostructure, from the deformation potential, acoustic and piezoelectric phonons together with alloy-disorder scattering and ionised impurity scattering, have been calculated [1, 2]. It is now known that for mobilities below 1000m^{2}V^{-1}s^{-1} and at temperatures less than approximately 5K, the most important scattering mechanism is due to elastic scattering from the ionised impurities [3, 4]. In order to reduce the magnitude of this scattering, high quality structures (where the residual scattering due to background impurities is low) and thick spacer layers of undoped Al$_{0.3}$Ga$_{0.7}$As (to separate the 2DEG from the donors) are used [5, 6]. However, in order to deplete these structures at reasonable voltages, spacer layers cannot be too thick and most typical device layers have limiting mobilities in the region of 100m^{2}V^{-1}s^{-1}. The magnitude of these mobilities reflects a smooth random impurity potential, consistent with mean free paths in the 2DEG of several microns. With this in mind, it seemed inexplicable that in the early experiments, the quantisation of the conductance in surface gated wires deteriorated on a length scale which was an order of magnitude lower than this value [7].

In order to understand the difference between restricted and unrestricted 2DEG's, it is necessary to understand how the potential from the large numbers of randomly positioned donors appears to the electrons in the 2DEG. Basically because the spatial separation of the electrons and the impurities is very much greater than the mean spacing of the donors, the core potential due to individual donors is masked by the combined effect from the tails due to many donors. This gives rise to a potential which varies, or is correlated on a length scale (~200nm) very much greater than the average spacing of the donors. The importance of this correlation length is that it is several times the size of the Fermi wavelength of the electrons in the 2DEG (~40nm) and so provides an inefficient scattering

mechanism. When a constriction is formed, the conduction band bottom rises to a height E_c above the conduction band bottom in the bulk 2DEG [8]. This saddle like potential barrier causes a reduction in the kinetic energy of the electrons, increasing their Fermi wavelength and making them more susceptible to scattering by the slowly varying random impurity potential. In addition, this potential barrier causes a reduction in the local carrier concentration, which continues to reduce as the constriction narrows. As the carrier concentration reduces, there is a reduction in the screening of the random impurity potential [9]. This causes the correlation length of the potential to reduce until the fluctuations in the potential cause the 2DEG to become highly inhomogeneous and eventually break up into isolated puddles of charge [10].

Nixon et al. [11] have analysed the effect of these fluctuation on the conduction through 200nm and 600nm long quantum wires using the parameters provided by Timp et al. [7]. Conduction through each wire was analysed for various different random configurations of impurities. They found that fluctuations in the random impurity potential generally caused the destruction of quantisation in wires 600nm long. In 200nm long wires, the quantisation of the conductance was generally well resolved. However even in these short wires, the effect of the fluctuations could be observed for particular random configurations of donors. This latter point will be investigated experimentally in Section 6.4, where it will be shown that sampling different regions of the 2DEG (i.e. a different random impurity configuration) can substantially effect the quality of the quantisation.

Nixon et al. estimated a correlation length of approximately 200nm from the calculated potential fluctuations. This length scale is consistent with good quantised conductance in the short wire and severe fluctuations in the longer wire degrading the quantisation. However although the general trends in the experiments can be understood using the calculations, they do tend to over-estimate slightly the size of the fluctuations. The important assumption in Nixon's work is the inclusion of all the donors as a fully ionised, random distribution of

charge. This assumption also has important consequences for calculation of scattering times and mobilities. Using Fermi's Golden Rule, the assumption of N_d fully ionised and randomly distributed donors gives the lowest order scattering rate τ as

$$\frac{1}{\tau} \propto N_d \sum_q \left| v(\underline{q}) \right|^2 \delta \left(\varepsilon\,(\underline{k}_F + \underline{q}) - \varepsilon\,(\underline{k}_F) \right) \tag{6.1}$$

where $v(\underline{q})$ is the Fourier transform of the appropriately screened potential $v(\underline{r})$ due to a donor with position vector $\underline{r}$ [12, 13]. This shows clearly that if the potential is over-estimated, then the scattering rate and hence the mobility in the 2DEG will be under-estimated. It is therefore no surprise that under the same assumptions, mobility calculations are generally lower than those obtained experimentally [1, 12, 14].

Lassnig has extensively investigated these mobility calculations and finds that it is indeed the treatment of the donors which is at fault [15]. The problem is that the independent impurity approximation is not valid at long wavelengths because it neglects important contributions from the interference between neighbouring impurity potentials [16]. Lassnig finds that introducing a potential correlation function to approximate more accurately the real potential, can lead to substantial increases in the calculated mobility of the electrons in a 2DEG. For instance, a GaAs-Al$_{0.4}$Ga$_{0.6}$As heterostructure with a doping density of 3×10^{17}cm^{-3} silicon impurities and a 2DEG carrier concentration of 5×10^{11}cm^{-2}, has a calculated mobility of 5.5cm^{2}V^{-1}s^{-1} and 9.2cm^{2}V^{-1}s^{-1} for uncorrelated and correlated potentials respectively. Éfros et al. have shown that correlations can arise physically if not all of the impurities are ionised [17]. This is because the electrons can redistribute themselves amongst the impurities in order to minimise the energy of the system and this results in a more uniform charge distribution and hence a smoother potential. The authors go on to calculate the effect on the

mobility when the correlations in the position of occupied donors are frozen in at a temperature of 100K and when electrons can still redistribute themselves at helium temperatures. The significance of these calculations to the measurements discussed in this chapter will be discussed in Section 6.5.4.

6.3 Experimental Scattering in Quantum Wires

The experiments of Timp et al. which were modelled by Nixon et al. were carried out on a GaAs-Al$_{0.3}$Ga$_{0.7}$As heterostructure in which the 2DEG is formed 42nm away from a δ-doped layer of 4×10^{16}m^{-2} silicon donors. In the experiments described in this chapter, the separation of the donors from the 2DEG is only 11nm which means that the random impurity potential will be much stronger. Therefore when forming a constriction in these shallower structures, it would be reasonable to expect the length scale over which the quantisation of the conductance persists to be shorter. Figures 6.1-4 show the results obtained for 100nm, 200nm, 400nm and 500nm long quantum wires in this shallow heterostructure. These measurements refer to Experiments 14, 8, 17 and 28 respectively, see Chapter 5, Section 5.5. The 100nm wire in Figure 6.1 shows three well resolved and three or four more poorly resolved steps. For the longer, 200nm wire in Figure 6.2, the steps are still very clear, however now the differential conductance peaks are much lower. This observation can immediately be explained in terms of the correlation length of the random impurity potential being shorter than 200nm. In this case, fluctuations occur along the length of the wire which will tend to smear out the singularity associated with the bottom of each sub-band. For the 400nm and 500nm wires in Figure's 6.3 and 6.4 there is no longer any quantisation of the conductance and the resonance structure on the curves is associated with strong scattering from fluctuations [18].

Figure 6.1: The quantised conductance and its differential for a 100nm quantum wire in a shallow (A686) GaAs-$Al_{0.3}Ga_{0.7}As$ heterostructure at 1.2K.
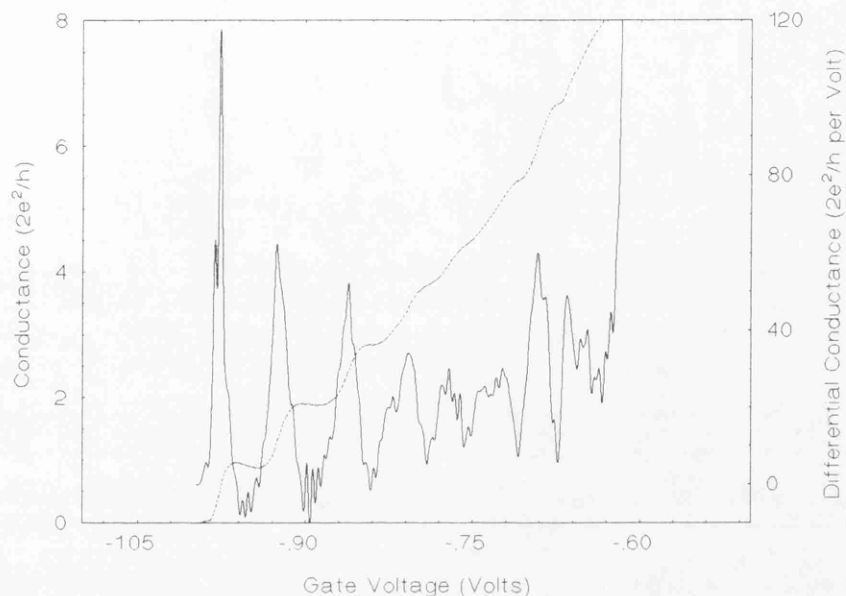
Figure 6.2: The quantised conductance and its differential for a 200nm quantum wire in a shallow (A686) GaAs-$Al_{0.3}Ga_{0.7}As$ heterostructure at 1.2K.
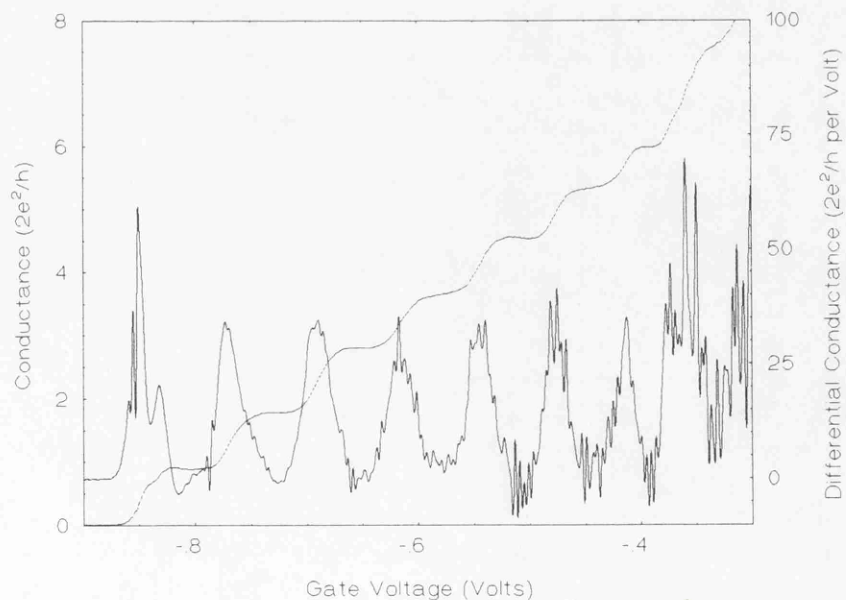
Figure 6.3: The quantised conductance for a 400nm quantum wire in a shallow (A686) GaAs-$Al_{0.3}Ga_{0.7}As$ heterostructure at 1.2K.
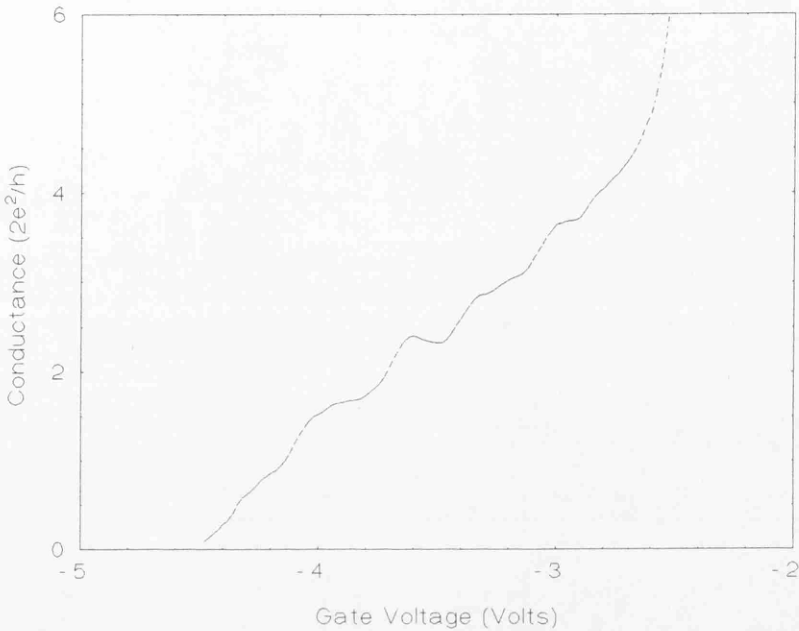
Figure 6.4: The quantised conductance for a 500nm quantum wire in a shallow (A686) GaAs-$Al_{0.3}Ga_{0.7}As$ heterostructure at 1.2K.
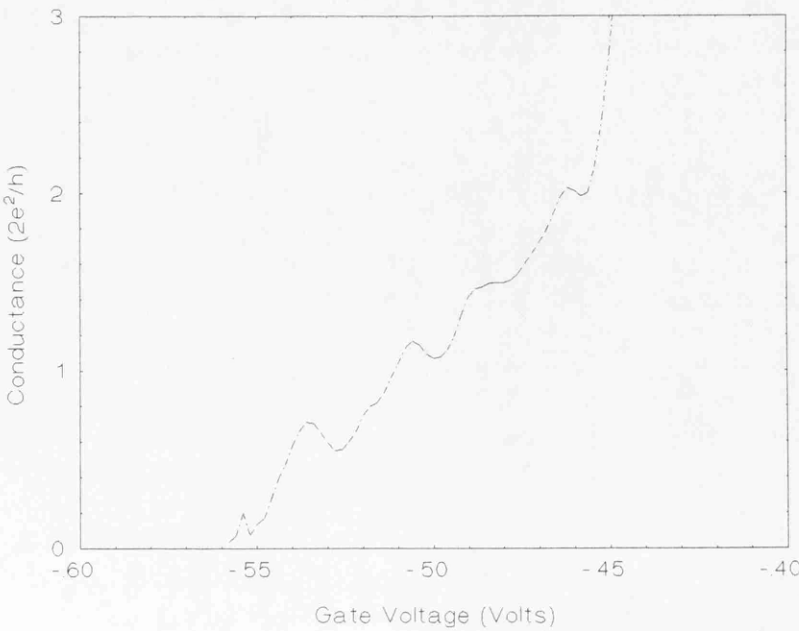
The effect of fluctuations in a wire is best explained by picturing the wire as a multi-mode transmission line [18-20], see Chapter 1, Section 1.3.2. In this case, the quantisation is robust to inter-mode scattering from fluctuations involving small changes in the k-space vector, because these events do not alter the current through the device. The idea is that all forward modes are occupied until they reach cut-off. Electrons that scatter from mode i into a higher mode j can be exactly compensated for by scattering from mode j to mode i. It is in fact only backscattering into partially occupied backward flowing modes which alters the current and degrades the quantisation. An important signature of backscattering events is the observation of resonant peaks and dips in the conductance [21, 22]. These resonant states are due to new modes opening and cutting off as the effective channel width varies because of the fluctuations. Where the channel widens, new modes open up and electrons undergo forward scattering into these modes. When the channel narrows again, the modes cut-off and electrons are backscattered, thus lowering the conductance. If the electron enters the mode which propagates in the wider region through a tunnelling process then subsequent forward scattering can result in a resonance that will tend to increase the conductance of the wire.

For longer wires, more of these fluctuations occur in the constriction until its width and hence its conductance is no longer determined simply by the gate guiding potential. The more complex effects due to fluctuations in the random impurity potential need to be taken into account and in general these fluctuations will destroy the quantisation. The effects of scattering processes due to fluctuations in the impurity potential have been extensively studied by Laughton et al. [23]. The authors calculate that the majority of scattering is forward, due to the slowly varying random potential and that resonances can be simulated by scattering and tunnelling into evanescent modes.

6.4 Quantum Wires as a Probe of the Local Potential Landscape

In the measurements discussed in the previous section, the voltage supplied to each of the gates which form the wire are equal and the potential well is thus formed equi-distant distance from each of the electrodes. However, it has been shown that by applying a different voltage to each half of the split gate, it is possible to shift the potential well laterally to either side of this central position and so change the region of the 2DEG through which the electrons move [24]. Using this method, it should be possible to investigate the spatial extent of the random nature of the potential by mapping out the effect of potential fluctuations on the conductance quantisation in the 2DEG.

This was indeed carried out for various wires in the shallow (A686) GaAs-$Al_{0.3}Ga_{0.7}As$ heterostructure and in particular, data for three of these wires (100, 200 and 400nm) is presented in Figure's 6.5-7. The curves presented in these figures refer to Experiments 14, 8 and 17 respectively, see Chapter 5, Section 5.5. The data shows the conductance of the wires in units of $2e^2/h$ measured at 1.2K. The surface plots consist of twenty or so different sets of data which are plotted as a function of both the average of and the difference between the voltages applied to each of the two electrodes which form the wire. The difference between the two gate voltages is a measure of the lateral position of the conducting channel whereas the mean gate voltage is a measure of the depletion. For each of the plots, the average gate voltage at which a particular conductance plateaux occurs varies as the differential gate voltage scans between ±500mV. The details and magnitudes of these variations are sample dependent and also strongly vary when each device is cycled through room temperature before being re-measured at 1.2K. This latter point can be explained by the effects of different donor configurations giving rise to a different random impurity potential, in addition to
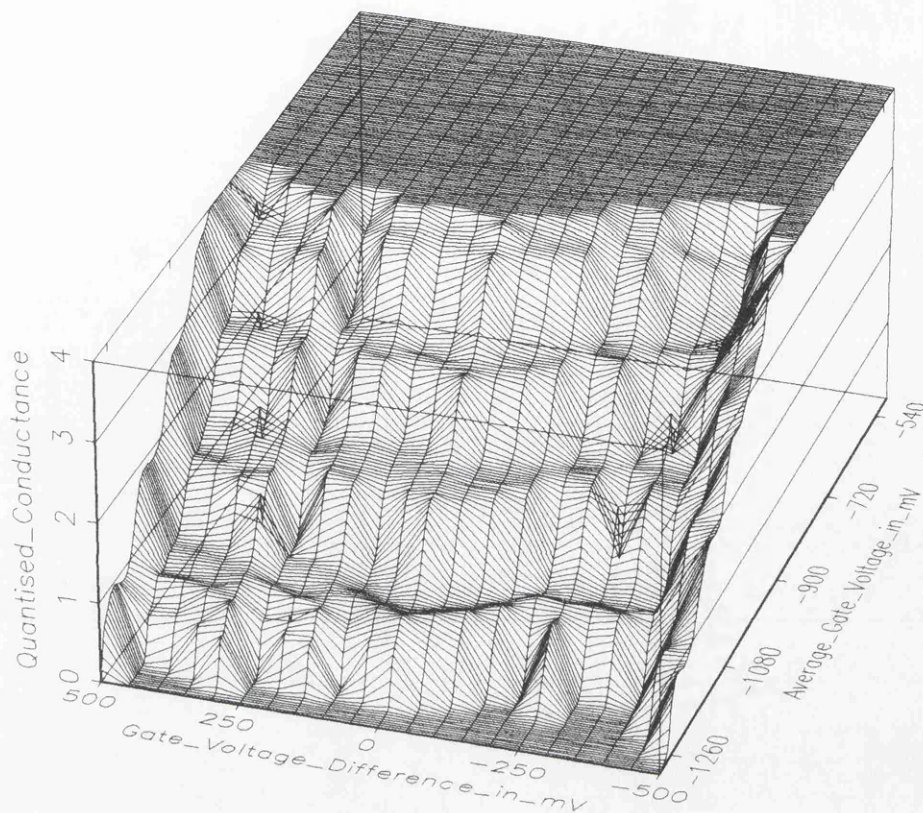
Figure 6.5: The quantised conductance in units of $2e^2/h$ is presented for a 100nm long wire (Experiment 14) measured at 1.2K. This surface plot is a function of both the average and the difference between the voltages applied to each of the two electrodes which form the wire.
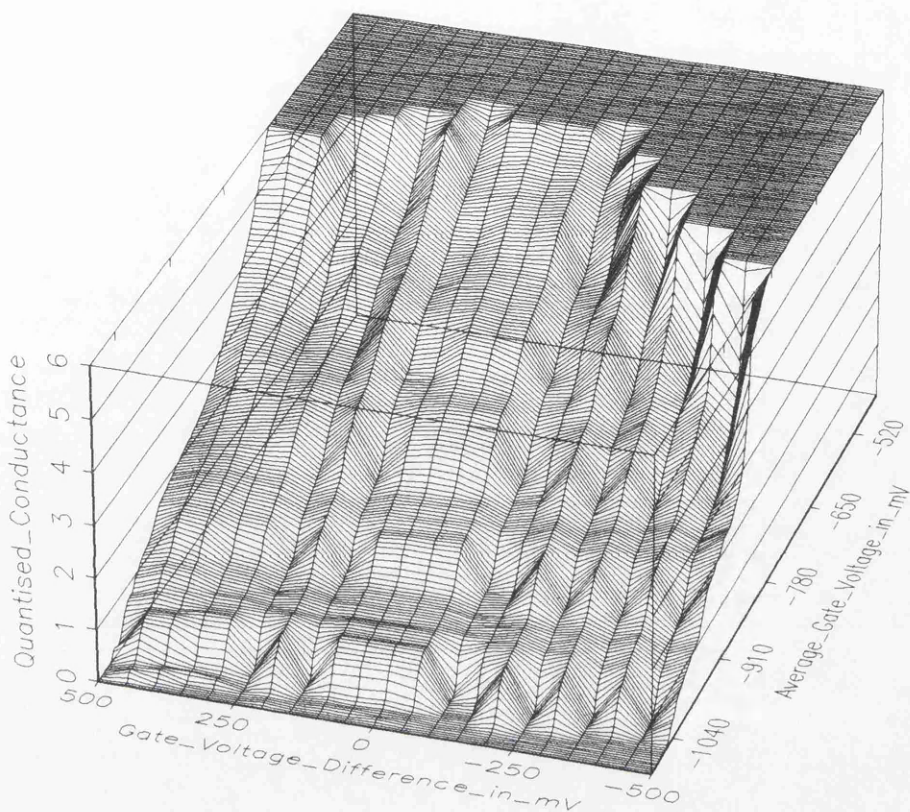
Figure 6.6: The quantised conductance in units of $2e^2/h$ is presented for a 200nm long wire (Experiment 8) measured at 1.2K. This surface plot is a function of both the average and the difference between the two voltages applied to each of the two electrodes which form the wire.
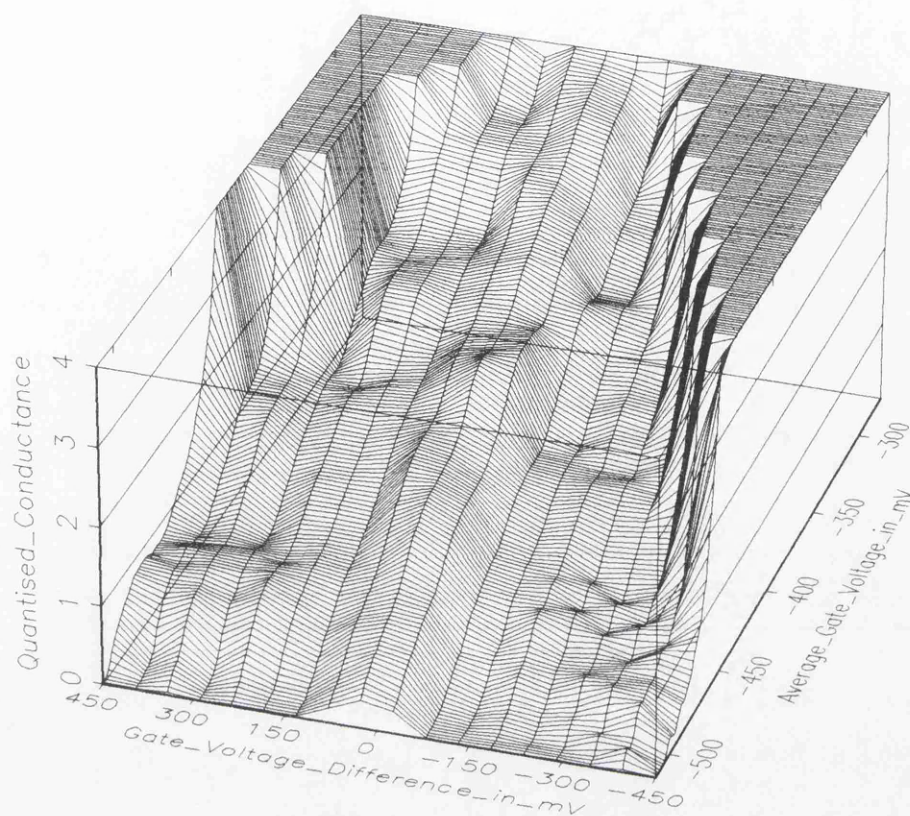
Figure 6.7: The quantised conductance in units of $2e^2/h$ is presented for a 400nm long wire (Experiment 17) measured at 1.2K. This surface plot is a function of both the average and the difference between the voltages applied to each of the two electrodes which form the wire.

possible small contributions from irregularities in the topography of the gates. It is apparent from inspection of Figure 6.7, that the size of these variations are very much greater in 400nm wire. In addition the surface plots for the 100nm and 200nm wires show that despite the seemingly complicated behaviour of the traces, the quantisation remains robust to scattering over the entire range of the scan.

This is in sharp contrast to the plot of the 400nm wire. In this case, only resonances are observed when the voltages on the two gates are equal, but a strong first plateau develops in the differential voltage range: 200→400mV. The deformation of the confinement potential as the well narrows due to squeezing up against one of the electrodes is also very clear. The energy levels rise with three quantised plateaux at 250mV reducing to two (at 350mV) and then one (at 450mV), see Figure 6.8.

Figure 6.8: Quantisation of the conductance in a 400nm wire formed in a shallow (A686) GaAs-$Al_{0.3}Ga_{0.7}As$ heterostructure (Experiment 17). The measurements were carried out at 1.2K, at various differential biases, the values for which are included in the graph.
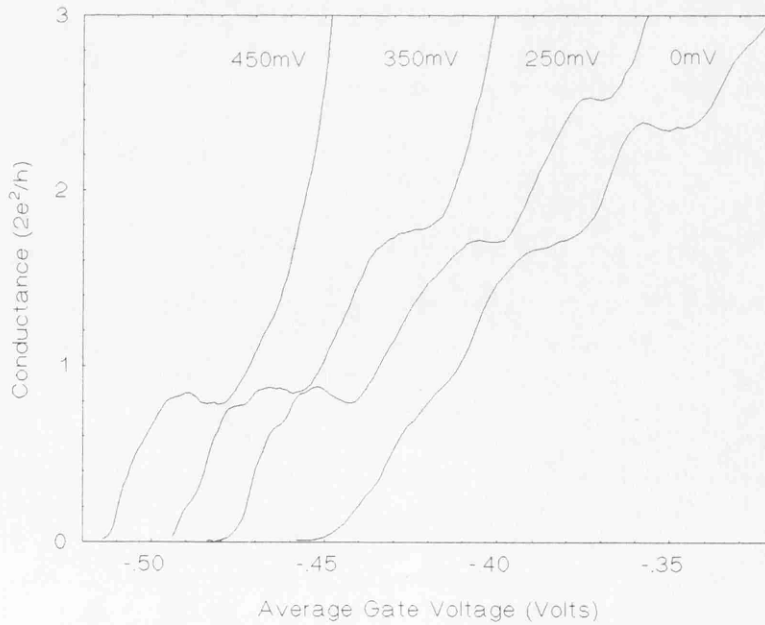
There is some sign of the second and third plateaux when scanning the potential in the other direction, however there are strong resonances superimposed on the traces and these in fact destroy the first plateau. The simplest interpretation of these observations is that the shorter wires sweep through a length which is smaller than the average spacing of the fluctuations in the random impurity potential. This is in fact in good agreement with the measurements presented in the previous section. For the longer wires, the length involved is comparable with the spacing of the fluctuations and this strongly degrades the quantisation. The measurements at different voltage differentials is effectively moving the conducting channel around the fluctuations and in doing so, maps out the local scattering topography. In this picture, Figure 6.7 is mapping the effects of stronger and weaker fluctuations in the centre and right hand regions of the wire.

6.5 Potential Fluctuations and Mobility Calculations

The following section describes models for transport in quantum wires and bulk 2DEG mobilities developed by Davies et al. [25]. The wire model calculates the conductance through quantum wires, taking into account the effect of fluctuations in the random impurity potential. The mobility model calculates the expected mobility in a bulk 2DEG assuming good screening of the random impurity potential. These calculations will be compared with the measured properties of the 200nm wire discussed in Section 6.3 and the bulk mobility of the 2DEG in which the wire was formed.

6.5.1 The Wire Model

The structure modelled is a GaAs-$Al_{0.3}Ga_{0.7}As$ heterostructure with $4\times10^{15}m^{-2}$ donors assumed to be fully ionised and randomly distributed in a δ-layer

separated from the 2DEG by 11nm of undoped $Al_{0.3}Ga_{0.7}As$. The Fermi energy is treated as pinned by surface states in the middle of the GaAs band gap, thus defining an equi-potential surface and allowing the superposition of the gate and donor potentials into a single 'bare' potential. The simple Thomas-Fermi approximation is used to determine the electron density $n(\underline{r})$ at a position $\underline{r}$ in the wire, see Equation 6.2 where the arguments of the Heaviside function $\Theta(E_F-E_c(\underline{r}))$ are the Fermi energy E_F and the conduction band energy $E_c(\underline{r})$.

$$n(r) = \frac{m^*}{\pi\hbar^2}\left(E_F - E_c(\underline{r})\right)\Theta\left(E_F - E_c(\underline{r})\right) \qquad (6.2)$$

This approximation gives the electron density at point $\underline{r}$ and depends only on the potential at that point. It therefore requires the Fermi wavelength of the electrons to be much smaller that the fluctuation length scale to be useful. It should work reasonably well at high electron densities but may well be inaccurate just before depletion. Poisson's equation is solved with this electron density in order to calculate the contribution of the electrons to the bare potential. These two potentials are then substituted into Schrödinger's equation, which is solved for the eigenvalues $\theta_{n,x}(y, x)$ at n values along the length x of the wire. This effectively maps out the variations in the potential in x due to the random positioning of the donors. These eigenvalues are then used to determine a new estimate for the electron density in the wire at the n different points for which eigenvalues were calculated. Once again these electron densities can be used with Poisson's equation and indeed the entire procedure is repeated until a self consistent potential is obtained. Finally, in order to determine the range of potentials through which the electrons move, the above calculations need to be carried out for each gate voltage. In order to model the transport through the constriction, the propagation between each of these n sites is calculated using the recursive Green's function technique. This information is then used to construct a transmission matrix from which the conductance can be determined.

Figure 6. 9:The simulation of the quantisation of the conductance in a 200nm long quantum wire in the shallow (A686) GaAs-$Al_{0.3}Ga_{0.7}As$ heterostructure is presented. Quantisation with no random impurity scattering (Clean), and for 4×10^{15} (Full Density) and 1×10^{15} (Reduced Density) randomly positioned donors is illustrated.
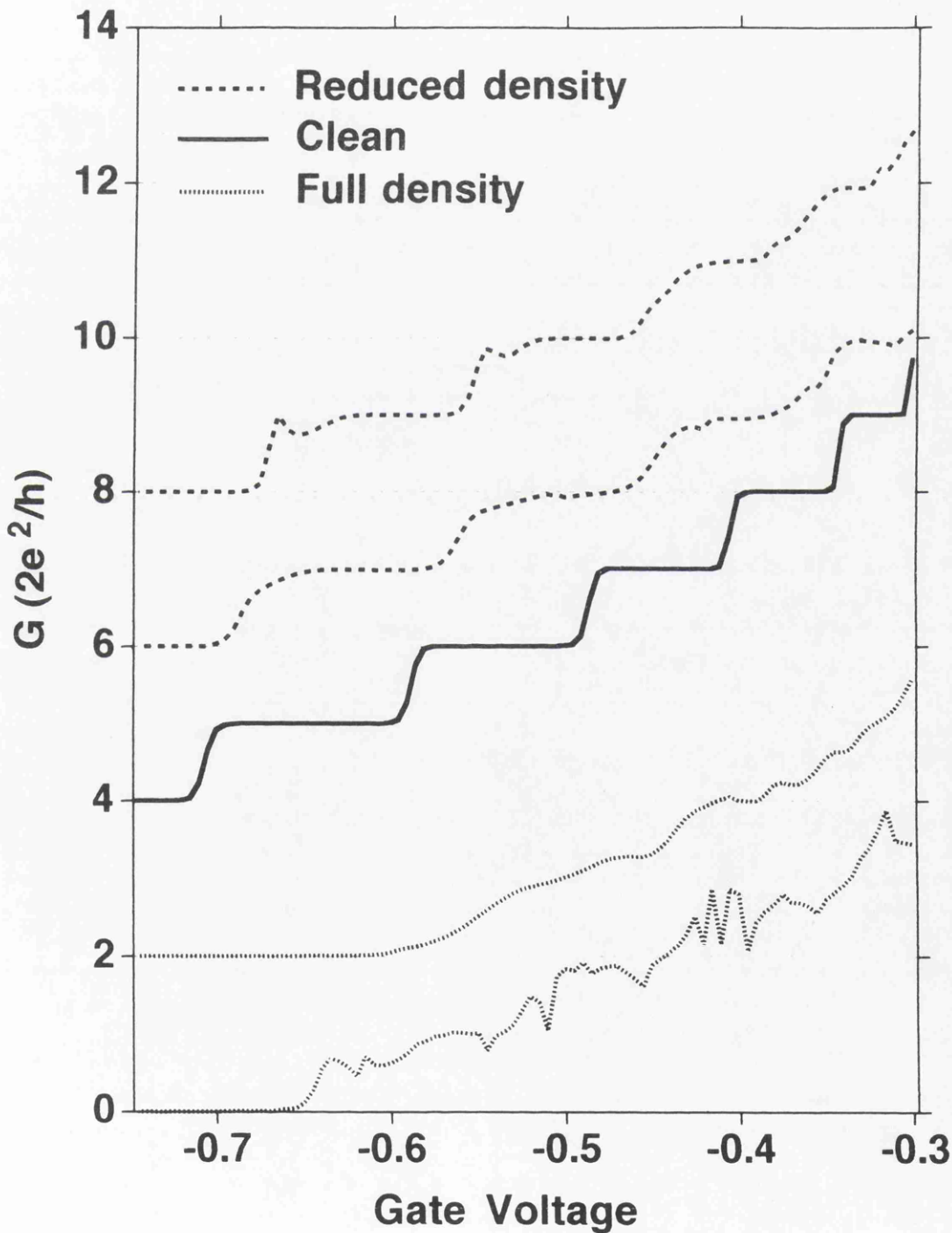
6.5.2 Comparing Wire Calculations with Experiments

Figure 6.9 details various results for the calculation of the conductance of a 200nm wire on the shallow (A686) GaAs-Al$_{0.3}$Ga$_{0.7}$As heterostructure. The calculation labelled 'Clean' is for the wire with no random impurity scattering and shows the expected quantisation of the conductance in units of $2e^2/h$. The traces labelled 'Full density' are the calculation including the effect of fluctuations in the random impurity potential. Clearly the magnitude of the fluctuations are greatly over-estimated by the model because no trace is left of the quantisation which strongly contradicts the experimental result presented in Figure 6.2. In order to gain some idea of the amount by which the fluctuations are over-estimated, the calculations are repeated but this time including only 25% of the donors as randomly distributed and treating the other 75% as a smooth background potential. These calculations are represented by the curves labelled 'Reduced density' and are clearly similar to the experimental result. As with the 'Full density' calculations, there are two traces, each of which corresponds to a different random distribution of donors. Comparing the traces shows that the detailed structure is very sensitive to the particular random impurity potential. The differences between the two 'Reduced density' calculations are found to be similar to the variations between quantised conductance measured in different regions of the 2DEG, or the same region after thermally cycling the sample through 100K or so.

In addition to the conductance of the wire, the effect of the potential fluctuations on the effective Fermi energy (i.e. after subtracting the energy of the saddle point potential) of the electrons in a constriction biased at -0.4V was also calculated. These results are presented in Figures 6.10-12 as grey scale plots, where the range is from 0 to 25meV as the scale varies from white to black. The variation in the electron energy effectively maps out the relative magnitude and

Figure 6.10: Calculation of Fermi energy of electrons in a 200nm long quantum wire (Experiment 8) in the shallow (A686) GaAs-Al$_{0.3}$Ga$_{0.7}$As heterostructure. The wire is biased at -0.4V and the potential landscape is treated as smoothly varying.
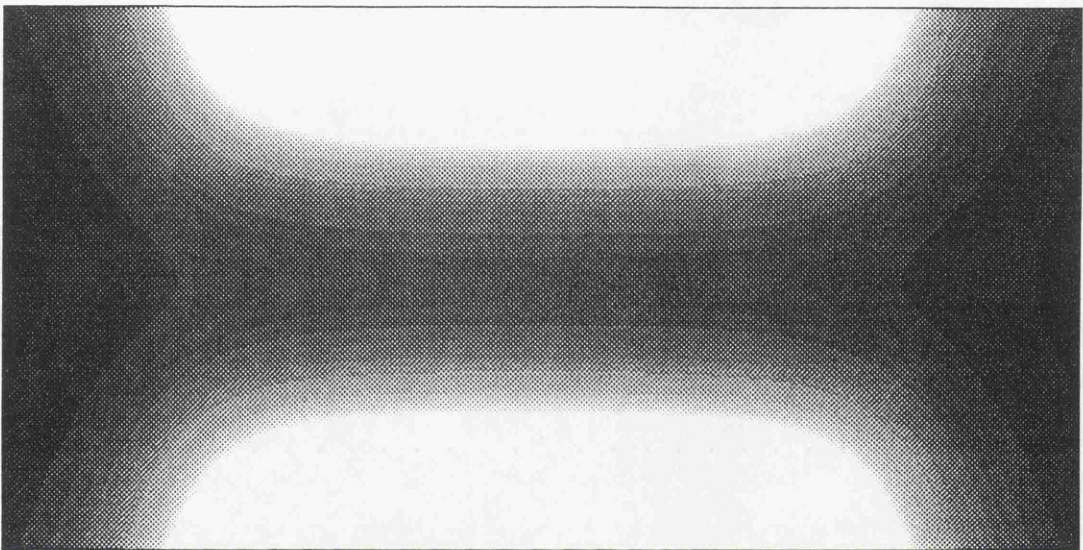
Clean
A686, 200 × 80 nm gate
320 × 160 nm
Energy from 0 to 25 meV

Figure 6.11: Calculation of the effect of potential fluctuations on the Fermi energy of electrons in a 200nm long quantum wire (Experiment 8) in the shallow (A686) GaAs-Al$_{0.3}$Ga$_{0.7}$As heterostructure. The calculation includes the effect of the random positioning of 4×10^{16} silicon donors.
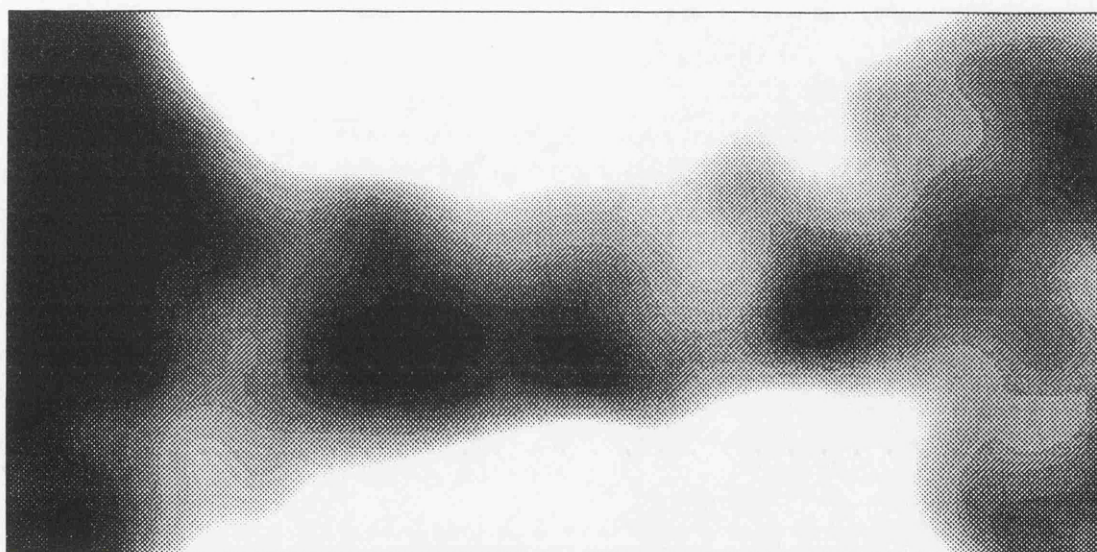
Filthy 2
A686, 200 × 80 nm gate
320 × 160 nm region plotted
Energy from 0 (white) to 25 meV (black)

Figure 6.12: Calculation of the effect of potential fluctuations on the Fermi energy of electrons in a 200nm long quantum wire (Experiment 8) in the shallow (A686) GaAs-Al$_{0.3}$Ga$_{0.7}$As heterostructure. The calculation includes the effect of 1×10^{16} randomly positioned silicon donors, with the remaining 3×10^{16} treated as a smooth background potential.
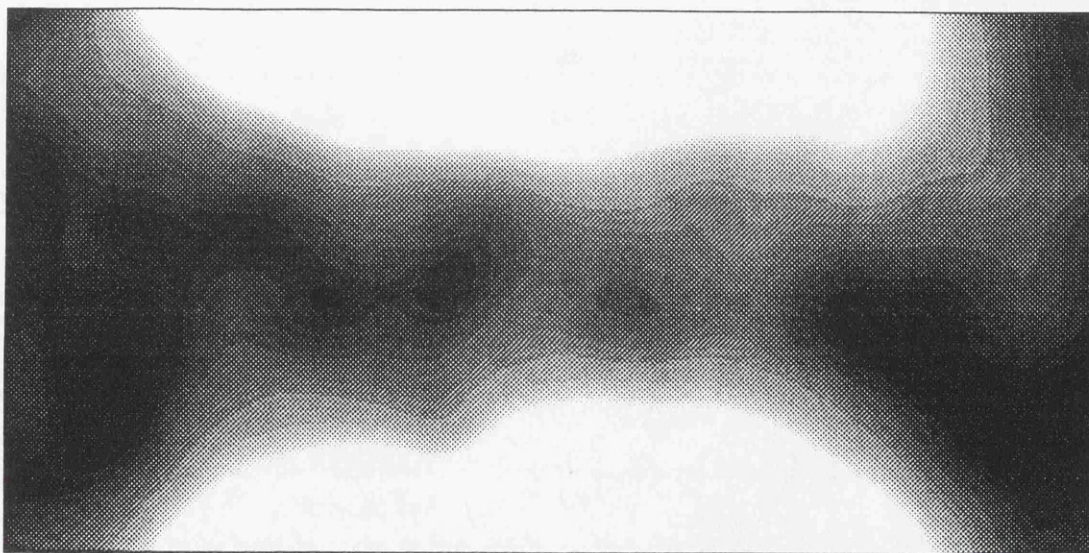
Quarter 3
A686, 200 × 80 nm gate
320 × 160 nm region plotted
Energy from 0 (white) to 25 meV (black)

position of the fluctuations and allows a direct physical insight into the degradation of the conductance quantisation. Figure 6.10 gives a clear demonstration of how an ideal quantum wire forms, with the effect of the saddle point potential on the distribution of the electrons clearly visible. The calculations for the 'Full density' of randomly distributed ionised donors are shown in Figure 6.11. The constriction is highly in-homogeneous, with puddles of electrons and regions almost depleted of carriers. The estimated magnitude of the fluctuations is approximately 4.5meV which is comparable to the experimental sub-band spacing at this voltage (see Chapter 5, Section 5.5.2). Fluctuation of this magnitude would cause strong backscattering of electrons which would destroy the quantisation. The 'Reduced density' calculations in Figure 6.12 give much smaller fluctuations of approximately 2.5meV and in this case forward scattering will be dominate and the quantisation will be robust, in good agreement with the experimental result (see Figure 6.2).

6.5.3 Comparing Experimental and Calculated Mobility

Assuming successive scattering events are independent, then Fermi's Golden Rule can be used to determine the mean free path l and hence the mobility μ in the 2DEG, see Equation 6.3.

$$\frac{1}{\mu} = \frac{\hbar k_F}{el} = \frac{2\pi m^*}{e\hbar} N_\delta \sum_q \left| v(\underline{q}) \right|^2 \delta\left(\varepsilon\left(\underline{k}_F + \underline{q}\right) - \varepsilon\left(\underline{k}_F\right) \right) \tag{6.3}$$

where $v(\underline{q})$ is the Fourier transform of the Thomas-Fermi screened potential $v(\underline{r})$, N_δ is the density of the donors and $\delta(\ )$ is the Dirac delta function [12, 13]. Using Fang-Howard wavefunctions for the electrons in the 2DEG, the calculated mobility for $4\times10^{16}\mathrm{m}^{-2}$ fully ionised randomly distributed donors is $6\mathrm{m}^2\mathrm{V}^{-1}\mathrm{s}^{-1}$. The agreement with the experimental values of $20\text{-}23\mathrm{m}^2\mathrm{V}^{-1}\mathrm{s}^{-1}$ obtained on various

shallow (A686) heterostructures is very poor. Calculating the mobility for only 25% random donors and treating the remaining 75% as a smooth background potential gives an enhanced estimate for the mobility of $24m^2V^{-1}s^{-1}$ which is in much better agreement with the measured values.

6.5.4 Discussion

The comparison between the calculations and the experiments show a clear over estimation of the effect of scattering by the random impurity potential both in the bulk 2DEG and in a 200nm wire. The only way to reconcile the calculations and the experiments is to smooth the potential in some manner; however the physical process which could cause this to occur is unclear.

In the initial calculations of the characteristics of the bulk 2DEG and devices, it was assumed that all the donors were ionised and randomly positioned. It is difficult to see that there could be much wrong with the assumption of $\sim 4\times 10^{16}m^{-2}$ ionised donors because electrostatically, this charge is required in order to obtain the observed carrier concentration ($5.8\times 10^{15}m^{-2}$) in the 2DEG, see Equation 5.1 in Chapter 5, Section 5.1 [26]. With this in mind, the reduced scattering surely indicates that the impurity potential is not truly random and is correlated to some degree. Invoking correlations in order to more accurately model experimental mobility calculations has been established in work carried out on deeper slab doped heterostructures [17, 27]. Éfros et al. have in fact calculated the contribution to the mobility by allowing correlations in the position of occupied donors to minimise the energy of the system [17]. In particular, for a 10nm spacer GaAs-Al$_{0.3}$Ga$_{0.7}$As heterostructure, the differencein the mobility is a factor of three, changing from $\sim 5m^2V^{-1}s^{-1}$ to $\sim 15m^2V^{-1}s^{-1}$. The difficulty in applying this picture to the 10nm spacer structure described in this chapter, is that Éfros' calculations were for slab doped samples where the proportion of occupied donors in the region close to the spacer is large. It was mentioned above that this

is not the case for the heterostructure discussed here, where a δ-layer of donors is deposited [28, 29]. In this case, the possible smoothing of the random impurity potential from only a small number of occupied donors must be considered. Some work has in fact been carried out in this area by Buks et al. where good agreement is found between the experimental mobility and an effectively 'correlated' calculation [30].

6.6 Conclusion

The quantisation of the conductance in a shallow GaAs-Al$_{0.3}$Ga$_{0.7}$As heterostructure has been found to be robust to scattering in wires up to 200nm in length. Wires in excess of this length are found to be strongly affected by resonant back-scattering. However the quantisation can be recovered at 400nm if the potential well is laterally shifted away from any scattering centres. The characteristics of these devices were found to agree with models if and only if the magnitude of the fluctuations in the random impurity potential were reduced from 4.5meV to 2.5meV. This same factor was also required to explain the difference between the calculated and measured mobility. A qualitative explanation of the reduced scattering was put forward in terms of low temperature correlations in the position of occupied donors and this picture is supported by similar mobility research carried out by Buks et al. [30].

In Appendix C, an expression is derived using Fermi's Golden Rule for the transport mean free path l of electrons in a 2DEG due to the screened potential from the random positioning of N_d ionised donors in a δ-layer, see Equation 6.4 where $\hbar q$ represents the momentum transferred during the scattering process [31].

$$\frac{1}{l} = \frac{1}{v_F} \frac{1}{\tau_{total}} = \frac{1}{v_F} \frac{1}{2\pi\hbar} \int_0^{2k_F} \frac{\left(q^2 / 2k_F^2\right)}{\sqrt{1-\left(q / 2k_F\right)^2}} N_d \left|\tilde{v}(\underline{q})\right|^2 dq \qquad (6.4)$$

In Equation 6.4, $N_d \left|\tilde{v}(\underline{q})\right|^2$ are the Fourier components of the potential due to all the donors. Defining $C(q)$ as the power spectrum of the Fourier components of the scattering potential, see Equation 6.5.

$$C(q) = N_d \left|\tilde{v}(\underline{q})\right|^2 = N_d \left(\frac{e^2}{4\pi\kappa\epsilon_0}\right)^2 \left|\frac{2\pi}{q+q_{TF}}\left[e^{-sq} - e^{-(s+2c)q}\right]\right|^2 \qquad (6.5)$$

and substituting this into Equation 6.4 gives

$$\frac{1}{l} = \frac{1}{v_F} \frac{1}{2\pi\hbar} \int_0^{2k_F} \frac{\left(q^2 / 2k_F^2\right)}{\sqrt{1-\left(q / 2k_F\right)^2}} C(q) dq \qquad (6.6)$$

The integral in Equation 6.6 sums over the competing effects due to the q^2 term and the dominant exponentially decaying term in the power spectrum, e^{-2sq}. The integral over the product of these two terms effectively weights the different contribution which each q scattering event makes to the degradation of the transport mean free path. The effect of the fluctuations on the mean free path are dominated by there magnitude $\left|\tilde{v}(\underline{q})\right|^2$ but there is also an important effect due to a spatial correlation. This correlation manifests itself as a length scale over which the potential is fairly uniform. Its effect is most easily seen by looking at the autocorrelation function $c(r)$ of the random potential [32, 33]. This function

expresses the total potential in one part of the 2DEG $V(\underline{r}+\underline{r}')$ in terms of that in another part $V(\underline{r})$ by evaluating the overlap integral i.e.

$$c(r) = \langle V(\underline{r})V(\underline{r}+\underline{r}')\rangle_{r'}$$

(6.7)

Now the Wiener-Khintchine theorem states that the Fourier transform of the autocorrelation of a function $f(x)$ is the squared modulus of the transform of $f(x)$. Hence for Equation 6.7 we have

$$c(r) = \int_{-\infty}^{+\infty} |V(\underline{q})|^2 \frac{e^{i\underline{q}\cdot\underline{r}}}{(2\pi)^2} d^2\underline{q} = \int_{-\infty}^{+\infty} C(q) \frac{e^{i\underline{q}\cdot\underline{r}}}{(2\pi)^2} d^2\underline{q}$$

(6.8)

Evaluating Equation 6.8, assuming that screening is good (i.e. that the approximation $q+q_{TF}\approx q_{TF}$ is valid) gives [34]

$$c(r) \approx 2\pi \frac{N_d}{q_{TF}^2}\left(\frac{e^2}{4\pi\kappa\varepsilon_0}\right)^2$$

$$\times \left\{\frac{2s}{r^2+(2s)^2}^{3/2} + \frac{2(s+2c)}{\left[r^2+(2(s+c))^2\right]^{3/2}} - 2\frac{2(s+c)}{\left[r^2+(2(s+c))^2\right]^{3/2}}\right\}$$

(6.9)

The magnitude of particular fluctuations (Equation 6.9 as $r\rightarrow0$) are seen to decay asymptotically as $1/s^2$. The correlation between these fluctuations reduces to zero on a scale of a few $r\approx2s$ and it is this that sets the length scale in the 2DEG not the spacing of the donors. Clearly the potential varies slowly on the scale of the Fermi wave length of the electrons and this can lead to reduced scattering, allbeit as a weaker effect than a reduction in the magnitude of the fluctuations. In one dimensional structures one therefore has two distinct regimes. When the length of the constriction is less than the correlation length quantisation should be robust to

scattering from fluctuations. But when the correlation length is less than the length of the constriction the the relative size of the magnitude of the fluctuations compared to the sub-band spacing is important.

Finally it is important to keep in mind that both the work presented here [35] and that of Buk's et al [30] are only estimates of the possible importance of electron correlations and a full quantum mechanical calculation of the scattering will be required if this issue is to be properly resolved.

References

[1] W. Walukiewicz, H. E. Ruda, J. Lagowski, H. C. Gatos, Phys. Rev. B 30, 4571 (1984).

[2] S. Das. Sarma, Condense Systems of Low Dimensionality, edited by J. L. Beeby et al., (Plenum Press, New York), (1991).

[3] J. J. Harris, C. T. Foxon, K. W. J. Barnham, D. E. Lacklison, J. Hewett, C. White, J. Appl. Phys. 61, 1219 (1987).

[4] J. J. Harris, C. T. Foxon, D. E. Lacklison, K. W. J. Barnham, Superlattices Microstruct. 2, 889 (1986).

[5] L. Pheiffer, K. W. West, H. L. Störmer, K. W. Baldwin, Bull. Am. Phys. Soc. 34, 549 (1989).

[6] J. J. Harris, C. T. Foxon, D. Hilton, J. Hewett, C. Roberts, S. Auzoux, Surface Sci. 229, 113 (1990).

[7] G. Timp, R. Behringer, S. Sampere, J. E. Cunningham, R. E. Howard, Proceedings of the International Symposium on Nanostructure Physics and Fabrication, College Station, Texas, edited by M. A. Reed and W. P. Kirk (Academic, New York), 331 (1989).

[8] M. Büttiker, Phys. Rev. B41, 7906 (1990).

[9] J. H. Davies, J. A. Nixon, Phys. Rev. B 39, 3423 (1989).

[10] J. A. Nixon, J. H. Davies, Phys. Rev. B 41, 7929 (1990).

[11] J. A. Nixon, J. H. Davies, H. U. Baranger, Phys. Rev. B 43, 12638 (1990).

[12] T. Ando, J. Phys. Soc. Jpn. 51, 3900 (1982).

[13] T. Ando, A. B. Fowler, F. Stern, Rev. Mod. Phys. 54, 437 (1982).

[14] F. Stern, Appl. Phys. Lett. 43, 974 (1983).

[15] R. Lassnig, Solid State Commun., 65, 765 (1988).

[16] E. Conwell, V. F. Weisskopt, Phys. Rev. 77, 388 (1950).

[17] A. L. Éfros, F. G. Pikus, G. G. Samsonidze, Phys. Rev. B 41, 8295 (1990).

[18] M. Büttiker, Y. Imry, R. Landauer, S. Pinhas, Phys. Rev. B 31, 6207 (1985).

[19] M. Büttiker, Phys. Rev. Lett. 57, 1761 (1986).

[20] M. Büttiker, IBM J. Res. Dev. 32, 317 (1988).

[21] C. S. Chu, R. S. Sorbello, Phys. Rev. B 40, 5941 (1989).

[22] P. Bagwell, Phys. Rev. B, 10354 (1990).

[23] M. J. Laughton, J. R. Barker, J. A. Nixon, J. H. Davies, Phys. Rev. B 44, 1150 (1991).

[24] J. G. Williamson, C. E. Timmering, C. J. P. M. Harmens, J. J. Harris, C. T. Foxon, Phys. Rev. B42, 7675 (1990).

[25] J. H. Davies, I. A. Larkin, E. V. Sukhorukov (Accepted J. Appl. Phys 1995).

[26] A. R. Long, J. H. Davies, M. Kinsler, S. Vallis, M. C. Holland, Semicond. Sci. Technol. 8, 1581 (1993).

[27] F. G. Pikus, A. L. Éfros, Sov. Phys. JETP 69 (3), 558 (1989).

[28] E. F. Schubert, J. Vac. Sci Technol. A8, 2980 (1990).

[29] K. Kohler, P. Ganser, M. Maier, J. Crystal Growth 127, 720 (1993).

[30] E. Buks, M. Heiblum, Y. Levinson, Hadas Shtrikman,

[31] A. Das, A. C. Melissinos, Quantum Mechanics: A Modern Introduction, (Gordon and Breach Science Publishers), 1986.

[32] E. G. Steward, Fourier Optics: An Introduction, Ellis Horwood), 1987.

[33] J. H. Davies, Lecture Notes, Unpublished.

[34] J. H. Davies, G. Timp, Heterostructures and Quantum Devices, (Academic Press), 385 (1994).

[35] C. Barton, J. H. Davies, E. Skuras, M. C. Holland, A. R. Long, 22nd International Conference on the Physics of Semiconductors (Vancouver: World Scientific), 1994.

Chapter 7

The aims of the project were to develop high temperature quantisation of the conductance in surface split gated constrictions. This has been successfully demonstrated with fully resolved sub-band structure above 4.2K apparent in a GaAs-Al$_{0.3}$Ga$_{0.7}$As heterostructure δ-doped with 4×10^{16} silicon atoms 11nm away from the 2DEG plane. The experimental reduction in spacing of sub-bands as the depth of the 2DEG increases has also been found to be in good agreement with calculations. In all the measurements on various heterostructures no systematic difference has been found between the point at which the sub-band structure smears with temperature and the point at which it smears with increasing source-drain bias V_{sd} so long as an equivalent electron temperature is defined such that $eV_{sd} \equiv 4k_B T$.

The possibility of increasing the temperature performance of devices still further does not seem very promising. Two possible paths are increasing the Fermi energy or decreasing the depth of the 2DEG. However reducing the distance between the surface and the 2DEG would substantially increase the tunneling current through the surface barrier. Any decrease in the spacer thickness is also problematic due to the large increases in the random impurity scattering which would drastically reduce the ballistic mean free path. Similarly, increasing the Fermi energy requires a decrease in the spacer thickness. In any case the bulk carrier concentration is already close to that necessary for the occupation of a second sub-band which would greatly increase the scattering. These problems can

be side stepped by moving to material structures with smaller band gaps materials where the effective mass of the electron is lower.

One problem that has become apparent in the course of the project is that the both the mobility and the length scale over which the quantisation is robust to scattering are poorly understood. The problem is that simply treating the donors as a fully ionised random distribution of charge gives far too much scattering than is observed experimentally. In fact, calculations over estimate the magnitude of the potential fluctuations by at least a factor of two. This is taken as evidence for some smoothing mechanism which could be due to correlations in the position of ionised donors. There is evidence for a small residual occupation of some donors at low temperatures because illumination increases both carrier concentration and mobility in the 2DEG by some 10%. In order to say anything further the scattering from such a partially occupied layer of donors needs to be considered.

The differences between the optimised GaAs-$Al_{0.3}Ga_{0.7}As$ heterostructure and one in which the $Al_{0.3}Ga_{0.7}As$ spacer is replaced by AlAs have also been extensively investigated. GaAs-AlAs can have higher mobilities but this reflects substantial free charge at low temperatures surrounding the donor region. This effectively screens some of the potential fluctuations due to the donors and as such is not a good measure of how much scattering there will be in a given wire because on forming the constriction this charge will most probably be depleted.

Appendix A

The Landauer-Büttiker Formalism

In order to accurately describe conduction through a region of space which has a particular transmission probability, it is necessary to take account all possible reflection and transmission processes associated with the various paths or leads which communicate with the region. Each lead (α, β, χ, δ) is assumed to be in thermal equilibrium with a reservoir characterised by a particular chemical potential ($\mu_{\alpha,\beta,\chi,\delta}$) above the equilibrium value of μ. In this picture, the total transmission probability $T_{\alpha\beta}$ between the leads α and β, can be expressed as

$$T_{\alpha\beta} = \sum_{n=1}^{N_\alpha} \sum_{m=1}^{N_\beta} \left| t_{\beta\alpha,mn} \right|^2 \tag{A1}$$

where $t_{\beta\alpha,mn}$ is the transmission probability amplitude from mode n in lead α to mode m in lead β. The sum accounts for the contribution to the total transmission probability from all the occupied sub-bands (N_α and N_β) in leads α and β. Consider a mode m propagating in lead α. This lead α will carry a current given by $(2e/h)N_\alpha\mu_\alpha$. Now a fraction of this current $T_{\alpha\beta}/N_\alpha$ will be transmitted into lead β, and a fraction R_α/N_α will be reflected back into reservoir α where the reflection probability R_α is given by

$$R_\alpha = \sum_{n=1}^{N_\alpha} \sum_{m=1}^{N_\alpha} \left| r_{\alpha\alpha,mn} \right|^2 \qquad (A2)$$

where $r_{\alpha\alpha,mn}$ is the reflection probability amplitude from mode n in lead α to mode m in lead α. The net current I_α propagating in lead α will be the sum of the incident current and reflected current such that

$$I_\alpha = \frac{2e}{h}(N_\alpha \mu_\alpha - R_\alpha \mu_\alpha) \qquad (A3)$$

However there is also a contribution to the current in lead α from the fraction of charge injected into the other leads connected to the sample which is then transmitted into lead α, see Equation A4 where the sum is over all the other leads in the system.

$$I_\beta = -\frac{2e}{h}\sum_{\beta}^{\beta \neq \alpha} T_{\beta\alpha}\mu_\beta \qquad (A4)$$

Hence adding A3 and A4 gives the actual net current propagating in lead α as

$$I_\alpha = \frac{2e}{h}\left\{ (N_\alpha - R_\alpha)\mu_\alpha - \sum_{\beta}^{\beta \neq \alpha} T_{\beta\alpha}\mu_\beta \right\} \qquad (A5)$$

Equation A5 was initially derived by Büttiker and is the generalisation to multi-leads of the two lead Landauer formula, see Equation 1.28, Chapter 1, Section 1.3.2. Hence the current in Equation A5 is related to the chemical potential via the conductance matrix

$$G_{\beta\alpha} = \frac{2e^2}{h}\left[(N_\beta - R_\beta)\delta_{\beta\alpha} - T_{\beta\alpha}\right] \tag{A6}$$

such that

$$I_\beta = \frac{1}{e}\sum_\alpha G_{\beta\alpha}\mu_\alpha \tag{A7}$$

Now current conservation requires that the total current incident in lead β must be equal to the sum of the total current leaving through all other leads. Hence

$$I_\beta = \frac{2e}{h}(N_\beta - R_\beta)\mu_\beta = \frac{2e}{h}\sum_\alpha^{\alpha\neq\beta} T_{\alpha\beta}\,\mu_{\alpha\beta} \tag{A8}$$

and so

$$(N_\beta - R_\beta) - \sum_\alpha^{\alpha\neq\beta} T_{\alpha\beta} = 0 \tag{A9}$$

Inspecting Equation A9 it is clear that the columns of $G_{\beta\alpha}$ must sum to zero. In addition, if all the chemical potentials are equal, then no current should flow in the system. Thus, setting Equation A7 to be equal to zero and substituting for $G_{\beta\alpha}$ gives

$$(N_\beta - R_\beta) - \sum_\alpha^{\alpha\neq\beta} T_{\beta\alpha} = 0 \tag{A10}$$

Inspecting Equation A10 it is clear that all the rows of $G_{\beta\alpha}$ must also sum to zero. Hence

$$\sum_{\alpha} T_{\beta\alpha} = \sum_{\alpha} T_{\alpha\beta} \qquad (A11)$$

Equations A11 and A8 can be used to simplify Equation A5 to give the simplified Landauer-Büttiker equation for the current flow in lead α taking into account reflection and transmission between all the leads in the system, see Equation A12.

$$I_\alpha = \frac{2e}{h} \sum_{\alpha}^{\alpha \neq \beta} T_{\beta\alpha}(\mu_\beta - \mu_\alpha) \qquad (A12)$$

Transport has now been described quite generally, in the sense that propagation in a system of n leads, can be fully understood by n equations of the type given in Equation A12.

Consider the example given in Figure A1, where their are two sets of leads either side of a barrier which has a transmission coefficient T. A current flows in a single mode from lead 1 to lead 2 such that $I_1 = I$ and $I_2 = -I$. In addition their are also weakly coupled leads (3 and 4) which draw negligible current i.e. $I_3 = I_4 = 0$ and have chemical potentials μ_3 and μ_4 respectively.

Figure A1: Schematic representation of a four terminal measurement of a region of space with a transmission probability T.
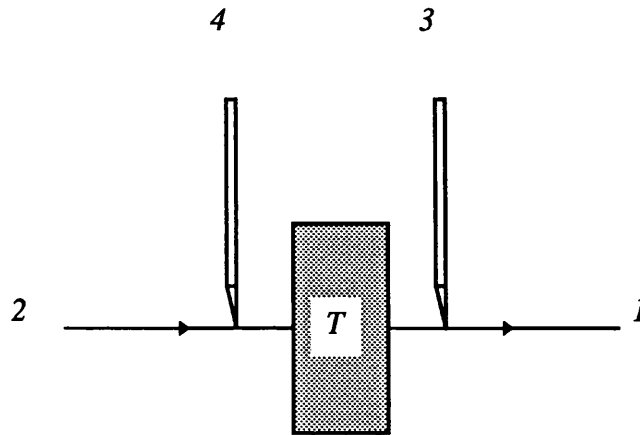
The two terminal conductance of the system is given by

$$G_{12,34} = \frac{eI}{\mu_3 - \mu_4}$$
(A13)

In order to calculate the four terminal conductance it is necessary to solve Equation A12 for the difference in the chemical potential μ_3-μ_4 between leads *3* and *4*. If this is done, the four terminal conductance is obtained as a function of the transmission probabilities between the various leads, see Equation A14.

$$G_{12,34} = \frac{2e^2}{h} \frac{(T_{31}T_{42} - T_{32}T_{41})}{(T_{21}T_{31} + T_{21}T_{32} + T_{31}T_{23})}$$
(A14)

Appendix B

Smearing of the Conductance Quantisation with Increasing Source-Drain Bias

The circuit used for measuring the conductance of a particular device is given in Figure B1.

Figure B1: Circuit diagram of the electrical configuration for the smearing of the conductance quantisation with increasing source-drain bias.
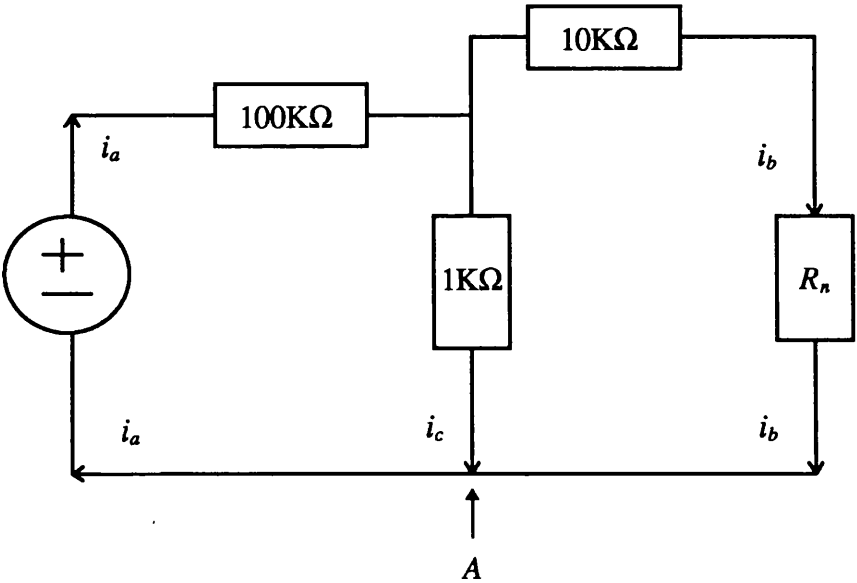
All the values shown are resistance's in $K\Omega$. The excitation voltage V from the lock in amplifier is essentially applied across a potential divider ($100K\Omega$:$1K\Omega$)

before being dropped across a 10KΩ resistor in series with the device. The device resistance R_n is measured at a fixed excitation voltage as a function of the gate voltage. The measurement is repeated at a series of higher excitation voltages until the quantisation of the resistance becomes completely smoothed out. In order to determine at what voltage a particular conductance plateaux smears at, it is necessary to know the actual voltage developed across the device as a function of the gate voltage. Because the resistance of the device changes with the applied gate voltage, the voltage developed across the device for each plateaux will be different. As a result, each plateaux will be subject to a different source-drain bias for the same excitation voltage. In order to determine these smearing voltages, Kirchhoff's rules for the algebraic sums of currents and voltages are applied to the circuit given in Figure B1.

$$-i_a + i_b + i_c = 0 \tag{B1}$$

$$-V + V_{100} + V_1 = 0 \tag{B2}$$

and

$$-V_1 + V_{10} + V_n = 0 \tag{B3}$$

If the voltage developed across the 100KΩ, 10KΩ and 1KΩ resistors are given respectively by V_{100}, V_{10} and V_1 and the voltage generated across the device with a resistance R_n in KΩ (i.e. n propagating sub-bands) is V_n, then applying Ohm's law to B1-3 and solving for V gives

$$V = \frac{(1110 + 101R_n)V_n}{R_n} \tag{B4}$$

Equation B4 now allows the voltage dropped across the device V_n (corresponding to that experienced by the nth plateaux) to be determined. Equation 1.38 from Chapter 1 Section 1.3.4 can now be used to determine an equivalent electronic smearing temperature T_n for each of the n propagating sub-bands, see Equation B5

$$T_n \equiv \frac{eV_n}{4k_B}$$
(B5)

An important consideration in the analysis above is the errors that can be expected in an estimation of an electronic smearing temperature. These errors come mainly from contact resistance's due to non-ideal Ohmic contacts and uncertainty in the circuit resistance's. The typical contact resistance's in the measurements presented in Chapter 5 were generally of the order of 450Ω. The uncertainty in the circuit resistance's are ±1%, giving a combined error of ±3%. Hence the expected random error associated with the estimation of the electronic smearing temperatures is given by Equation B6 where n is the sub-band index.

$$\delta T_e \approx \pm\left(3\% + 100\frac{450}{h/2ne^2}\right)$$
(B6)

Finally the use of a low frequency a.c. signal, instead of a d.c. bias, also introduces a systematic error into the analysis due to the variation in the voltage across the device at different points in the a.c. cycle. Hence all the measurements are internally consistent but care must be taken in treating the results in more than a semi-quantitative manner.

Appendix C

Impurity Scattering in a 2DEG

Elastic Impurity scattering in a two dimensional electron gas can be treated as a time dependent perturbation problem where the perturbation acts only for a finite time. In this case the problem can be solved through the application of Fermi's Golden Rule

$$W_{fi} = \frac{2\pi}{\hbar} \left| V_{fi} \right|^2 \delta \left(\varepsilon_f - \varepsilon_i \right) \tag{C1}$$

where W_{if} describes the transition rate from an initial state i to any final state f and V_{fi} denotes the matrix element associated with the perturbing Hamiltonian i.e. an actual scattering centre, see Equation C2.

$$V_{fi} = \left\langle \phi_f \left| \hat{V} \right| \phi_i \right\rangle \tag{C2}$$

The eigenstates of the initial and final states each have a well defined momentum associated with free electron motion in a 2DEG, see Figure C1.

$$\phi_i = \frac{1}{\sqrt{A}} e^{i \underline{k} \cdot \underline{r}} \quad \text{and} \quad \phi_f = \frac{1}{\sqrt{A}} e^{i(\underline{k} + \underline{q}) \cdot \underline{r}} \tag{C3}$$

For this process the eigenstates are plane waves, normalised to a density of one particle in an area A of the 2DEG, see Equation C3.

Figure C1: Illustration of the elastic scattering of an electron with wavevector $\underline{k}$ through an angle θ to a final state with wavevector $\underline{k}+\underline{q}$.
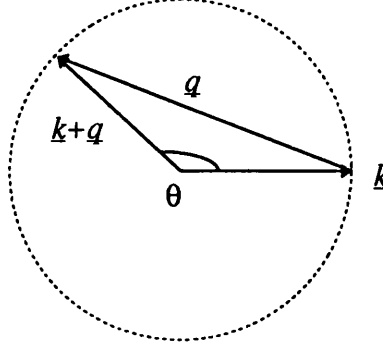
The problem is now reduced to finding the probability that a particle with wavevector $\underline{k}$ ends up in a state with a wavevector $\underline{k}+\underline{q}$. In order to resolve this, it is necessary to find the matrix element of the perturbation Hamiltonian between these two states i.e.

$$V_{fi} = \left\langle \underline{k}+\underline{q} \left| \hat{V} \right| \underline{k} \right\rangle = \int \phi_f^* \hat{V} \phi_i dr^2 = \frac{1}{A} \int e^{i(\underline{k}+\underline{q})\cdot\underline{r}} v(\underline{r}-\underline{r_i}) e^{i\underline{k}\cdot\underline{r}} dr^2 \qquad (C4)$$

where the perturbation operator is just the energy of interaction $v(\underline{r}-\underline{r_i})$, which is the potential energy at a point $\underline{r}$ in the plane of a 2DEG, due to a donor at a height s above $\underline{r_i}$, see Equation C5.

$$v(\underline{r}-\underline{r_i}) = \frac{e^2}{4\pi\kappa\varepsilon_0} \left[\frac{1}{\sqrt{\left|r-\underline{r_i}\right|^2 + s^2}} - \frac{1}{\sqrt{\left|\underline{r}-\underline{r_i}\right|^2 + (s+2c)^2}} \right] \qquad (C5)$$

Substituting Equation C5 into Equation C4 and evaluating the integral gives

$$V_{fi} = \frac{1}{A} \frac{e^2}{4\pi\kappa\varepsilon_0} \frac{2\pi}{q} \left[e^{-sq} - e^{-(s+2c)q} \right] = \frac{1}{A} \tilde{v}(\underline{q})$$ (C6)

where

$$\tilde{v}(\underline{q}) = \frac{e^2}{4\pi\kappa\varepsilon_0} \frac{2\pi}{q} \left[e^{-sq} - e^{-(s+2c)q} \right]$$ (C7)

is the Fourier transform of the scattering potential $v(\underline{r}-\underline{r_i})$. If the density of electrons in the 2DEG is high, then the potential from the donors will be screened somewhat. To take account of this factor, the linear Thomas-Fermi screening approximation is used, the effect of which is to introduce the Thomas-Fermi wavevector $q_{TF}=2/a_0$ where a_0 (=10nm) is the scaled Bohr radius for GaAs. Thus Equation C7 becomes

$$\tilde{v}(\underline{q}) = \frac{e^2}{4\pi\kappa\varepsilon_0} \frac{2\pi}{q+q_{TF}} \left[e^{-sq} - e^{-(s+2c)q} \right]$$ (C8)

and substituting into C1 gives the scattering rate as

$$W_{fi} = \frac{2\pi}{\hbar} \frac{1}{A^2} \left| \tilde{v}(\underline{q}) \right|^2 \delta\left(\varepsilon(\underline{k}+\underline{q}) - \varepsilon(\underline{k}) \right)$$ (C9)

All that is required now is to sum Equation C9 over all the possible final states to account for all possible changes in the wavevector $\underline{q}$ i.e. the total scattering rate from state i, due to a single impurity is given by

$$\frac{1}{\tau_i} = \sum_q W_{fi}\left(\underline{k}+\underline{q},\underline{k}\right)$$

This can be express in the form of an integration for incident electrons with wavevectors $\underline{k}_F$, see Equation C10 where the pre-factor is the density of states in two dimensional k-space.

$$\frac{1}{\tau_i} = \sum_q W_{fi}\left(\underline{k}_F+\underline{q},\underline{k}_F\right) = \frac{A}{(2\pi)^2}\int W_{fi}\left(\underline{k}_F+\underline{q},\underline{k}_F\right)d\underline{q} \qquad (C10)$$

The scattering from AN_d independent impurities (where N_d is the density of donors in the δ-layer) is then simply

$$\frac{1}{\tau_{total}} = AN_d \times \frac{1}{\tau_i} = AN_d \times \frac{A}{(2\pi)^2}\int W_{fi}\left(\underline{k}_F+\underline{q},\underline{k}_F\right)d\underline{q}$$

$$= \frac{N_d A^2}{(2\pi)^2}\int \frac{2\pi}{\hbar A^2}\left|\tilde{v}(\underline{q})\right|^2 \delta\left(\varepsilon\,(\underline{k}_F+\underline{q})-\varepsilon\,(\underline{k}_F)\right)d\underline{q}$$

evaluating the delta function and putting in the limits of integration gives

$$\frac{1}{\tau_{total}} = \frac{N_d A^2}{(2\pi)^2}\int\limits_0^{2k_F} \frac{2\pi}{\hbar A}\left|\tilde{v}(\underline{q})\right|^2 d\underline{q} \qquad (C11)$$

The only problem with C11 is that it weights all scattering events equally. This means that events involving a large change in the electron's wavevector contribute just as much to the scattering rate as small angle scattering. In transport experiments, one measures a scattering rate associated with a transport lifetime which is robust to small angle scattering. However scattering involving large angles effect the current and hence the transport lifetime to a much greater degree.

Consider the picture illustrated in Figure C1. The component of the scattered electron's motion parallel to its original direction is proportional to $cos\theta$. Hence, it would be reasonable to expect that the change in this function would be a good measure of the importance of the scattering event. Weighting the transport lifetime by including the change in this function (1-$cos\theta$ or $q^2/2k_F^2$) does in fact give a good comparison with experimental data. The total lifetime associated with the scattering is now

$$\frac{1}{\tau_{total}} = \frac{N_d A^2}{(2\pi)^2} \int_0^{2k_F} \frac{2\pi}{\hbar A^2} \frac{q^2}{2k_F^2} \left| \tilde{v}(\underline{q}) \right|^2 d\underline{q} \tag{C12}$$

Writing Equation C12 in terms of the mean free path l and converting from $d\underline{q}$ to dq gives

$$\frac{1}{l} = \frac{1}{v_F} \frac{1}{\tau_{total}} = \frac{1}{v_F} \frac{N_d}{2\pi\hbar} \int_0^{2k_F} \frac{\left(q^2\!\!\big/2k_F^2\right)}{\sqrt{1-\left(q\!\!\big/2k_F\right)^2}} \left| \tilde{v}(\underline{q}) \right|^2 dq \tag{C13}$$

Substituting C8 into C13 and evaluating the integral gives the final expression for scattering in a two dimensional electron gas with an electron density n_{2D} as

$$\frac{1}{l} \approx \frac{N_d}{32\pi n_{2D}} \left[\frac{1}{s^3} + \frac{1}{(s+2c)^3} - 2\frac{1}{(s+c)^3} \right] \tag{C14}$$